



# **Fretting Wear Studies of Aeroengine Materials**

By Hian Ping Soh BSc (Hons.)

**GEORGE GREEN LIBRARY OF  
SCIENCE AND ENGINEERING**

Thesis submitted to the University of Nottingham for the degree of  
Doctor of Philosophy, June 2006

## **TABLE OF CONTENTS**

### **Contents**

1. Abstract .....	i
2. Acknowledgements .....	iii
3. List of Tables .....	v
4. List of Figures.....	vii
5. Notations.....	xv

### **Chapter 1: Introduction**

1.1 Historical review of aviation engines .....	1
1.2 Gas turbine engines and splined joint couplings .....	2
1.3 Mechanical problems of splined joint couplings .....	3
1.4 Transmission materials for design requirements.....	5
1.5 Research motivation and scope of thesis.....	7

### **Chapter 2: Literature review**

#### 2.1 Introduction

2.1.1 Historical review on tribology .....	17
--------------------------------------------	----

#### 2.2 Friction and surface damage mechanisms

2.2.1 Definition of friction .....	18
2.2.2 Classification of surface damage mechanisms .....	19

#### 2.3 Fretting wear

2.3.1 Reviews on fretting.....	20
2.3.2 Fretting mechanism .....	22
2.3.3 Fretting parametric types.....	24

#### 2.4 Prevention methods

2.4.1 Introduction .....	31
2.4.2 Surface engineering .....	32
2.4.3 Lubrication – boundary lubrication regime .....	33

#### 2.5 Fretting wear model

2.5.1 Contact mechanics and fretting wear simulation methodology ....	36
-----------------------------------------------------------------------	----

## **Chapter 3: Aeroengine transmission materials**

<b><u>3.1 General</u></b> .....	59
<b><u>3.2 Super S/CMV (SCMV)</u></b>	
3.2.1 Material characteristic.....	60
3.2.2 The effect of gas nitriding.....	60
<b><u>3.3 AerMet®100 (A100)</u></b>	
3.3.1 Material characteristic.....	62
3.3.2 The effect of alloying elements .....	64
<b><u>3.4 Inconel 718 (718)</u></b>	
3.4.1 Material characteristic.....	66
3.4.2 Strengthening precipitates.....	67
3.4.3 Temperature effect on oxidation behaviour .....	68

## **Chapter 4: Methods**

### **4.1 Specimen preparation**

4.1.1 Test specimens and heat treatments .....	86
4.1.2 Cross-sectioned samples for metallographic examination .....	87

### **4.2 Test equipment for fretting wear evaluation**

4.2.1 Specimen attachment .....	88
4.2.2 Relative displacement generation .....	89
4.2.3 Measurement of tangential force .....	89
4.2.4 Normal load application .....	90
4.2.5 Acquisition of mechanical data .....	90
4.2.6 Calibration of servo electromagnetic vibrational rig .....	91
4.2.7 Centralising of force-displacement loop .....	92

### **4.3 Assessment and characterisation of wear surface**

4.3.1 Surface profilometry .....	92
4.3.2 Scanning electron microscopy (SEM) .....	93
4.3.3 Transmission electron microscopy (TEM) .....	94
4.3.4 X-ray Diffraction (XRD) .....	95
4.3.5 Energy dispersive X-rays (EDX) .....	95

## **Chapter 5:The effect of nitriding and minimal lubrication on Super S/CMV alloy**

<u>5.1 Introduction</u> .....	110
<b><u>5.2 Methods</u></b>	
5.2.1 Materials and specimens .....	110
5.2.2 Fretting tests .....	111
5.2.3 Characterisation .....	111
<b><u>5.3 Results</u></b>	
5.3.1 Coefficient of friction evolution.....	112
5.3.2 Wear coefficient evolution .....	113
5.3.3 Microscopic examination of wear scars.....	113
5.3.4 Finite element analysis .....	114
<u>5.4 Discussion</u> .....	116
<u>References</u> .....	120

## **Chapter 6:The effect of moderate temperatures on Inconel 718 superalloys**

<u>6.1 Introduction</u> .....	137
<b><u>6.2 Methods</u></b>	
6.2.1 Materials and specimens .....	138
6.2.2 Characterisation .....	138
<b><u>6.3 Results</u></b>	
6.3.1 Coefficient of friction evolution .....	138
6.3.2 Wear coefficient evolution .....	139
6.3.3 Wear volume .....	139
6.3.4 Wear surface profiles .....	139
6.3.5 Microscopic examination of wear scars .....	140
6.3.6 Elemental and X-ray diffraction analysis .....	141
6.3.7 Observation of $\gamma'$ -, $\gamma''$ - and $\delta$ - phases .....	142
<u>6.4 Discussion</u> .....	142
<u>References</u> .....	148

## **Chapter 7:The effect of different material combinations on fretting wear**

<b><u>7.1 Introduction</u></b> .....	164
<b><u>7.2 Methods</u></b>	
<b>7.2.1 Materials and specimens</b> .....	165
<b>7.2.2 Fretting tests</b> .....	165
<b>7.2.3 Characterisation</b> .....	165
<b><u>7.3 Results</u></b>	
<b>7.3.1 Coefficient of friction evolution</b> .....	165
<b>7.3.2 Wear coefficient evolution</b> .....	167
<b>7.3.3 Microscopic examination of wear scars</b> .....	168
<b>7.3.4 Oxidised wear debris</b> .....	171
<b>7.3.5 EDX analysis</b> .....	173
<b><u>7.4 Discussion</u></b> .....	173
<b><u>7.5 Summary</u></b> .....	179
<b><u>References</u></b> .....	179
<b><u>Chapter 8:Final discussion</u></b> .....	199
<b><u>Chapter 9: Conclusions</u></b> .....	206
<b><u>Chapter 10:Future work</u></b> .....	209

## **Abstract**

As long as there is a certain degree of flexibility i.e. relative motion, the contacting surface of a mechanical component will experience fretting damage, in the form of fretting wear and/or fretting fatigue, depending on the loading conditions and performance requirements.

In the present investigations, the fretting wear behaviour of aeroengine materials were studied by both experimental (mainly gross slip regime) and finite element approaches involving the various aspects of fretting variables (applied normal load, strokes, wear duration, material hardness, lubrication and etc.) that affects the material tribosystem. The aeroengine materials are the Super S/CMV and AerMet®100 ultrahigh strength steel alloys and Inconel 718 nickel-base superalloys. The present works highlights a number of issues important to fretting damage, which involves studying: (1) the effect of nitriding and lubrication on Super S/CMV steel experimentally and wear data validation and prediction by FEM based on a modified Archard's equation; (2) the effect of moderate temperature on the fretting behaviour of Inconel 718 alloy; (3) the different material combinations (Super S/CMV, AerMet®100, and Inconel 718) on fretting wear.

The following experimental tools are utilised to investigate the morphological changes of the contacting surfaces during fretting. A simple crossed round-on-flat arrangement was used to determine the coefficients of friction and the wear coefficients applicable to the contact configuration and loading conditions. Surface topography changes were investigated by scanning electron microscopy (SEM) and transmission electron microscopy (TEM). The presence of various phases and elements were analysed by x-ray diffraction

(XRD) and energy dispersive x-ray (EDX). The wear depth and wear width were profiled using a surface profilometer for the wear coefficient calculation. The use of FE simulation was to validate and predict the wear data. The evolution of contact geometry and contact variables, including contact pressure and relative slip were studied. The implications of these predicted results are discussed with respect to fretting fatigue prediction, leading to new insight into the experimentally-observed effects of slip regime on crack initiation.

## **Acknowledgements**

First and foremost, I would like to take this opportunity to extend my gratitude to many people for their support in making this research a possible achievement. I would like to thank my research supervisors, Dr. Ian R McColl and Dr. Sean B Leen for their patience and guidance throughout the years. Special thanks to Keith Dinsdale and Aubrey Martin, for providing me the essential technical knowledge in preparation for the experimental work and providing guidance in operating the laboratory equipments. I am also grateful to Nicola Bock and Julie Wells for helping me out with the microscopy sessions and developing my TEM negatives. As for my research group, UTC Gas Turbine Transmission Systems, I would like to thank Dr. Jian Ding, for sharing his knowledge about contact mechanics and discussion on his research (similar research background), Dr. Wei Siang Sum (Derek) and Dr. Christian Ratsimba for the discussion about spline coupling designs, and finally, Paul Wavish for sharing his thoughts/suggestions on fretting rig design. Also, many thanks to Dr. Thomas Hyde and Nina Banerjee for providing me the aeroengine materials and gas-nitriding my samples. It was a great pleasure to work with the school technicians and my fellow UTC researchers.

Most importantly, my warmest gratitude is extended to my family for their unconditional moral support and encouragement through all the ups and downs of my research and studies. Also, to my fellow gamelan musicians (Matthew Godfrey, Timothy Williams, Jim Walker, Stewart McCoy, Helen Aldred, Ceri Howells, Hazlyna Kamaruddin) Kayu Gangsa, I would like to thank them for their encouragement and their teaching on teamwork and patience throughout my write-up period. Ah yes, many thanks to Nusantara (Maziah Omar, Alan Humberstone, Norman Musa, Ingrid Yew) for developing my creativity that has helped me during

the difficult times of my work - relaxation. Lastly, I am indebted to Mark Krohn, whom has helped me in proof-reading and correcting my drafts of this thesis.

This was funded by Rolls Royce plc and was carried out at the Rolls Royce University Technology Centre for Gas Turbine Transmission System at the University of Nottingham.

***“No idea is so soaring but it will readily put forth roots”*** *-Thoreau-*

## LIST OF TABLES

- Table 3-1 Chemical composition of the specimen material (mass%).
- Table 3-2 The mechanical properties of the various aeroengine materials.
- Table 3-3 Detailed descriptions for each nitrided sub-layer (Refer to Figure 3-2a).
- Table 5-1 Fretting test conditions.
- Table 5-2 Measured final COF, scar depth/width and wear coefficient (after 5,000 cycles).
- Table 5-3 Averaged debris thickness and debris oxygen content from nitrided-against-nitrided and non-nitrided-against-nitrided flat specimens.
- Table 5-4 Comparison of wear coefficient between boundary-lubricated and non-lubricated tests from the nitrided flat-against-non-nitrided round test.
- Table 5-5 Elemental analysis of worn surface (boundary-lubricated) and unworn surface area (mass %) from the nitrided flat-against-non-nitrided round.
- Table 5-6 Predicted maximum wear depths and widths for flat specimens (non-lubricated condition).
- Table 6-1 Fretting test conditions.
- Table 6-2 The average COF and wear coefficient for the four test temperatures.
- Table 6-3 Average adhered debris thickness across scar corresponding to the worn specimens of the four temperature tests.
- Table 6-4 Wear volume versus temperature fretting tests.
- Table 6-5 EDX analyses (mass%) on the worn flat surface for the four test temperatures.
- Table 6-6 Dimension of  $\delta$  phase estimated from the worn flat specimen at each test temperature.
- Table 6-7 Free energies of formation for the key oxides formed at 727°C under conditions of static oxidation [8].

- Table 7-1** Fretting test conditions.
- Table 7-2** Initial maximum Hertzian stress.
- Table 7-3** The steady-state COF (after 5,000 cycles) for the various material pairs at 500 N tested for a duration of 100,000 cycles.
- Table 7-4** (a) The averaged wear coefficient data of the self-against-self pairs and (b) self-against-nonsel pairs fretted at 500 N and 100,000 wear cycles as a function of stroke.
- Table 7-5** Loose wear debris colours collected from the fretting test.
- Table 7-6** EDX analyses of the worn surfaces (mass%): (a) Self-against-self pairs and (b) self-against-nonsel pairs.

## **LIST OF FIGURES**

- Figure 1-1 General arrangement of three shafts, high-bypass aeroengines [2].
- Figure 1-2 A FE model of a spline coupling connection [17].
- Figure 1-3 Schematic representation of a spline coupling: (a) axial section and (b) cross-section [17].
- Figure 1-4 The importance of mechanical properties that is used for selected combat aircraft [18].
- Figure 1-5 Distribution of materials in structural application throughout the twentieth century [18].
- Figure 1-6 Maximum operating temperatures of existing aeroengine materials [18].
- Figure 2-1 Debris formation caused by mechanical interlocking between contacting asperities [27].
- Figure 2-2 Determination of fretting regimes based on friction log [28].
- Figure 2-3 Different regimes of wear dependent on the slip amplitudes [39, 40].
- Figure 2-4 Feng and Uhlig [51] experimentally showed that the amount of material removal is proportional to applied normal load at constant slip amplitude.
- Figure 2-5 Wear damage is accelerated when both fretting and normal vibration are combined [53].
- Figure 2-6 Ejection of debris is determined by the direction of motion and contact geometry [56].
- Figure 2-7 Classification of different surface engineering methods for various applications [70].
- Figure 2-8 Various surface modification choices available for improving the hardness profile of steels [4].

- Figure 2-9 Production of various engineered surfaces thicknesses by different plating and deposition techniques [71].
- Figure 2-10 Polar diagram representing the parameters used to determine suitable coating type [72].
- Figure 2-11 Detailed classification of lubrication modes for tribological applications [74].
- Figure 2-12 Stribeck curve representing different lubrication regimes changes with coefficient of friction as a function of lubricant parameter,  $\eta VP^{-1}$  [74].
- Figure 2-13 Different boundary lubrication regimes associated with the change in load in relation to sliding velocity [75].
- Figure 2-14 A two-dimensional FE simple round-on-flat model [89].
- Figure 2-15 Contact pressure comparison between FE predicted and Hertzian analytical solution under a normal load of 1200 N [89].
- Figure 2-16 Sub-surface stresses comparison between FE predicted and Hertzian analytical solution under a normal load of 1200 N [89].
- Figure 2-17 Flow chart representing the methodology used in modelling the wear simulation tool [92].
- Figure 3-1 An etched SCMV alloy surface that reveals tempered martensite and white particles.
- Figure 3-2 (a) A micrograph showing cross-section view of an etched nitrided SCMV (Refer to Table 3-3), (b) a micrograph plan view of the nitrided layer (porous-like), and (c) XRD analysis of the nitrided layer.
- Figure 3-3 Schematic illustration of wear resistance as a function of the distance from the surface that varies from different nitride zones [8].
- Figure 3-4 Measured microhardness versus surface depth plot on the nitrided layer for SCMV.
- Figure 3-5 The time-temperature transition diagram of A100 [15].

- Figure 3-6 Low magnification of A100 alloy after etching.
- Figure 3-7 Different parts of the gas turbine engine components operate at various temperatures [32].
- Figure 3-8 The etched Inconel 718 surface revealing some twin boundaries.
- Figure 3-9 The time-temperature transition diagram of 718 [27].
- Figure 3-10 The different mechanisms involved in the glaze oxide formation at elevated temperature application [36].
- Figure 3-11 The sequences of  $\text{Cr}_2\text{O}_3$  protective layer formation [37]
- Figure 4-1 Drawings of (a) untreated specimen blanks and (b) flat and round specimens. All dimensions are in mm scale.
- Figure 4-2 Microhardness (HV0.1) versus distance from surface after heat treatment and removal of decarburized layer for Super S/CMV, AerMet®100, and Inconel 718. Each data point represents one hardness reading.
- Figure 4-3 Schematic arrangement of fretting drive and data acquisition.
- Figure 4-4 Photographs of the (a) complete fretting rig and (b) the controlling unit.
- Figure 4-5 Fretting wear machine: (a) Specimen mounting blocks and drive arm arrangement and (b) a pair of mounted specimen.
- Figure 4-6 Lower specimen mounting block and high temperature LVDT.
- Figure 4-7 Upper specimen mounting block (inverted) and strain gauged drive arm.
- Figure 4-8 Experimental tangential load versus displacement. Each loop consisting of 60 data points.
- Figure 4-9 Schematic arrangement used to calibrate (a) tangential force and (b) relative displacement.
- Figure 4-10 Calibration curves for (a) tangential force and (b) relative displacement [1].

- Figure 4-11 Centralised average waveforms for (a) tangential force and (b) relative displacement for  $N$  to  $N+3$  cycles [1].
- Figure 4-12 Typical two-dimensional wear depth and width profiles of (a) flat and (b) round specimens.
- Figure 4-13 Typical three dimensional surface profiles for worn specimens: (a) flat and (b) round.
- Figure 5-1 The force-displacement loop from the nitrided-against-nitrided test for the various wear cycle interval (50  $\mu\text{m}$  and 500 N).
- Figure 5-2 Coefficient of friction from the round-against-flat tests: Curve A: non-lubricated, Curves B and D: upper and lower bounds for boundary lubrication, and Curve C: typical for boundary lubrication. Contact load = 500 N, stroke = 50  $\mu\text{m}$ .
- Figure 5-3 The BEI of the boundary-lubricated nitrided-against-non-nitrided test, taken on the flat specimen.
- Figure 5-4 BEI cross sections on the centre region of the worn nitrided flat specimen (nitrided-against-nitrided) tested at 50  $\mu\text{m}$  and 500 N, non-lubricated: (a) 9,000 cycles (b) 100,000 cycles. The wear scar section is parallel to the stroke direction.
- Figure 5-5 BEI images of nitrided flat specimen from the nitrided-against-nitrided test after 9,000 cycles, non-lubricated: (a) full scar width (b) higher magnification view of centre region. Applied load=500 N, stroke=50  $\mu\text{m}$
- Figure 5-6 BEI images of non-nitrided flat specimen from the non-nitrided-against-nitrided test after 18,000 cycles, non-lubricated: (a) full scar width (b) higher magnification view of centre region. Applied load=500 N, stroke=50  $\mu\text{m}$ .
- Figure 5-7 BEI images of nitrided flat specimen from the nitrided-against-nitrided test after 100,000 cycles, boundary lubrication: (a) full scar width, (b) higher magnification of the worn surface, and (c) nitrided layer near the wear scar periphery. Applied load=500 N, stroke=50  $\mu\text{m}$ .

- Figure 5-8 The essential tools for the fretting wear simulation programme: (a) A simple two-dimensional round-on-flat schematic model and (b) flowchart representing the loading history used to simulate the experimental fretting rig condition [2].
- Figure 5-9 FE predictions corresponding to the nitrided-against-nitrided test for 50  $\mu\text{m}$  stroke, 500 N load up to 18,000 cycles, non-lubricated: (a) Contact pressure and (b) slip distributions at instant of zero tangential displacement.
- Figure 5-10 FE predictions corresponding to nitrided-against-nitrided test for 50  $\mu\text{m}$  stroke and 500 N load up to 18,000 cycles, non-lubricated condition: (a) Normal stress  $\sigma_x$  and (b) shear stress  $\tau_{xy}$  ( $x$  parallel to surface and  $y$  normal to surface). This condition is at instant of maximum ( $+\delta^*$ ) tangential displacement.
- Figure 5-11 Variation of contact pressure distribution with the applied tangential displacement during 18,000<sup>th</sup> cycle under 185 N normal load case [2].
- Figure 6-1 COF evolution versus number of cycles and temperature.
- Figure 6-2 Steady-state COF (after 70,000 cycles) versus temperature.
- Figure 6-3 Experimental force-displacement loops at 200,000 cycles for different test temperatures. The enclosed area represents the amount of energy dissipated during fretting (refer to Table 6-1 for test conditions).
- Figure 6-4 Wear scar profiles taken after 200,000 cycles corresponds to the four temperature tests: (a) flat and (b) round specimen.
- Figure 6-5 BEIs of wear scars corresponding to the worn flat specimens after 200,000 cycles, test temperature: (a) 22°C, (b) 150°C, (c) 300°C, and (d) 450°C (refer to Table 6-1 for test conditions).
- Figure 6-6 High magnification SEI and BEI corresponding to the worn flat specimen after 200,000 cycles, test temperature: (a) BEI at 22°C, (b) SEI at 150°C, (c) BEI at 300°C, and (d) SEI at 450°C (refer to Table 6-1 for test conditions).

- Figure 6-7 BEI cross sections of wear scars on worn flat specimens after 200,000 cycles, test temperature: (a) BEI at 22°C ,(b) BEI at 150°C ,(c) SEI at 300°C, and (d) SEI at 450°C (refer to Table 6-1 for test conditions).
- Figure 6-8 Schematic diagram representing the interchanging alloying elements within the glaze oxide.
- Figure 6-9 XRD detection of oxide phases corresponds to the 718 alloy wear debris: (a) at 22°C and (b) 450°C. Note that Figure 6-9(a) represents the XRD data for the 22°C, 150°C and 300°C cases (qualitatively similar).
- Figure 6-10 BEI of the  $\delta$  phase (white precipitate) versus temperature where the samples were taken from worn flat specimen and fretted for 2 hours 47 min: (a) 22°C, (b) 150°C, (c) 300°C and (d) 450°C (refer to Table 6-1 for test conditions).
- Figure 6-11 TEM micrographs of 718 alloy at 450°C: (a) General structure of 718 material ,(b) Dark field image of  $\gamma''$  ,(c) Bright field image of  $\gamma''$  and (d)  $\gamma''$  SAD patterns on the (111) plane.
- Figure 6-12 Bright field imaging of the  $\gamma'$  and  $\gamma''$  phases at 450°C (sample taken from a worn flat specimen).
- Figures 7-1 The initial ‘run-in’ period of COF evolutions from the 100,000 cycles for the self-against-self and self-against-nonsel pairs at strokes of (a) 20  $\mu\text{m}$ , (b) 50  $\mu\text{m}$ , and (c) 100  $\mu\text{m}$  (Refer to Table 7-1 for the test conditions).
- Figure 7-2 The backscattered images (BEI) of the worn surface tested and wear debris morphology at 20  $\mu\text{m}$ , 500 N and 100,000 cycles: (a) SCMV<sub>(f)</sub>//SCMV<sub>(r)</sub>, (b) A100<sub>(f)</sub>//A100<sub>(r)</sub>, and (c) 718<sub>(f)</sub>//718<sub>(r)</sub>, (d) SCMV<sub>(f)</sub>//SCMV<sub>(r)</sub>, (e) A100<sub>(f)</sub>//A100<sub>(r)</sub>, and (f) 718<sub>(f)</sub>//718<sub>(r)</sub> (refer to Table 7-1 for the test conditions).
- Figure 7-3 Backscattered images (BEI) of the worn surface tested at 50  $\mu\text{m}$ , 500 N and 100,000 cycles: (a) SCMV<sub>(f)</sub>//SCMV<sub>(r)</sub>, (b) A100<sub>(f)</sub>//A100<sub>(r)</sub>, and (c) 718<sub>(f)</sub>//718<sub>(r)</sub>.

- Figure 7-4 Backscattered images (BEI) of the worn surface tested at 100  $\mu\text{m}$ , 500 N and 100,000 cycles: (a)  $\text{SCMV}_{(\text{f})}/\text{SCMV}_{(\text{r})}$ , (b)  $\text{A}100_{(\text{f})}/\text{A}100_{(\text{r})}$ , (c)  $718_{(\text{f})}/718_{(\text{r})}$ , (d) the backscattered image (BEI) showing uniform distribution of the wear debris on the wear scar at 100  $\mu\text{m}$ , and (e) the secondary image (SEI) showed the worn surface to have regular wear topography feature.
- Figure 7-5 BEI of the worn areas on the flat specimens at a stroke of 20  $\mu\text{m}$ : (a) End of contact edge ( $\text{SCMV}_{(\text{f})}/718_{(\text{r})}$ ), (b) Along all scar length ( $\text{SCMV}_{(\text{f})}/\text{A}100_{(\text{r})}$ ) and, (c) Contact edges along scar width ( $718_{(\text{f})}/\text{A}100_{(\text{r})}$ ).
- Figure 7-6 BEI of the worn areas on the round specimens at a stroke of 20  $\mu\text{m}$ : (a) Along all scar width ( $\text{SCMV}_{(\text{f})}/718_{(\text{r})}$ ), (b) Centre region ( $\text{SCMV}_{(\text{f})}/\text{A}100_{(\text{r})}$ ) and, (c) Along all scar width ( $718_{(\text{f})}/\text{A}100_{(\text{r})}$ ).
- Figure 7-7 BEI of the worn areas on the flat specimens at a stroke of 50  $\mu\text{m}$ : (a) Along all scar width ( $\text{SCMV}_{(\text{f})}/718_{(\text{r})}$ ), (b) Centre region ( $\text{SCMV}_{(\text{f})}/\text{A}100_{(\text{r})}$ ) and, (c) Random along scar width ( $718_{(\text{f})}/\text{A}100_{(\text{r})}$ ).
- Figure 7-8 BEI of the worn areas on the round specimens at a stroke of 50  $\mu\text{m}$ : (a) Along all scar width ( $\text{SCMV}_{(\text{f})}/718_{(\text{r})}$ ), (b) Along all scar width ( $\text{SCMV}_{(\text{f})}/\text{A}100_{(\text{r})}$ ) and, (c) Along all scar width ( $718_{(\text{f})}/\text{A}100_{(\text{r})}$ ).
- Figure 7-9 BEI of the worn areas on the flat specimens at a stroke of 100  $\mu\text{m}$ : (a) Along all scar width ( $\text{SCMV}_{(\text{f})}/718_{(\text{r})}$ ), (b) Along all scar width ( $\text{SCMV}_{(\text{f})}/\text{A}100_{(\text{r})}$ ) and, (c) Along all scar width ( $718_{(\text{f})}/\text{A}100_{(\text{r})}$ ).
- Figure 7-10 BEI of the worn areas on the round specimens at a stroke of 100  $\mu\text{m}$ : (a) Along all scar width ( $\text{SCMV}_{(\text{f})}/718_{(\text{r})}$ ), (b) Along all scar width ( $\text{SCMV}_{(\text{f})}/\text{A}100_{(\text{r})}$ ), and (c) Along all scar width ( $718_{(\text{f})}/\text{A}100_{(\text{r})}$ ).
- Figure 7-11 BEI of the different debris morphological features for the various material pairs (from flat specimen): (a) Smeared debris at 20  $\mu\text{m}$  stroke ( $\text{SCMV}_{(\text{f})}/\text{SCMV}_{(\text{r})}$ ) (b) Semi-particulate and smooth debris layers at 50

$\mu\text{m}$  stroke ( $\text{SCMV}_{(f)}//\text{A}100_{(r)}$ ), (c) Particulate-like debris feature of the three self-against-nonself pairs at  $100 \mu\text{m}$  stroke ( $\text{SCMV}_{(f)}//718_{(r)}$ ).

- Figure 7-12 The cross-sectioned view of the different debris layer thickness :(a)  $20 \mu\text{m}$ , (b)  $50 \mu\text{m}$ , and (c)  $100 \mu\text{m}$ .
- Figure 7-13 The cross-sectioned view confirming the crack initiation site at  $20 \mu\text{m}$ : (a)  $\text{SCMV}$  alloy and (b)  $\text{A}100$  alloy.
- Figure 7-14 The surface profiles of both worn flat and round specimens involving self-against-self pair fretted  $500 \text{ N}$  for  $100,000$  cycles.
- Figure 7-15 The surface profiles of both worn flat and round specimens involving the self-against-nonself pair fretted at  $500 \text{ N}$  for  $100,000$  cycles.
- Figure 7-16 (a) Contact pressure versus number of cycles distribution and (b) FE predicted wear depth for  $\text{SCMV}_{(f)}//\text{A}100_{(r)}$  at  $500 \text{ N}$  and  $50 \mu\text{m}$  stroke.

## **NOTATIONS**

$a$	contact half-width
$\bar{a}$	acceleration of the Upper Specimen Mounting Block
$E^*$	composite Young's modulus of the two contacting bodies
$dh$	local increment of wear depth
$H$	hardness of the material
$k$	dimensional Archard wear coefficient
$K$	dimensionless wear coefficient
$m_{us}$	the mass of Upper Specimen Mounting Block
$N$	number of wear cycles
$N_t$	total number of wear cycles
$p_o$	maximum Hertzian contact pressure
$p(x)$	contact pressure as a function of x-position
$P$ or $P_N$	applied normal load on the specimens
$P_E$	applied load on the end of the level arm of the fretting rig
$R$	relative curvature
$R^f$	radius of the flat surface
$R^c$	radius of the cylindrical surface
$dS$	increment of local sliding distance
$S$	total (accumulated) slip distance
$T$	tangential force
$T_{dr}$	drive force
$T_{max}$	maximum friction force during one fretting cycle
$V$	total wear volume
$x, y$	coordinates

## **Greek symbols**

$\delta$	applied stroke
$\delta^*$	applied stroke half-amplitude

$\delta_t$	relative displacement
$\mu$	coefficient of friction
$\nu^f$	Poisson's ratio of the flat body
$\nu^c$	Poisson's ratio of the cylindrical body
$\sigma_x, \sigma_y$	normal stresses on planes perpendicular to the x, y axes
$\tau_{xy}$	shear stress in x-y plane

### **Subscripts, Superscripts**

c	the round body
f	the flat body

---

## **Chapter 1: Introduction**

---

### **1.1 Historical review of aviation engines**

A jet engine continuously takes in air and accelerates it by a large amount. The efficiency of the process is defined by the ratio of the compressed volume of air to the exhaust volume. The engine generates thrust because of the acceleration of the air via four stages (induction, compression, ignition, exhaust) – the equal and opposite force this acceleration produces is the required thrust (Newton's third law). The advantage of the jet engine is its efficiency at high speeds and high altitudes. The earliest attempts at jet engines were hybrid designs, where compression was driven by an external power source. In this system, the air is compressed by a fan driven by a conventional gasoline engine. Three known examples of this sort of design were Henri Coanda's Coanda 1910 aircraft, Campini Caproni CC.2, and the Japanese Tsu-11 engine. None were entirely successful and the CC.2 ended up being slower than a traditional design with the same engine [1].

The key to the successful jet engine was the implementation of a gas-turbine approach, extracting energy to drive the compressor from the engine itself. Work on such a “self-contained” design started in England in 1930 when Sir Frank Whittle submitted patents using a single turbine stage in the engine exhaust to drive a centrifugal compressor [2]. Unaware of Whittle's work, in 1935 Hans Von Ohain started work on a similar design in Germany. Unlike Whittle's design, Ohain used hydrogen as a fuel, which he credited for his early success. The follow-on designs culminated in the HeS-1 engine, which was fitted into the He 178 air frame and flew

in August 1939; the He 718 was the world's first jet plane. Across the channel, Whittle had significant problems in getting government research funding for his design, but with private funding, he was able to get a test engine running in 1937, this however was very large and unsuitable for use in an aircraft. By 1939, the engine had started looking useful and Whittle's company, Power Jets Ltd, began to receive funding from the Air Ministry. In 1941, a flyable version of the engine called W.1, developing 4kN of thrust was fitted to the Gloster E28/30 air frame, and flew in May 1941. One problem with both of these early designs was that the compressor (a centrifugal type) worked by "throwing" air outward from the intake to the sides of the engine. This led to a very large cross section for the engine, as well as having the air flowing in the wrong direction after compression. However, Anselm Franz of Junkers Motoren addressed this problem with the introduction of the axial-flow compressor.

## **1.2 Gas turbine engines and splined joint couplings**

Gas turbine engines can vary significantly in both size and power output and are used in a diversity of applications; as propulsion units in automobiles, trains, naval ships, for the power generation of electricity, pumping of natural resources (gas and oil), and to power both civil and military aircraft ; it is the latter two applications that form the basis of this thesis. Nonetheless, these machines share the same principal function, which is to produce a jet of high-speed exhaust gases for propulsion purposes. Rolls Royce, Alstom, General Electric, and Pratt and Whitney are the few main suppliers and manufacturers of aero-gas turbine engines. The layout of an aero-gas turbine engine, shown in Figure 1-1, is characteristic of the Rolls Royce approach to engine design, which shows a triple-spool arrangement. This means that the engine has three concentric, independently rotating shaft systems, each rotating at

significantly different speeds, and each associated with a separate turbine-compressors pair. The three shaft systems are the low pressure (LP), intermediate pressure (IP), and high pressure (HP). The rotational speeds of the LP, IP, and HP are approximately 3,000 rpm, 7,000 rpm, and 10,000 rpm, respectively. The torque transmitted by each shaft differs; the largest torque of about 135 kNm is on the LP shaft with 30 kNm and 75 kNm of torque are on the IP and HP shafts, respectively. The spline-joint coupling is a widely used effective component for torque transmission for shafts (gas turbine engine, helicopter, automotive, naval, and power generation plants) [3] while allowing easy dismantling for servicing requirements. An example of a spline-joint connection is shown in Figure 1-2. The spline teeth can be either straight or helical and the tooth profile can vary in pressure angle and working depths [4]. For straight splines, the tooth is projected radially and can be fitted only to parallel axes. Helical splines are becoming the more predominant choice because they are stronger and easier to fit [5]; sometimes, helical splines are also known as flexible splines. The internal spline can be formed by gear shaping while the external spline is commonly broached. Axial and cross-section views of a spline coupling are shown in Figure 1-3a and b. This conforming contact geometry enables effective transmission of torque while maintaining some degree of flexibility for radial and circumferential relative motion. To reduce stress concentration at the end of engagement region (i.e.  $z = 0, a_1$ ), spline teeth are sometimes barreled.

### **1.3 Mechanical problems of splined joint couplings**

Spline-joint coupling life has been increased by reducing the peak stresses within the coupling by tooth and shaft geometry optimisation; the fatigue life of the shaft and spline has been increased by design improvements. Nonetheless, according to

Mitchell [7], there is no such thing as a static joint and in service, a certain degree of relative motion will be experienced by contacting surfaces, such as the spline teeth, contributed to by tooth barrelling (incomplete contact geometry) and allowable degrees of misalignment (both axial and angular displacement). Relative slip of small amplitude will occur between the contacting tooth surfaces giving rise to fretting damage, which may limit the lifespan of the coupling. Ku and Valtierra [8] investigated the effect of tooth barrelling, angular misalignment, lubrication, material types and surface treatments on wear in splines. Because of the flexible design, the device inevitably will experience varying loading conditions (depending on speed as well) in situations where bending moments are induced by thrust-induced engine carcass deflections and gyroscopic effects during take-off/manoeuvres. Damage can be in the form of plain fatigue, fretting fatigue, and fretting wear. Variables like slip and stress (shear and normal) are, possibly, the primary factors that induce fretting damage on the contacting spline teeth. Vingsbo and Soderberg [9] have mapped the relation between wear and fatigue life as a function of slip amplitude. The availability of numerical methods of contact analysis has made it possible to analyze both slip and contact pressure distributions by means of the boundary element method and finite element methods, allowing quantitative comparison between measured and predicted data. For example, McFarlane et al. [10] were able to make comparisons between experimental measurements and boundary element predictions for a spline coupling. Leen et al. [11] used the finite element method to predict the slip and contact pressure distribution. Such methods provide vital information of salient fretting parameters because fretting wear is highly dependent upon slip and pressure history. Over the years, much work has been conducted to investigate the fretting wear phenomenon. The fretting wear on spline couplings were studied experimentally

by Olver and co-workers [12] using three different methods. It was concluded that cyclic pressure is likely to cause displacement of contacting teeth which may possibly lead to fretting wear. Another study conducted by Olver and Medina [13, 14], maps the relation between regime of friction to the contact pressure distributions between male and female teeth during rotation. A significant finding from the work was that applied misalignment or bending moment, caused the contact to oscillate up and down the teeth in an axial direction during rotation, thereby causing cyclic stresses and fatigue, and a complex cycle of pressure and slip was related to the occurrence of fretting wear damage. The investigation used the boundary element method. A modelling technique for fretting wear was also developed by Ding [15], who simulated the fretting wear in a two dimensional round-on-flat arrangement based, on a modified Archard equation, using the finite element method. Ding [16] used this approach to investigate the effect of slip regime on fretting wear-induced stresses. Ratsimba et al. [17] have investigated fretting wear via a series of spline tests under varying loading conditions, mainly cyclic torque and axial load with superimposed rotating bending moment and fluctuating torque. The work of [15-17] were carried out as part of a programme with a primary aim of developing a reliable life determining methodology for fretting damage prediction.

#### **1.4 Transmission materials for design requirements**

There are many factors, which influence the material choice for transmission components. These includes, properties that affect structural efficiency, cost of ownership, and cost-effective design. These issues are interlinked with the mechanical properties of the material – tensile strength, proof strength, ductility etc.

Structural materials used in the aircraft industry require a balance of physical and mechanical properties to enable their safe and efficient use. A commercial transport aircraft may be required to fly for a service life of as much as 60,000 hours, spread over perhaps thirty years and encompassing 20,000 flights, and in this lifetime it may taxi on runways for a distance in excess of 100,000 miles [18]. During this lifetime it will also experience adverse climatic conditions, repetitive thermal cycles and, of course, many hundreds of thousands of minor fatigue cycles imposed during the major ground-to-air excursions. To a larger extent, the duty cycles imposed upon an aeroengine mirror those suffered by the airframe, except that the thermal cycle is a more dominant element. Military aircraft are required to survive perhaps one tenth of the life of civil transport, with a service life of typically 6,000 hours, while load levels induced by accelerations during manoeuvre are high in military aircraft in comparison to civil transport (Figure 1-4). The proportions of aircraft structures produced in competing materials for aircraft newly built in 1960, 1980 and projected for 1995 are identified in Figure 1-5. It is important to recognise that aeroengines introduce the requirement for efficient performance at more elevated temperatures in relatively confined spaces and hence currently force the use of high density, high temperature materials; for example, nickel-based superalloys. Typical maximum temperatures for existing and projected materials are shown in Figure 1-6. It must be recognised that the cost of ownership of an aircraft, military or civil, throughout its service life may exceed the cost of purchase by at least a factor of two. Much of this cost is incurred in the maintenance of an airworthy structure, i.e. in the inspection for and replacement of, damaged and worn parts. The resistance of a material to degradation by wear, fatigue and corrosion therefore has a strong influence on the in-service costs of an aircraft.

The requirements developed for aeroengine materials are effectively the results of fifty or more years of practical experience. Thus, the prime importance of fatigue and corrosion resistance is a result of the natural susceptibility of the alloys that are in predominant use. The history of aeroengine materials development during these five decades reveal that minor changes within type have been achieved relatively easily, taking perhaps ten years to introduce a new alloy composition. Changes out of material type, from metallic design to polymeric composite, have proved almost impossibly difficult, taking as much as thirty years and requiring the development of an entirely new engineering environment. Overall, the outcome is that efforts are still being made to improve the quality and performance of materials to achieve an acceptable level of both physical and mechanical properties for future purposes.

### **1.5 Research motivation and scope of thesis**

The choice of material is important and must represent a compromise between cost of material/manufacture and performance. These advanced materials (steel alloys, titanium alloys, and nickel-based alloys, etc.) should accommodate any possible structural changes while torque is transmitted, subjecting the contact surfaces to variations of loading conditions. The fundamental performance requirements are good tribological and mechanical properties, with a primary purpose of minimising fretting damage. The proposed advanced materials in this thesis are particularly related to Rolls Royce plc but will typically also of more general interest. The objectives of this thesis are as follows:

- ❖ To undertake and examine experimental studies on the tribological behaviour of candidate aeroengine transmissions materials such as Super S/CMV and AerMet®100 (ultrahigh strength steel alloy) and Inconel 718 (nickel-based

superalloy), using a round-on-flat fretting wear arrangement. This work will look into the effect of some of the key fretting variables: (1) gas nitriding, (2) lubrication regime, (3) temperature, and (4) material combination.

- ❖ Use an existing finite element model, developed by Ding [15], to simulate and thus further validate the fretting wear of round-on-flat contact. This method is useful for a general understanding of the effect of damaging factors (slip, contact stresses) on fretting wear and fretting fatigue.

This thesis will progress to the following chapters:

**Chapter 2:** A review of past and present research related to fretting damage and methodologies used for the analyses (experimental, analytical solutions, and numerical methods).

**Chapter 3:** This section reviews the material characterisation of the candidate aeroengine transmission materials of this study.

**Chapter 4:** This chapter covers the laboratory preparations (specimen and heat treatments), experimental procedures (fretting rig), and wear assessment tools (surface profilometry, scanning electron microscopy, x-ray diffraction, etc) used in the testing of this thesis.

**Chapter 5, 6, and 7:** These chapters describe, in detail, the observations of the parametric studies carried out on the frictional behaviour of Super S/CMV, AerMet®100, and Inconel 718 in fretting wear. Chapter 5 refers to the investigation on gas nitrided Super S/CMV, under non-lubricated and boundary lubricated conditions and the determination of whether or not there are any advantages in having both the round and flat specimen gas nitrided. Chapter 6 describes the effect of temperature on the Inconel 718 tribological characteristics and the phenomenon

behind the wear resistance improvement. Chapter 7 discusses the fretting wear behaviour of different combinations of Super S/CMV, AerMet®100 and Inconel 718 as a function of stroke.

**Chapter 8:** This is a discussion on the results of the experimental and numerical analyses.

**Chapter 9:** This chapter presents the conclusions of the research.

**Chapter 10:** This chapter describes recommendations for future work.

## **References**

1. B. Gunston, "The development of Jet and Turbine Aeroengine", 2<sup>nd</sup> edition, Patrick Stephens Limited (PSL), Somerset, United Kingdom
2. J. Golley, F. Whittle, and B. Gunston, "Genesis Of The Jet: Frank Whittle and the Invention of the Jet Engine", Airlife Publishing Ltd, 1997
3. M. Neale, P. Needham, and R. Horrell, " Coupling and Shaft Alignment", Mechanical Engineering Publications Limited (London), 1991
4. D.W. Dudley, "How to design involute splines", Prod Engng, October 1975, pp.75-80
5. A. D. Deutschman, W. J. Michels, and C. E. Wilson, "Machine Design: Theory and Practice", Macmillan (New York), 1975
6. D.W. Dudley, "When splines need stress control", Prod Engng, December 1975, pp.56-59
7. G. Mitchell, "An airline view of the corrosion problem", Ind. Corr., p11-17 in Friction, lubrication and wear, 18, A.S.M Handbook, pp.244-247, ASM International, Ohio, USA, 1983
8. P.M. Ku and M.L. Valtierra, "Spline wear-effects of design and lubrication," *Journal of Engineering for Industry, Transactions of the ASME*, Nov., 1975, pp.1257-1263
9. O. Vingsbo and S. Soderberg, " On fretting maps", *Wear*, 1988, 20, pp. 131-147
10. C. W. R. McFarlane, E. J. Williams, and T. H. Hyde, " The Comparison of the Boundary Element Analysis of a High Performance Spline Coupling with

Experimental Measurement”, *Coupling and Shaft Technology got Aerospace Transmission*, IMechE One Day Seminar, Solihull, England, 9<sup>th</sup> June 1999

11. S. B. Leen, I. J. Richardson, I.R. McColl, E.J. Williams, and T.R. Hyde, “Macroscopic fretting variables in a splined couplings under combined torque and axial load”, *Journal of Strain Analysis*, 2001, Vol. 36, No. 5, pp. 481-496
12. D. P. Davies, A. V. Olver, R. F. Baker, and S Medina, “Fretting and Wear of Splined Couplings”, *Coupling and Shaft Technology got Aerospace Transmission*, IMechE One Day Seminar, Solihull, England, 9<sup>th</sup> June 1999
13. S. Medina and A. V. Olver, “Regimes of contact in spline couplings”, *Trans. ASME J. Tribology*, 216 (J), 2001, 124, pp. 351-357
14. S. Medina and A. V. Olver, “An analysis of misaligned spline couplings”, *Proc. Instn. Mech. Engrs J. Engineering Tribology*, 216 (J), 2002, pp. 269-279
15. J. Ding, “Modelling of Fretting Wear”, University of Nottingham, 2003
16. J. Ding, S. B. Leen, and I. R. McColl, “The effect of slip regime on fretting wear-induced stress evolution”, *International Journal of Fatigue*, 2004, 26, pp. 521-531
17. C. H. H. Ratsimba, S. B. Leen, I. R. Richardson, I.R. McColl, and E. J. Williams, and T.R. Hyde, “Fatigue of a representative aeroengine splined coupling under torque overload”, *Aerospace Transmissions Technology into the 21<sup>st</sup> Century*, IMechE European Seminar, Marseilles, France, 17-18 May, 2001

18. H.W. Flower, 'High Performance Materials In Aerospace', Chapman & Hall, 1995

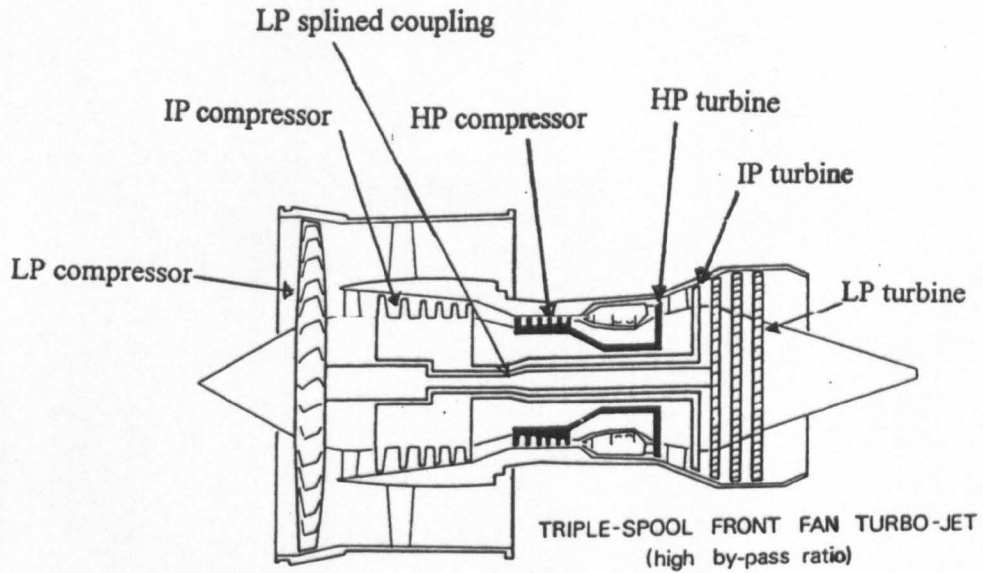


Figure 1-1: General arrangement of three shaft, high-bypass aeroengines [2].

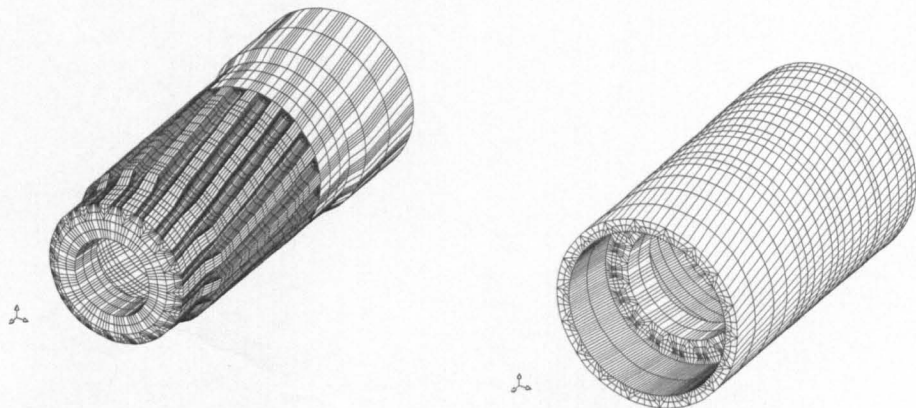


Figure 1-2: A FE model of a spline coupling connection [17].

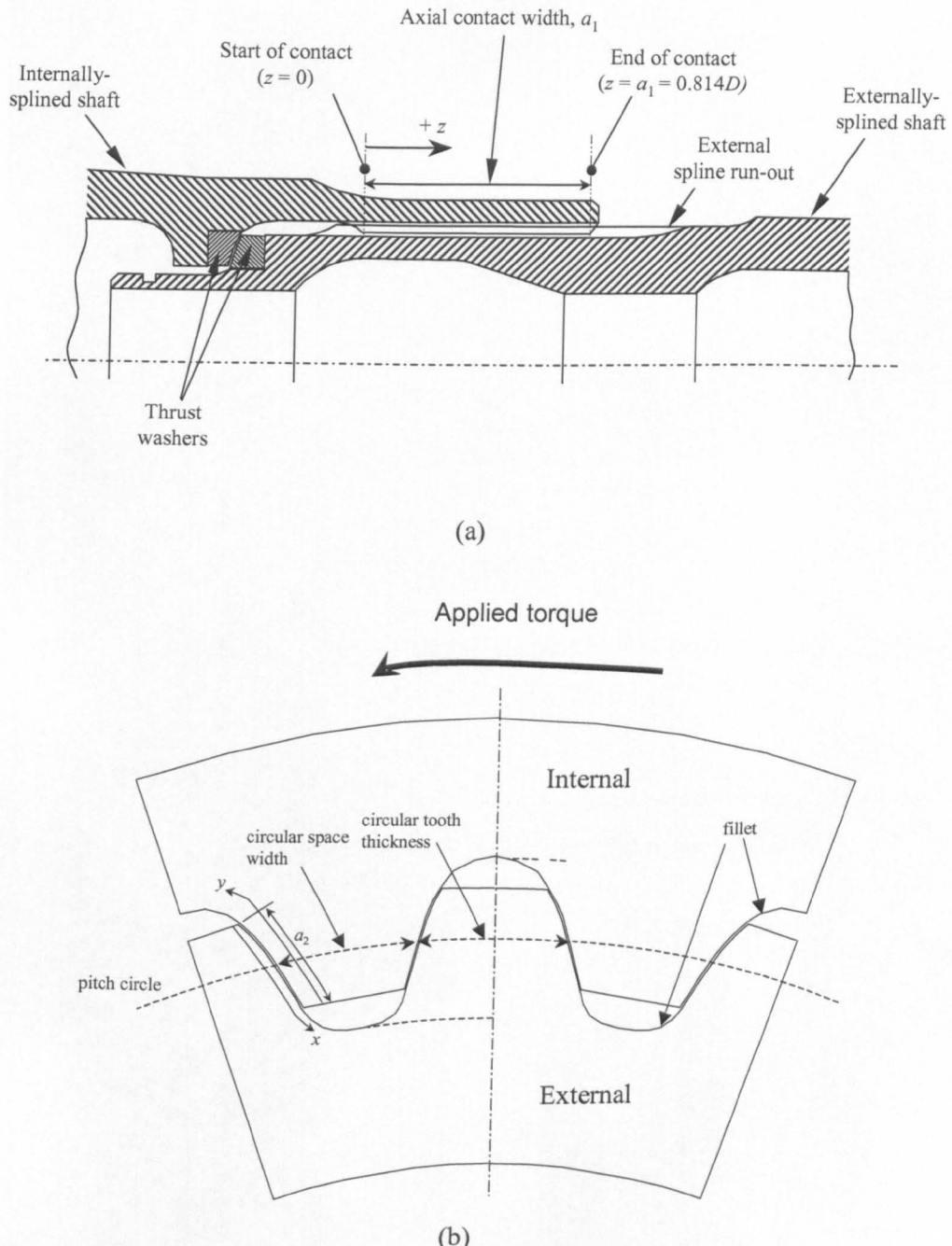


Figure 1-3: Schematic representation of a spline coupling: (a) axial section and (b) cross-section.

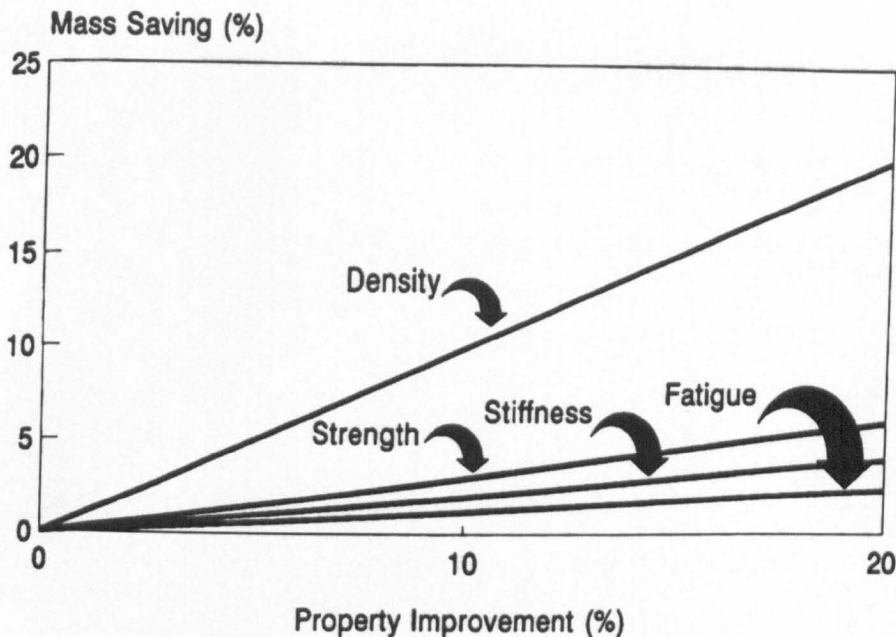


Figure 1-4: The importance of mechanical properties that is used for selected combat aircraft [18].

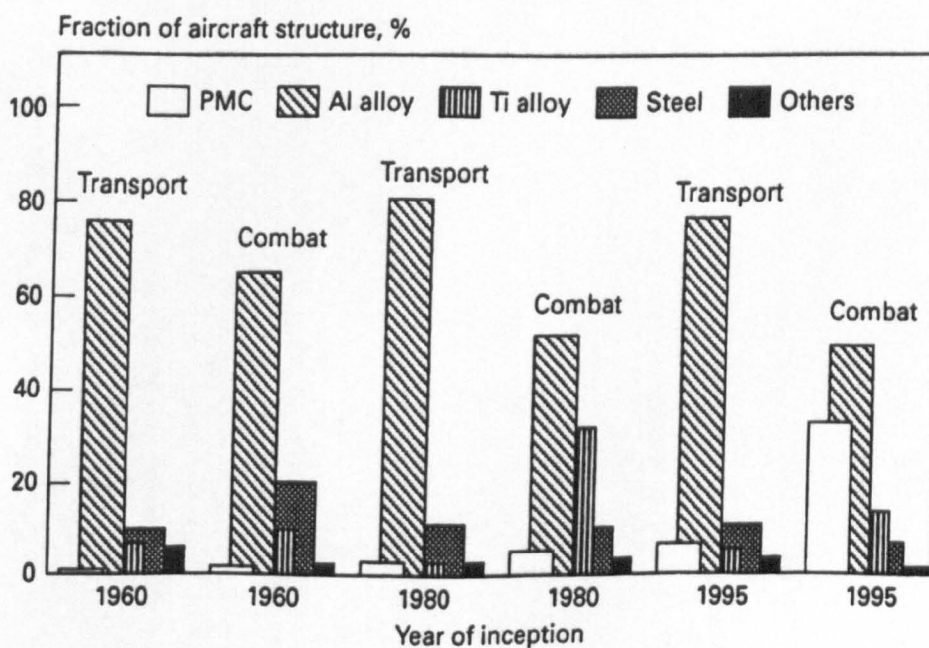


Figure 1-5: Distribution of materials in structural application throughout the twentieth century [18].

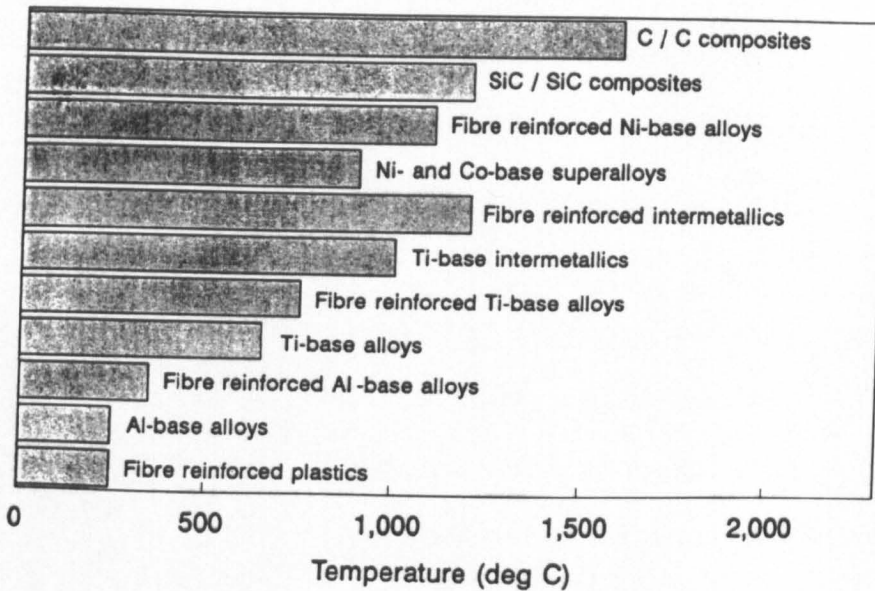


Figure 1-6: Maximum operating temperatures of existing aeroengine materials [18].

---

## Chapter 2: Literature review

---

### **2.1 Introduction**

#### ***2.1.1 Historical review on tribology***

In 1966, the word and concept of tribology was first enunciated in a report of a Committee of the British Department of Education and Science [1]. In it, tribology, derived from the Greek “tribos” meaning “rubbing”, was defined as “The science and technology of interacting surfaces in relative motion and of associated subjects and practices”. This subject embraces not just the study of rubbing surfaces but the fundamentals behind the concept, including a great deal of investigation into every aspect of friction, lubrication, and wear.

Tribology is recognised as a vital ingredient of our technological age, largely because of its multi-disciplinary nature - which sees it embracing physics, chemistry, metallurgy, and mechanical engineering - and because the concept of tribology has been universally neglected or even overlooked in the past. The consequences of research into tribology can have significant impacts on economic growth (in terms of operation and maintenance costs) and changes in technology (machinery tools, transmission engine, etc.). The D.E.S has stated that in the UK alone, between 1.3% and 1.6% of the gross national product could be saved, if greater attention were paid to tribology. These saving figures have launched tribology on its successful road to widespread recognition within aeronautical engineering [2]. In Japan, the practice of tribology has been adopted into their maintenance engineering in monitoring industrial plants (maintenance forms a large economic section, ranging from 3% to

4% of the gross national product) [3]. Nonetheless, there is still much to learn about tribology, and the implementation of this discipline into practice (engineering and design) requires the need for ongoing research and development programmes.

## **2.2 Friction and surface damage mechanisms**

### ***2.2.1 Definition of friction***

Friction can be defined as the resistance encountered by one body sliding or rolling over another. The degree of friction expressed as friction coefficient ( $\mu$ ), or coefficient of friction (COF), is the ratio between the frictional force ( $F$ ) and normal load ( $P$ ). The first two laws of friction defined by Leonardo da Vinci and redefined by Amontons are as follows [4]:

1. *Friction force is proportional to the applied load*
  2. *Friction force is independent of the apparent contact area.*
- The third law of friction, normally attributed to Coulomb, states:
3. *Frictional force is independent of sliding velocity*

Amontons deduced his laws based on his experimental work using metals and wood, all lubricated with pork fat; his materials therefore experienced boundary lubrication. The First and Second Law are often obeyed for unlubricated sliding, and this is true for most metals and many other materials, but not for polymers [4]. The Third Law is rather less well founded and well received than the first two. It was noticed (based on common observation) that the ‘static friction’ (which defines the limiting tangential load to normal load ratio from a static condition) is greater than ‘kinetic friction’ (which defines the tangential load to normal ratio between sliding surfaces). In other words, the frictional force required to initiate relative movement is greater than sustain it. The use of these laws has been observed to give relatively good correlation

with the experimental data over a limited range of test conditions. However, their use can be restricted due to the changes in the physical nature of materials altered by wear action or other factors.

### ***2.2.2 Classification of surface damage mechanisms***

Friction and surface damage processes are inevitable when two surfaces undergo some form of relative movement (e.g. fretting) under load. Therefore, understanding of various friction and surface damage mechanisms is necessary for one to make the right selection of materials, coatings, surface treatment, liquid lubricant, and operating conditions for a given application. Considerable savings can be made by reduction of friction and controlling surface damage. The different types of mechanisms encountered in most surface damage cases are: (1) surface cracking (plain fatigue, fretting fatigue); (2) Wear (abrasive, sliding, adhesive, polishing, fretting, rolling contact, impact); (3) and Erosion (solid particle, cavitation, liquid impingement, slurry, corrosion) [4]. Surface damage rarely exists in a single form. It is quite typical to encounter at least three or four of these types in any surface damage case simultaneously, e.g. fretting is a very intricate phenomenon and its wear mechanism involves various forms of wear modes.

For most engineers friction is really rather a nuisance and the aim of the engineering designer is virtually always to bring about the transmission of mechanical power with the lowest possible frictional losses. It is believed that friction originates from complicated molecular-mechanical interactions between contacting bodies and that these interactions differ from one application to another; this depends on several factors, such as intrinsic properties of the mating materials, operating conditions, speed, load, and lubricant. The nature of this phenomenon and associated

complexities have led to friction models (Coulomb model and Bowden and Tabor model) that can be based on geometric arguments (surface roughness and asperity interlocking), mechanical property-based arguments (shear properties of the solids and of the substances between the surfaces), fluid dynamics approaches, considerations of electro-static forces between surface atoms, and chemical compatibility arguments [5]. The following sections will discuss information that is relevant to fretting wear as a topic and the current research in this field.

## **2.3 Fretting wear**

### ***2.3.1 Reviews on fretting***

In the past, numerous unsatisfactory definitions of fretting have been proposed in relevant studies and literature, which typically lack generality by concentrating on only one aspect of this complex process, e.g. the production of oxide debris during fretting. A satisfactory general definition is given in [6] where fretting is described as a form of wear which occurs when wear mechanisms act together under conditions of small-amplitude oscillatory movement between contacting components, which are usually nominally at rest. It can either cause localised wear or initiate fatigue cracks, which may drastically lower the fatigue strength of some components. One of the immediate consequences of the process in normal atmospheric conditions is the production of oxide debris, hence the term fretting corrosion. The movement is usually the result of external vibration, but in many cases it is the consequence of one of the contact members being subjected to a cyclic stress that leads to a more damaging aspect of fretting, depending on the loading history and/or conditions. If the component fails due to cracking, the term “fretting fatigue” or “contact fatigue” is used. Because vibration is one of the main causes of the fretting movement, many engineering components are likely to experience fretting damage. In short, fretting

wear can be considered as a form of wear when contacting bodies are subjected to small amplitude oscillatory motion, usually tangential, and material removal is observed. However, fretting wear is a complex process involving several sub-wear participants, including adhesive wear, surface fatigue wear, delamination wear, corrosive wear and abrasive wear, and is described exhaustively in several review papers [7-10].

Eden, Rose, and Cunningham, who reported the first fretting case in 1911 [11], found that brown oxide debris was forming in the steel grips of their fatigue machine in contact with a steel specimen. In 1927, the first fretting case study was conducted by Tomlinson [12] to investigate the phenomenon, who went on to design two machines to replicate the oscillation motion between two annuli in the first case, and an annulus against a flat in the second case. He coined the phrase ‘fretting corrosion’ based on the resultant red iron oxide debris on the steel specimens and established that the damage could be caused by slip amplitudes as small as 125 nm. Further development of fretting studies by Warlow-Davies [13] found a subsequent reduction in fatigue strength of between 13% and 17% during fretting damage on steel specimen. Investigations conducted by McDowell et al. [14] showed a similar trend due to the conjoint action of fretting and fatigue. In 1958, Fenner and Field [15] demonstrated that fretting greatly accelerated the crack initiation process depending on the loading history i.e. for normal fatigue, crack initiation may account for 90% of fatigue life, whereas for fretting fatigue, initiation occurs corresponds to less than 5% of the fatigue life. Fouvry et al. [16] introduced an energy approach relating the wear extension to the interfacial dissipated energy. Recent advances in wear quantification (based on energy approaches) have been conducted for conventional repeated sliding

conditions in which the transition from mild to severe wear is related to the transition from elastic shakedown to plastic shakedown responses of the material [17, 18]. For instance, a recent study has shown that to predict wear rates of metallic structures under fretting it is essential to consider the elasto-plastic response of the structure. This aspect has been analysed by Fouvry et al. [19] and Kapoor [20]. More recently, Fridrici et al. [21] used the Smith-Watson-Topper criterion to predict the crack nucleation of shot-peened alpha/beta Ti-6Al-4V alloy under fretting wear influence. This method used the recorded tangential force, normal force, COF and the mechanical properties of the materials to calculate the normal and tangential stress distributions by contact mechanics calculation. The methodology gave an insight into how fretting wear and fretting fatigue (i.e. cracking) are related.

### ***2.3.2 Fretting mechanism***

There have been many reported fretting mechanisms with numerous attempts to identify the sequencing events. Godfrey et al. [22] concluded that adhesion resulted from contact and once broken fine particles were dislodged and oxidised. They also found that alternating motion was not a necessary condition for fretting and surface fatigue. Work by Taylor and Waterhouse [23], and Schmidt et al. [24] confirmed this finding. The proposed fretting mechanism sequences are divided into three stages, as follows [25]:

#### ***1. The initial stage***

When two metallic surfaces are brought into contact under normal conditions, a natural oxide metal surface layer initially protects the surfaces. Disruption of this oxidised film, by the wear process, results in metal-to-metal contact

leading to adhesion and metal transfer. This is found to dictate the subsequent wear damage.

## 2. *Debris formation*

The debris is the final product of the oxidised fretted metal during the wear process. This debris accumulates to form beds of compacted oxidised debris, which act to reduce metallic contact between contacting bodies. Results show that in most cases, natural third bodies i.e. debris, formed during fretting protect the rubbing surfaces due to the load carrying capacity of the wear debris.

## 3. *The steady-state*

This involves a general disintegration and dispersion of the zones affected by the initial stages of the wear action, and is recognised by a mixture of debris and metal in the wear contacts. Abrasion is not the significant factor in fretting wear; fatigue separation probably promotes most of the damage at this stage.

In fretting the generated debris is of utmost importance for the fretted surfaces by providing a load-carrying plateau, which can reduce the wear rate from severe to mild levels. Debris production depends on the wear mechanism in the fretting process. Samuels et al. [26] explained that debris formation by adhesion typically occurs in the initial stage of fretting. Mechanical interlocking of these asperities partly contributes to the formation of debris particles. Kayaba and Kato [27] schematically show the proposed phenomenon in Figure 2-1. The damage mode and intensity of wear depends strongly on the contact conditions, according to which the whole range of fretting can be divided into four regimes. Berthier et al. [28] constructed a friction log

to explain the sequences involved in the mechanism based on their wear debris studies (third-body action in fretting). They argued that the debris, which they refer to as the ‘third body’, adheres to both itself and the solid surfaces, referred to as the ‘first bodies’. The friction log used to describe the sequences is divided into four parts (Figure 2-2):

- (i) Elimination of the ‘natural pollution’ surface screens (oxide layer).
- (ii) Increase in specimen interaction, accompanied by an increase in friction as well as the corresponding first body structural changes (occurrence of subsurface damage).
- (iii) Metallic particle detachment or debris bed formation and gradual passage from two- to three- body contact.
- (iv) Continuation of debris formation and ejection giving steady state wear.

### ***2.3.3 Fretting parametric types***

It has been reported that up to 50 factors might influence the magnitude and rate of the fretting wear process [29]. In fretting wear, the predominant wear mechanism is related to the magnitude of the COF. The COF is a complex function of many variables such as the applied normal load, the magnitude of slip, the surface roughness, lubrication, oxidation behaviour of the surface and temperature. The following sections discuss the influence of these variables in relation to fretting wear behaviour.

- ***Slip amplitude***

Several authors, for example, Wright [30] and Feng et al. [31] hypothesised the notion that the wear per unit distance of sliding is greater under fretting conditions than continuous sliding conditions, because of the abrasive wear produced by the

entrapment of particles between the interfaces. Ward [32] has shown that the fretting wear rate for mild steel is greater than under continuous sliding conditions of 25 mm. On the other hand, Halliday et al. [33] and Halliday [34] have suggested wear rates approaching zero for unlubricated mild steel at amplitudes below 100  $\mu\text{m}$ . Most researchers agree that sliding motion is a necessary requirement for fretting damage even under amplitudes as small as 0.1  $\mu\text{m}$ . Charney [35] and Aoki [36] found that wear damage reduces when the amplitude was less than 100  $\mu\text{m}$ . For Ohmae et al. [37], and Aladham et al. [38], wear damage was constant at 100  $\mu\text{m}$ . Vingsbo and Soderberg [39, 40] have mapped the relation between the slip amplitude and normal load of the four different slip regimes of fretting wear (Figure 2-3). The level of slip amplitude at which slip occurs depends on factors such as the normal load and the mechanical properties of the materials. They reported that there are four regimes of wear dependent on the amplitude of slip, namely: (i) stick (ii) partial slip (iii) gross slip, and (iv) reciprocating sliding wear. Bill [41] explained the apparent slip regime variations in terms of debris movement capability. At low amplitudes, most of the debris is retained within the contact area, whereas at high amplitudes the debris is forced to accumulate at the periphery of the wear interface. This in turn reduces metal-to-metal contact and distributes the load more uniformly over the apparent fretted region, thereby mitigating the fretting wear rate. There have been controversial findings on the transition values from fretting wear to sliding wear. Toth [42] suggested 50  $\mu\text{m}$ , Lewis and Didsbury [43] concluded that the transition was at 70  $\mu\text{m}$ , whilst Vingsbo et al. [44] and Zhang et al. [45] found the value for the transition period to be about 300  $\mu\text{m}$ . The variation in the upper and lower limits of stroke for the case of true fretting is dependent on other parameters and the amplitude

measuring techniques, i.e. the point where the amplitude is finally measured. Baker and Olver [46] carried out a direct observation on fretting wear using a sapphire disc rubbed against a steel sphere, under both lubricated and dry conditions. The results showed a change in wear mechanism at approximately 200 µm stroke length, linking this transition regime to the wear debris behaviour; fretting wear is characterised by debris remaining within the contact, whilst reciprocating sliding wear is associated with debris being removed rapidly from the contact. Chen and Zhou [47] found that wear coefficient and wear volume, at a constant sliding distance, were the most appropriate parameters for identifying the transition amplitude (at 300 µm) between fretting wear and reciprocating sliding wear.

Recently, the availability of advanced technology (e.g. finite element modelling) has allowed a comprehensive study on the effect of slip regime on fretting wear, as well as an understanding of how fretting wear and fretting fatigue interact, based on the transition between partial slip and gross slip. Jin and Mall [48] used the modified shear stress range (MSSR) parameter in their numerical analysis. Similarly, Ding et al. [49] investigated the effect of slip using a modified version of Archard equation to investigate the evolution of sub-surface stress field.

- ***Normal load and contact conditions***

For many engineering situations, the real areas of contact are almost proportional to the applied total load for a wide range of deformation characteristics. In most practical cases of conforming surfaces, plastic deformation is expected at high contacting points, as established by Bowden and Tabor [50]. However, in certain cases, the real contact areas may be less than the apparent contact areas (for example, sphere on flat and cylinder on flat) but the situations still conforms to the elastic

theory of Hertzian contact because the overall contact is determined by the elastic stress field developed in the bulk of the material. The real contact area ( $A$ ) is directly proportional to the applied load ( $P$ ) and hence,  $A = \frac{P}{H}$  where  $H$  is the indentation hardness and is roughly equal to three times the yield stress in tension. Because fretting only occurs at contacting areas, the amount of wear should be directly proportional to the applied load, if the amplitude of slip is constant. Feng and Uhlig [51] have confirmed this experimentally (Figure 2-4). The influence of the normal load on the contact conditions in fretting was investigated by Bryggman and Soderberg [52] who found that while increasing the normal load may suppress wear, it also causes accelerated fatigue fracture, as well as increasing the depth of the subsurface deformed zone. De Gee, Commissaris, and Zaaij [53] investigated the impact of variable loading conditions on fretting wear using sintered aluminium powder (SAP) and the results indicated (Figure 2-5) that combined loading is more damaging than simple loading. Similar work has investigated using the energy wear approach to predict the lifetime of a hard coated, high speed steel under constant and variable loading conditions [54]. Iwabuchi [55] examined the effect of normal load on wear volume changes in the presence of oxide particles. Without the presence of oxide particles, the normal load increases with increasing wear volume. When oxide particles are added to the contact interface, at low load, the wear volume is negative and oxide particles are trapped within the grooves forming a semi-compacted layer. As the load increases, wear damage is found to be greater due to the abrasive wear from the wear particles. If load increases further, the wear rate is reduced again due to complete wear debris compaction that protects the contact surfaces.

- *Type of contact*

The type of contact geometry dictates the degree of debris retention in the contact region and the contact pressure distribution (stress fields). The ease of debris escaping from the contact region is an important factor for the fretting process itself and the level of surface damage (for example, in a machine). The resultant wear differs according to the contact shape, due to the contact pressure distribution for a flat-on-flat arrangement for example differing from that of a cylinder-on-flat arrangement. For a flat-on-flat arrangements, the maximum pressure peaks are located at both contact edges while for a cylinder-on-flat arrangement, the maximum pressure peak is located in the central region. Flat surfaces (large contact area) tend to retain more debris within the contact region and the wear damage is more likely to be sporadic, whereas for round surfaces (smaller contact) the debris can escape more easily. Investigation by Kuno and Waterhouse [56] showed that the escape of debris in the crossed-cylinder arrangement (Figure 2-6) is greatly influenced by the direction of motion and the contact geometry. Studying the effect of contact geometry, mainly contact stress distributions, proved to be important for lifing prediction of mechanical components used in industrial applications [57, 58].

- *Frequency*

Soderberg, Bryggman and McCullough [59] investigated the fretting wear behaviour of both low carbon steel (AISI 1018) and austenitic stainless steel (AISI 304) using a series of vibration frequencies (in the range 10 – 20,000 Hz). The frequency of vibration was found to influence both the contact conditions and the rate of surface damage. The experiments showed that two cases of fretting contact can be distinguished and related to the displacement amplitude. At low displacement

amplitude, the contact situation was characterised by partial stick at the interface and the frequency has little effect on the wear rate. However, in low amplitude fretting, material damage by surface degradation and fatigue crack initiation is usually of more concern and both of these parameters are found to be greatly accelerated by an increase in frequency. In high amplitude fretting, in contrast, gross slip occurs at the interface and wear becomes the dominant damage mode. At these conditions, variations in frequency appear to have little effect on fretting wear and related mechanisms; it may be possible to apply high frequency [60] fretting to obtain accelerated testing.

- *Number of cycles*

In general, the longer the specimens remain in contact, the greater the material removal by fretting. A similar relationship has been observed previously whereby the amount of material removed is very nearly proportional to the number of cycles, if the test is carried out under steady state conditions. The situation has evolved from a two-body contact to a three-body contact. Similar behaviour was noted with other using a range of materials, including purely metallic combinations, metals against chalk, ceramics etc, under both cyclic and continuous running. In conclusion, particle detachment starts in the very first cycles; particle elimination can take very much longer depending on the trapping conditions in the contact. Yan [61] found that the critical amplitudes of tangential force and displacements were found to decrease with an increasing number of cycles, concluding that this phenomenon was related to the shrinkage of the stick zone, which may be a complex process related to plastic deformation and strain hardening on the contact surfaces.

- ***Wear debris***

Over the past decade, considerable attempts have been made to explain this role of wear debris, and whether the presence of wear debris in the contact region is detrimental or beneficial. Godet et al. [62-64] argued that mechanisms such as adhesion, abrasion and fatigue are only particle detachment mechanisms. A real wear process should be governed not only by particle detachment or “source”, but also elimination of wear particles or “sink” [65]. They named the transport of wear debris from inside the contact to outside as a kind of third-body flow and suggested that this third-body flow can be affected by contact shape, kinematics, contact dynamics, third-body properties and so on, based on the velocity accommodation model.

The role of debris on steel specimens has been demonstrated by carrying out tests where the fretting surfaces were periodically separated and the debris removed, resulting in an increase in the wear rate. Conversely, the introduction of wear debris between surfaces reduces the wear rate; the resultant surfaces were hardly damaged and showed signs of slight polishing. The debris is said to exhibit thixotropic (viscous fluid) behaviour [66] and load-carrying capacity; red oxides ( $\text{Fe}_2\text{O}_3$ ) have better load carrying capacity than grey oxide ( $\text{Fe}_3\text{O}_4$ ). Note, however, that the presence of a uniform bed does not, in all circumstances, guarantee surface protection. Sherrington and Hayhurst [67] studied the evolutionary behaviour of debris density in conjunction with COF in dry sliding steel contacts, as wear debris is believed to be responsible for the development of a number of physical phenomena in dry sliding. Work done by Varenberg et al. [68] showed that the role of wear debris was dependent on the dominant wear mechanism of fretting wear.

## **2.4 Prevention methods for fretting wear**

### ***2.4.1 Introduction***

Contacting components subjected to fretting may be affected by wear and/or fatigue induced cracking. Wear should always be considered early in the design process, and not just as an afterthought. Two main concerns that a designer has to consider are: (i) to establish whether significant wear will occur in service, and if so, to take steps to reduce the rate of wear to an acceptable level within the economic and other constraints imposed on the design, and (ii) an understanding of the factors which control wear phenomena in order to propose palliative minimisation methods. To minimise these tribological problems, palliatives such as surface coating or other superficial treatments, e.g. lubrication, are commonly used to improve the lifespan of the surfaces.

Protection steps to reduce fretting wear are extremely diverse. According to Beard [69], it is useful to know whether the cause of surface damage is by force- or displacement-controlled fretting type before the appropriate measurement is taken. The partial slip case is associated with the force-controlled fretting where increasing the COF, or the normal load, will reduce the slip. For displacement-controlled fretting, where slip is occurring over the contact interface, the amplitude is constant and wear will be reduced by reducing the normal load as well as the COF. Note that this current investigation is part of a methodology development to be validated against load-controlled laboratory spline testing. The following sections shall explore the benefits of surface engineering and lubrication methods in preventing surface damage.

### 2.4.2 Surface engineering

The recognition that a very large number of engineering components can either deteriorate progressively or fail catastrophically through surface-related phenomena has led to the establishment of the interdisciplinary subject of surface engineering. Surface engineering can be defined as the application of both traditional and innovative technologies to produce a composite material with superior properties, that are unattainable from individual pure substrate (e.g. pure metal).

There are two common objectives in the use of surface engineering for tribological applications (i) to improve the wear resistance of the surface material, and (ii) to modify its frictional behaviour. The flowchart in Figure 2-7 represents a summary of the availability methods for different applications. Surface treatments that radically change the chemical composition of the surface are divided into two categories [70]:

- *Surface modification*: this method involves foreign atoms or ions being introduced into the existing surface by diffusion or by bombardment.
- *Surface coating*: this method involves an entire foreign material layer being applied onto the surface.

Most of these coating/modified structures are harder and more brittle than the substrate, which if it is not strong enough will plastically deform in the contact region, where local stresses can be high. The coating-substrate integrity determines the durability of a wear resistant layer towards surface damage [41]. Figure 2-8 shows the comparisons of the process temperatures and depth of hardened material produced by various methods of surface modification to steels. In the application of surface coatings, Figure 2-9 shows the typical thicknesses of engineering surface layers produced by various plating and deposition techniques. Assigning surface treatments

to design cases is rather a daunting task, as there are certain factors that need further consideration. Carton et al. [72] developed a methodology in determining a suitable choice of coating against fretting for different applications. A distinction was made between thick and thin coatings using contact mechanics. Four axes in the polar diagram present the parameters that are involved in the development of the methodology (Figure 2-10). The four different axes are as follows:

- the intrinsic properties of the surface (elastic modulus, yield strength, fatigue strength)
- properties associated with the coating-substrate interface, residual stresses, binding strength
- the running condition of tribological systems (load ratio, contact width in the stick and slip domain, COF)
- the material regime (crack depth, wear depth, crack initiation time)

The polar diagram concomitantly describes the difference in behaviour between the coatings. Sung [73] studied the application of different surface treatments on rotors. He concluded that in order to develop a proper coating material relation, at least the following tribological characteristics are required at least: optimal hardness, good coating-substrate integrity, and durable and easily shearable tribo-film forming capability.

#### **2.4.3 Lubrication – boundary lubrication regime**

The life of mechanical components can be prolonged by choice of a suitable lubricant. Lubricants reduce friction in machine components by producing a physical or chemical barrier between surfaces that slide or roll past each other. This barrier can involve a film of solid, liquid, or gaseous material that can be sheared with low

resistance, without causing any damage to the surface. A detailed classification of lubrication modes is shown in Figure 2-11 and the differentiation of various modes are shown on the Stribeck curve (Figure 2-12) [74], which describes the frictional behaviour of different lubrication regimes. The Stribeck curve illustrates the change in COF as a function of the lubricant parameter,  $\eta VP^{-1}$ . The three main lubrication modes may be distinguished as (i) hydrodynamic lubrication, (ii) elastohydrodynamic lubrication, and (iii) boundary lubrication.

Ideally, load-bearing surfaces are separated by a hydrodynamic or elastohydrodynamic oil film. When this oil film breaks down under high loads, high temperatures or low speeds, asperity contact occurs and boundary lubrication (BL) conditions are said to exist. BL is often defined as “a condition of lubrication in which friction and wear between two surfaces in relative motion are determined by the properties of the lubricant other than bulk viscosity.” Under BL conditions, the COF value varies from approximately 0.007 to 0.5. For wear coefficient ( $k$ ), the values varied from  $10^{-2}$  to  $10^{-8}$  [75]. Figure 2-13 shows that changes in load in relation to sliding velocity, which can cause three different BL regimes with different levels of  $k$ . In the mild wear regime,  $k$  is less than  $10^{-7}$  and wear rates are very low. This is the regime required for prolonging the lifespan of machine elements. The damage-controlled regime is characterised by a higher  $k$  of  $10^{-7}$  to  $10^{-4}$ . In this regime, some surface changes can be expected but the level of damage is tolerable. In the surface-damage wear regime, high wear occurs typically gives  $k$  value between  $10^{-6}$  and  $10^{-3}$  and the surfaces are damaged by scuffing. Rowson et al. [76] studied the pitting sequences of lubricated surfaces on lubricated discs. The topographical changes were based on the hackle theory (the asperity is plastically deformed by a

sliding/rolling action to form a hackle). It is believed that the fractured hackle (posterior end) gouged the surface (during further cyclic stress) and provided a potential site for crack initiation (at the posterior end) in which the crack may be extended by the chemical and hydraulic action of the lubricant.

Lubricant reduces friction in machine components by producing a film that separates moving surfaces. By using oil with the correct viscosity, friction and wear in machines can be kept to a minimum level. Lee and Ludema [77] studied this phenomenon based on the assumption that the lubricant carries part of the applied load and asperities carry the remaining load by solid contact and adhesion. Similar work by Blencoe and Williams [78] suggested that the lubricants rheology properties dictate its capability of load sharing during relative motion and the type of additives to be added for improvement (protection). There are three types of oil-soluble BL additives used in formulating oils and greases. They are (i) lubricity agents, (ii) extreme-pressure agents, and (iii) anti-wear additives. McFadden et al. [79] studied the performance of the lubricant and lubricant additives in the BL regime. Zhou and Vincent [80] studied the fretting phenomenon using various lubricant types. For the partial slip regime, solid lubricant is a better choice and it functions more efficiently when fretting takes place. Alternatively, oil and grease protects the contact area efficiently when fretting takes place in the gross slip regime. Under grease lubrication, the effect of amplitude and applied normal load on fretting wear was investigated experimentally by Zhou et al. [81]. The data indicated that material hardness played an important role in determining the type of wear mechanism. For example, abrasive wear dominates with materials of dissimilar hardness, whilst adhesive wear dominates for materials of identical hardness. Again, there is a

possibility of residual oil penetration into cracks, causing further damage. The effect of displacement in relation to the COF can be associated with the degree of oil penetration into the fretted area. The larger the displacement amplitude, the more likely the fretted area is to be covered by a larger portion of the oil and hence, the more likely a reduction of COF [82].

## **2.5 Fretting wear model**

### ***2.5.1 Contact mechanics and fretting wear simulation methodology***

The most common and simplest wear model proposed in tribology is the Archard model, which relates the wear volume to the normal force and the sliding distance [83]. The Archard model is effective assuming that there are no changes in the wear surfaces as a result of the sliding process or otherwise. In deriving his well-known wear equation, he used the adhesion-asperity-deformation model of Bowden and Tabor. Because such a relation does not integrate the COF variable, it has been demonstrated that it fails to correctly predict the extent of wear, particularly for contact situations displaying fluctuation of COF. Unlike crack nucleation analysis, quantifying wear is more difficult, because there is no universal and well-formulated wear model, especially in situations concerning wear induced by debris formation. For some situations, where wear debris is more easily eliminated from the contact area and more metal-to-metal contact is maintained, the influence of debris can be reasonably neglected (a purely contact-based wear problem). Some analytical techniques [84-87] were developed based on these assumptions to study the fretting wear phenomenon. Johansson [88] presented a finite element (FE) solution, which incorporates a local implementation of Archard's equation to evaluate the change of contact geometry and the associated changes in contact pressure. More recently, Ding

[89] developed a finite element-based wear simulation method, using a commercial FE code, based on a modified version of the Archard equation. The numerical approach was applied to a two-dimensional cylinder-on-flat fretting configuration (Figure 2-14) for gross slip and partial slip conditions. The accuracy of the unworn FE model was validated using the well-known analytical solutions for the Hertzian stress distribution [90]. The contact pressure distribution is as follows:

$$p(x) = p_o \sqrt{1 - \frac{x^2}{a^2}} \quad (2-1)$$

The half width contact area  $a$  and maximum contact pressure  $p_o$ , are given as respectively:

$$a = \left( \frac{4PR}{\pi E^*} \right)^{1/2} \quad (2-2)$$

$$p_o = \left( \frac{PE^*}{\pi R} \right)^{1/2} \quad (2-3)$$

where  $P$  is the applied normal load per unit length, and  $E^*$  is a compound modulus as for the contacting bodies under the plane strain condition, given by:

$$E^* = \left( \frac{1 - (\nu^f)^2}{E^f} + \frac{1 - (\nu^r)^2}{E^r} \right)^{-1} \quad (2-4)$$

where  $E^f$  and  $E^r$  are the elastic moduli of the flat and round bodies, respectively and  $\nu^f$  and  $\nu^r$  are the Poisson's ratios. The relative curvature  $R$  is as follows:

$$R = \left( \frac{1}{R^f} + \frac{1}{R^r} \right)^{-1} \quad (2-5)$$

with  $R^f$  and  $R^r$  as the contact surfaces radii. The FE predicted contact pressure is in agreement with the Hertzian analytical solution as shown in Figure 2-15. The sub-

surface  $x$  and  $y$  directions normal stresses along the vertical  $y$ -axis (principal stresses) are given as [90]:

$$\sigma_x = -\frac{P_o}{a} \left\{ a^2 + 2y^2 \right\} \left( a^2 + y^2 \right)^{-\frac{1}{2}} - 2y \quad (2-6)$$

$$\sigma_y = -\frac{P_o}{a} \left( a^2 + y^2 \right)^{-\frac{1}{2}} \quad (2-7)$$

Figure 2-16 shows a comparison between the analytical stress distributions and the corresponding FE predictions, with both methods agreeing with each other.

The main building block used for developing the fretting wear simulation tool was based on Archard's equation [91], which can be written as follows:

$$\frac{V}{S} = K \frac{P}{H} \quad (2-8)$$

where  $V$  is the total wear volume,  $P$  is the normal load,  $K$  is the dimensionless wear coefficient,  $H$  is the hardness (MPa) of the material and  $S$  is the total slip distance between the contacting surfaces. To simulate the evolution of the surface profiles, it is necessary to determine the wear depth locally as a function of horizontal contact position,  $x$ , i.e. at each contact node of the FE model. Following McColl et al. [92] and Medina and Olver [93], the final product of the modified Archard equation used to predict local increment of wear depth ( $dh$ ) is

$$dh = kp(x)dS \quad (2-9)$$

where  $k$  is the dimensional wear coefficient,  $p(x)$  is the local pressure, and  $dS$  is the increment local sliding distance. Equation (2-9) implies that the incremental wear depth at a given point on the contact is proportional to the wear coefficient, the contact pressure and the increment of slip distance. Note that  $k$  is estimated from experimental data in which the total slip distance is assumed to be approximately

equal to  $4\delta^*N_t$ , where  $\delta^*$  is the applied half stroke amplitude corresponding to the representative slip value discussed above. The flow chart in Figure 2-17 shows an overview of the methodology of the fretting wear simulation by Ding [89].

One of the most important challenges for the general application of the above method is minimisation of the wear simulation time i.e. when fretting wear assessment involves complex design such as aeroengine spline couplings. According to Ding [89], assessment of the slip distributions during different stages of the tangential force-displacement cycle has established that the total slip distance for the complete cycle can be satisfactorily estimated from the slip distance, corresponding to the application of the positive tangential displacement only. This simplification has significantly reduced the simulation time.

## References

1. Oxford Dictionary of English, *Oxford University Press*, 2005
2. *Lubrication(tribology) education and research.*, Jost Rep., Department of Education and Science, HMSO, London, 1966, pp. 4
3. Y. Kimura, "Maintenance tribology: its significance and activity in Japan", *Wear*, Vol. 207, 1997, pp.63-66
4. I.M. Hutchings, "Friction and Wear of Engineering Materials", *Butterworth Heinemann*, Suffolk, 2001
5. P. J Blau, "The significance and use of the friction coefficient" *Tribology International*, 34, 2001, pp. 585-591
6. R.B. Waterhouse, "Friction, Lubrication, and Wear: Fretting Wear", A.S.M Handbook, ASM International, Ohio, 1992
7. Neyman and O. Olszewski, "Research on fretting wear dependence on hardness ration and coefficient of friction of fretted couple", *Wear*, 1993, Vol. 162-164, pp. 939-943
8. R.B. Waterhouse, *Fretting Corrosion*, Pergamon, Oxford, 1972, pp. 232-234
9. L. Berthier, L. Vincent and M. Godet, "Fretting fatigue and fretting wear", *Tribology International*, 1989, Vol. 22, No. 4, pp. 238-239
10. T. Warburton, "The fretting of mild steel in air", *Wear*, 1988, Vol. 131, pp. 384-385
11. E.M. Eden, W.N. Rose, and F.L. Cunningham, "Endurance of Metals", *Proceedings Institution of Mechanical Engineers*, 1911, Vol. 4 , pp. 839-974
12. G.A Tomlinson, "The rusting of steel surfaces in contact", *Proc. R. Soc.(London) A*, 1927, Vol. A115, pp. 472-482

13. E.J. Warlow-Davies, "Fretting Corrosion and Fatigue Strength", *Proceedings Institution of Mechanical Engineers*, 1941, Vol. 46, pp. 32-38
14. J.R. McDowell, "Fretting Corrosion Tendencies of Several Combinations of Materials", *Symposium on Fretting Corrosion*, STP 144, American Society for Testing and Materials, 1953, pp. 2439
15. A.J. Fenner and J.E. Field, "La Fatigue dans les Conditions de Frottement", *Rev. Metall.*, 1985, Vol. 55, pp. 475-485
16. S. Fouvry, Ph. Kapsa, and L. Vincent, "Analysis of sliding behaviour for fretting loadings: determination of transition criteria", *Wear*, Vol. 185, 1995, pp. 35-46
17. S. Fouvry, "Shakedown analysis and fretting wear response under gross slip condition", *Wear*, Vol. 251, 2001, pp. 1320-1331
18. S. Fouvry, Ph Kapsa, and L. Vincent, "An elastic-plastic shakedown analysis of fretting wear", *Wear*, Vol. 247, 2001, pp. 41-54
19. S. Fouvry, T. Liskiewicz, Ph Kapsa, S. Hannel, and E. Sauger, "An energy description of wear mechanisms and its applications to oscillating sliding contacts", *Wear*, Vol. 255, 2003, pp. 287-298
20. A. Kapoor, "Wear by plastic ratchetting", *Wear*, Vol. 212, 1997, pp. 119-130
21. V. Fridrici, S. Fouvry, P. Kapsa, and P. Perruchuat, "Impact of contact size and geometry on the lifetime of a solid lubricant", *Wear*, Vol. 255, 2003, pp. 875-882
22. D. Godfrey, "Investigation of Fretting by Microscopic Observation", *NACA*, Report No. 1009, 1951
23. D.E. Taylor, and R.B. Waterhouse, "Sprayed molybdenum coatings as a protection against fretting fatigue", *Wear*, 1972, Vol. 20, pp. 401-407

24. R.D Schmidt and D.P Feris, " New material resistant to wear and corrosion to 100°C", *Wear*, 1975, Vol. 32, pp. 279-289
25. P.L Hurricks, " The Mechanism of Fretting-A Review", *Wear*, 1970, Vol. 15, 389-409
26. L.E. Samuels, E.D. Doyle, and D. M. Turley, " Sliding wear mechanisms", *Fundamental of Friction and Wear of Materials*, ASM, Ohio, 1980, pp. 31-41
27. T. Kabaya and K. Kato, " Wear of Materials", *ASME*, New York, 1979
28. L. Vincent, J. Berthier, M.C. Duboury, and M. Godet, " Mechanics and materials in fretting", *Wear*, 1992, Vol. 153, pp. 135-148
29. J. M. Dobromirski, "Variables of Fretting Process: Are There 50 of Them?", *Standardisation of Fretting Fatigue Test Methods and Equipment*, ASTM STIP 1159, 1992, pp. 60-66
30. K.H. R. Wright, " An Investigation of Fretting Corrosion", *Proceedings Institution of Mechanical Engineers*, 1952, Vol. 1, Series D, pp. 556-574
31. M. Feng and B.G Rightmire, " An Experimental Study of Fretting", *Institution of Mechanical Engineers*, 1956, Vol. 170, pp. 1055-1060
32. R. Ward, " A Comparison of Reciprocating and Continuous Sliding Wear", *Wear*, 1970, Vol. 15, pp. 423-434
33. J. S. Halliday and W. Hirst, " The Fretting Corrosion of Mild Steel", *Proceedings Royal Society of London*, 1956, Series A, Vol. 236, pp. 411
34. J.S. Halliday, " Experimental Investigations of Some Processes Involved in Fretting Corrosion", *Institution of Mechanical Engineers :Conference on Lubrication and Wear*, October 1956, pp. 640-646

35. H. Charney, " Fundamental of Interfacial Slip Damping", MS thesis, Department of Mechanical Engineering, Massachusetts Institute of Technology, June 1970
36. S. Aoki, T. Fujimara, I. Furukama, " Fretting of Bearing Steel by Rolling Contact", *Bulletin of the Japan Society of Precision Engineering*, 1947, Vol. 2, No. 3, pp. 238-245
37. N. Ohmae and T. Tsukizue, " The effect of slip amplitude on fretting ", *Wear*, 1974, Vol. 27, pp. 281-294
38. D. Aladham and J. Warburton, " The unlubricated fretting wear of mild steel in air", *Wear*, 1985, Vol. 106, pp. 177-201
39. O. Vingsbo and S. Soderberg, "Wear of Materials", 1987, *ASME*, pp. 885-894
40. O. Vingsbo and S. Soderberg, " On Fretting Maps", *Wear*, 1988, Vol. 126, pp. 131-147
41. R.C. Bill, "Fretting wear and fretting fatigue- how are they related? " ,*Trans. ASME Journal of Lubrication Technology*, 1983, Vol. 105, pp. 230-238
42. L. Toth, " The investigation of the steady state of steel fretting", *Wear*, Vol. 20, 1972, pp. 277
43. M. J. Lewis and P. B. Didsbury, " The rubbing fretting behaviour of mild steel in air at room temperature: the effect of load, frequency, slip amplitude and test duration, as reported by R.B. Waterhouse, in D. Scott (ed.)", *Treatise on Materials Science and Technology*, Vol. 13, *Wear*, Academic Press, New York, 1979
44. O. Vingsbo and J. Schon, " Gross slip criteria in fretting", *Wear*, 1993, Vol. 162-164, pp. 347-356

45. X. Zhang, C. Zhang, and C. Zhu, "Slip amplitude effects and microstructural characteristics of surface layer in fretting wear of carbon steel", *Wear*, 1989, Vol. 134, pp. 297-309
46. R. F. Baker and A.V. Olver, "Direct observations of fretting wear of steel", *Wear*, Vol. 203-204, 1997, pp. 425-433
47. X. Chen and Z. R. Zhou, "Study on transition between fretting and reciprocating sliding wear", *Wear*, Vol. 250, 2001, pp. 665-672
48. O. Jin and S. Mall, "Effects of slip on fretting behaviour: experiments and analyses", *Wear*, Vol. 256, 2004, pp. 671-684
49. J. Ding, S. B. Leen, and I. R. McColl, "The effect of slip regime on fretting wear-induced stress evolution", *International Journal of Fatigue*, 26, 2004, pp. 521-531
50. F. P. Bowden and D. Tabor, "The Friction and Lubrication of Solid", *Oxford University Press*, 1950, pp. 19
51. M. Feng and H.H. Uhlig, "Fretting Corrosion of Mild Steel in Air and Nitrogen", *Journal of Applied Mechanics*, 1954, Vol. 21, pp. 395-400
52. U. Bryggman and S. Soderberg, "Contact conditions in fretting", *Wear*, 1986, Vol. 110, pp. 1-17
53. W. J. De Gee, C. P. L. Commisaris, and J. H. Zoat, *Wear*, 1964, Vol. 7, pp. 535
54. T. Liskiewicz, S. Fouvry, and B. Wendler, "Impact of variable loading conditions on fretting wear", *Surface and Coatings Technology*, 163-164, 2003, pp. 465-471
55. Iwabuchi, "The role of oxide particles in the fretting wear of mild steel", *Wear*, 1991, Vol. 151, pp. 301-311

56. M. Kuno and R. B. Waterhouse, "The effect of oscillatory direction on fretting wear under crossed cylinder contact conditions", *Eurotrib 89 Proceedings of the 5<sup>th</sup> International Congress on Tribology*, Helsinki, 1989, Vol. 3, pp. 30-35
57. R. Magaziner, O. Jin, and S. Mall, "Slip regime explanation of observed size effects in fretting", *Wear*, Vol. 257, 2004, pp. 190-197
58. H. K. Kim and Y. H. Lee, "Influence of contact shape and supporting condition on tube fretting wear", *Wear*, Vol. 255, 2003, pp. 1183-1197
59. S. Soderberg, U. Bryggman, and T. McCullough, "Frequency Effects in Fretting Wear", *Wear*, 1986, Vol. 101, pp. 19-34
60. K. Schouterden, B. Blanpain, J. P. Celis and O. Vingsbo, "Fretting of titanium nitride and diamond-like carbon coatings at high frequency and low amplitude", *Wear*, Vol. 181-183 (1), February 1995, pp. 86-93
61. P. Yan, "The effect of number of cycles on the critical transition boundary between fretting fatigue and fretting wear", *Wear*, Vol. 160 (2), 1993, pp. 279-289
62. M. Godet, "The third-body approach: a mechanical view of wear", *Wear*, 1984, Vol. 100, pp. 437-452
63. Y. Berthier, L. Vincent and M. Godet, "Velocity accommodation in fretting", *Wear*, 1988, Vol. 125, pp. 25-38
64. M. Godet, Y. Berthier, and J. Lancaster, "Wear modeling: using fundamental understanding or practical experience?", *Wear*, 1991, Vol. 149, pp. 325-340
65. M. Godet, "Third-bodies in tribology", *Wear*, 1990, Vol. 136, pp. 29-45

66. Ch. Colombie, Y. Berthier, A. Flouter, L. Vincent, and M. Godet, " Fretting: Load Carrying Capacity of Wear Debris", *Journal of Tribology*, 1984, Vol. 106, pp. 194-201
67. Sherrington and P. Hayhurst, " Simultaneous observation of the evolution of debris density and friction coefficient in dry sliding steel contacts", *Wear*, Vol. 249, 2001, pp. 182-187
68. M. Varenberg, G. Halperin, and I. Etsion, " Different aspects of the role of wear debris in fretting wear", *Wear*, Vol. 252, 2002, pp. 902-910
69. J. Beard, " The Rational Selection of Palliatives for Avoidance of Fretting", *Tribology-Friction, Lubrication and Wear, Fifty Years On, Conference Proceeding Institution of Mechanical Engineers (London)*, 1-3 July 1987, Vol. 1, pp. 311-319
70. J.A. Williams, " Engineering Tribology", *Oxford Science Publications*, New York, 1998
71. K. Kubiak, S. Fouvry, and A.M. Marechal, "A practical methodology to select fretting palliatives: Application to shot peening, hard chromium and WC-Co coatings", *Wear*, Vol. 259, 2005, pp. 367-376
72. J. F. Carton, A.B. Vannes, and L. Vincent, "Basis of a coating choice methodology in fretting", *Wear*, 1995, Vol. 185, pp. 47-57
73. H.C Sung, " Tribological characteristics of various surface coating for rotary compressor valve", *Wear*, 1998, Vol. 221, pp. 77-85
74. A.Z. Seri, " Tribology: friction, lubrication and wear", Hemisphere, London, 1980
75. R. S. Fein, "Boundary Lubrication ©", *Journal of the Society of Tribologists and Lubrication Engineers*, 1991, pp. 1005-1008

76. D.M. Rowson and Y.L. Wu, "The sequential observation of the pitting process in debris", *Wear*, No. 70, 1981, pp. 383-393.
77. Y.Z. Lee and K.C. Ludema, "The shared-load wear model in lubricated sliding: scuffing criteria and wear coefficient", *Wear*, No. 138, pp. 13-22.
78. K.A. Blencoe and J. A. Williams, "Friction of sliding surfaces carrying boundary films", *Wear*, No. 203-204, 1997, pp. 722-729 \*
79. McFadden, C. Sato, and N.D. Spencer, "Adsorption and surface chemistry in tribology", *Tribology International*, Vol. 30, No.12, 1997, pp. 881-888.
80. Z. R. Zhou and L. Vincent, "Lubrication in fretting – a review", *Wear*, Vol. 225-229, 1999, pp. 962-967
81. Z. R. Zhou, Q.Y. Liu, M.H. Zhou, L. Tanjda, P. Kapsa, and L. Vincent, "An investigation of fretting behaviour of several metallic materials under grease lubrication", *Wear*, No. 33, 2000, pp. 69-74 \*
82. Q. Y. Liu and Z.R. Zhou, "Effect of displacement in oil-lubricated fretting", *Wear*, No. 239, 2000, pp. 237-243
83. J. M. Martin, C. Grossiord, T. Le Mogne, and J. Igarashi, " Transfer films and friction under boundary lubrication", *Wear*, Vol. 245, 2000, pp. 107-115
84. H. C. Meng and K. C. Ludema, " Wear models and predictive equations: their form and content", *Wear*, Vol. 181-183, 1995, pp. 443-457
85. L. A. Galin, I. G. Korovchinsky, "Axisymmetric contact problem of the theory of elasticity in the presence of wear", *J. Appl. Math. Mech.*, 41, 1977, pp. 826-831
86. G. Korovchinsky, P. T. Rajeev, and T.N Farris, "Wear in partial slip contact", *J. Tribol.*, Vol. 123, 2001, pp. 848-856

87. L. Johansson, "Numerical simulation of contact pressure evolution in fretting", *J. Tribol.*, Vol. 116, 1994, pp. 247-254
88. M. Oqvist, " Numerical simulation of mild wear using updated geometry with different step size approaches", *Wear*, Vol. 249, 2001, pp. 6-11
89. J. Ding, "Modelling of Fretting Wear", Ph.D Thesis, University of Nottingham, 2003
90. K. L. Johnson, " Contact Mechanics", *Cambridge University Press*, Cambridge, 1985
91. J. F. Archard, "Contact and rubbing of flat surfaces", *J. Applied Phys.*, 1953, Vol. 4, pp.981-988
92. I. R. McColl, J. Ding, and S. B. Leen, " Finite element simulation and experimental validation of fretting wear", *Wear*, Vol. 256, 2004, pp. 1114-1127
93. S. Medina and A. V. Olver, "An analysis of misaligned spline couplings", *Proc. Instn. Mech. Engrs: J Engineering Tribology.*, Vol. 216, Part J, 2002, pp. 269-279

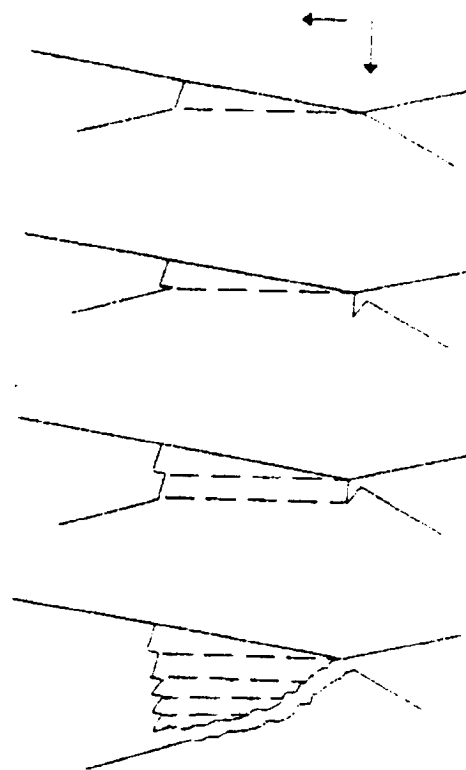


Figure 2-1: Debris formation caused by mechanical interlocking between contacting asperities [27].

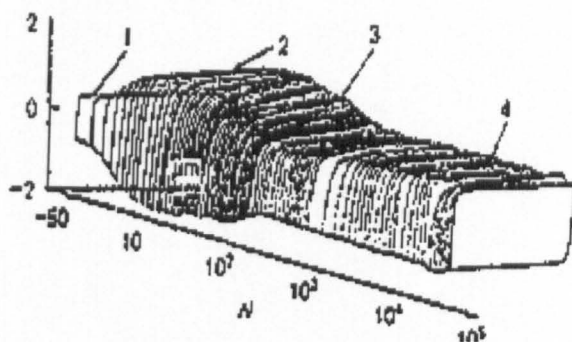


Figure 2-2: Determination of fretting regimes based on friction log [28].

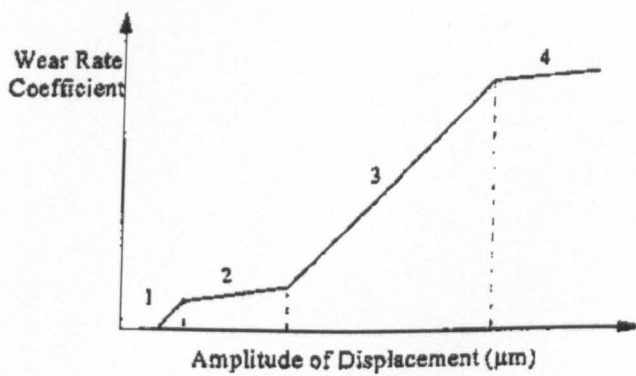


Fig. 1. The four wear regimes (after [2]).

Figure 2-3: Different regimes of wear dependent on the slip amplitudes [39, 40].

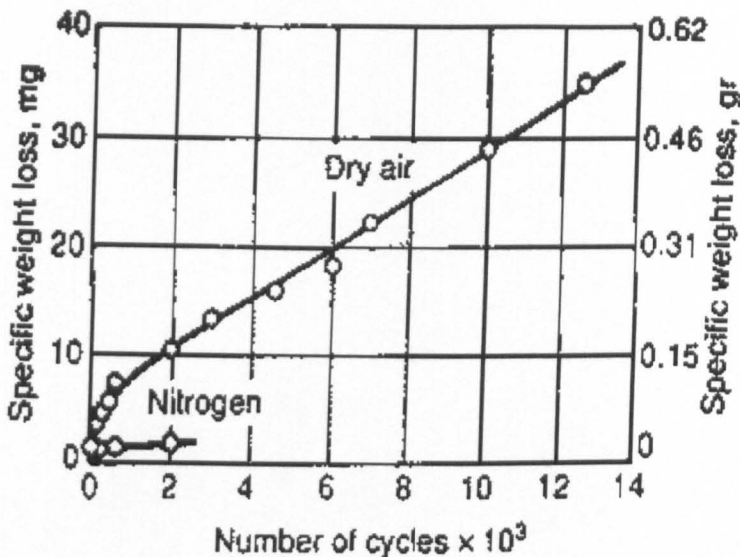


Figure 2-4: Feng and Uhlig [51] experimentally showed that the amount of material removal is proportional to applied normal load at constant slip amplitude.

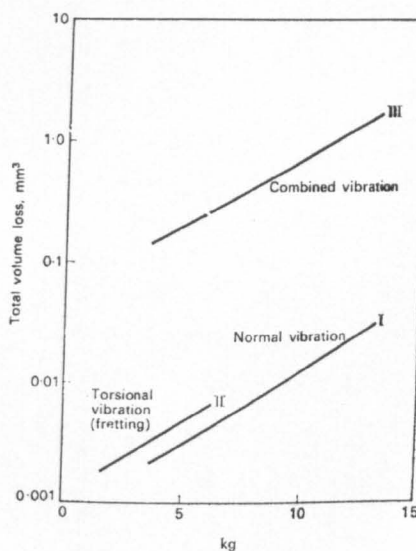


Figure 2-5: Wear damage is accelerated when both fretting and normal vibration are combined [53].

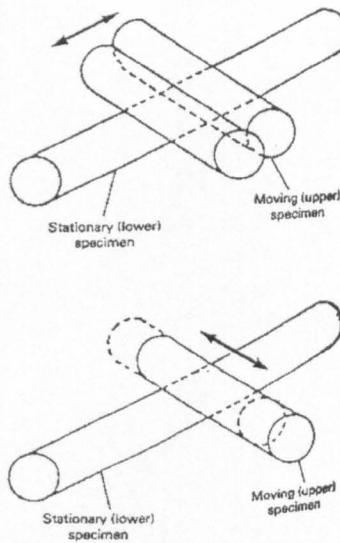


Figure 2-6: Ejection of debris is determined by the direction of motion and contact geometry [56].

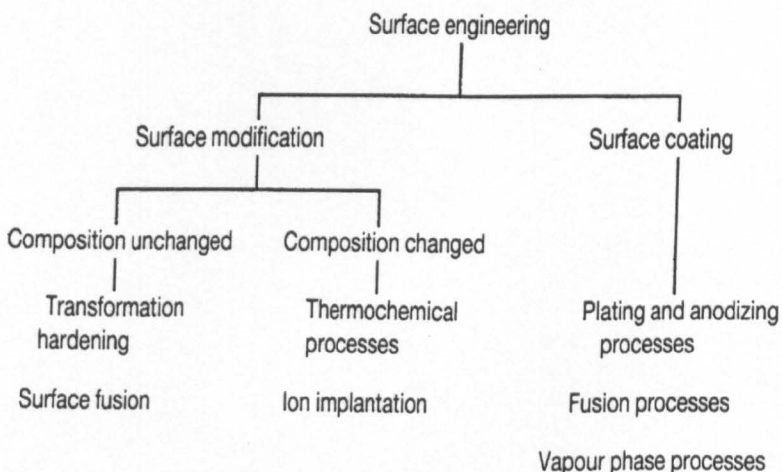


Figure 2-7: Classification of different surface engineering methods for various applications [70].

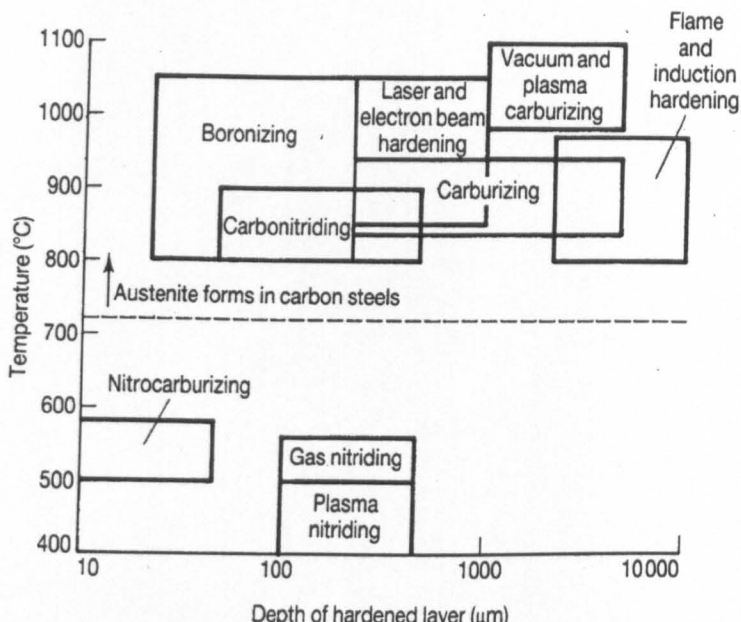


Figure 2-8: Various surface modification choices available for improving the hardness profile of steels [4].

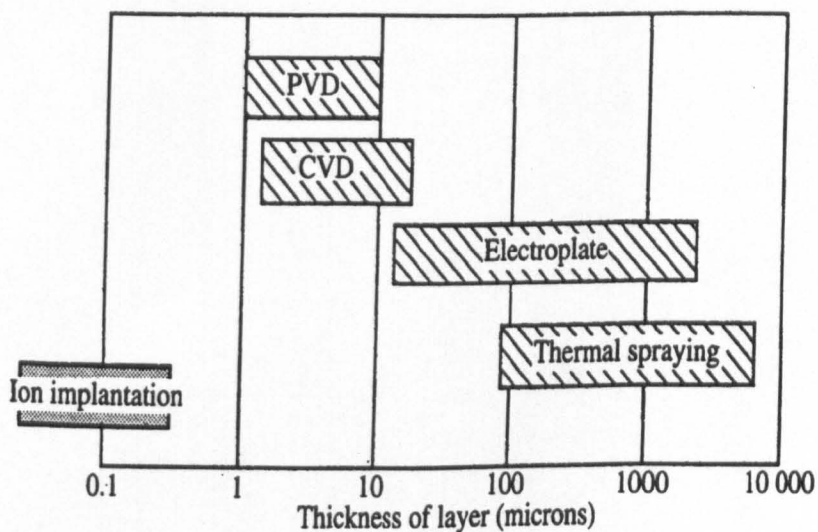


Figure 2-9: Production of various engineered surfaces thicknesses by different plating and deposition techniques [71].

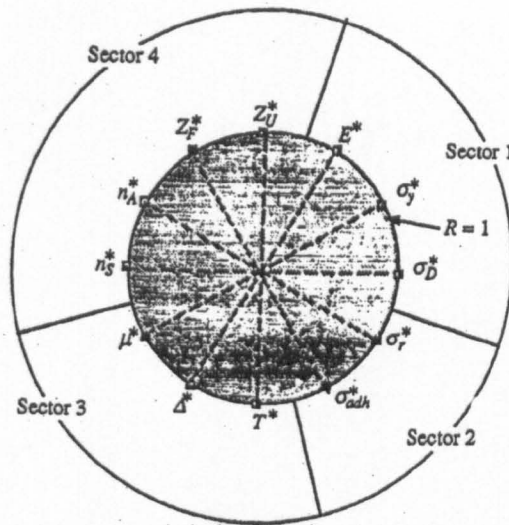


Figure 2-10: Polar diagram representing the parameters used to determine suitable coating type [72].

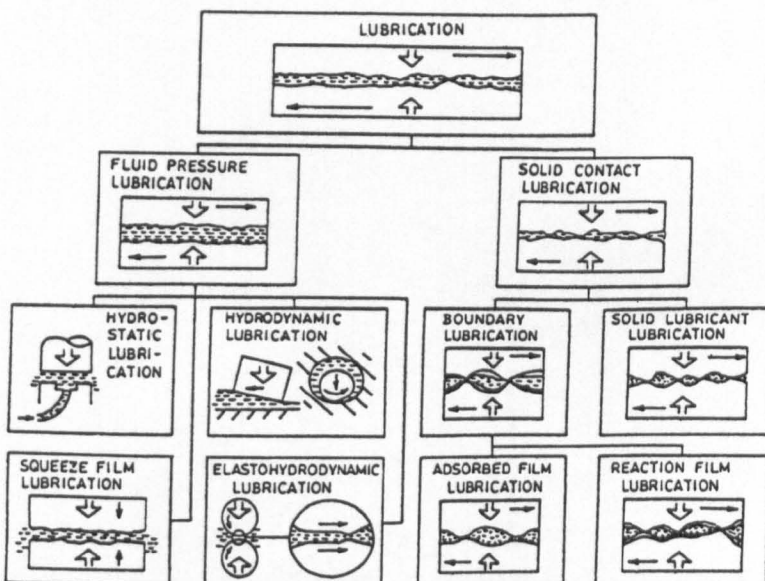


Figure 2-11: Detailed classification of lubrication modes for tribological applications [74].

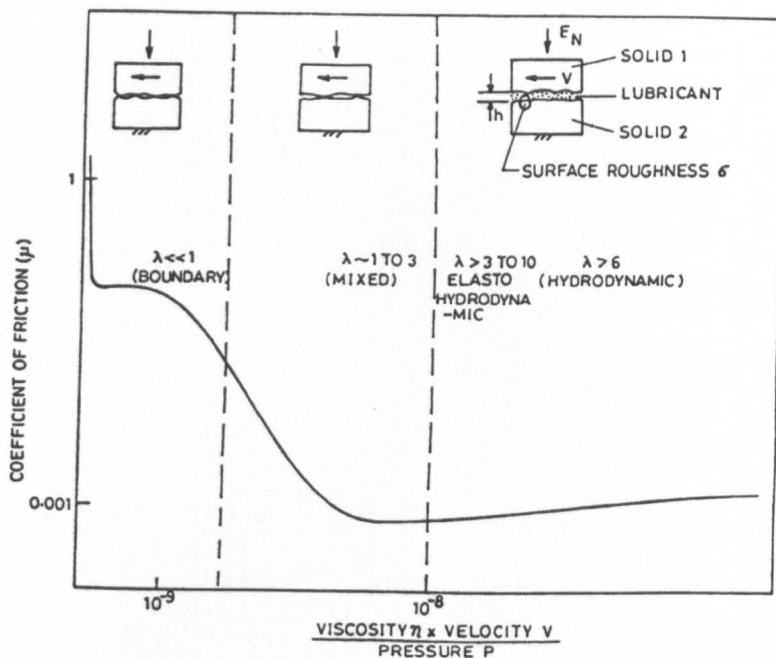


Figure 2-12: Stribeck curve representing different lubrication regimes changes with coefficient of friction as a function of lubricant parameter,  $\eta VP^{-1}$  [74].

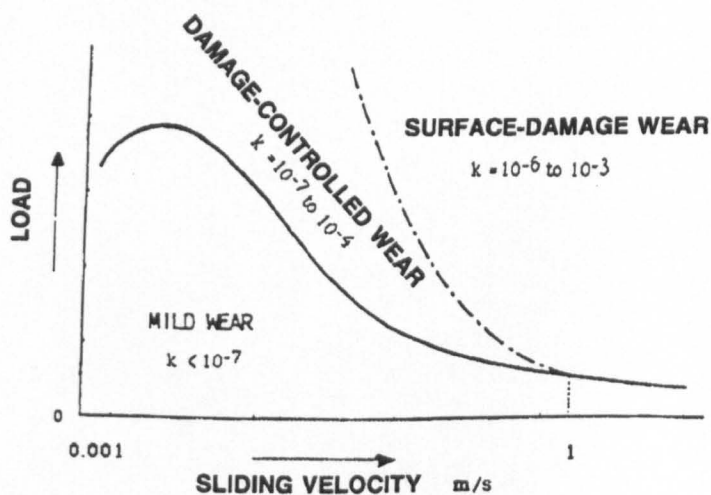


Figure 2-13: Different boundary lubrication regimes associated with the change in load in relation to sliding velocity [75].

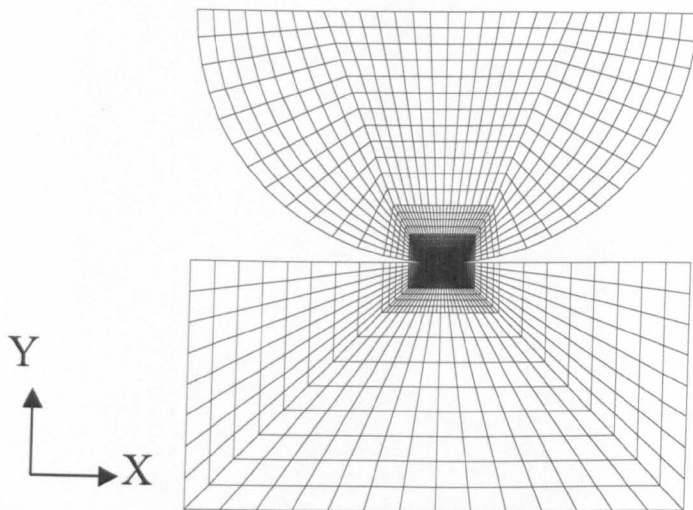


Figure 2-14: A two-dimensional FE simple round-on-flat model [89].

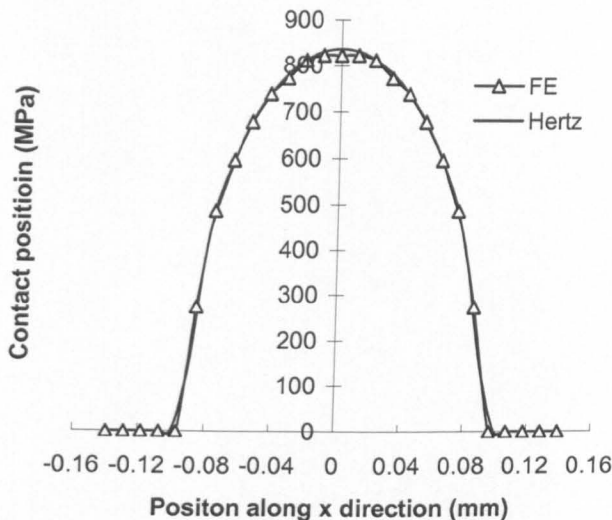


Figure 2-15: Contact pressure comparison between FE predicted and Hertzian analytical solution under a normal load of 1200 N [89].

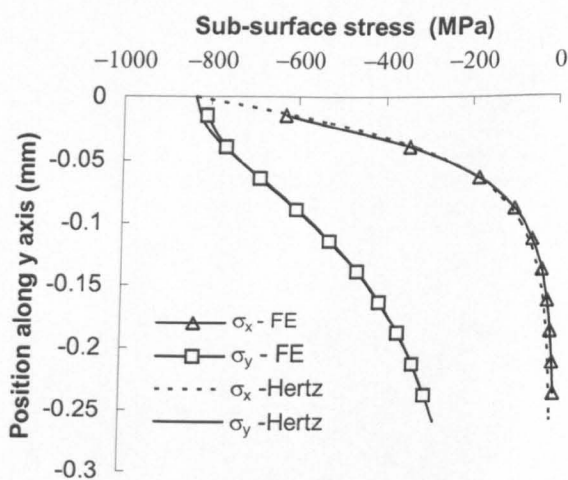


Figure 2-16: Sub-surface stresses comparison between FE predicted and Hertzian analytical solution under a normal load of 1200 N [89].

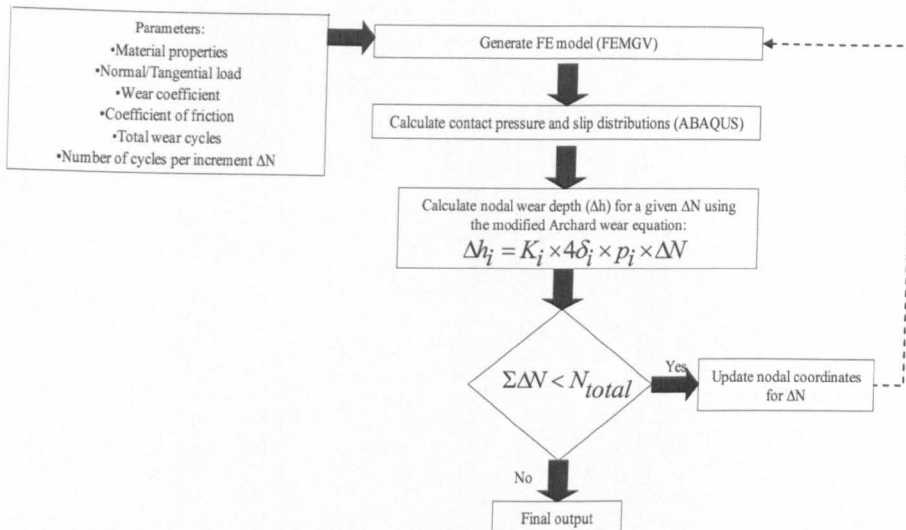


Figure 2-17: Flow chart representing the methodology used in modeling the wear simulation tool [92].

---

## **Chapter 3: Aeroengine transmission materials**

---

### **3.1 General**

The drive for increasing torque density and reducing the test costs in engine development provides the impetus for the development of a more scientific and accurate design methodology for spline couplings. Mechanical/structural design is essentially about arriving at the least expensive geometry, material and manufacturing combination that can avoid failure with a required safety margin. It is in the interest of aeroengine manufacturers such as Rolls Royce plc to improve their engine mainshafts (in terms of performance). The strategy is to make the couplings small as possible while optimizing torque transmission, and carry out material and component feature testing in parallel with the design work to reduce the risk of failing to meet the design objectives. Mechanical design for high performance transmission and couplings applications requires the following design criteria:

- Sufficient wear resistance to resist frictional wear or bearing stress
- Sufficient fatigue strength to withstand the high rotational speeds and hoop stresses
- High hardness to withstand rolling contact fatigue damage
- Temperature resistance up to 400°C
- Adequate resistance to corrosion/ stress corrosion
- Adequate toughness to withstand shock loads

In this chapter, the characteristics of candidate aeroengine transmission materials are discussed.

## **3.2 Super S/CMV (SCMV)**

### **3.2.1 Material characteristic**

Super S/CMV (SCMV) is based on BS 3S 132 (1976) [1] by Allvac Limited with the chemical composition (mass%) given in Table 3-1. This hardened steel alloy is an upgraded version of the Rolls Royce CMV, chromium-molybdenum-vanadium steel alloy, but with increased plain fatigue resistance and ultimate strengths [2]. The notch fatigue strength, ductility, and fracture toughness also had to be equivalent or better for stress concentration features. The material and mechanical properties of SCMV were improved by virtue of the three significant changes to the preparation and manufacturing process; (i) the higher strength was obtained by reducing the tempering temperature; (ii) employment of a triple vacuum melt route to improve fatigue performance; (iii) chemical composition alteration to improve the hardenability.

The SCMV alloy was heat-treated using the QT procedures (Austenite reversion → Tempering) [3] to acquire the mechanical properties given in Table 3-2. The microstructural detail of SCMV was revealed by etching the sample in 1% Nital for 30 seconds and is shown in Figure 3-1. Within the structure, tempered martensite was revealed as white nodular precipitates sitting on the lath packets.

### **3.2.2 The effect of gas nitriding**

In the 1920s and 1930s, gas nitriding was exclusively used to increase the surface mechanical strength. A temperature of approximately 500°C is typically used to impart the desirable properties of high strength and surface hardness. The major advantages with nitriding are the minimal dimensional changes and distortion of the treated component due to low processing temperature and the fact that the core

material does not undergo structural change. Nitriding is a commonly used technique for both gears and splines and is found to give improved wear characteristics. The most important effect is the increased hardness of the component surface, thus increasing the wear resistance, since wear rate is generally assumed to be inversely proportional to hardness. In addition, the coefficient of friction is sometimes considered as being inversely proportional to hardness, so that increased hardness tends to give a reduced coefficient of friction [4, 5]. A second effect of nitriding is the introduction of residual stresses in the surface; these are assumed to be compressive and thus, beneficial to fatigue life.

In this work, due to the use of gas nitriding in the target application, gas nitriding was carried out (a pressure of 1-2 atm.) in an atmosphere of 4 parts N<sub>2</sub> and 1 part H<sub>2</sub> for 60 hours at a temperature of 495 ± 5°C to achieve a hardness of ≥ 800 HV0.1 over a depth of 50 µm. The different sub-nitrided zones on the modified SCMV are shown in Figure 3-2a. The outermost zone, usually porous-like, contains two types of nitride that are γ'(Fe<sub>2,3</sub>N) and ε(Fe<sub>4</sub>N) [6-8] (Figures 3-2b and c). In general, this zone has a relatively low wear resistance but may serve as a lubricant reservoir that can therefore be beneficial to oxidative wear, for example. Primary parameters such as treatment time and nitrogen activity, dictate the amount of pore production. The next zone, a dense non-porous layer has good wear resistance due to the non-metallic characteristic of the hard nitrides; the form of the nitrides is determined by the chemical compositions of the underlying material/substrate. The diffusion zone (innermost zone) determines the mechanical properties (e.g. hardness) of the nitrided material but has a lower wear resistance (Figure 3-3), which in turn reduces with increasing depth below the surface. The microhardness-surface depth plot shown in

Figure 3-4 has managed to capture this characteristic. Nonetheless, the wear behaviour of a nitride layer is often assumed to be an integral reaction of the nitriding layer to wear loading, especially within the porous and non-porous zones. This was studied by Ramesh et al. [9] using structural steel (En24) and bearing steel (En31) under various loading conditions and slip regimes. The Straffelini et al. [10] studied the effect of nitriding under boundary lubrication conditions.

### **3.3 AerMet ® 100 (A100)**

#### **3.3.1 Material characteristic**

Over the decades, there has been extensive interest in the structure and mechanical properties of secondary hardening UHS steels. Works by Speich [11] has established the basis for a new generation of alloys containing nickel and cobalt where the combination of high strength and toughness was emphasised. These concepts led to the development of AF1410 steel and other ultrahigh strength steels with superior properties. Based on improved melting techniques and some alloy modification, Schimdt and Hemphills [12] developed a new high performance steel, A100, a modified version of AF1410, which exhibited even higher strength and toughness, and exceptional ductility compared to AF1410. A100 is a trademark of Carpenter Technology and was developed in the early 1990's. A100 is a Fe-Co-Ni-Mo-Cr-C system with a similar composition to AF1410 and HY180. The nominal composition (mass%) of A100 is listed in Table 3-1 [13, 14]. The significant difference is that A100 has a higher Ni composition. According to the U.S Patent for A100, this steel's high toughness is obtained through control of inclusion content by an improved refinement technique and fine tuning of oxygen and sulphur getters, such as cerium and lanthanum. Melting of A100 was conducted using vacuum induction melting (VIM) method to homogenise the elements. During VIM, the remaining sulphur was

transformed from chrome sulphide to less damaging oxysulphide precipitates. Further refinement of the alloy is via vacuum arc remelting (VAR), thereby removing principally gaseous ( $O_2$  and  $N_2$ ) and high vapour pressure (alkali metal) elements resulting in a more uniform as-cast ingot structure. Hence, the two-step melting process provides a desirable ingot with extremely low levels of residual elements.

The LQT heat treatment [15, 16] refines the packet structure directly; this complete treatment is suitable for achieving the appropriate mechanical properties (Table 3-2) of A100 (Figure 3-5):

- *Intercritical annealing (L)*

An intercritical anneal forms a high volume fraction of  $\gamma$ -phase. The  $\gamma$ -phase precipitates preferentially along martensite lath boundaries, producing a microstructure of parallel laths of alloy rich  $\gamma$  and well-tempered, alloy-lean  $\alpha_T$ . However, the  $\gamma$ -phase formed is slightly enriched in alloy content and largely re transforms during cooling, producing a “dual phase” structure that is a mixture of tempered ( $\alpha_T$ ) and fresh martensite ( $\alpha$ ). There is often a small amount of retained austenite during the process.

- *Austenite reversion (Q)*

The treatment involves heating the alloy into the stable austenite region, and quenched to retransform into martensite. The microstructure that results depends on the reversion temperature and holding time.

- *Intercritical tempering (T)*

During this treatment, a solute-rich  $\gamma$ -phase precipitates while the residual  $\alpha$  loses solute and tempers. The  $\gamma$ -precipitates form as small islands along the

lath boundaries of the martensite. Because of its high solute content and small size, most of the austenite is retained on subsequent cooling to room temperature. The result is that the transformation occurs under severe mechanical constraint, which encourages local volumes to transform into the martensite variants that are most compatible with the local stress rather than those that continue the pattern in a martensite packet.

The metallographic surface was etched using 1% Nital for 5 seconds to reveal the general microstructure of A100 as shown in Figure 3-6. Grain-size refinement processes that decrease the measure of grain size lower the ductile-brittle transition temperature [17].

### 3.3.2 The effect of alloying elements

The feature and degree of martensite/carbide refinement determines the relative optimum strengthening mechanisms of the alloy. The initial studies during the sixties and seventies focused on the microstructure and mechanical properties of simple Fe-M-C system where M would consist of one or more elements (such as Mo, W, Cr, etc.) which are known to cause secondary hardening [18]. The microstructure of steel containing cobalt was shown to exhibit a higher rate of  $M_2C$  carbide nucleation, increased particle refinement, and a decreased propensity for austenite reversion upon tempering. The precipitation of the fine  $M_2C$ -type carbides was attributed to the delayed recovery of the dislocation substructure of the martensite in Fe-Mo-C steels containing cobalt. Cobalt additions to Fe-Ni-Mo-C steels resulted in an increase in (1) the martensite ( $M_s$ ) temperature, (2) the activity coefficient of carbon resulting in enhanced diffusion, and (3) solid solution strengthening. Speich et al. [19] investigated the effects of carbon, chromium, molybdenum, and cobalt on the yield

strength, toughness, and tempering behaviour of martensitic 10Ni-Cr-Mo-Co steels. Maximum toughness was obtained when all coarse  $\text{Fe}_3\text{C}$  precipitate is replaced by fine dispersion of  $(\text{Mo}, \text{Cr})_2\text{C}$ . The effect of cobalt [20], chromium, and molybdenum is primarily responsible for the secondary hardening by causing the formation of a fine dispersion, replacing the coarse  $\text{Fe}_3\text{C}$  carbide. As for nickel, its effect on the alloy was lowering of the transition temperature so that completely ductile fracture is obtained at well below room temperature.

Olson et al. [21] extensively studied the strengthening mechanisms, with particular emphasis on carbide composition, crystal structure, and coarsening in these steels. The strengthening carbides and austenites were studied by Ayer et al. [22] using both transmission electron microscopy (TEM) and x-ray diffraction analysis on various ranges of tempering temperatures (427-593°C) for 5 hours. The maximum strength in A100 was achieved when tempered at 454°C due to the combination of delayed dislocation recovery of the martensitic matrix and the formation of needle-shaped precipitate that is coherent with the matrix. These precipitates were believed to be large  $\text{M}_2\text{C}$  carbides if aged at 510°C. At the optimum 482°C aging condition, some of this needle-shaped precipitate loses their coherency, as seen in the TEM bright field image. Tempering at higher temperatures resulted in loss of both strength and toughness, which was suggested to be the result of precipitate coarsening and the formation of unstable austenite. This discovery was in agreement with the work of Wang et al. [23] which stated that the higher the tempering temperatures (>530°C), the more the volume fraction of reverted austenite.

## **3.4 Inconel 718 (718)**

### **3.4.1 Material characteristics**

Modern high temperature alloys have undergone little change in chemical composition in the past thirty years, leaving little opportunity for “new” alloys, while the existing alloys are much improved. These materials have been used in the presence of combustion such as in turbine engines, reciprocating engines, and power plants. Figure 3-7 shows the engine parts that are operating at various ranges of high temperatures. Research into the tribological behaviour of high temperature alloys, particularly those used in gas turbine engine components, have shown that for nickel-base alloys a well-defined temperature exists above which significant reductions in friction and wear rates take place [24]. Under the sliding condition used, such transition temperatures of 150°C, 200°C, and 300°C are observed during like-on-like sliding in air for the Nimonic alloys N75, C263, and N108 respectively [25]. Above those transition temperatures, low wear and coefficient of friction (COF) were observed after a time while below it these parameters remain relatively high throughout.

718 alloy is one of the most widely used materials in the aviation industry [26]. 718 alloy, developed by the International Nickel Company in the late 1950’s for gas turbine applications, has excellent strength, ductility, and toughness. These mechanical properties showed negligible changes from -258 to 704°C [27] (Table 3-2). The chemical composition of 718 alloy is given in Table 3-1. Since 1963, this alloy has been the material choice for producing critical rotating parts, airfoils, supporting structures, and pressurised vessels. 718 alloy is favoured for its favourable precipitation kinetics, improved weldability, castibility, low cost, and ease of

manufacture. Sophisticated procedures have been developed to enhance the high strength mechanical properties by the application of various protective coatings. Undesirable losses of wear resistance of superalloys observed at high temperature, even in the presence of natural oxide scales, have prompted designers to plasma-nitride the surface. The conclusions made by Loh et al. [28, 29] were that plasma nitriding had improved the 718 alloy hardness by three times as well as reducing the COF. Surface damage occurs mostly on the nitrided, and eventually leads to the detachment of the layer after prolonged sliding.

### 3.4.2 Strengthening precipitates

718 is a precipitate-hardened type alloy and is primarily strengthened by  $\gamma''$  precipitate ( $\text{Ni}_3\text{Nb}$ ), although both  $\gamma'$  ( $\text{L}1_2$  type) and  $\gamma''$  ( $\text{DO}_{22}$ ) precipitates form during isothermal ageing [30]. The microstructure of 718 consists of equiaxed grains with numerous annealing twins and coarse MC-type carbide inclusions throughout the matrix (Figure 3-8).

718 alloy has a large number of phases, which either have a characteristic morphology or form in a specific temperature range such that tentative identification can be made if the thermal history is known. The body-centre-tetragonal  $\gamma''$  phase precipitates coherently with the matrix and forms in the approximate temperature range of  $704^\circ\text{C} - 900^\circ\text{C}$  (Figure 3-9). For  $\gamma'$  phase, it forms in the same approximate temperature range as  $\gamma''$  phase but at longer times.  $\gamma''$  precipitate strengthens by virtue of high coherency strain in the lattice, while  $\gamma'$  precipitate causes strengthening by shearing the disorder particles in the lattice. Paulois et al. [31] have found that the precipitation of  $\gamma'$  and  $\gamma''$  precipitates affected by the applied stresses. Tensile stress enhanced the formation of  $\gamma''$  precipitates, and compressive stress suppressed the

formation of  $\gamma''$  precipitates. He et al. [32] used transmission electron microscopy and x-ray diffraction calculation techniques to investigate the influence of solution temperature and coarsening behaviour during isothermal ageing of  $\gamma''$  precipitates. They found that coarse  $\gamma''$  precipitates could take the form either of high-density small cubic particles or else of ellipsoidal, disc-shaped particles.

### 3.4.3 Temperature effect on oxidation behaviour

An understanding of superalloy oxidation and how it is influenced by alloy characteristics and exposure conditions is essential for the process design and application of superalloys. Jian et al. [33] studied the oxidation behaviour of superalloys like 718 alloy under various corrosive oxidising and reducing environments (molten carbonate fuel cells). The 718 alloy was shown to have sufficient oxidation resistance under such an extreme conditions and this was attributed to the formed multilayer oxide scales, consisting of a mixture of the dispersed nickel-rich metallic phase and spinel oxide ( $\text{FeCr}_2\text{O}_4$ ). According to Greene et al. [34], alloy 718 exhibited a parabolic oxidation rate behaviour at high temperatures ( $700^\circ\text{C}$  -  $1347^\circ\text{C}$ ) and the mechanism of oxide scale formation varies with temperature. Hamdy et al. [35] cited that the alloy 718 surface experienced minimal wear owing to the formation of glaze oxides, a highly deformable wear resistant layer. This oxide scale begins forming at  $200^\circ\text{C}$  and develops fully at  $400^\circ\text{C}$  but breaks down at  $600^\circ\text{C}$  (due to local creep). According to Stott et al. [36], the glaze oxides consist mostly of nickel oxides ( $\text{NiO}$ ) at lower temperatures but both  $\text{NiO}$  and  $\text{Fe}_2\text{O}_3$  oxides above  $600^\circ\text{C}$ . The glaze oxide forms via one of three possible mechanisms (Figure 3-10):

1. Directly from transient oxide particles that remain stable and oxidation continues below the homogeneous film as a result of the initial severe deformation.
2. From grinding and smearing due to thermal softening of larger compressed oxide particles, resulting from the severe deformation and wear during the initial stages of sliding.
3. From continuous disruption and reformation phenomena during sliding.

The long-term oxidation behaviour of high temperature alloys is determined by the effectiveness of the oxide scale as a barrier to the transport of reactants and its resistance to mechanical failure. If it should crack or spall in service, the exposed metal surface may react with the environment, resulting in an increased rate of oxidation. Failure of the protective scale is particularly dominant during thermal cycling, since the stresses are rapidly induced and cannot be relieved by time-dependent creep. In addition, various other factors influence the onset of scale failure, including the extent of contact between the scale and metal at temperature, the residual scale-growth and interfacial stresses, the scale-metal bond strength, the scale-metal interface configuration, the possibility of alloy grain-boundary sliding and the properties of scale moulding microstructure. Under some circumstances, particularly if the surface is depleted in the protective elements, the healing layer may not be re-established and more rapidly growing basis-metal oxides may nucleate and grow.

The overall oxidation kinetics and the formation of glaze oxides are determined by the interaction between the dominant alloying elements (chromium, silicon, aluminium, niobium etc) and temperature range. Many high temperature alloys are based on iron, nickel and/or cobalt and rely on the establishment of  $\text{Cr}_2\text{O}_3$ ,  $\text{Al}_2\text{O}_3$ , and

$\text{SiO}_2$ , healing layers for protection [37]. These oxides are thermodynamically very stable with respect to the metal and have high melting points; transport processes through the scales are generally slow. A schematic representation showing the progressive development of  $\text{Cr}_2\text{O}_3$  layer is shown in Figure 3-11.

- As  $\text{NiO}$  grows more rapidly than the other oxides, the  $\text{NiO}$  nuclei overgrow and undercut the transient nuclei and a layer of essentially  $\text{NiO}$  is established.
- This later supplies oxygen at its dissociation pressure at the  $\text{NiO}$ -metal interfaces, which is sufficient to react with chromium to form the more stable  $\text{Cr}_2\text{O}_3$  in the alloys at or near the interface.
- Eventually a complete healing layer of  $\text{Cr}_2\text{O}_3$  is developed at that location. This is favoured by a high alloy interdiffusion coefficient, which ensures rapid replenishment of chromium as it is taken up as its oxide, and loses solubility and diffusivity of oxygen in the alloy, which allow chromium to diffuse to the surface without reacting to form internal oxide deep in the substrate.

## References

1. British Standard, 15<sup>th</sup> December 2002
2. T. Ford, " Mainshafts for the Trent", *Aircraft Eng. and Aerospace Tech.*, 69(6), 1997, pp. 555-560
3. J. W. Morris Jr., Z. Guo, and C. P. Krenn, " The source and control of the ductile-brittle transition in steel", *Steel Heat Treating in the New Millennium, An International Symposium in Honor of George Krauss*, Nov 1999, pp. 1-10
4. K. Kato, " Wear in relation to friction – a review", *Wear*, 241, 2000, pp. 151-157
5. A. Neyman and O. Olszewski, " Research on fretting wear dependence of hardness ratio and friction coefficient of fretted couple", *Wear*, 162-164, 1993, pp. 939-943
6. Nitron GmbH, " Plasma Nitriding In Comparison with Gas Nitriding", Germany ([www.nitron.com](http://www.nitron.com))
7. F. T. Hoffmann and P. Mayr, ASM Handbook, vol.18, " Friction, Lubrication, and Wear Technology-Nitriding and Nitrocarburizing", 1992, pp. 878-883
8. R. Leppanen and H. Jonsson, " Properties of Nitrided Components – A Result of the Material and the Nitriding Process", *Ovako Steel*, Report 1/1999, pp. 3-14
9. R. Ramesh and R. Gnanamoorthy, " Fretting wear behaviour of liquid nitrided structural steel, En24 and bearing steel, En31", *J. Materials Processing Technology*, 171, 2006, pp. 61-67

10. G. Straffelini, G. Avi, and M. Pellizzari, "Effect of three nitriding treatments on tribological performance of 42CrAlMo7 steel in boundary lubrication", *Wear*, 252, 2002, pp. 870-879
11. "G. R. Speich: In innovation in ultrahigh strength steel technology", *Proceedings 34<sup>th</sup> Sagamore Army Materials Research Conference*, G. B. Olson, M. Azrio, and E.S. Wright, eds., d.s Army Materials Technology Laboratory, Watertown, MA, 1990, pp 89-111
12. M. Schmidt and R. Hemphill: *Scripta Metallurgical Materialia*, 1991, v. 125, pp. 239-260
13. "Aermet100 Alloy", *Advanced Materials and Process*, Vol. 5, 1999, pp. 53-54
14. P. M. Novotny, "A100 alloy for aerospace structural applications", *34<sup>th</sup> Mechanical Working and Steel Processing Conference*, Oct 1990, pp. 275-281
15. K. Sato, "Improving the Toughness of Ultrahigh Strength Steel", PhD. Thesis, University of California, Berkeley, 2002
16. Z. Guo, K. Sato, T. K. Lee, and J. W. Morris , Jr. , " Ultrafine grain size through thermal treatment of lath martensitic steels" *Ultrafine Grain 2000, Proceedings of TMS Conference on Ultrafine Grain Size*, 2000, pp. 51-62
17. R. E. Dolby and J. F. Knoll, *Journal of Iron Steel Institution*, Vol. 210, 1972, pp. 857-865
18. P. M. Novotny, " An ageing study of Carpenter AetMet®100 alloy", *Speich Symposium Proceedings on Fundamental of Aging and Tempering in Bainitic Steel Products*, Oct 1992, pp. 215-236

19. G. R. Speich, D. S. Dobkowski, and L. F. Poster, "Strength and Toughness of Fe-10Ni Alloys Containings C, Cr, Mo and Co", *Metallurgical Transaction A*, 1973, Vol. 4, pp 303-315
20. J. Kely, "Cobalt in Superalloys", *Cobalt News*, 1998, Issue 3, pp 9-12
21. T. B. Cox and J. R Low, "An investigation of the plastic fracture of AISI 4340 and 18 Nickel—200 Grade Maraging Steels", *Metallurgical Transaction A*, Vol. 5, 1974, pp. 1457-1470
22. R. Ayer and P. M. Machmoir, "Transmission Electron Microscopy Examination of Hardening and Toughening Phenomena in A100", *Metallurgical Transaction A*, Vol. 214A, 1993, pp. 1943-1955
23. L. D. Wang, L. Liu, C. X. Ao, X. J. Liu, C. L. Chen, and M. K. Kang, "Investigation of Transmission for Ultra-high strength steel A100", *Journal of Material Science and Technology*, Vol. 16, No.5, 2000, pp. 491-494
24. A. Erdemir and G. R. Fenske, "Wear Resistance of Metals and Alloys", Chicago, Illinios, USA, ASM International, Metal Park, OH 44073, 1998, pp.89-100
25. F. H. Stott, D. S. Lin, G. C. Wood, and C. W. Stevenson, "The tribological behaviour of nickel and nickel-chromium alloys at temperature from 20°C to 800°C", *Wear*, Vol. 36, 1976, pp. 147-174
26. Nickel Development Institute, Nickel Magazine, September 2001, pp. 1-2
27. W. D. Klopp, "Nickel Base Alloys", *Aerospace Structural Handbook*, Jan 1995(revision), pp. 1-48

28. P. K. Aw, A. W. Batchelor, and N. L. Loh, "Failure mechanism of plasma nitrided Inconel 718 film", *Surface and Coating Technology*, Vol. 208, 1997, pp. 226-236
29. P. K. Aw, A. W. Batchelor, and N. L. Loh, "Structure and tribological properties of plasma nitrided surface films on Inconel 718", *Surface and Coating Technology*, Vol. 89, 1997, pp. 70-76
30. M. Sundraraman, P. Mukhopadhyay, and S. Banerjee, "Deformation of  $\gamma'$  in inconel 718", *Acta Metallurgica*, Vol. 36, 1988, pp. 847-864
31. D. F. Paulois, J. M. Oblak and D. S. Duvall, "Coherency Strengthening in Ni Base Alloys Hardened by  $DO_{22}$   $\gamma'$  precipitates", *Metallurgical Transaction A.*, Vol. 5, 1974, pp.143-153
32. J. H. He, S. Fukuyama, and K. Yokugawa, " $\gamma'$  precipitate in Inconel 718", *Journal of Material Science and Technology*, Vol. 10, 1994, pp. 293-303
33. L. Jian, C. Y. Yoh, and M. Farooque, "Oxidation behaviour of superalloys in oxidizing and reducing environmental", *Corrosion Science*, Vol. 42, 2000, pp. 1573-1585
34. G. A. Greene and C. C. Finfreck, "Oxidation of 718 in air at high temperatures", *Brookhaven National Laboratory*, United States Department of Energy, pp. 1-29
35. M. M. Hamdy and R. B. Waterhouse, "The fretting wear of Ti-6Al-4V and aged Inconel 718 at elevated temperature", *Wear*, Vol. 72, 1981, pp. 237-248
36. F. H. Stott, D. S. Lin, and G. C. Wood, "The Structure And Mechanism of Formation of the 'Glaze' Oxide Layers Produced on Nickel-Based Alloys

During Wear at High Temperatures”, *Corrosion Science*, Vol. 13, 1973, pp. 449-469

37. F. H. Stott, G. C. Wood, and J. Stinger, “The influence of alloying elements on the development and maintenance of protective scales”, *Oxidation of Metals*, Vol. 44, No. ½, 1995, pp. 113-145

Table 3-1: Chemical composition of the specimen material (mass%).

	A100	SCMV	718
<b>C</b>	0.21 – 0.27	0.35 – 0.43	-
<b>Fe</b>	Balance	Balance	11.2 – 22.1
<b>Mn</b>	0.10 max	-	-
<b>P</b>	0.003max	≤ 0.007	-
<b>S</b>	0.002 max	≤ 0.002	-
<b>Si</b>	0.1 max	0.1 – 0.35	-
<b>Ni</b>	11.0 – 12.0	≤ 0.3	50.0 – 55.0
<b>Cr</b>	2.5 – 3.3	3.0 – 6.35	17.0 – 21.0
<b>Mo</b>	1.0 – 1.3	0.8 – 1.10	2.8 – 3.3
<b>Co</b>	13.3 – 13.5	-	1.0
<b>Al</b>	0.001 max	-	0.2 – 0.8
<b>N</b>	0.001 max	-	-
<b>O</b>	0.001 max	-	0.65 – 1.15
<b>Ti</b>	0.01 max	-	0.65 – 1.15
<b>H</b>	-	-	-
<b>As</b>	-	≤ 0.008	-
<b>Sb</b>	-	≤ 0.002	-
<b>Sn</b>	-	≤ 0.008	-
<b>V</b>	-	0.15 – 0.25	-

Table 3-2: The mechanical properties of the various aeroengine materials.

	Temperature (°C)	Yield Strength (MPa)	Ultimate Tensile Strength (MPa)	Young's Modulus (GPa)	Possion's ratio ( $\nu$ )
<b>SCMV</b>	22	1240	1670	200	0.3
<b>A100</b>	22	1806	1965	194.4	0.3
<b>718</b>	22	1036	1340	211	0.3
	93	1172	1407	205	0.3
	204	1124	1365	202	0.3
	316	1096	1344	194	0.3
	427	1076	1317	186	0.3
	538	1069	1276	179	0.3

Table 3-3: Detailed descriptions for each nitrided sub-layer (Refer to Figure 3-2a).

	Layer	Description	Nitrogen (%)
<b>A</b>	White layer – $\epsilon$ Fe <sub>2</sub> N	Irregular porous-like structure. The pores are relatively big.	3.91
<b>B</b>	White layer – $\gamma$ Fe <sub>4</sub> N	Dense porous-like structure. The pores are relatively small and well compacted.	5.82
<b>C</b>	Diffusion zone	A mixture of core material and thin strips of nitrided layer. The nitrogen seen diffusing via the grain boundary	1.59-1.73
<b>D</b>	Core material (SCMV)	Untreated zone	0.54

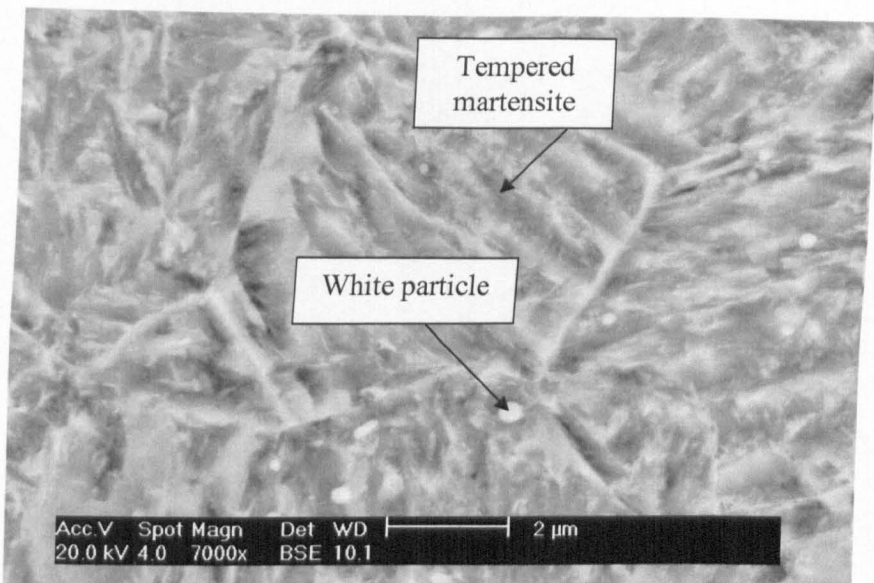
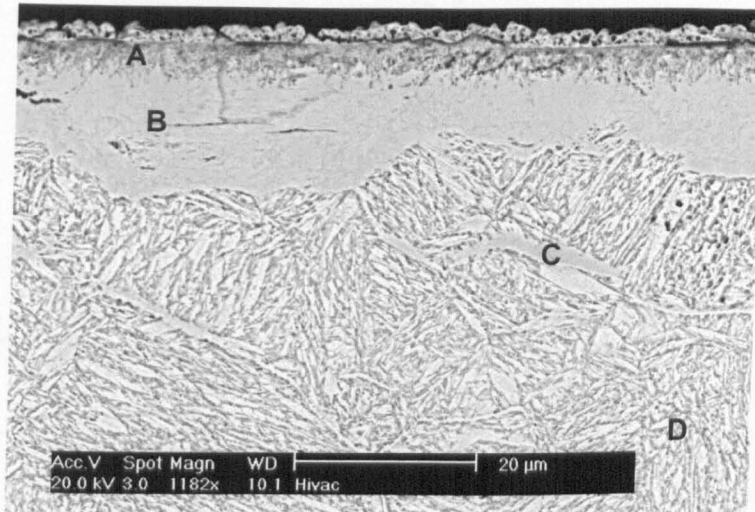
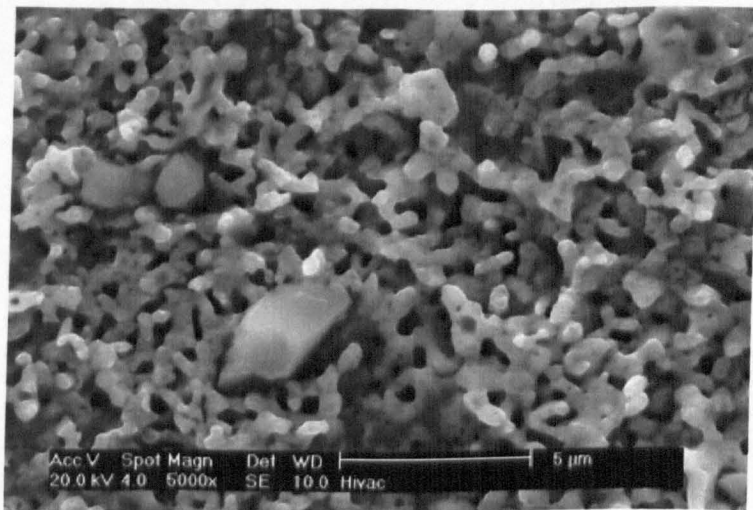


Figure 3-1: An etched SCMV alloy surface that reveals tempered martensite and white particles.

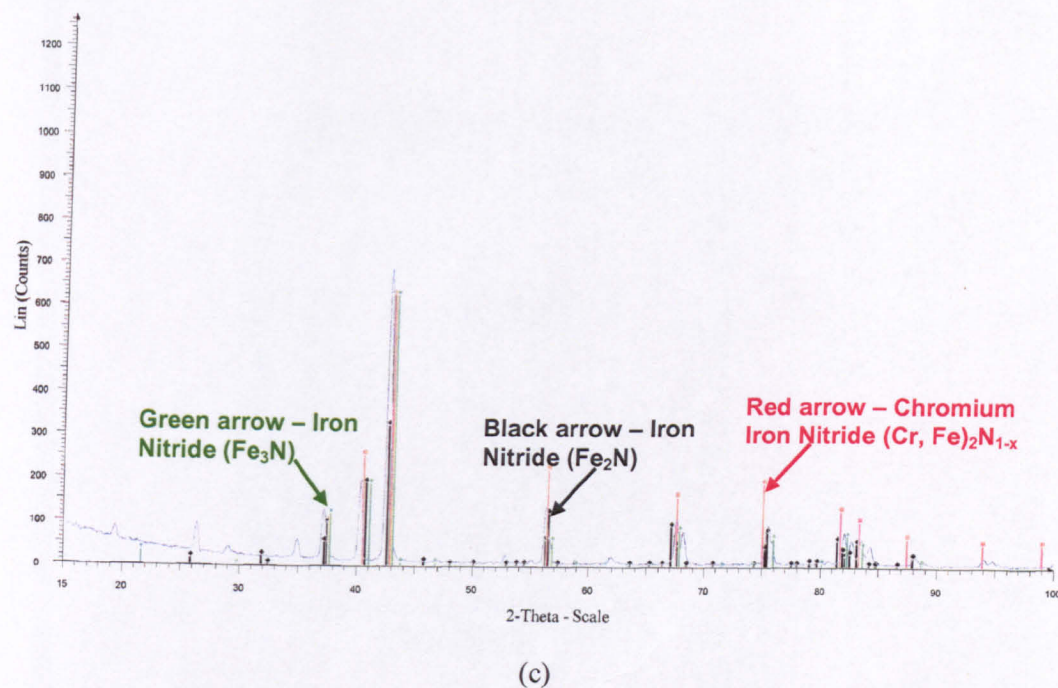


(a)



(b)

Figure 3-2 (cont'd): (a) A micrograph showing cross-section view of an etched nitrided SCMV (Refer to Table 3-3), (b) a micrograph plan view of the nitrided layer (porous-like), and (c) XRD analysis of the nitrided layer.



(c)

Figure 3-2: (a) A micrograph showing cross-section view of an etched nitrided SCMV (Refer to Table 3-3), (b) a micrograph plan view of the nitrided layer (porous-like), and (c) XRD analysis of the nitrided layer.

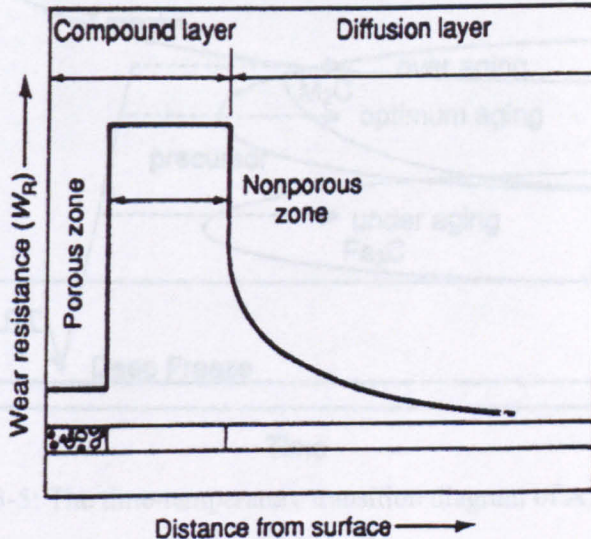


Figure 3-3: Schematic illustration of wear resistance as a function of the distance from the surface that varies from different nitride zones [8].

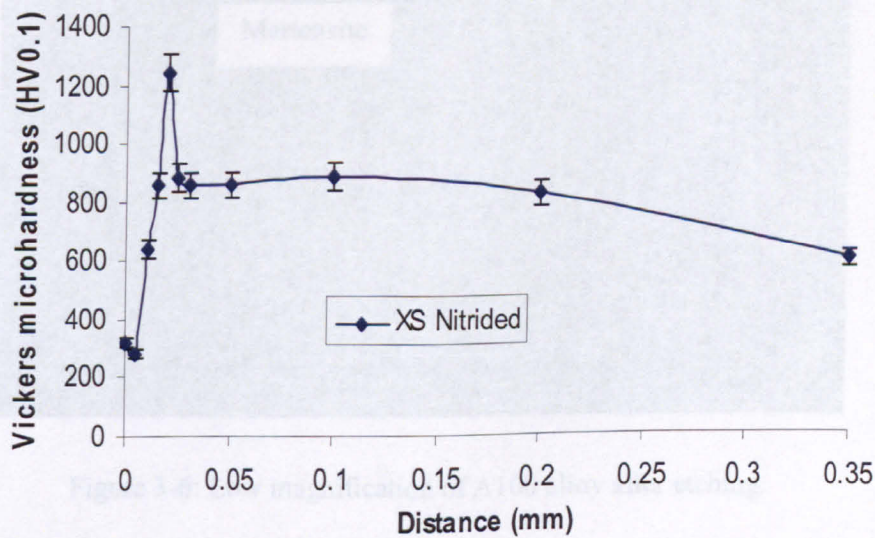


Figure 3-4: Measured microhardness versus surface depth plot on the nitrided layer for SCMV.

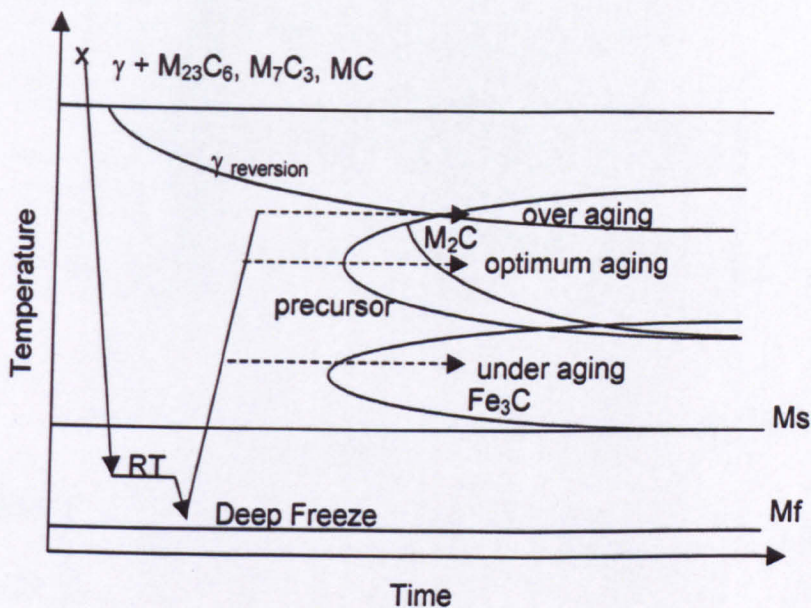


Figure 3-5: The time-temperature transition diagram of A100 [15].

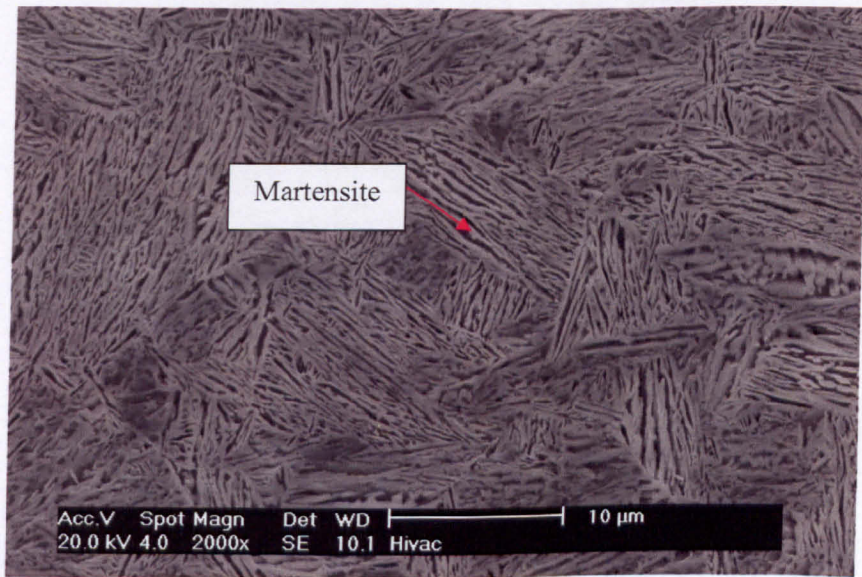


Figure 3-6: Low magnification of A100 alloy after etching.

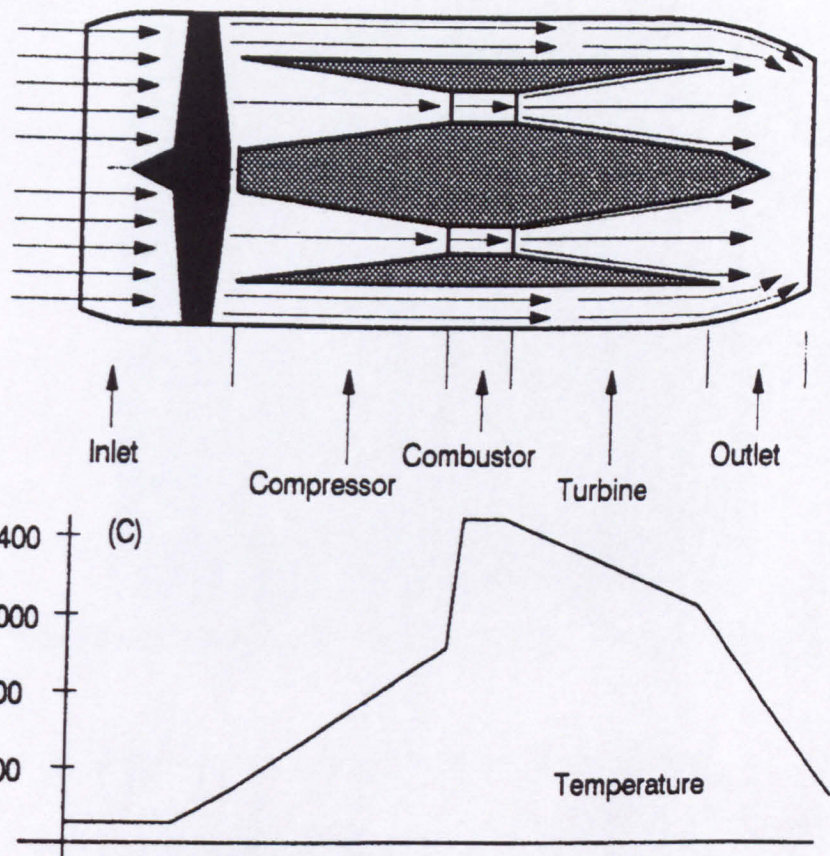


Figure 3-7: Different parts of the gas turbine engine components operate at various temperatures [32].

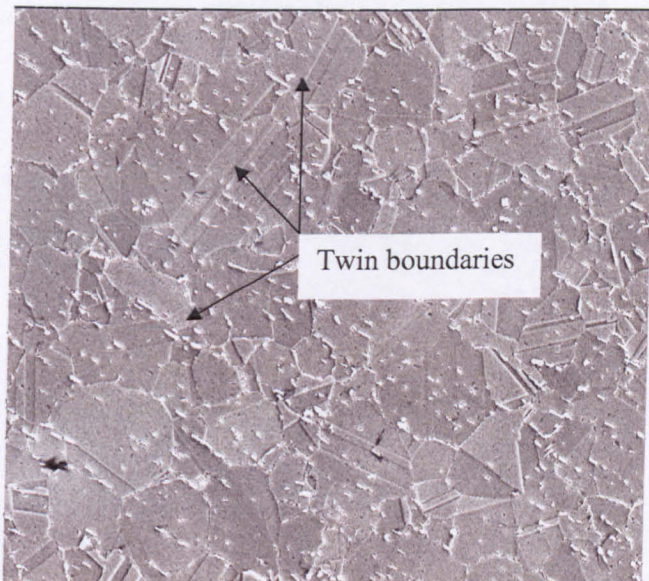


Figure 3-8: The etched 718 surface revealing some twin boundaries.

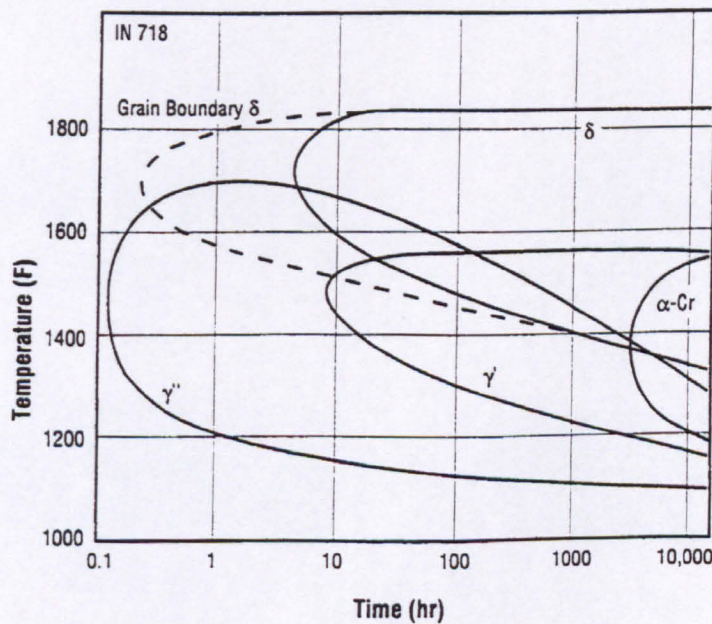


Figure 3-9: The time-temperature transition diagram of 718 [27].

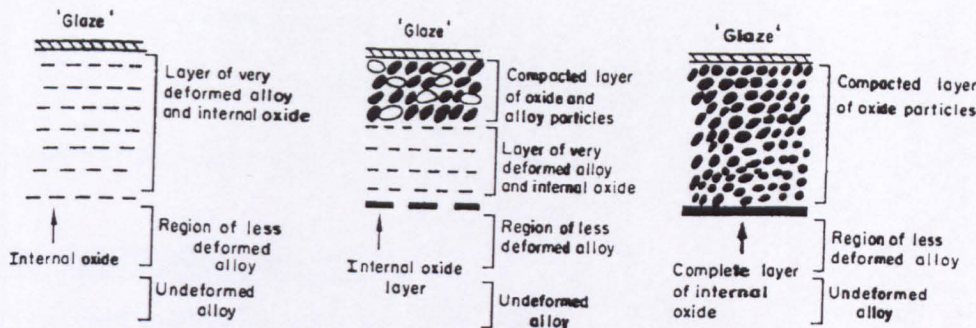


Figure 3-10: The different mechanisms involved in the glaze oxide formation at elevated temperature application [36].

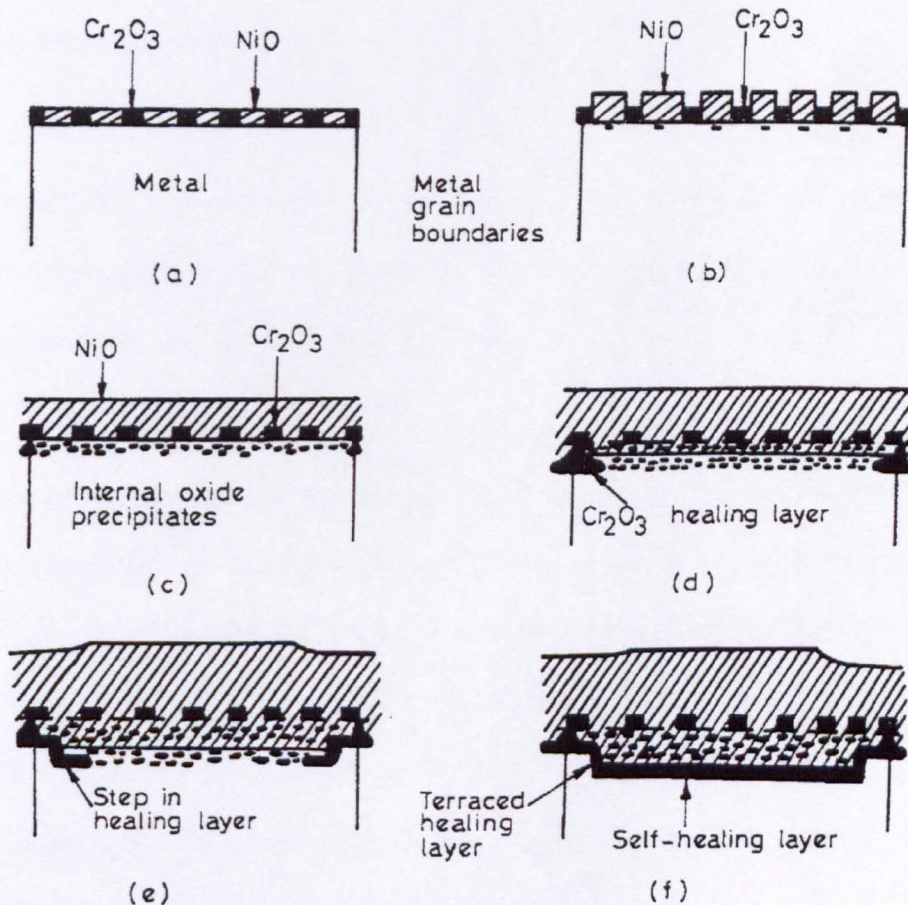


Figure 3-11: The sequences of  $\text{Cr}_2\text{O}_3$  protective layer formation [37].

---

## Chapter 4: Methods

---

### **4.1 Specimen preparation**

#### **4.1.1 Test specimens and heat treatments**

Untreated specimen blanks were manufactured from a forged block and for each blank, a pair of fixing holes was drilled into the specimen. The specimen blanks (Super S/CMV, AerMet®100, and Inconel 718) were then heat-treated according to the require specifications.

- ***Super S/CMV (SCMV)***

The blanks were solution-treated for 45minutes at 940°C, followed by a room temperature oil quench and tempering at 570°C for 2 hours and 15 minutes. Finally, the blanks were air-cooled to room temperature.

- ***AerMet® 100 (A100)***

For A100, the specimen blanks were initially supplied in the annealed (677°C for 4 to 6 hours) condition. This procedure softens the material for machining purposes but this also reduces mechanical properties. To improve the mechanical properties, the blanks were solution-treated at  $871 \pm 8^\circ\text{C}$  for 1 hour and air-cooled to 66°C in 1-2 hours, followed by a refrigeration period for 1 hour at -73°C and returned to room temperature. The final step involved ageing the blanks at  $482 \pm 6^\circ\text{C}$  for 5 hours and cooling to room temperature in less than 1hour.

- **Inconel 718 (718)**

The blanks were precipitate-hardened at 720°C for 8 hours and furnace-cooled to 620°C at a rate of 65°C per hour. Then, the blanks were held for 8 hours before being air-cooled to room temperature.

The final specimen geometries (Figure 4-1) were then profile ground ensuring that 1.0 mm of material was removed to eliminate any decarburised layer (for SCMV and A100 alloys). The round specimens had a contact radius of 12 mm and the flat specimens a width of 10 mm. The surface roughness ( $R_a$ ) of both round and flat specimens were approximately about 0.42  $\mu\text{m}$  and 0.37  $\mu\text{m}$ , respectively. All microhardness measurements (Vickers Microhardness) were made using a 0.1 kg indenter force across the mounted specimen surfaces. The plots have shown that SCMV, A100, and 718 alloys (Figure 4-2) have hardnesses of  $470 \pm 30 \text{ HV0.1}$ ,  $560 \pm 60 \text{ HV0.1}$ , and  $500 \pm 30 \text{ HV0.1}$ , respectively.

#### 4.1.2 Cross-sectioned samples for metallographic examination

A Struers Accutom-5 cut-off machine was used to section some worn specimens using an alumina abrasive cut-off wheel. The machine was set to operate with a preset cutting feed of  $0.030 \text{ mms}^{-1}$  and a grinding speed of 3000 rpm. The newly cut specimens were mounted in conductive black phenolic resin, which is suitable for microscopic examination. After mounting, the surface of interest was ground using different grades of silicone-carbide emery papers, ranging from P240grit (58.5  $\mu\text{m}$ ) to P1200grit (15.3  $\mu\text{m}$ ). In the final stage, the ground surface was polished using a diamond wheel, with a roughness of 6  $\mu\text{m}$  and moving down to 1  $\mu\text{m}$ .

## **4.2 Test equipment for fretting wear evaluation**

A purpose built fretting test machine was used to investigate fretting wear quantitatively under defined conditions with appropriate material combinations [1].

An electromagnetic vibrator generated the fretting motion and the normal load applied via the load arm (Figures 4-3, 4-4a, and 4-4b). Note that to control as small as 20 µm, the normal load is first imposed and the level arm then bridled onto the frame.

A data acquisition and evaluation strategy was developed for the characterisation of the mechanical contact response. It was based on the measurement of the contact displacement, tangential force, and normal load.

For the temperature test, cartridge heaters are mounted into the upper mounting body (UMB) and lower mounting body (LMB) (Figure 4-5a). The temperature was controlled by a heating unit (Figure 4-4b) and thermocouples (Figure 4-5a). During testing, a stream of cold air was blown over the strain gauge to ensure it did not overheat.

### **4.2.1 Specimen attachment**

Figures 4-5a and b show a display of the crossed round-on-flat specimen arrangement and the mounting blocks. The flat specimen was bolted to the fixed LMB while the round specimen was bolted to the detachable UMB, which was driven by the drive arm. The contact length is 10 mm.

A jig or precision bubble level was used to align the contacting blocks in both the parallel and perpendicular directions. This was to minimise misalignment during operation. A metal shim was laid in between the drive beam and UMB to prevent unnecessary component wear.

#### 4.2.2 Relative displacement generation

A 2000VA Deritron electro-magnetic vibrator, offset from the specimen axis by a spring hinged drive beam, generated the oscillatory relative displacement. The drive beam however controlled the magnitude of vibration in order to provide small relative displacements. The relative displacement ( $\delta_r$ ) between specimens was measured by a linear variable displacement transducer (LVDT). As shown in Figure 4-6, the LVDT was attached into a hollow plate that is implanted next to the LMB in which the loaded armature pad contacted with the UMB. During fretting, both the UMB and LVDT armature pad experienced relative displacement. The transmitted voltage signals (sinusoidal waveform) from the LVDT armature pad were monitored by the oscilloscope. The signals were translated by the signal-conditioning unit, and then recorded by a data acquisition system.

The sinusoidal waveform peak-to-peak displacement amplitude represented the applied stroke ( $\delta$ ), where  $\delta$  was half the peak-to-peak amplitude. The total distance travelled in one cycle was thus two times the applied stroke,

$$\text{Total sliding distance} = 2 \times \delta \quad (4-1)$$

#### 4.2.3 Measurement of tangential force

The tangential force was measured via the strain gauge attached to the end of the UMB (Figure 4-5). The drive force was composed of an inertia force and a tangential force giving

$$T_{dr} = T + m_{us} \ddot{a} \quad (4-2)$$

where  $T_{dr}$  is the drive force,  $T$  is the tangential force,  $m_{us}\bar{a}$  is the inertia force where  $m_{us}$  is the UMB mass and  $\bar{a}$  is the acceleration of the UMB. The tangential force was approximately equal to the drive force because  $\bar{a}$  was negligible.

Once the tangential force is measured, the coefficient of friction (COF) is the quotient of the maximum tangential force ( $T_{max}$ ) divided by the applied normal load ( $P$ ),

$$\mu = \frac{T_{max}}{P} \quad (4-3)$$

#### 4.2.4 Normal load application

The normal load between the fixed and detachable mounting blocks was applied via a dead weight loading method. This method involved a 4.9: 1 ratio of added weights onto the loading arm that is shown in Figure 4-4a. The applied normal load was calculated by

$$P_N = 4.9 P_E + 185 \text{ N} \quad (4-4)$$

where  $P_E$  is load applied to the end of the level arm and  $P_N$  is the load of interest.

#### 4.2.5 Acquisition of mechanical data

The evolution of the mechanical contact response was monitored by acquiring force-displacement loops at closely spaced time intervals during the fretting test (Figure 4-8). A data acquisition system set up to carry out this function was programmed using the HPVEE (Hewlett-Packard Visual Engineering Environment) software package. The system was divided into two sections, which consisted of a pre-processing data logger and a post-processing unit converter [2]. For the pre-processing data logger, an analogue signal from the oscilloscope was converted to digital data via the Analogue-to-Digital CIO-DAS 801 board supplied by Computer Boards Inc. Two channels were used during data recording. Each channel was to record a set of 600 data points

at a sampling rate of 1200 data per channel per second at frequency of 20 Hz. For the first 1 minute, raw data were collected every 5 seconds to observe the rapid changes of contact response. For the subsequent 2 minutes, data collection occurred every 15 seconds. With the remaining time of the experiment, data were collected at every 90 seconds since the contact tends towards a steady-state condition. A total of 60 data points per cycle were recorded for tangential force and relative displacement.

#### 4.2.6 Calibration of servo electromagnetic vibrational rig

The fretting rig needed to be calibrated according to the relevant standards. The evaluated parameters (tangential force and relative displacement) were calibrated as follows:

##### Tangential force

The strain gauge was calibrated by weights on the hanger's resting pad (Figure 4-9a) where 1 V is equivalent to 100 N (oscilloscope). The data logger was used to record a set of raw data corresponding to minimum and maximum voltage potential values ( $\pm 10$  V), which could be adjusted by altering the potentiometers.

##### Relative displacement

In calibrating the LVDT, a micrometer was used. The voltage-displacement response was amplified by the signal conditioning unit and recorded by the data acquisition system. The calibrated value was set so that 0.1 V corresponded to 10  $\mu\text{m}$  displacement (Figure 4-9b). The signal-conditioning unit readings were adjusted according to the specified direction of displacement ( $\pm 100$   $\mu\text{m}$ ). Moreover, the voltage could be adjusted to correspond to a specified magnitude experienced by the LVDT. The plots for both calibrated instruments are shown in Figure 4-10 (a) and (b).

#### 4.2.7 Centralising of force-displacement loop

For the force-displacement loop of a specific cycle  $N$ , the maximum and minimum point were considered. Four data loops from  $N$  to  $N+3$  cycles were picked. Both maximum and minimum values of the data were averaged to give a mean value. The original data were subtracted from the mean value to give the centralised tangential force and relative displacement waveforms. Figures 4-11a and b show an example of the centralised waveforms. The averaged centralised force-displacement loop represents the specific  $N^{\text{th}}$  cycle.

### 4.3 Assessment and characterisation of wear surface

For several decades, research groups who have an interest in the measurement and characterisation of surface topography have studied parameters of potential value for characterising wear. The surface topography of even the most highly polished engineering surfaces show irregularities appreciably larger than atomic dimensions and many different methods have been employed to study their topography. Some involve examination of the surface by electron or light microscopy, or by other optical methods, while others employ the contact of a fine stylus, electrical or thermal measurements, and X-ray determinations.

#### 4.3.1 Surface profilometry

One of the most common methods of assessing worn surfaces is via surface profilometry. In this study, the wear scar was profiled with a SURFCOM 200 by a fine conical-shaped stylus. The stylus was dragged smoothly and steadily across the wear scar raising and falling according to the topography. The profiled relative vertical and horizontal displacements were converted by the LVDT into electrical signals, which were then amplified. The magnitudes of both outputs were digitised.

Collective data points of  $x$  and  $y$  traverses (Figures 4-12a and 4-12b) generated a graphical representation of the wear scar profile. It must be borne in mind that this differs from the genuine cross-section through the surface due to different magnifications employed. For both vertical and horizontal axis, the magnifications used ranged from  $\times 500$ ,  $\times 1000$ , and  $\times 2000$ , depending on the size of the scar. By superimposing both unworn and worn profiles, the relative wear depth and width were determined. The wear volume of material removal was profiled by a three-dimensional (3D) profilometer. A graphical representation of wear volume profile is shown in Figure 4-13(a) and (b). Wear volume was calculated using Simpson's rule.

Depending on wear scar dimensions, the profiling parameter varied as follows:

Magnifications	$\times 250$ ; $\times 500$
Sampling points/ interval	56 points per trace line/ 0.02 mm
Traverse distance (mm)	0.1; 0.2

An average of five unworn volume profiles (round and flat) were calculated as well as the worn profiles to determine the relative wear volume error. The relative error (%) of wear volume is a product of the worn volumes divided by unworn volume. For wear coefficient calculation, 2D wear measurements were used since the finite element model is two dimensional. The purpose measuring the wear scar in 3D is to determine the relative loss of material and for comparison purposes.

#### 4.3.2 Scanning electron microscopy (SEM)

The SEM is a multifunction instrument capable of: a) producing topographic images similar to those of the optical microscope but at higher magnifications up to

×200,000 with very much larger depths of field, b) produce maps showing variations in atomic number across specimen surface, and c) elemental analyses of specimen volume down to a few cubic microns. The wear scars were examined using the XL30 Phillips ESEM. The surface was scanned with a 20 keV electron beam with a concentrated spot size of 3.0  $\mu\text{m}$ , and a working distance of 10 mm. Two imaging mode signals were used in the SEM as follows: -

*Backscattered electrons* These are electrons from the primary beam which are scattered from the specimen with energies comparable with that of the primary beam. The number of these electrons is sensitive to the local atomic number of the specimen. The resolution quality of the image is 100 nm.

*Secondary electrons* This is a better option for measuring topographical images due to its high-resolution (5 nm) quality. These originate from inelastic collisions between the high-energy primary beam electron and electrons in the specimen.

#### 4.3.3 Transmission electron microscopy (TEM)

According with conventional design, the electron gun consists of a sharp pointed tungsten filament, typically 0.1 mm in diameter, heated to approximately 2600°C. This produces a normal beam of electrons accelerated through a potential difference, typically up to 200 kV. The JEOL 2000FX TEM was used here to examine the microstructures of the specimen using both imaging and diffraction pattern modes. To transmit information from the specimen, the specimen was to have a thickness of less than 200 nm. Therefore, the 3 mm diameter specimen has to be electro-polished down to the specified dimension.

The solution used for electropolishing 718 alloy involves a combination of perchloric acid, liquid nitrogen, and ethanol. Electropolishing of 718 is done at approximately

25 volts and 2 to 4 amps for 10 to 20 seconds using a stainless steel beaker as cathode. Finally, the disc is removed from the beaker and rinsed in fresh methanol to remove any contaminants.

#### 4.3.4 X-ray Diffraction (XRD)

The bulk materials were investigated using the D500 Siemen Kristalloflex 810. The diffractometer method was employed for the analyses. The X-ray beam was generated by exciting the copper filament with a 90 kV excitation voltage. The X-ray wavelength is 2.289 nm ( $\text{Cr } K_{\alpha}$ ). Before activation, the active face of the sample was orientated normal to the axis of rotation. The detector rotates at twice the angular velocity of the sample ( $\theta$ ), so the sample was symmetrically positioned to the angle rate at which X-rays are diffracted from the sample. The output was fed to a chart recorder and/or a computer data logger, together with a signal related to  $2\theta$  (rotation degree). The spectrum was recorded using a PC. The unknown spectrums were compared with reference spectra as such in the Powder Diffraction File database. The following parameters were used for the analyses:

Start angle ( $\theta$ )	15; 40
End angle ( $\theta$ )	100
Step angle ( $\theta$ )	0.02
Step time (s)	2

#### 4.3.5 Energy dispersive X-ray analysis (EDX)

This technique was used to detect the energy (keV) and number of the characteristic X-rays emitted by the specimen, allowing elemental analysis. A CDUT™ LEAP DETECTOR coupled with the SEM was used for carrying out chemical/elemental

analysis on the samples. The digitised data from the spectrum was displayed using Edax software with the current voltage and rate of X-ray detected phases as the *x* and *y* axes respectively.

## **References**

1. J. Ding, "Modelling of Fretting Wear", Ph.D Thesis, University of Nottingham, 2003
2. T. R. Hyde, "Development of a representative specimen for fretting fatigue of spline joint couplings", Ph. D Thesis, University of Nottingham, 2002

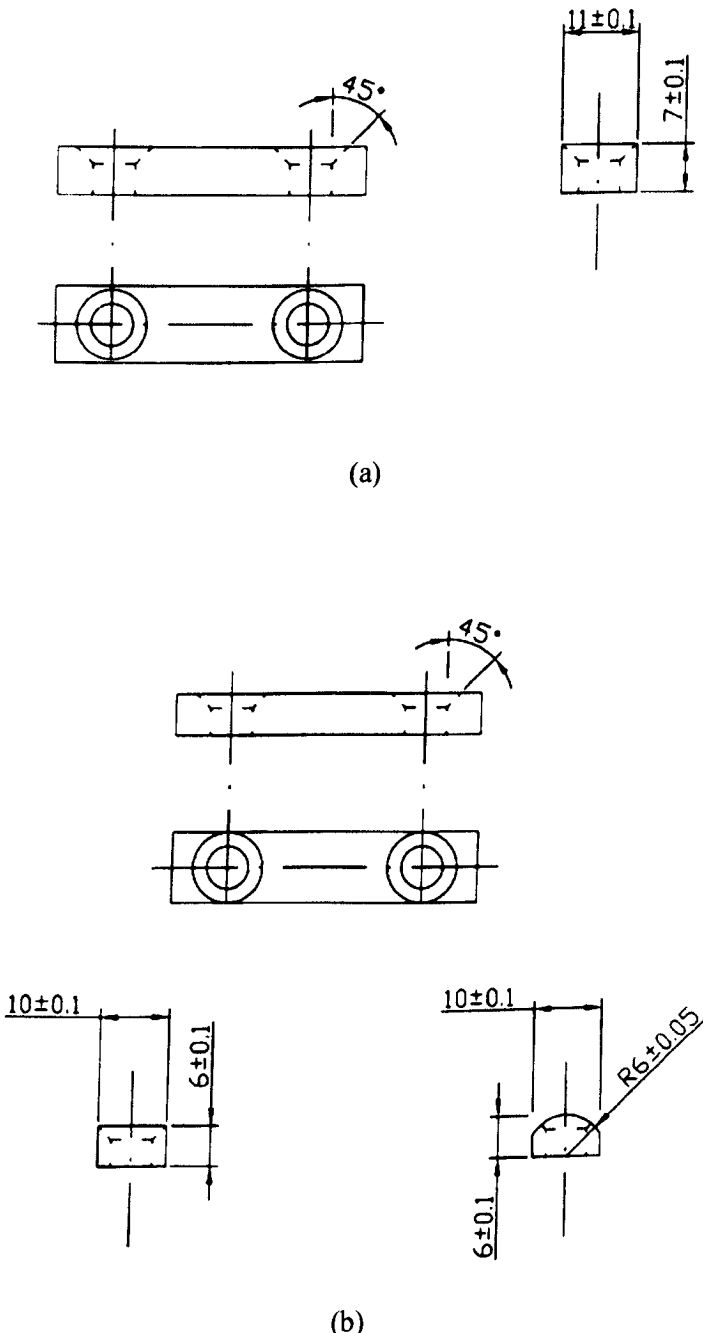


Figure 4-1: Drawings of (a) untreated specimen blanks and (b) flat and round specimens. All dimensions are in mm scale.

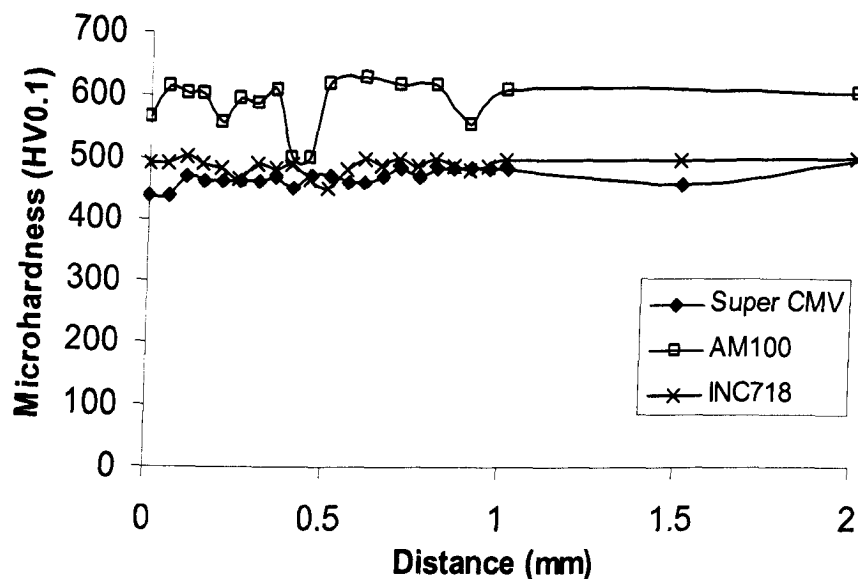


Figure 4-2: Microhardness (HV0.1) versus distance from surface after heat treatment and removal of decarburized layer for Super S/CMV, AerMet®100, and Inconel 718. Each data point represents one hardness reading.

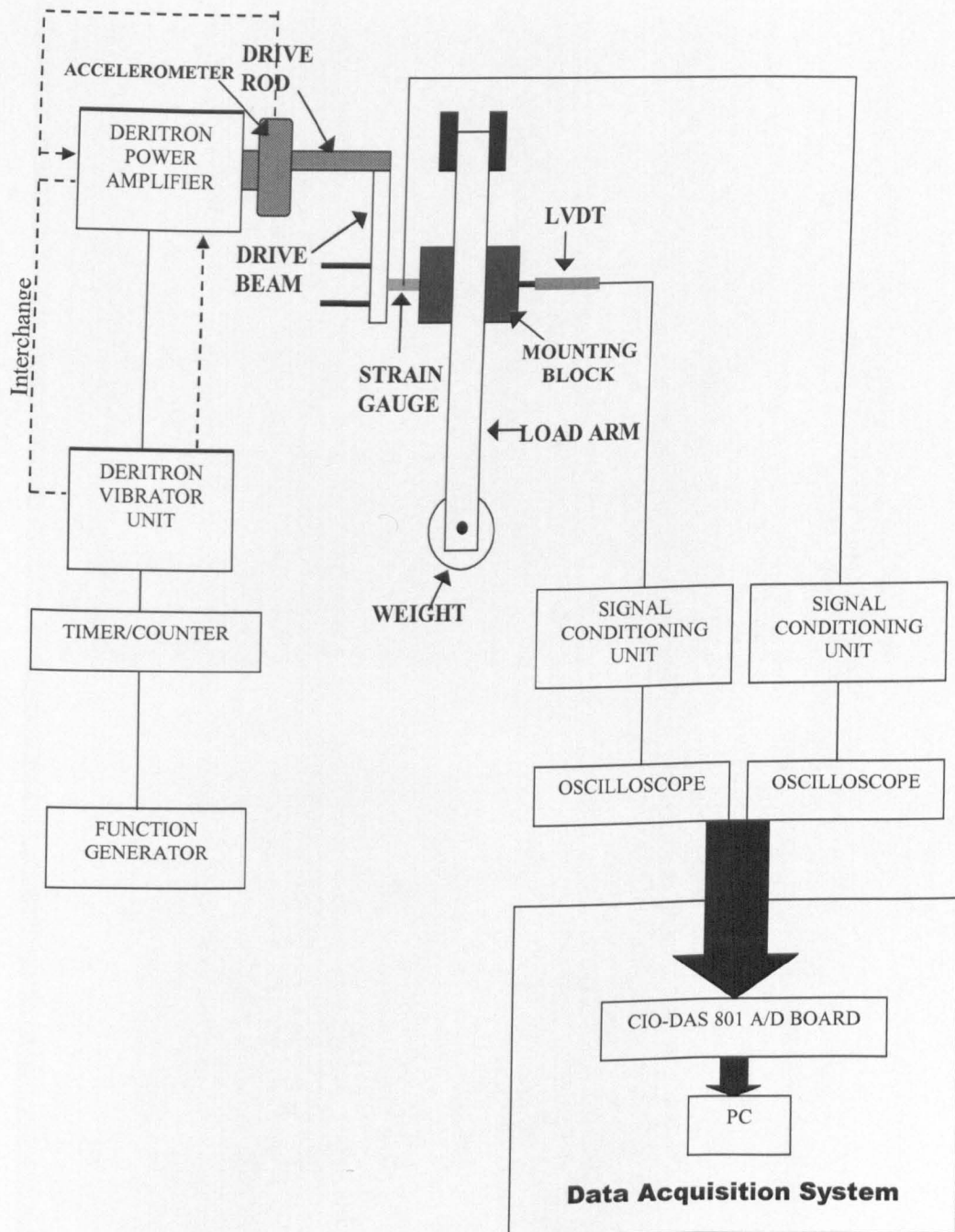
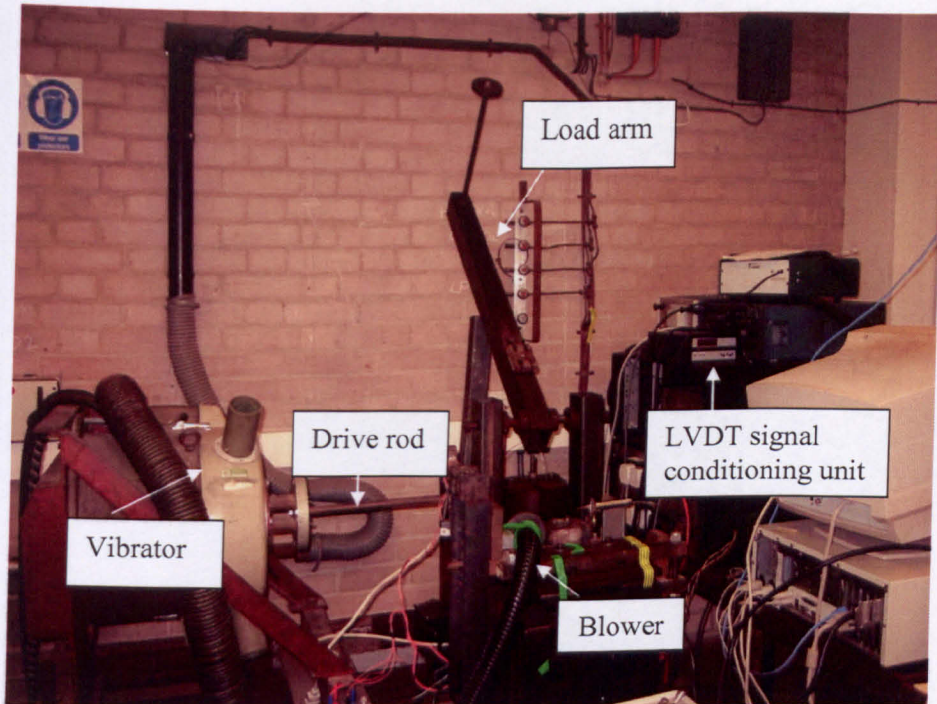
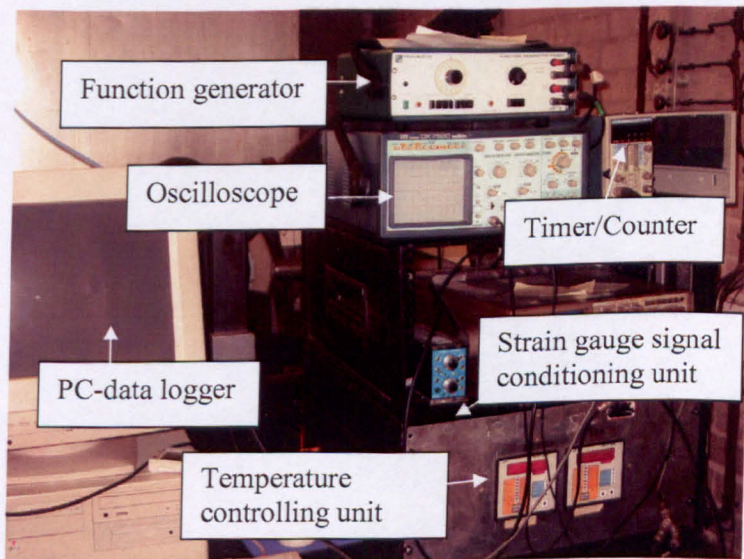


Figure 4-3: Schematic arrangement of fretting drive and data acquisition.



(a)



(b)

Figure 4-4: Photographs of the (a) complete fretting rig and (b) the controlling unit

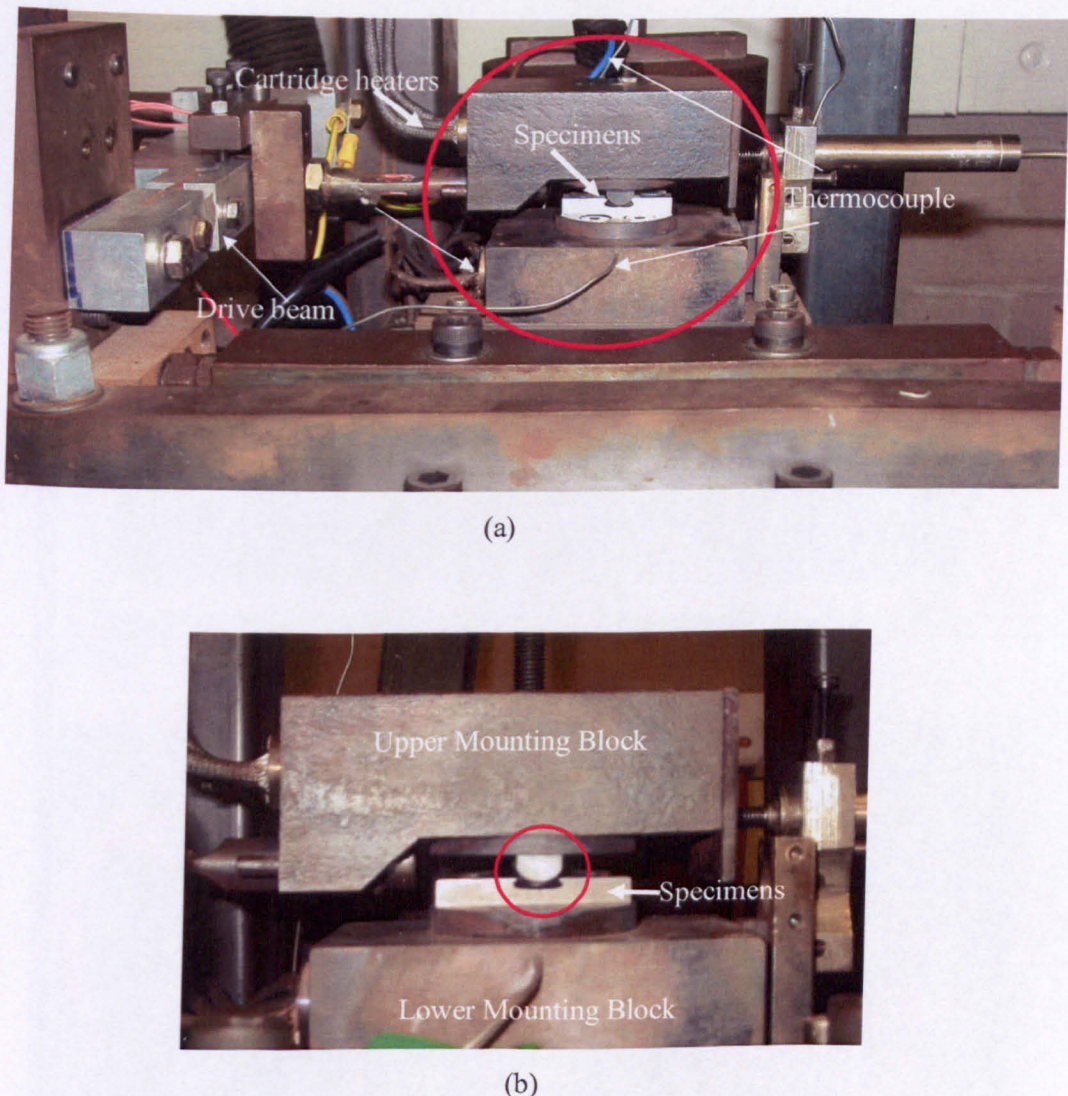


Figure 4-5: Fretting wear machine: (a) Specimen mounting blocks and drive arm arrangement and (b) a pair of mounted specimen.

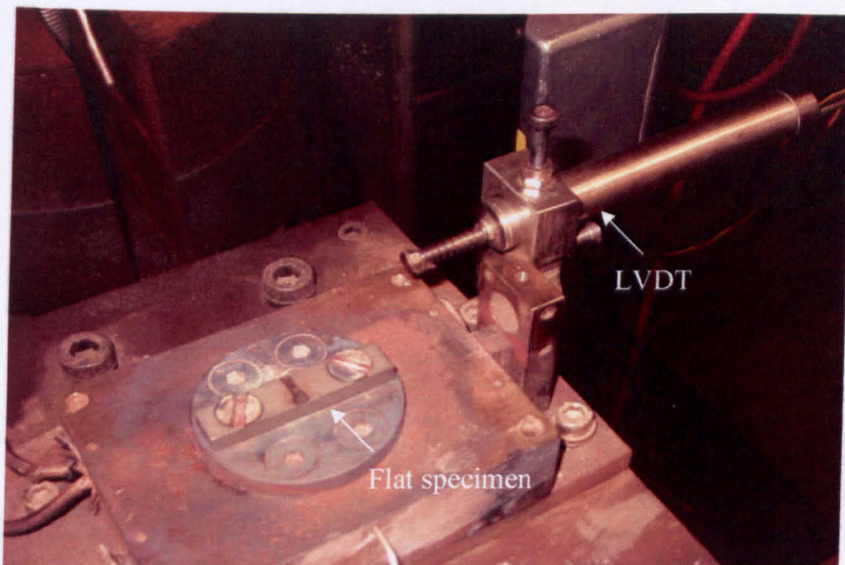


Figure 4-6: Lower specimen mounting block and high temperature LVDT



Figure 4-7: Upper specimen mounting block (inverted) and strain gauged drive arm.

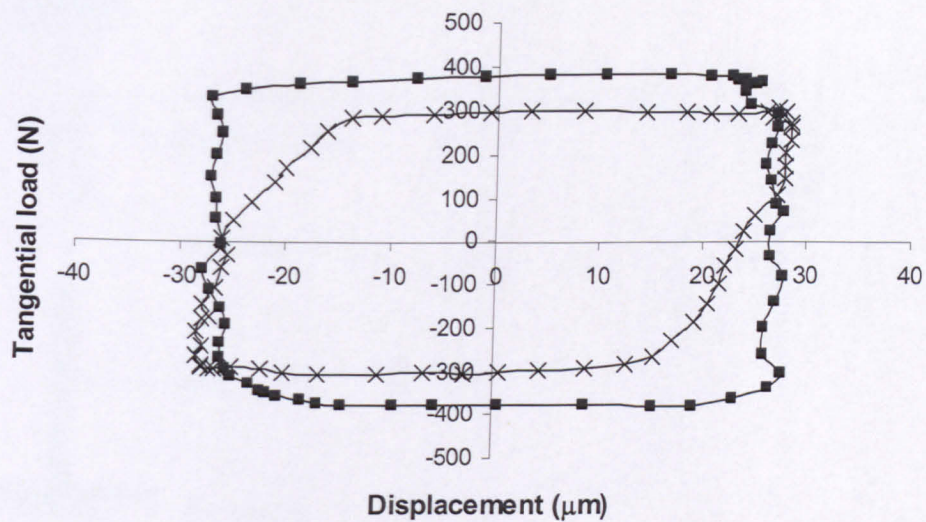
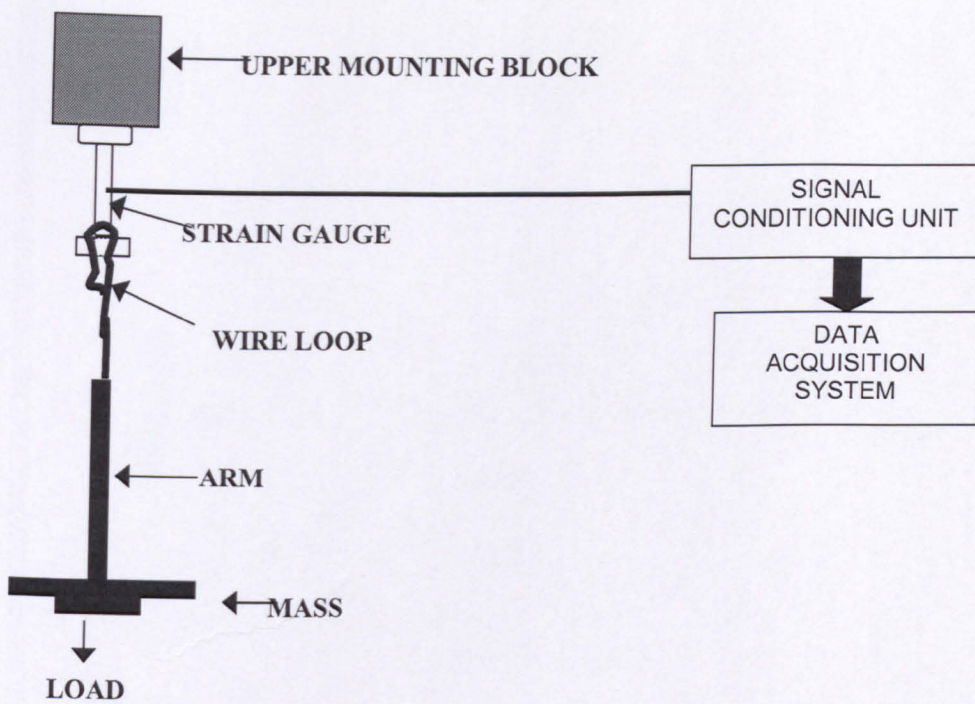
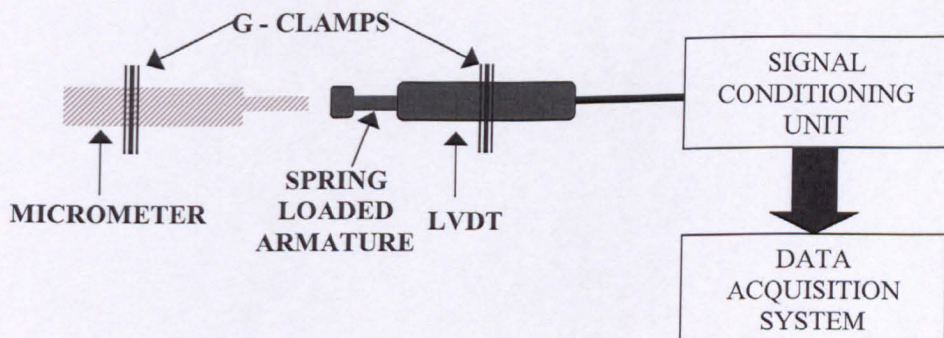


Figure 4-8: Experimental tangential load versus displacement. Each loop consisting of 60 data points.

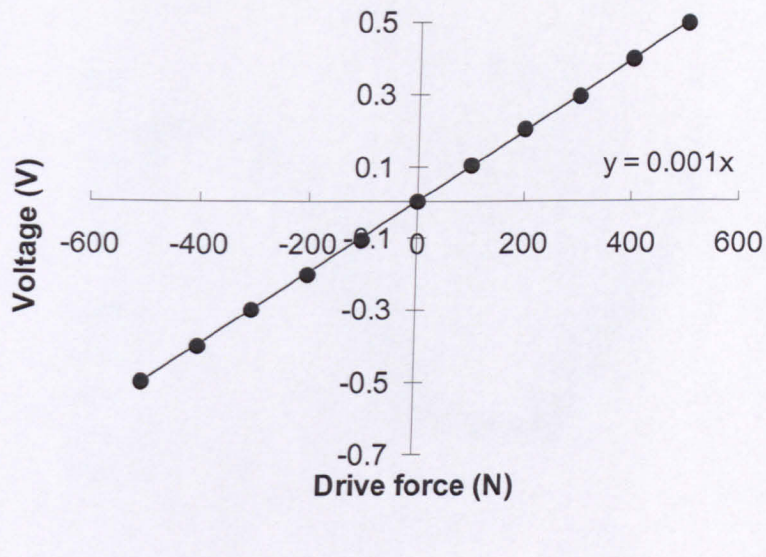


(a)

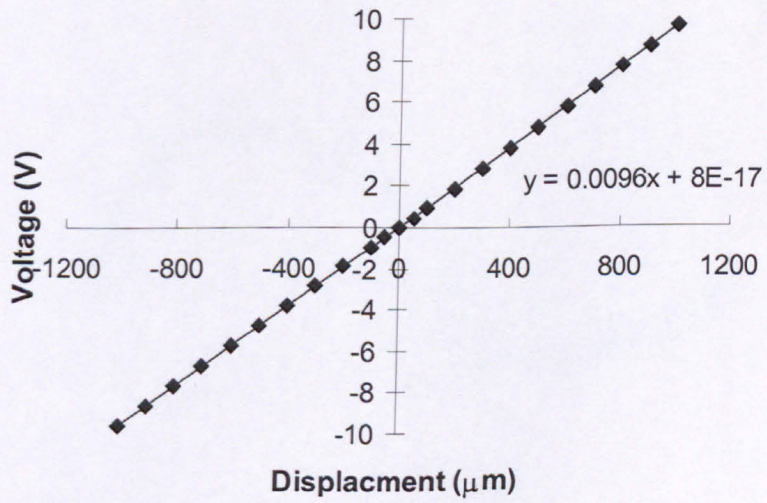


(b)

Figure 4-9: Schematic arrangement used to calibrate (a) tangential force and (b) relative displacement.



(a)



(b)

Figure 4-10: Calibration curves for (a) tangential force and (b) relative displacement [1].

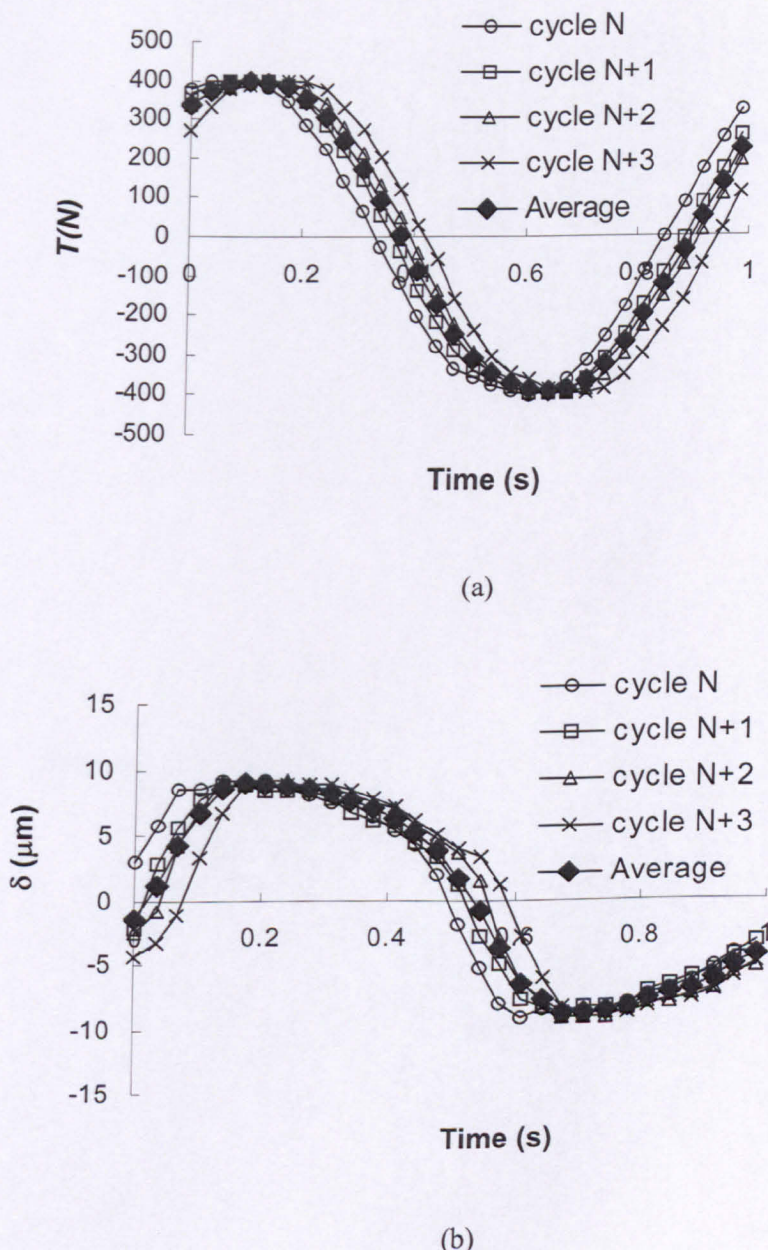


Figure 4-11: Centralised average waveforms for (a) tangential force and (b) relative displacement for  $N$  to  $N+3$  cycles [1].

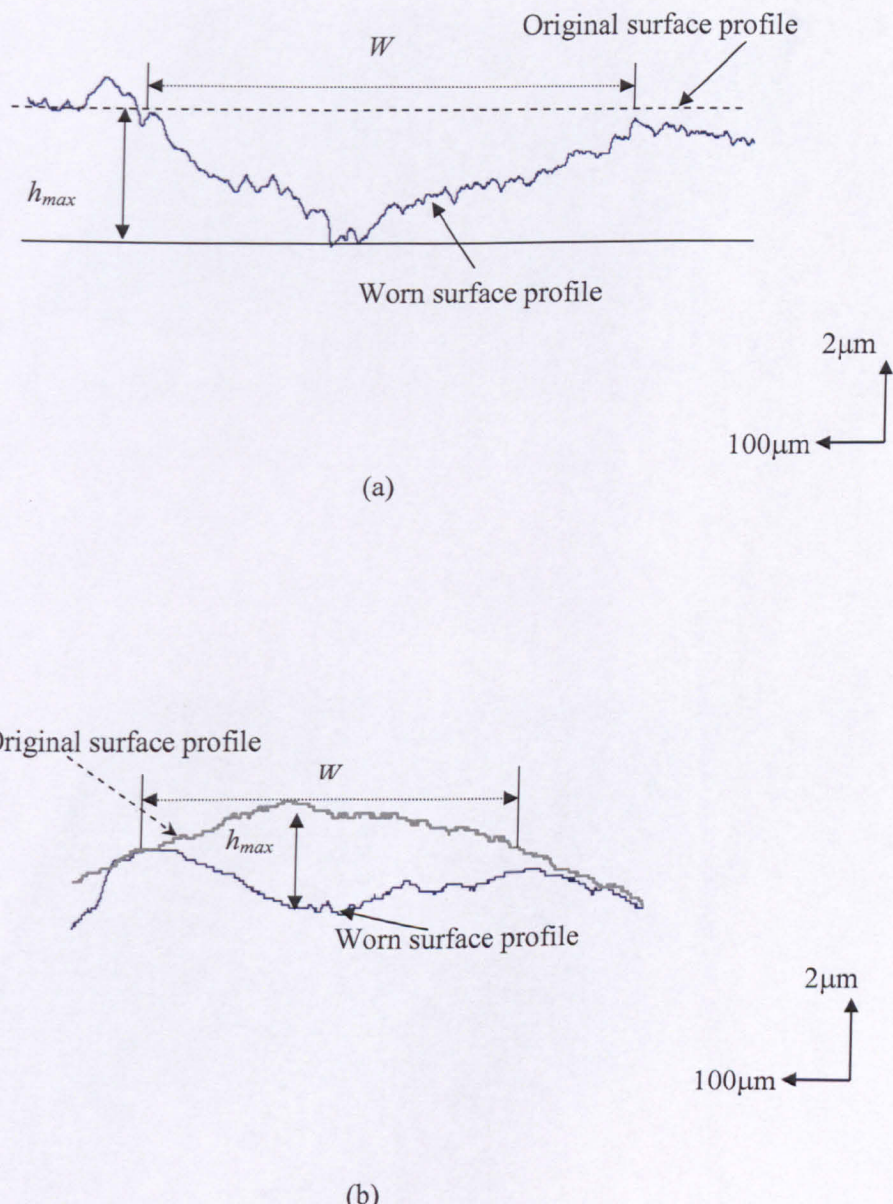


Figure 4-12: Typical two-dimensional wear depth and width profiles of (a) flat and (b) round specimens

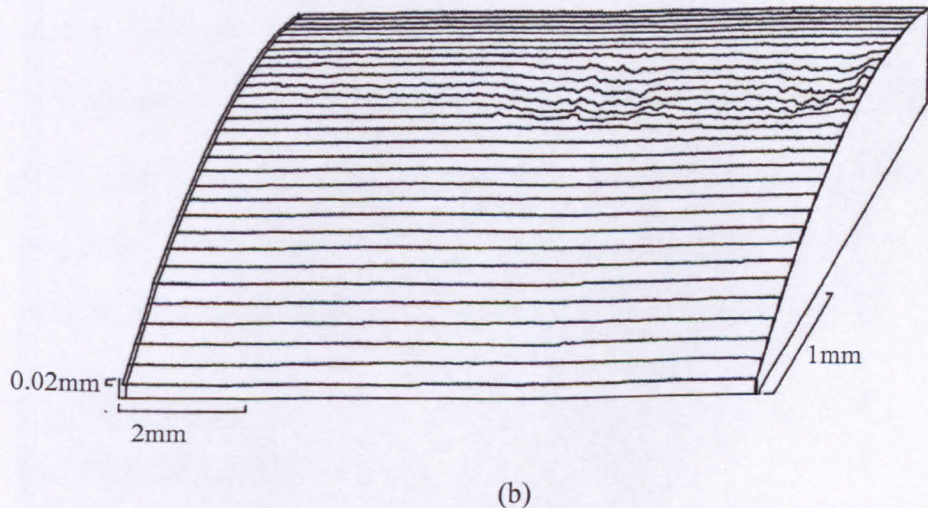
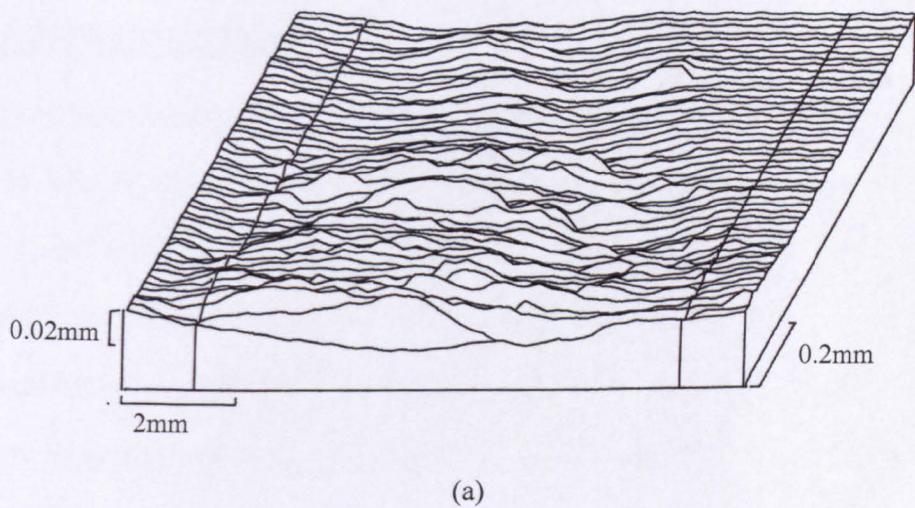


Figure 4-13: Typical three-dimensional surface profiles for worn specimens: (a) flat and (b) round.

---

## **Chapter 5: The effect of gas nitriding and boundary lubrication on Super S/CMV alloy**

---

### **5.1 INTRODUCTION**

This chapter investigates the effect of gas nitriding and boundary lubrication on the Super S/CMV alloy, through different combinations of nitrided and non-nitrided flat and round specimens, and for a range of test durations up to 100, 000 cycles. The non-nitrided/nitrided combination was chosen to study the effect of boundary lubrication on Super S/CMV fretting wear behaviour, as this is the combination used by the industrial sponsor in mainshaft splines. A quantity of 0.1ml of oil applied to the prospective contact region on the flat specimen was used to simulate typical lubrication practice for the particular spline application. The boundary-lubricated condition creates a thin lubricant film on the contacting surfaces. All tests employed a contact load of 500 N, equivalent to an initial maximum Hertzian contact pressure of 550MPa, and 50  $\mu\text{m}$  stroke, that is conditions representative of those at the  $z = 0, a_1$  position of the spline coupling [1]. The experimental wear data was used to validate Ding's [2] finite element fretting wear simulation tool, while also providing information on the effect of contact stresses on fretting wear phenomenon.

### **5.2 METHODS**

#### **5.2.1 Materials and specimens**

The fretting specimens were manufactured from a high strength S/CMV steel to BS 3S 132 (1976), but subjected to cleaner processing (refer to section 3.2). The specimens were heat treated according to the method specified in Section 4.1.3,

Following final machining, a number of specimens were gas nitrided (pressurised at 1-2 atm.) in an atmosphere of 4 parts nitrogen and 1 part hydrogen for 60 hours at a temperature of  $495 \pm 5^\circ\text{C}$  to achieve a hardness of  $\geq 800 \text{ HV0.1}$  over a depth of 50  $\mu\text{m}$  (refer to Figure 3-2 of section 3.2.3).

### 5.2.2 Fretting tests

Fretting tests were carried out using the specimen arrangement given in Section 4.2.1. The test conditions are summarised in Table 5-1. The fretting rig operating procedure can be found in sections 4.2.3 and 4.2.4. Three material combinations were tested: (i) non-nitrided-against-non-nitrided, (ii) nitrided-against-non-nitrided, and (iii) nitrided-against-nitrided. In all cases, the ‘white layer’ associated with nitriding was not removed prior to testing, consistent with the industrial sponsor’s service practice.

### 5.2.3 Characterisation

Adhered debris was not removed prior to characterisation of the wear scars. Fretting scars and transverse sections through the specimens (worn and unworn) were assessed by scanning electron microscopy/energy dispersive analysis (SEM/EDX), using a beam voltage of 20 keV and a working distance of 10 mm. Both secondary electron (SEI) and backscattered electron (BEI) imaging were used. Transverse sections through unworn nitrided specimens were etched in 1% nital for 1 minute. Wear depths were obtained by stylus profilometry using a 2  $\mu\text{m}$  tip radius stylus. All the microhardness measurements were made using a 0.1 kg indenter force and each reported value is the average of 10 indentations.

The unworn and worn contact surfaces, both non-lubricated and boundary-lubricated conditions, were analysed by energy-dispersive X-ray (EDX) to identify the element contents.

## **5.3 RESULTS**

### **5.3.1 Coefficient of friction evolution**

#### ***(a) Effect of gas nitriding at various wear cycles***

Table 5-1 shows the results of a large number of tests covering the four different permutations of nitrided and non-nitrided round and flat specimens for three different durations of 9,000, 18,000, and 100,000 cycles. The results presented include steady state COF, wear scar dimensions and the calculated wear coefficient for both round and flat specimens. The COF values are averaged over the major part of each test duration, but exclude the initial stage of each test, during which the COF increased to an essentially steady value. The data showed that the COF ranged from 0.71 up to 0.91 and that the different nitrided surface combinations have no clear discernible effect on the evolution of COF or the final value. The force-displacement loop was characteristic of gross-slip and showed little dependence on wear cycles once the COF had stabilised (Figure 5-1).

#### ***(b) Effect of boundary lubrication at various wear cycles***

Figure 5.2 shows the effect of boundary lubrication on COF evolution. It includes 'typical' curves obtained as non-lubricated (curve A) and boundary-lubricated (curve C), and upper (curve B) and lower (curve D) extremes for the boundary-lubricated tests. For the non-lubricated tests, the final COF was  $0.8 \pm 0.06$ , attained after only about 1200 cycles. The results for the boundary-lubricated tests covered the region bounded by curves B and D, but in all cases the final COF approached, or slightly exceeded, that of the non-lubricated tests. The number of cycles required for this to occur varied from  $\approx 20,000$  to  $\approx 200,000$ . The wide distribution of results for the boundary-lubricated specimens is attributed, largely, to variations in the quantity and

distribution of oil initially added to the contact surfaces. A black paste was seen to accumulate at the periphery of the wear scar (Figure 5-3).

### 5.3.2 Wear coefficient evolution

Table 5-2 includes calculated wear coefficients obtained from the profilometer traces using the modified Archard wear equation. It is apparent that the wear coefficient decreased with increasing test duration, and that the tests involving nitrided/non-nitrided combinations tended to exhibit the higher values of early wear. Table 5-3 provides an estimate of the average adhered debris layer thickness obtained from transverse sections through the scars on both nitrided and non-nitrided specimens (there was no discernible debris thickness between nitrided and non-nitrided specimens), and the average relative oxygen content in the debris (obtained by EDX).

For the boundary-lubricated tests, it is clear from Table 5-4 and Figure 5-2 that the wear coefficient diminishes with decreasing COF. It should be noted that these tests only considered the nitrided/non-nitrided combination. The data also reveals that the wear coefficient,  $k$ , for the boundary-lubricated case is significantly lower than the non-lubricated lubrication ( $k = 7 \times 10^{-8} \text{ MPa}^{-1}$ ) case. For curves B, C and D, the  $k$  values are  $2 \times 10^{-8} \text{ MPa}^{-1}$ ,  $1 \times 10^{-8} \text{ MPa}^{-1}$ , and  $0.1 \times 10^{-8} \text{ MPa}^{-1}$ , respectively.

### 5.3.3 Microscopic examination of wear scars

#### *(a) Effect of gas nitriding at various wear cycles*

Figures 5-4a and b show typical transverse sections from the centre of scars on nitrided flat specimens after 9,000 and 100,000 cycles, respectively. At 9,000 cycles, the carburised residual white layer exhibits a network of cracks that are replaced at 100,000 cycles by delamination cracks, the white layer having been essentially removed. Figures 5-5a and b indicate that at 9,000 cycles the porous nitride layer is

still essentially intact. The micrographs also show that some oxide debris resides on the wear track. For the case where the surface is non-nitrided, a substantial amount of wear debris was produced, subsequently oxidised and compacted to form agglomerates (Figures 5-6a and b). Eventually, over time, the agglomerates form a relatively thick layer that covers the substrate and protects it from severe wear. Hence, little wear would be expected to occur. The worn surface profiles for tests carried out up to 9,000 cycles and 18,000 cycles are effectively identical.

#### ***(b) Effect of boundary lubrication at various wear cycles***

In the presence of a thin lubricant film, the wear characteristics changed, in particular surface fracturing was seen on the fretted surface (Figures 5-7a and b). As suggested by Figure 5-7c, lubricant is likely to be absorbed into the porous layer. The wear surface of the boundary-lubricated and unworn non-lubricated cases were analysed by EDX. In Table 5-5, the carbon content on the worn surface of the boundary-lubricated case is approximately 5 times greater than that of the unworn non-lubricated surface (about 30 mass% & 6 mass% respectively) and the oxygen level is about 20-25 mass%. Also, the iron level in the fractured surface is about half the value of the corresponding non-lubricated test (about 45 mass% and 81 mass% respectively) and the chromium concentration was negligible (2-3 mass%). The high carbon indicates the presence of oil residue.

#### **5.3.4 Finite element analysis**

##### ***Nitriding pair variations from 9,000 to 18,000 wear cycles***

Figure 5-8a shows a schematic representation of the two-dimensional (2D) model of the round-against-flat (four-node plane strain element) used to run the wear simulation, which uses the wear simulation technique of Ding [2], as described in

Chapter 2. The Young's modulus and Poisson's ratio for both round and flat are taken as 200 GPa and 0.3, respectively. The simulation parameters used are identical to the experimental conditions, that is 500 N applied load and 50  $\mu\text{m}$  stroke. The simulation loading history involved a constant applied load and superimposed maximum tangential displacement ( $+\delta^*$ ), while keeping the COF constant (Figure 5-8b). The  $k$  from Table 5-2 were used for the simulation and the predicted wear scar data (wear depth and width) for the different permutations of nitrided and non-nitrided flat and round specimens are shown in Table 5-6. Note that the 9,000 cycles and 18,000 cycles analysis used different  $k$  values, viz. each uses the corresponding value from Table 5-2. The FE-predicted results for the different nitrided permutations are qualitatively similar. Therefore, only the nitrided-against-nitrided is presented here for discussion.

Figures 5-9a and b show the predicted worn contact pressure and slip distributions for different numbers of cycles. The contact pressure distribution is predicted to quickly become essentially uniform (Figure 5-9a), but wear is predicted to have little effect on the magnitude of slip (Figure 5-9b). Figures 5-10a and b show the corresponding normal stress,  $\sigma_x$  and shear stress,  $\tau_{xy}$  distributions across the worn surface, for the row of integration points immediately below the surface ( $\approx 5\mu\text{m}$  depth). Note that these distributions correspond to the instant of maximum tangential displacement,  $\delta^*$ , i.e. the end of step 2 of Figure 5-8b. It can be seen that the maximum tensile stress ( $\sigma_x$ ) quickly diminishes with wear from an initial (no-wear) value of about 530 MPa to about 260 MPa (after 18,000 cycles) and furthermore moves across the scar from the left-hand side to the right-hand side (Figure 5-10a). The maximum shear stress

$(\tau_{xy})$  shows a less significant decrease with wear and also moves across the contact width (Figure 5-10b). It is clear that the instantaneous positions of peak traction and shear stresses are predicted to move significantly across the contact due to the effect of wear. The reason for this can be deduced from the worn contact pressure distributions of Figure 5-11b [2], which show snapshot distributions of contact pressure for a series of different instants in the 18,000<sup>th</sup> fretting cycle. The key point to note from this figure is that at certain instants, in particular  $\delta^*$ , for example, (which corresponds to Figures 5.10), there is zero contact pressure across most of the width of the specimen, including in particular the left hand side. Only the right-hand side has non-zero pressure and this distribution is non-Hertzian. It can be anticipated that symmetric non-Hertzian peaks will also occur on the other side of the contact at the other end of contact travel ( $-\delta^*$ ). This effect is due to the worn slider touching the ends of the wear scar on the flat. This causes the peak traction stress which corresponds to the instant  $\delta^*$ , to move to the right hand side of the contact width i.e. the instantaneous trailing edge is now located on the right hand side due to the instantaneous pressure being zero over most of the contact width. An unworn solution for this instant would predict the peak traction stress (trailing edge) to be on the left-hand side (Figure 5-10a). The explanation for the change in location of instantaneous peak  $\tau_{xy}$  is similar.

## **5.4 DISCUSSION**

### **a) Effect of stress on wear – FE prediction versus experimental observation**

The stress components of Figures 5-10a and b are the salient parameters controlling fatigue crack initiation and early crack growth. The predicted trends in magnitude and location of the peak values of these stresses are consistent with the transverse

section of Figures 5-4a and b, which show that the early network of cracks in the centre of the scar are removed by 100,000 cycles, with limited delamination cracking then being apparent. The diminishing (and moving) stresses are insufficient to drive the cracks deeper into the surface or to reinitiate cracks as the surface is worn away. There are, of course, no tensile stresses directly applied to the flat specimens in the fretting test, hence, the cracks would be expected to arrest as they grow out of the contact stress field. The resistance to fatigue cracking would also be aided by the residual compressive stresses expected in the diffusion layer of the nitrided specimens [3]. This is a complex process, whereby the early cracking, which occurs under the initially high stresses, is countered by the effects of wear, both in terms of the removal of material, and the attenuation and movement of the peak stresses.

**b) Effect of gas nitriding and boundary lubrication on wear**

The presence, or otherwise, of the nitrided layer had little effect on COF, which ranged from  $\approx 0.7$  to  $\approx 0.9$ . However, the presence of one nitrided surface generally resulted in higher wear coefficients over the shorter duration (9,000 and 18,000 cycle) tests. When both surfaces in contact were either nitrided or not nitrided, then the wear coefficients for the two surfaces were similar. The general trend is for the wear coefficient to decrease with increasing test duration, although this perhaps is least apparent when neither specimen is nitrided. For specimens that were nitrided most of the wear is contained within the white layer or a few microns into the diffusion layer. For the tests reported on here, the assumption that the local wear, for a particular material pair, is simply controlled by the local slip and local contact pressure is not fully justified. For example, the wear coefficient averaged over the 100,000 cycle tests is approximately 40% of that for the 9,000 cycle tests. A wide range of factors

may contribute to this, including early fragmentation of the white layer, particularly the outer porous layer. Table 5-2 shows that although the decrease in wear coefficient with test duration is far more pronounced for those tests involving nitrided specimens, the non-nitrided specimens also exhibited a reduced wear coefficient over the longer duration tests. The adhered debris may affect the measured wear coefficient for all test durations; however, comparison with the wear dimensions in Table 5-3 suggests that the volume of adhered debris was not strongly dependent on test duration. Therefore, the effect of adhered debris on the measured wear volumes would be greatest for the shorter duration tests, i.e. if the wear coefficient were calculated using the volume of material worn rather than that lost, the decrease in wear coefficient with test duration would be more pronounced. The lower COF at the start of each test could result in greater initial slip. However, the FE simulations indicate that the slip distribution is only marginally affected by COF (under displacement-controlled conditions) and test duration (Figure 5-9b) and, therefore, is unlikely to make a significant contribution. This leaves the dependence of wear coefficient on contact pressure and trapped debris. The presence of trapped debris is known to result in 'velocity accommodation' [4] and this may increase with duration (and wear) as the contact pressure diminishes. The scars are covered with patches of debris and these may themselves result in less wear and be more effective at preventing direct metal-to-metal contact and wear as the contact pressure decreases, particularly as the debris oxide content increases (Table 5-5). Nevertheless, the FE-predicted wear dimensions in Table 5-6 show relatively good agreement with the trends exhibited by the measured data, although it required the use of the individual wear coefficients listed in Table 5-2.

Based on Figure 5-7a, it is believed that the lubricant exhibits a load-sharing capability whilst asperities (wear debris) carry the remainder of the load by solid contact and adhesion [5]. The low  $k$  value trend supports the idea of load-sharing by the lubricant and surface. The observed fretted surface suggests that boundary-lubrication protects the contact surface during fretting, provided the lubricant film is uniformly distributed across the contact area and experiences minimal shifts of lubricant flow during wear. During this period, the contact load is likely to be partially supported by the lubricant film (low shear stress), with the contact surface experiencing minimal contact and the film redistributing the contact stresses, local reduction in shear stresses (abrasion) and contact forces (adhesion). The stability of the distributed lubricant film can be associated with the FE-predicted contact pressure characteristic. The contact pressure influences the spread of the lubricant over the surface and the contact width represents the lubricated area (Figure 5-8a). The lubricant film may also have controlled the level of oxygen exposure (oxidation) and penetration. The EDX results (Table 5-5) show that the iron ( $\approx 33$  mass%) and carbon ( $\approx 30$  mass%) contents were similar in the pits. This may also mean that some debris has escaped from the wear scar, hence, the high iron count. In the event of a crack being present and the lubricant flowing into the crevice, potential corrosive agents may form through a chemical reaction and this could cause further damage (stress corrosion cracking) [5-12]. The presence of cracks was observed during the early cycles of 9,000 up to 18,000 (shown in Figure 5-4a) with cracks propagating into the substrate. This may initiate at the pores of the porous structure and the lubricant may tend to flow into the cracks, causing further crack propagation. Hence, the cracks remain open, enlarge with time and are likely to occur at the periphery. However, competition will arise between fretting wear and fretting fatigue and this influences

the cracking propagation. Another possible explanation would be the effect of residual stresses on crack propagation. It has been reported that the XRD-measured compressive stress (from nitriding) is approximately  $880 \pm 200$  MPa [13], with the measurement taken from an unworn specimen. The fretting wear simulation had predicted the compressive stress to be approximately 940 MPa (at zero cycle). Based on the given values, the assumption is that the compressive stress is sufficiently high to suppress further cracking.

## References

1. S. B. Leen, T. R. Hyde, E. J. Williams, A. A. Becker, I. R. McColl, T. H. Hyde, and J. W. Taylor, "Development of a representative test specimen for frictional contact in spline joint couplings", *Journal of Strain Analysis*, Vol. 45(6), 2000, pp. 521-544
2. J. Ding, Modelling of Fretting Wear, Ph.D Thesis, University of Nottingham, 2003
3. F. T. Hoffmann and P. Mayr, ASM Handbook, Vol.18, "Friction, Lubrication, and Wear Technology-Nitriding and Nitrocarburizing", 1992, pp. 878-883
4. Y. Berthier, L. Vincent and M. Godet, "Velocity accommodation in fretting", *Wear*, 1988, Vol. 125, pp. 25-38
5. Y.Z. Lee and K.C. Ludema, "The shared-load wear model in lubricated sliding: scuffing criteria and wear coefficients," *Wear*, 138, 2000, 13-22
6. K.H. R. Wright, "An Investigation of Fretting Corrosion", *Proceedings Institution of Mechanical Engineers*, 1952, Vol. 1, Series D, pp. 555-574

7. D.M. Rowson and Y.L. Wu, "The sequential observation of the pitting process in debris", *Wear*, No. 70, 1981, pp. 383-393
8. K.A. Blencoe and J. A. Williams, "Friction of sliding surfaces carrying boundary films", *Wear*, No. 203-204, 1997, pp. 722-729
9. McFadden, C. Sato, and N.D. Spencer, "Adsorption and surface chemistry in tribology", *Tribology International*, Vol. 30, No.12, 1997, pp. 881-888
10. Z. R. Zhou and L. Vincent, "Lubrication in fretting – a review", *Wear*, Vol. 225-229, 1999, pp. 962-967
11. Z. R. Zhou, Q.Y. Liu, M.H. Zhou, L. Tanjda, P. Kapsa, and L. Vincent, "An investigation of fretting behaviour of several metallic materials under grease lubrication", *Wear*, No. 33, 2000, pp. 69-74
12. Q. Y. Liu and Z.R. Zhou, "Effect of displacement in oil-lubricated fretting", *Wear*, No. 239, 2000, pp. 237-243
13. P. Wavish, " The effects of the resultant nitrided white layer on the fatigue properties of a Super CMV alloy steel under four-point bending", M.Eng. Dissertation, University of Nottingham, 2002

Table 5-1: Fretting test conditions.

<b>Contact load</b>	500 N
<b>Initial maximum Hertzian stress</b>	550 MPa
<b>Stroke</b>	50 $\mu\text{m}$
<b>Frequency</b>	20 Hz
<b>Number of cycles</b>	9,000; 18,000; 100,000
<b>Room temperature</b>	14-20°C
<b>Relative humidity</b>	40-55%
<b>Lubricant</b>	Mobil Jet Oil II (22 cSt. at 25°C)

Table 5-2: Measured final COF, scar depth/width and wear coefficient (after 5,000 cycles).

Nitrided status*		No. of cycles	COF	Max depth on flat (μm)	Max width on flat (mm)	Wear coefficient $\times 10^8$ (MPa <sup>-1</sup> )	
Flat	Round					Flat	Round
N	N	9,000	0.82	2.9	0.639	4.1	5.0
		18,000	0.71	3.5	0.697	2.9	2.5
		100,000	0.90	8.1	1.086	1.8	1.9
N	P	9,000	0.84	5.8	0.589	7.6	5.3
		18,000	0.88	3.4	0.778	2.9	5.4
		100,000	0.88	5.3	0.966	1.2	1.2
P	N	9,000	0.87	4.6	0.516	5.3	5.2
		18,000	0.76	7.1	0.801	5.3	4.4
		100,000	0.91	12.2	0.950	4.0	1.9
P	P	9,000	0.83	3.3	0.415	3.0	3.7
		18,000	0.91	7.0	0.525	4.1	4.3
		100,000	0.78	8.7	1.027	1.8	2.1

- 'N' indicates nitrided, 'P' indicates not nitrided

Table 5-3: Averaged debris thickness and debris oxygen content from nitrided-against-nitrided and non-nitrided-against-nitrided flat specimens.

No. of cycles	Debris thickness (μm)	Relative oxygen mass content
9,000	1.7	1
18,000	2.2	1.3
100,000	1.2	5.3

Table 5-4: Comparison of wear coefficient between boundary-lubricated and non-lubricated tests from the nitrided flat-against-non-nitrided round test.

Curves	Wear coefficient $\times 10^{-8}$ (MPa $^{-1}$ )	No. of cycles
<b>Non-lubricated</b>	7	1,200
<b>Upper bound</b>	2	20,000
<b>Typical</b>	1	180,000
<b>Lower bound</b>	0.1	200,000

Table 5-5: Elemental analysis of worn surface (boundary-lubricated) and unworn surface area (mass %) from the nitrided flat-against-non-nitrided round.

	C	O	Fe	Cr
<b>Fractured surface</b>	30-33	20-25	20-45	2
<b>Unworn</b>	6	2	81-84	3

Table 5-6: Predicted maximum wear depths and widths for flat specimens (non-lubricated condition)

Nitrided status*		No. of cycles	FE -prediction	
Flat	Round		Max depth (μm)	Width (mm)
N	N	9000	3.9	0.678
		18000	5.0	0.632
N	P	9000	5.5	0.777
		18000	4.6	0.893
P	N	9000	4.8	0.725
		18000	3.6	0.623
P	P	9000	3.3	0.623
		18000	3.7	0.626

\* 'N' indicates nitrided, 'p' indicates not nitrided

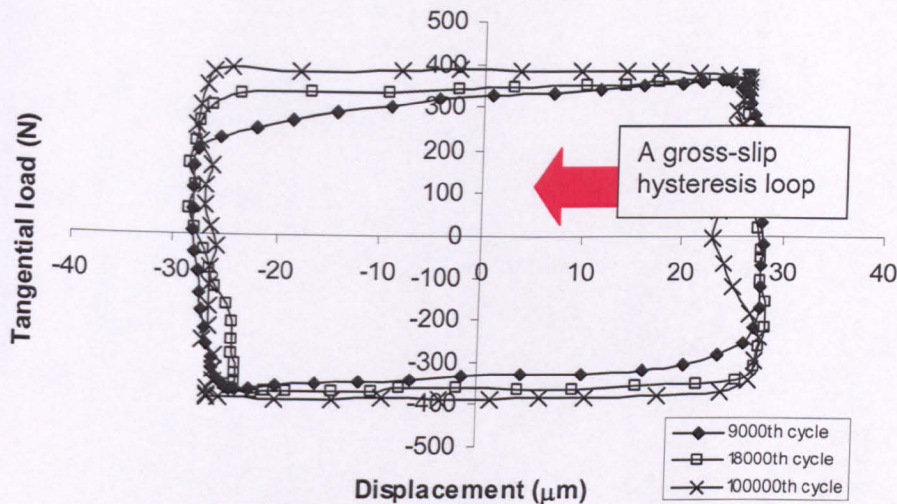


Figure 5-1: The force-displacement loop from the nitrided-against-nitrided test for the various wear cycle interval (50  $\mu\text{m}$  and 500 N).

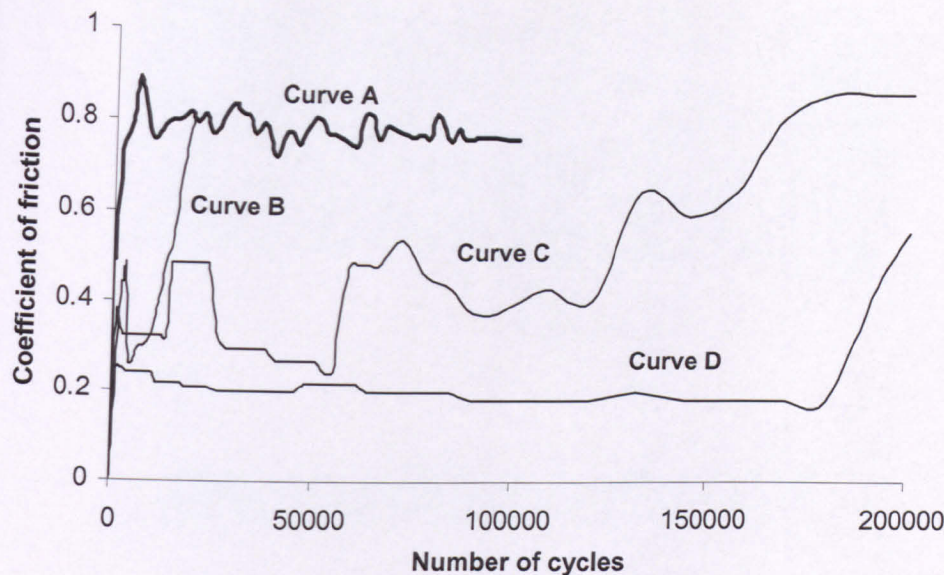


Figure 5-2: Coefficient of friction from the round-against-flat tests: Curve A: non-lubricated, Curves B and D: upper and lower bounds for boundary lubrication, and Curve C: typical for boundary lubrication. Contact load = 500 N, stroke = 50  $\mu\text{m}$ .

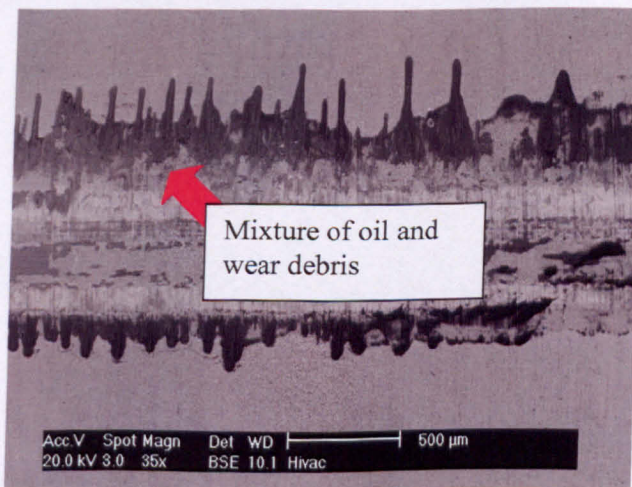
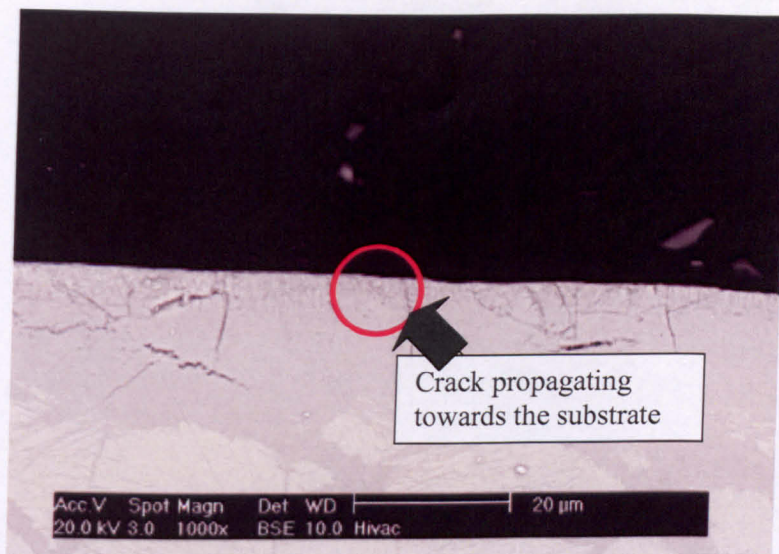
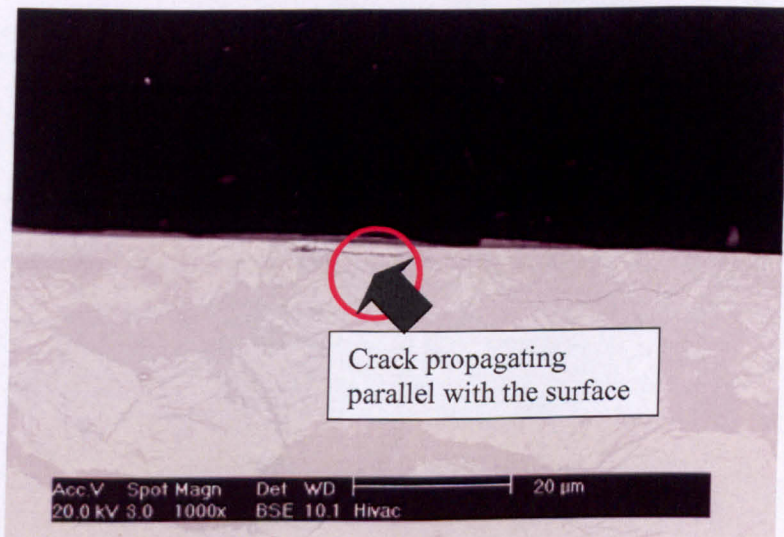


Figure 5-3: The BEI of the boundary-lubricated nitrided-against-non-nitrided test, taken on the flat specimen.

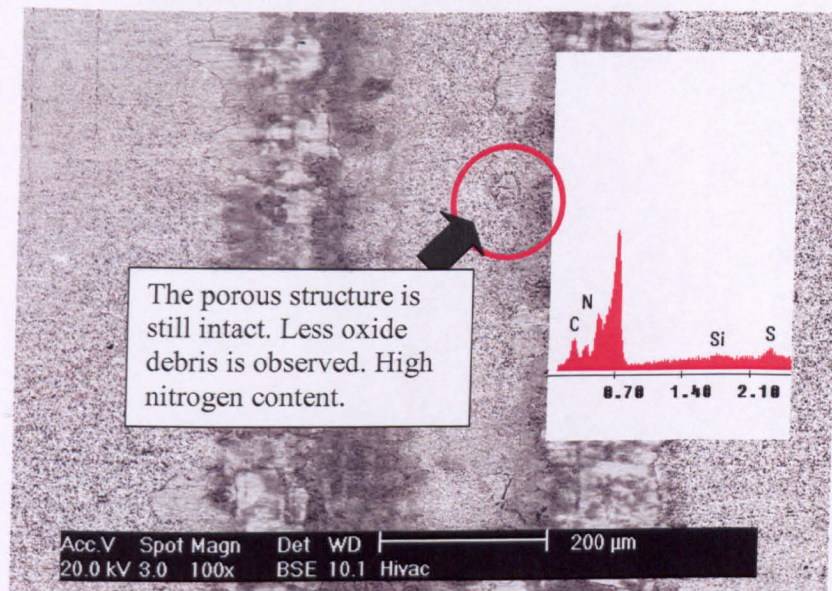


(a)



(b)

Figure 5-4: BEI cross-sections on the centre region of the worn nitrided flat specimen (nitrided-against-nitrided) tested at 50 μm and 500 N, non-lubricated: (a) 9,000 cycles (b) 100,000 cycles. The wear scar section is parallel to the stroke direction.

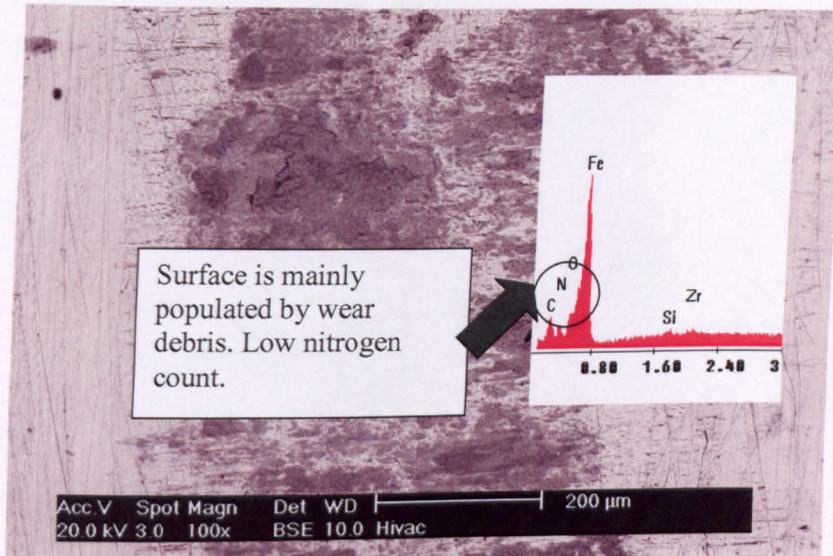


(a)

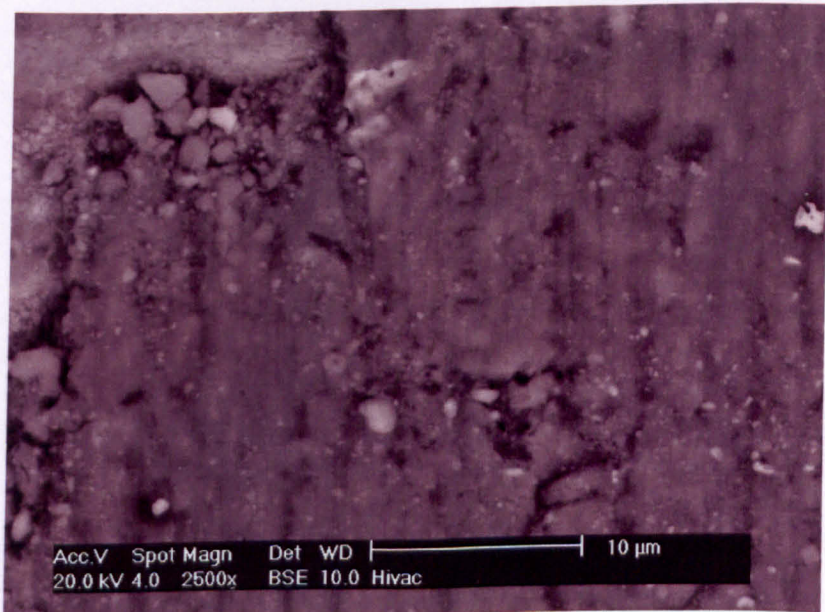


(b)

Figure 5-5: BEI images of nitrided flat specimen from the nitrided-against-nitrided test after 9,000 cycles, non-lubricated: (a) full scar width (b) higher magnification view of centre region. Applied load=500 N, stroke=50 µm

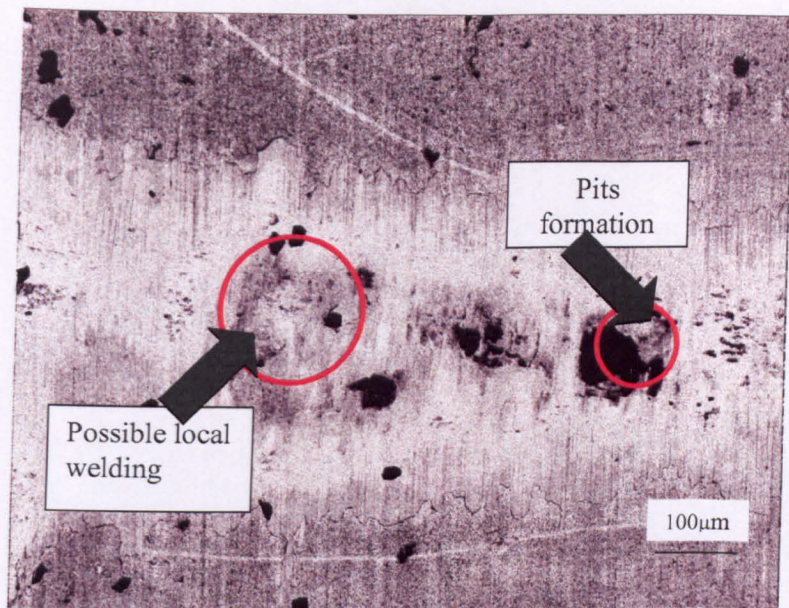


(a)

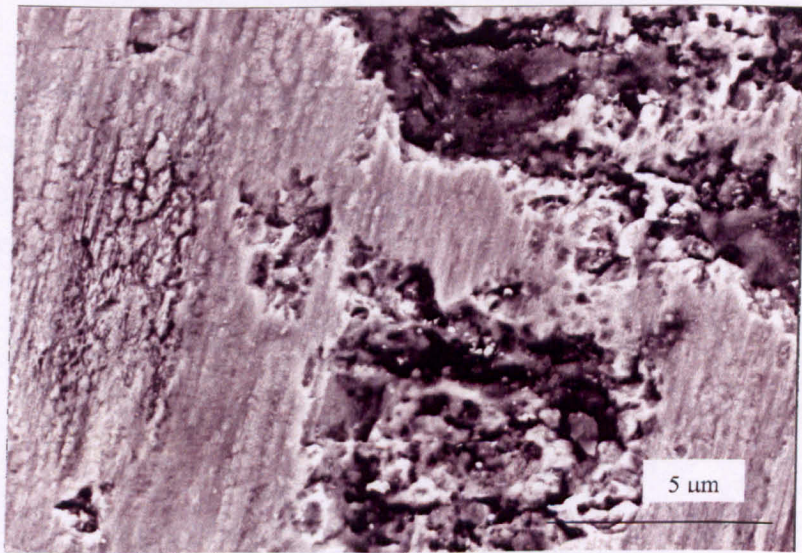


(b)

Figure 5-6: BEI images of non-nitrided flat specimen from the non-nitrided-against-nitrided test after 18,000 cycles, non-lubricated: (a) full scar width (b) higher magnification view of centre region. Applied load=500 N, stroke=50 µm

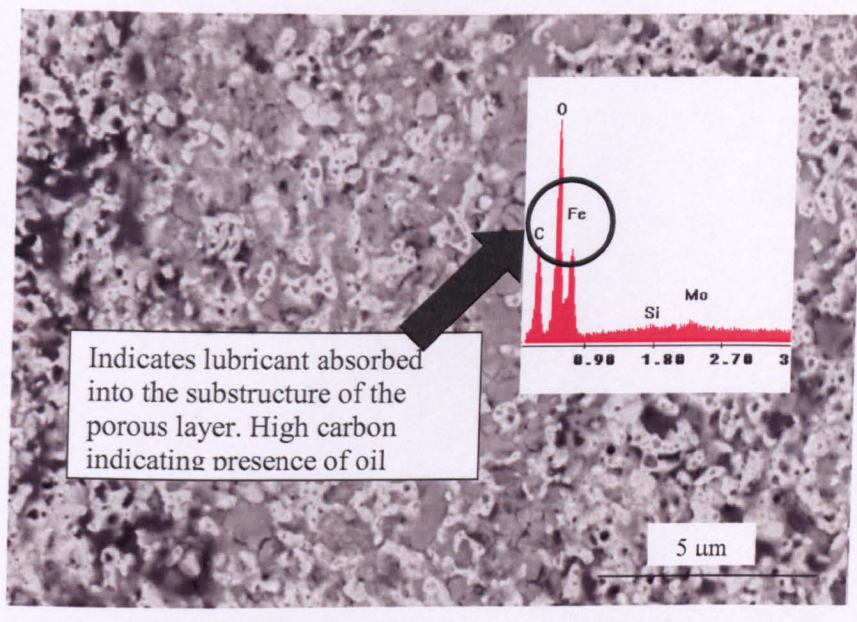


(a)



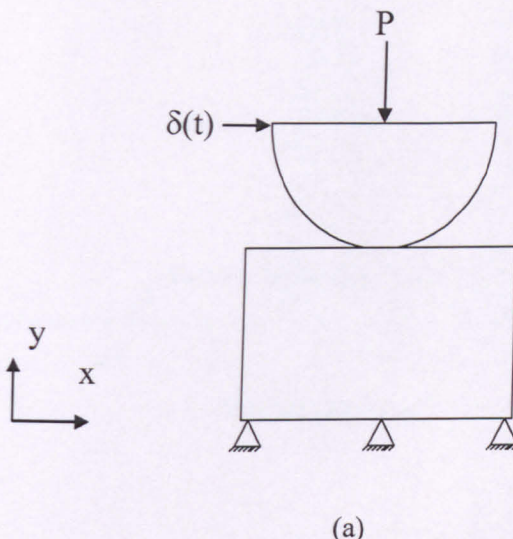
(b)

Figure 5-7 (cont'd): BEI images of nitrided flat specimen from the nitrided-against-nitrided test after 100,000 cycles, boundary lubrication: (a) full scar width, (b) higher magnification of the worn surface, and (c) nitrided layer near the wear scar periphery. Applied load=500 N, stroke=50  $\mu\text{m}$ .

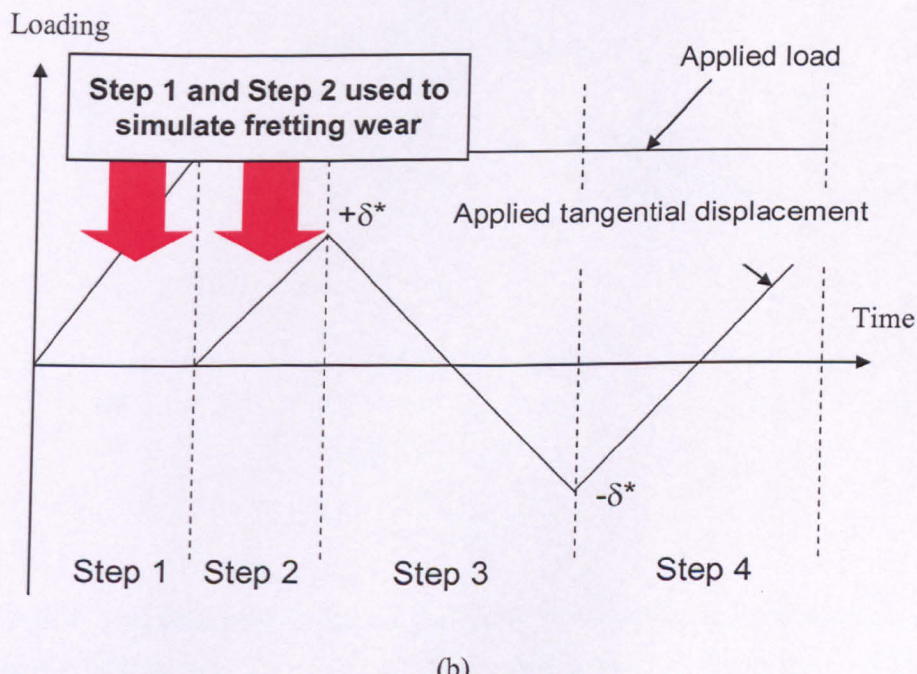


(c)

Figure 5-7: BEI images of nitrided flat specimen from the nitrided-against-nitrided test after 100,000 cycles, boundary lubrication: (a) full scar width, (b) higher magnification of the worn surface, and (c) nitrided layer near the wear scar periphery. Applied load=500 N, stroke=50 μm.



(a)



(b)

Figure 5-8: The essential tools for the fretting wear simulation programme: (a) A simple two-dimensional round-on-flat schematic model and (b) flowchart representing the loading history used to simulate the experimental fretting rig condition [2].

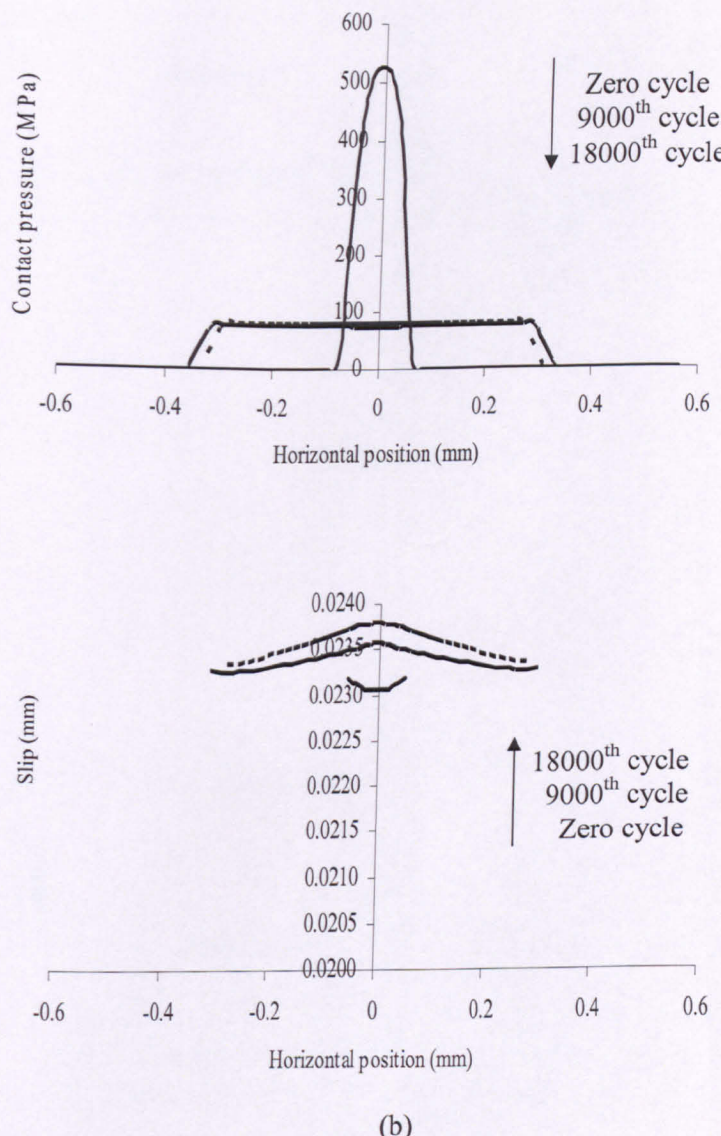


Figure 5-9: FE predictions corresponding to the nitrided-against-nitrided test for 50  $\mu\text{m}$  stroke, 500 N load up to 18,000 cycles, non-lubricated condition: (a) Contact pressure and (b) slip distributions at instant of zero tangential displacement.

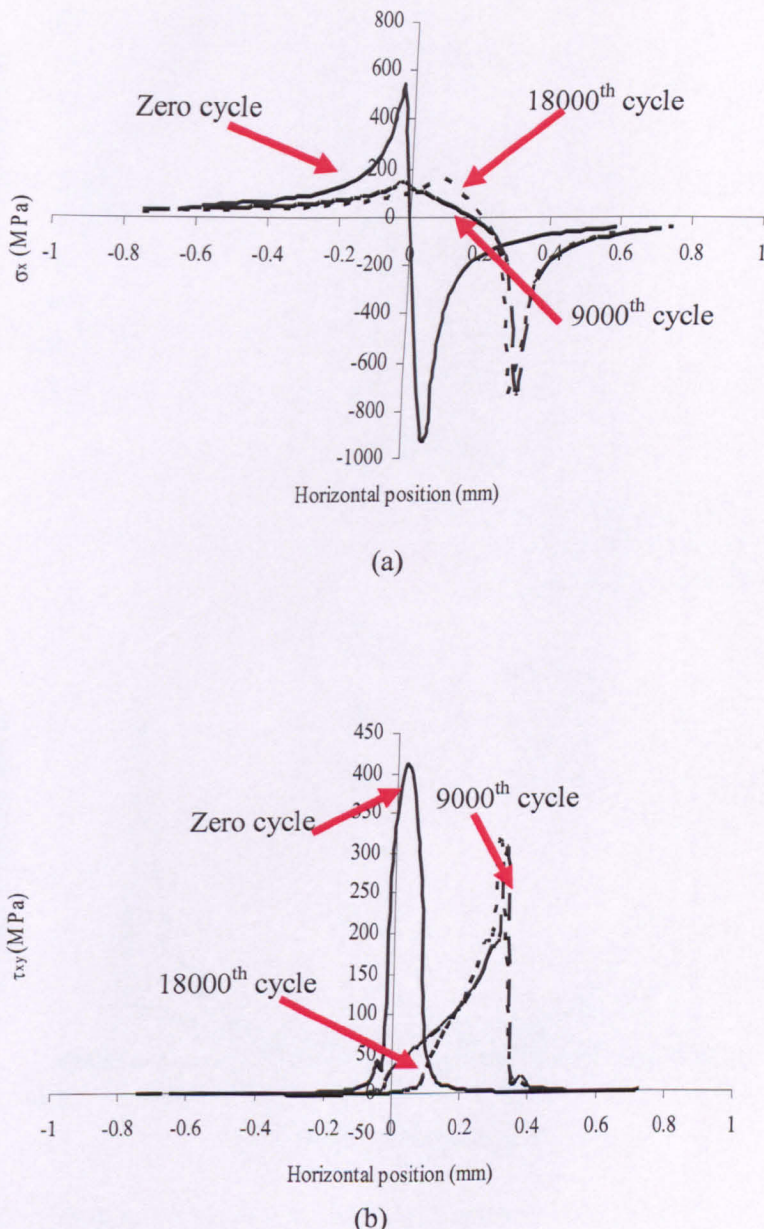


Figure 5-10: FE predictions corresponding to nitrided-against-nitrided test for 50  $\mu\text{m}$  stroke and 500 N load up to 18,000 cycles, non-lubricated condition: (a) Normal stress  $\sigma_x$  and (b) shear stress  $\tau_{xy}$  ( $x$  parallel to surface and  $y$  normal to surface). This condition is at instant of maximum ( $+\delta^*$ ) tangential displacement.

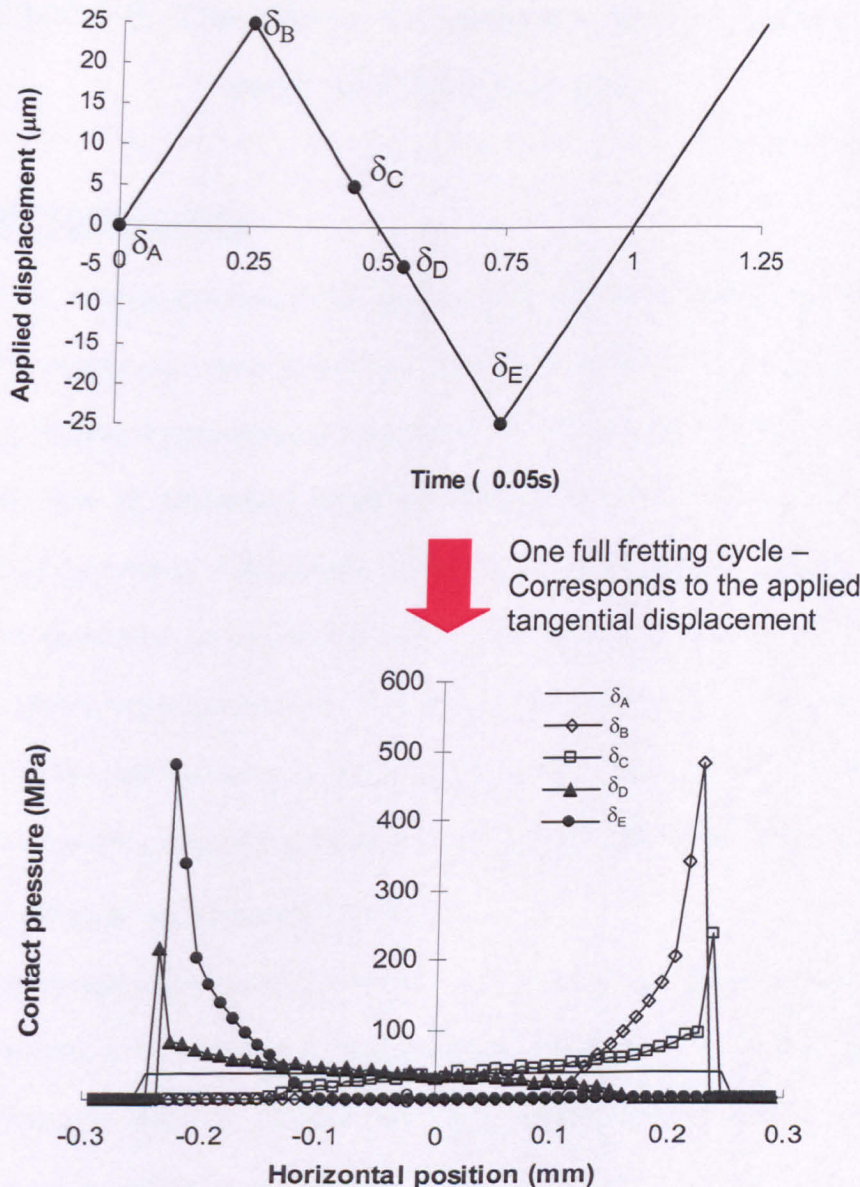


Figure 5-11: Variation of contact pressure distribution with the applied tangential displacement during 18,000<sup>th</sup> cycle under 185 N normal load case [2].

---

## **Chapter 6: The effect of moderate temperatures on Inconel 718 superalloy**

---

### **6.1 INTRODUCTION**

It has been reported that high temperature wear is a serious problem experienced by industrial machinery, power generation units, traction plants and turbine engines. Wear at elevated temperatures is accentuated by the increased kinetics of surface oxidation, loss of mechanical properties (strength & hardness), and changes in tribological parameters. This chapter focuses on an investigation into the effect of moderate temperature on the fretting wear characteristics of Inconel 718 (718) alloy through experimental examination. 718 alloy, a ternary Ni-Cr-Fe metal, has been adopted in the manufacturing of spline couplings for military aircraft jet engines where the operating temperature exceeds 450°C; this is significantly higher than the 150°C experienced in commercial turbofans.

The wear resistant behaviour of 718 alloy is known to improve with temperature [1]. This is believed to be attributed to the formation of glaze oxides. Waterhouse [2] has studied 718 alloy from room temp to about 600°C but this chapter will focus on more specific loading and stroke conditions for the application of interest, viz. aeroengine spline couplings, and will also focus on a more specific and limited temperature range. Also, this chapter will examine the fretted surface morphology, which was not dealt with by Waterhouse in detail. Consequently, in this work, the test conditions involved a 500 N applied load (initial maximum Hertzian pressure,  $p_0$ , 554MPa) and 50  $\mu\text{m}$  stroke for different test temperatures in the range of 22°C to 450°C.

## **6.2 METHODS**

### **6.2.1 Materials and specimens**

The specimen heat treatments and procedures are the same as described in section 4.1 and section 4.2. The test conditions are listed in Table 6-1. This experimental work involves the study of the fretting wear behaviour of self-against-self specimen combinations using the crossed round against flat configuration.

### **6.2.2 Characterisation**

The microscopic assessment procedures and methods are the same as in section 4.3. The unworn surface was etched in Aqua Regia (20ml HNO<sub>3</sub>/ 60ml HCl) for 5 seconds to reveal the general microstructure of 718.

## **6.3 RESULTS**

### **6.3.1 Coefficient of friction evolution**

Figure 6-1 shows the measured evolution of coefficient of friction (COF) with increasing number of fretting cycles for each temperature. The initial value of COF decreases with increasing temperature from about 0.88 at 22°C to about 0.56 at 450°C. For the 22°C test, the COF is seen to generally increase slowly over the next 200,000 cycles to an almost steady state value of about 1.0. For the higher temperature tests, the COF is found to decrease with increasing numbers of fretting cycles, with the 300°C value becoming lower than the 450°C value for intermediate numbers of cycles, viz. between about 11,000 cycles and 125,000 cycles. The COF values for  $N > 125,000$  cycles, follow the trend of the higher the temperature, the lower the COF. The lowest recorded COF value of 0.34 corresponds to large numbers of fretting cycles, about  $N > 170,000$  cycles, for the 450°C case. In order to quantitatively present the effect of temperature on COF, an average COF value is

calculated using the data for numbers of cycles greater than 5000. These average values are presented in Table 6-2.

Defining a steady-state condition for each test temperature as being established after 70,000 wear cycles, the corresponding steady-state COF values are shown in Figure 6-2 as a function of temperature. The force-displacement loops are characteristic of gross-slip (Figure 6-3).

### 6.3.2 Wear coefficient evolution

From Table 6-2, it is apparent that the wear coefficient ( $k$ ) decreases with increasing temperature, and that the 22°C case has the highest  $k$  value of  $0.36 \times 10^8 \text{ MPa}^{-1}$ ; the calculation takes into account the presence of the adhered debris layer on the wear scar. The average thickness of the debris layer in Table 6-3 is estimated by taking several measurements of the wear scar from the cross-sectioned snapshots.

### 6.3.3 Wear volume

The data in Table 6-4 provides the total wear volume measurements of each temperature test. As the temperature increases, the amount of material loss with fretting wear decreases. The largest and smallest amount of material loss correspond to the 22°C case and 450°C case with a value of  $0.05046 \text{ mm}^3$  and  $0.00258 \text{ mm}^3$  respectively.

### 6.3.4 Wear surface profiles

The worn surface profiles of the round and flat specimens for each case study are shown in Figures 6-4a and b. The profiles showed that the surface roughness reduces with increasing temperature and surface damage is minimised. These characteristics

are observed on the worn round and flat specimens but are more pronounced on the flat specimens.

### 6.3.5 Microscopic examinations of wear scars

#### **(a) 22 °C**

A BEI of a wear scar from the 22°C test is shown in Figure 6-5a. The wear track was covered by wear debris that was randomly scattered. The debris was disrupted with the worn substrate partially exposed. A higher magnification BEI (Figure 6-6a) reveals the possibility of material transfer during wear (visible profiling lines). The highly magnified cross-sectioned image also shows possible debris layers fracturing (Figure 6-7a).

#### **(b) 150 °C**

A relatively thick layer was adhered to the wear track shown in Figure 6-5b. It had a well-compacted (Figure 6-6b) and smooth morphology (Figure 6-7b). The transverse section showed a consistent array of debris layer adhering to the substrate. A BEI also revealed possible loose debris on the periphery of the wear scar. Visible profiling lines are seen across the wear scar.

#### **(c) 300 °C**

In Figure 6-5c, the wear track is covered with thick compacted debris layer (with a smooth morphology) that is continuous with some loose debris (relatively fine) resting on top of the compacted debris. There is no evidence of surface cracking (Figure 6-6c). In Figure 6-7c, the transverse section shows a relatively consistent layer along the scar length.

**(d) 450 °C**

A small amount of debris adhered to the wear scar (Figure 6-5d). The transverse section from the BEI shows a thin layer adhering on the wear scar (Figure 6-7d). This structure appeared to have a smooth finish (Figure 6-6d).

### **6.3.6 Elemental and X-ray diffraction analysis**

Table 6-5 shows the average EDX data of the alloying elements corresponding to each temperature test. Each reported value is the average of 5 readings. There is no clear trend regarding changes of the alloying elements. However, the general finding is that traces of oxygen are detected for the four test temperatures, with an average value of  $\approx 20$  mass%. Also, the analysis detected the presence of chromium, iron, and nickel but the reading showed no dramatic changes in mass composition. For the aforementioned metal elements, the measured values are 14 mass%, 14 mass%, and 44 mass% respectively. A schematic representation of the critical elements present within the glaze oxide is shown in Figure 6-8. The glaze is subdivided into three regions, which are (i) oxide layer, (ii) oxide/substrate interface, and (iii) substrate. However, EDX does not reveal the type of oxides present within the oxide of the glaze.

Trevorite ( $\text{NiFe}_2\text{O}_4$ ) is a potential oxide phase that has been detected on the 22°C, 150°C and 300°C cases by XRD analysis and the EDX data did clearly indicate the presence of iron, nickel, and chromium present within the oxide of the glaze. Nickel is detected as a metallic phase present in all samples tested at 22°C, 150°C, and 300°C (Figure 6-9a). At 450°C , two oxide phases were detected within the oxide of the glaze. These are the chromite ( $\text{FeCr}_2\text{O}_4$ ) and trevorite ( $\text{NiFe}_2\text{O}_4$ ), types of spinel

oxide (Figure 6-9b). The EDX data further confirmed the presence of iron, nickel , and chromium.

### 6.3.7 Observation of the $\gamma'$ , $\gamma''$ and $\delta$ -phases

The microstructural behaviour of the  $\gamma'$ ,  $\gamma''$  and  $\delta$ -phases were monitored by both SEM and TEM methods. The samples were from the worn flat specimens fretted for 2hours 47minutes. Selected-area-diffraction (SAD) patterns of each phase were also taken in configuration with the TEM analyses. The morphological changes of the  $\delta$  phase, at various temperatures are shown in Figures 6-10a, b, c, and d. At 22°C,  $\delta$  precipitates were randomly scattered within the material, i.e. the matrix and grain boundaries. As the temperature increases (150°C, 300°C, and 450°C), the  $\delta$  phase forms larger elongated precipitates. The dimensions of  $\delta$  phase are listed in Table 6-6.

The general microstructure of 718 with its various strengthening precipitates are shown in Figure 6-11a. Two variant  $\gamma''$  ( $Ni_3Nb$ ) precipitates (Figures 6-11b and c) were identified and the region examined is marked. The diffraction crystallography patterns of the possible  $\gamma/\gamma'/\gamma''$  are shown in Figure 6-11d. The diffraction patterns suggest that  $\gamma'$  and  $\gamma''$  phases overlap each other on the <111> type plane [3]. In Figure 6-12,  $\gamma'(Ni_3Al)$  is seen as the small spheroidal black precipitate next to the ellipsoidal precipitate which is  $\gamma''$ .

## 6.4 DISCUSSION

### a) *The effect of temperature on wear*

The time taken for the glaze and substrate to become fully effective in supporting the load, and thus reducing the COF and wear, is directly dependent on the applied temperature, i.e. the time taken for the glaze layer to form shortens with increasing

temperature. This suggests that less additional energy is required, and surface damage decreases with temperature. The force-displacement loops in Figure 6-3 showed gradual reduction of the loop size with increasing temperature. This wear characteristic suggests that the wear resistant property of 718 material improves with temperature. The observations described in Section 6.3.5 clearly indicate that temperature is a major driving force for adhesion between particles and formation of load-bearing compacted debris layers, i.e. glaze oxide. It is believed that a temperature as low as 150°C is sufficient to pre-sinter the wear debris and increases the surface kinetics of oxidation. These conditions are not impossible and Jiang et al. [4] have been able to demonstrate the above assumptions. Adhesive forces and sintering tend to take effect at more elevated temperature and this is demonstrated by experimental work carried out by Jiang on Nimonic 80A at 20°C, 150°C, and 250°C. It has been suggested that at 250°C, sintering becomes a significant factor and there is a tendency for the formation of a smooth glaze oxide on top of the compacted oxide layers (Figure 6-5). The 150°C case was intermediate, with some development of a smooth load-bearing area between the particle layers. This temperature range did not permit strong adhesion of the compacted debris as it was easily removed by ultrasonic cleaning; loose compacted debris was left behind in acetone solution. A similar situation was encountered for the current investigation corresponding to the tests carried out from 22°C to 300°C (Figures 6-5b and c). The visibility of profiling lines clearly indicated the wear debris was not solidly sintered together.

Also of note was the formation of compacted debris layers close to the centre of wear scars, where debris retention would be greatest (Figures 6-5). Away from the centre of the point of contact, there would be more scope for debris removal, by being

pushed out from the sides of the contact area. It is believed that the presence of compacted debris layers of "glaze-type" will offer more physical protection than non-glaze type. This assumption has been justified with respect to the reduction of COF,  $k$ , and material removal (Section 6.1, 6.2, and 6.3)[5, 6].

b) *The effect of temperature on strengthening precipitates and oxidation*

The mechanical properties of 718 alloy are known to improve with increasing temperature. The stability of this alloy is determined by the coherency of the strengthening precipitates such as  $\gamma'$  and  $\gamma''$  (Figures 6-11d). The misfit of the structures causes strain and this may have work-hardened the material thereby improving the mechanical properties. In general, work-hardening is associated with an increasing number of dislocations and their entanglement, which causes an increase in strength and hardness, bearing in mind that this process also reduces ductility. Within the temperature range from 22°C to 450°C (Figures 6-10), it is unlikely that there will be any dramatic changes to occur on the precipitates. Alternatively, the heat energy may have been utilised by dislocations to enhance the oxidation process during fretting.

It has been reported that the state of the surface and the presence of defects (i.e. dislocations, cracks and grain boundaries) has an effect on the oxidation kinetics [7]. The reasoning behind this is greater activation of wear surfaces due to the wear process, as a result of a higher level of dislocations at the surface of the deformed metal. These dislocations act as sinks for metal ion diffusion pathways between the metal/oxides interface, preventing pore formation at the interface. The presence of pores is believed to inhibit ion diffusion through the oxide layer and slow the oxidation rate. No pores have been observed on the oxide layer (Figures 6-7).

Similarly, the cracks and grain boundaries in the outer layer of the forming oxide layers act as routes for the passage of oxygen ions. When these flaws exist, it is the distance between the flaw tips and metal/oxide interface that is important for controlling the oxidation rate of debris [8].

The key point is that the misfit of strengthening precipitates is the main source of dislocations and this has great consequences for the oxidation rate. Nonetheless, it is crucial to ensure the  $\delta$  precipitates (brittle) do not coarsen as this metallurgical change affects the mechanical properties and possibly induces failure by brittle-transgranular fracture.

### c) *The effect of temperature on glaze oxide formation*

The key factors that control the glaze oxide formation have been identified in this research. The fretting wear behaviour of 718 was studied by Hamdy [1] for a range of temperatures. This research has been able to confirm these key findings. This research shows that the contacting surface experienced minimal wear owing to the formation of a glaze oxide, that is a highly deformable layer with good wear resistance and low shear stress. It was often considered that this thermal scale begins to form at 200°C and is fully developed at temperatures above 400°C (Figure 6-4).

Therefore, the following criteria for the glaze oxide formations are as follow:

1. There is a specific minimum temperature or threshold which needs to be exceeded to form the glaze oxide. In this case, it is believed that the threshold starts at approximately about 150°C, based on experimental observations, i.e. reduction of COF and  $k$ .
2. The level of alloying elements and compositions plays a crucial role in determining the glaze oxide phases and the chemical bonding. Also, the

existence of pre-oxidised wear debris, which acts as a precursor for the oxide phase formation, helps determine the glaze oxide [9-11]. This reaction is dictated by the Gibbs free energies (Table 6-7)[8]. The EDX and XRD results clearly indicated the presence of a mixture of spinel oxides within the glaze layer. This does not rule out the presence of metal oxide phase types, namely iron oxide ( $\text{Fe}_3\text{O}_4$  and  $\text{Fe}_2\text{O}_3$ ) phase and nickel oxide ( $\text{NiO}$ ) phase, but chromium oxide phase ( $\text{Cr}_2\text{O}_3$ ) was only detected after 600°C and above [5]. A possible explanation for not detecting these oxide phases is perhaps that they may have co-existed and shared similar crystal structures.

3. The availability of surface defects, which may enhance the kinetics of oxidation.
4. The stability of the metal/oxide interface with respect to the differences in mechanical properties. To avoid fracturing of this oxide scale, the underlying substrate should be harder (high elastic modulus) than that of the oxide scale (low elastic modulus) [12]. When a structure is thin (e.g. oxide scale), it has little influence on the stress field and only transmits it. Strains were imposed by the substrate. This situation creates a stable and strong oxide-substrate interface. For example, high thermal stresses caused by fluctuation of thermal expansion coefficient within the layer. Upon cooling down, this causes cracking of the wear-resistant oxide layer.
5. The wear debris residence time is crucial for the formation of glaze layer as well as shape integrity. The level of sintering determines the aforementioned statement.

It is apparent that the presence of the glaze oxide is advantageous with respect to a change in wearing behaviour i.e. a change from severe wear to mild wear of the fretted surface. This is also evidently proven by the surface profiling where a rather rough profile was seen on the 22°C case (Figure 6-4a). For the 450°C case (Figure 6-4b), the surface profile was relatively smooth, similar to the unworn surface. Also, material loss is reduced due to the recycling effect of wear debris either from the existing loose debris or from the glaze layer. The glaze layer formed at 150°C and 300°C consisted of mainly of  $\text{NiFe}_2\text{O}_4$ , while at 450°C the glaze layer consisted of a mixture of  $\text{NiFe}_2\text{O}_4$  and  $\text{FeCr}_2\text{O}_4$ .

Based on microscopic observations, the mechanisms involved in the glaze oxide formation for 718 alloy are as follows :

- *Mechanism 1:* During the initial stage, wear debris is generated due to the relative motion of the metal surfaces. Some of this wear debris may be removed by the fretting action to become loose wear debris – others are retained within the wear track. Those retained are gradually compacted by repeated fretting and fracture while freely moving between the rubbing surfaces. The wear debris undergoes partial oxidation due to frictional heating from repeated fretting action. A mixture of metallic debris and oxidised debris is found within the compacted debris layer. Competition arises between the existing compacted debris layer and uncovered bulk material. The compacted debris layer breaks down to form more wear debris which can be abrasive and promote further wear especially on the exposed metallic surface. This mechanism is reflected by the 22°C case.
- *Mechanism 2:* The pre-oxidised wear debris at the centre point is work-hardened by the fretting action. As the temperature increases, the compacted wear debris is

continuously sintered leading to further consolidation, thereby forming a solid structure which is strongly adherent to the underlying material, hence, forming a hard and protective layer. Material loss is reduced by recycling the existing loose debris and perhaps from the larger fractured compacted debris layer. The 150°C, 300°C and 450°C cases did exhibit the morphology as described. However, the compacted debris layer corresponding to the 150°C and 300°C cases is not solidly sintered and adherent. Nonetheless, the compacted layer is able to accommodate the applied load.

## References

1. M. M. Hamdy and R. B. Waterhouse, "The fretting wear of Ti-6Al-4V and aged Inconel 718 at elevated temperature", *Wear*, Vol. 72, 1981, pp. 236-148
2. F. H. Stott, D. S. Lin, G. C. Wood, and C. W. Stevenson, "The tribological behaviour of nickel and nickel-chromium alloys at temperature from 20°C to 800°C", *Wear*, Vol. 36, 1976, pp. 146-174
3. D. F. Paulois, J. M. Oblak and D. S. Duvall, "Coherency Strengthening in Ni Base Alloys Hardened by DO<sub>22</sub> γ" precipitates", *Metallurgical Transaction A.*, Vol. 5, 1974, pp.143-153
4. J. Jiang, F. H. Stott, and M. M. Stack, "The Role of Triboparticles in Dry Sliding Wear", *Tribol. Int.*, Vol. 31 (5), 1998, pp. 245-256
5. F. H. Stott, D. S. Lin, and G. C. Wood, "The Structure And Mechanism of Formation of the 'Glaze' Oxide Layers Produced on Nickel-Based Alloys

During Wear at High Temperatures”, *Corrosion Science*, Vol. 13, 1973, pp. 449-469

6. F. H. Stott, G. C. Wood, and J. Stinger, “The influence of alloying elements on the development and maintenance of protective scales”, *Oxidation of Metals*, Vol. 44, No.1/2, 1995, pp. 113-145
7. J. Molgaard and V. K. Srivastava, “The Activation Energy of Oxidation in Wear”, *Tribo. Int.*, 16, 1983, pp. 305-314
8. J. Molgaard, “A Discussion of Oxidation, Oxide Thickness, and Oxide Transfer in Wear”, *Wear*, 40, 1976, pp. 277-291
9. G. Beranger and M. Lanthesir, “Oxidation of Iron-Nickel alloy”, pp. 223-237
10. I. A. Inman, P. K. Datta, H. L. Du, J. S. Burnell-Gray, S. Pierzgalski and Q. Luo, “Studies of high temperature sliding wear of metallic dissimilar interfaces”, *Tribo. Int.*, Vol. 38 (9), September 2005, pp. 812-823
11. I. A. Inman, S. Datta, H. L. Du, J. S. Burnell-Gray and Q. Luo, “Microscopy of glazed layers formed during high temperature sliding wear at 750 °C”, *Wear*, Vol. 254 (5-6), March 2003, pp. 461-467
12. J. F. Carton, A.B. Vannes, and L. Vincent, “Basis of a coating choice methodology in fretting”, *Wear*, 1995, Vol. 185, pp. 46-57

Table 6-1: Fretting test conditions.

<b>Contact load</b>	500 N
<b>Initial maximum Hertzian stress</b>	784 MPa
<b>Stroke</b>	50 $\mu\text{m}$
<b>Frequency</b>	20 Hz
<b>Number of cycles</b>	200,000
<b>Room temperature</b>	22°C; 150°C; 300°C; 450°C
<b>Relative humidity</b>	40-55%
<b>Material combinations</b>	718 vs. 718

Table 6-2: The average COF and wear coefficient for the four test temperatures.

<b>Temperature(°C)</b>	<b>COF</b>	<b>Wear coefficient <math>\times 10^8</math> (MPa)</b>	
		<b>Flat</b>	<b>Round</b>
22	0.94	0.36	0.04
150	0.70	0.28	0.09
300	0.49	0.20	0.04
450	0.49	0.02	0.03

- Note that the average COF values obtained as an arithmetic mean of sample values after 5,000 cycles.

Table 6-3: Average adhered debris thickness across scar corresponding to the worn specimens of the four temperature tests.

Temperature (°C)	Thickness (μm)
22	6.18
150	3.13
300	2.25
450	1.63

Table 6-4: Wear volume versus temperature fretting tests.

Temperature (°C)	Wear volume (mm <sup>3</sup> )		Total wear volume (mm <sup>3</sup> )
	Flat	Round	
22	0.018	0.032	0.050
150	0.015	0.021	0.036
300	0.002	0.039	0.042
450	0.001	0.014	0.015

Table 6-5: EDX analyses (mass%) of the worn flat surface for the four test temperatures.

Temp (°C)	O	Al	Ni	Fe	Cr	Nb	Ti	Mo
(Unworn)	1.82	1.16	53.68	18.07	-	6.35	1.20	-
22	15.04	0.64	45.27	15.30	14.78	4.64	1.20	2.80
150	22.29	0.58	41.95	13.93	14.11	4.27	0.93	2.20
300	23.10	0.62	40.72	13.62	13.07	4.30	0.80	2.93
450	13.56	0.54	46.58	16.07	14.82	3.36	0.80	2.69

Table 6-6: Dimension of  $\delta$  phase estimated from the worn flat specimen at each test temperature.

Temp (°C)	Width ( $\mu\text{m}$ )	Length ( $\mu\text{m}$ )
22	0.4 – 1	2 – 5
150	0.1 – 0.8	0.5 – 7
300	0.1 – 0.8	0.5 – 11
450	1.6 – 4	8 – 20

Table 6-7: Free energies of formation for the key oxides formed at 727°C under conditions of static oxidation [8].

Oxides	$\Delta G_{727^\circ\text{C}} (\text{kJ. Mol}^{-1})$
$2\text{Cr} + 1 \frac{1}{2} \text{O}_2 \rightleftharpoons \text{Cr}_2\text{O}_3$	-861.6
$\text{Fe} + \frac{1}{2} \text{O}_2 \rightleftharpoons \text{FeO}$ (dominant state above 500°C)	-197.2
$3\text{Fe} + 2\text{O}_2 \rightleftharpoons \text{Fe}_3\text{O}_4$ (favoured state between 200°C to 500°C)	-780.8
$2\text{Fe} + 1 \frac{1}{2} \text{O}_2 \rightleftharpoons \text{Fe}_2\text{O}_3$ (favoured state below 200°C)	-556.8
$\text{Ni} + \frac{1}{2} \text{O}_2 \rightleftharpoons \text{NiO}$	-150.7

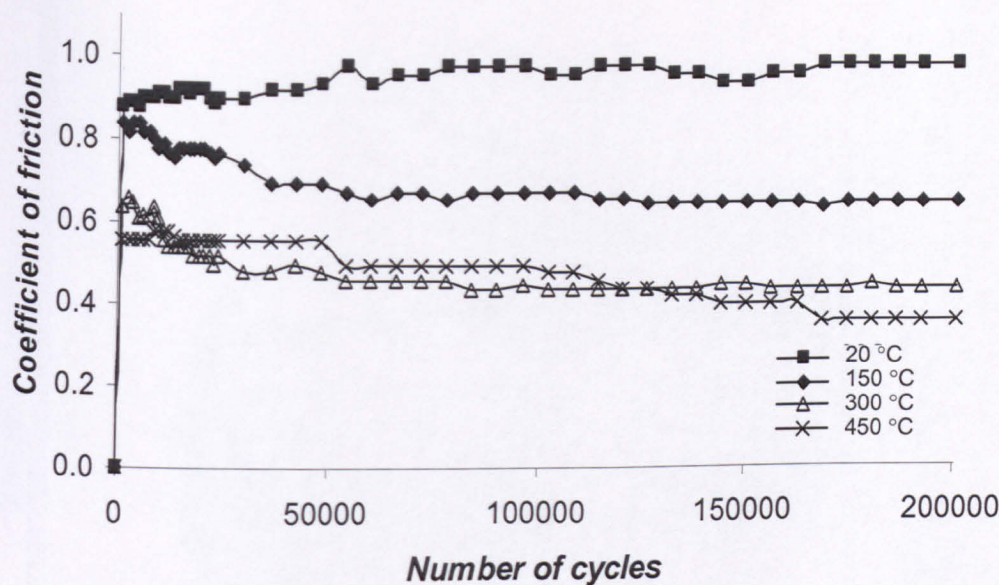


Figure 6-1: COF evolution versus number of cycles and temperature.

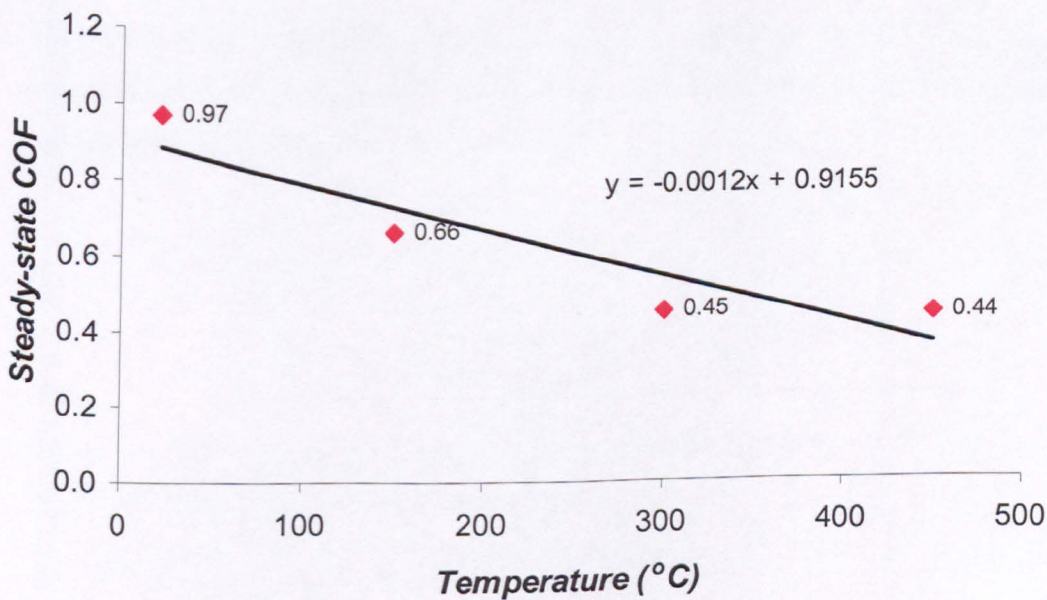


Figure 6-2: Steady-state COF (after 70,000 cycles) versus temperature.

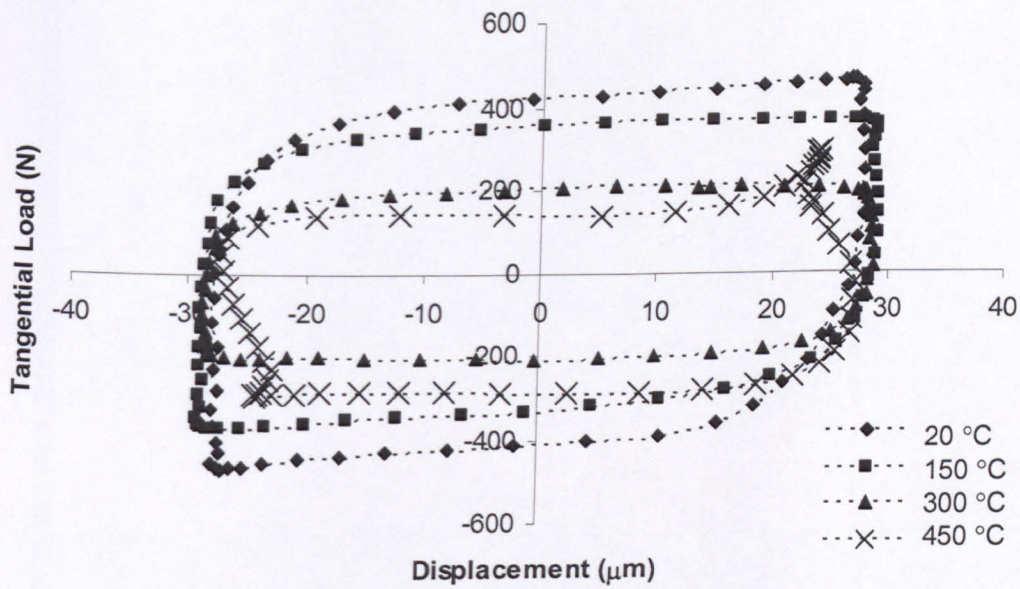


Figure 6-3: Experimental force-displacement loops at 200,000 cycles for different test temperatures. The enclosed area represents the amount of energy dissipated during fretting (refer to Table 6-1 for test conditions).

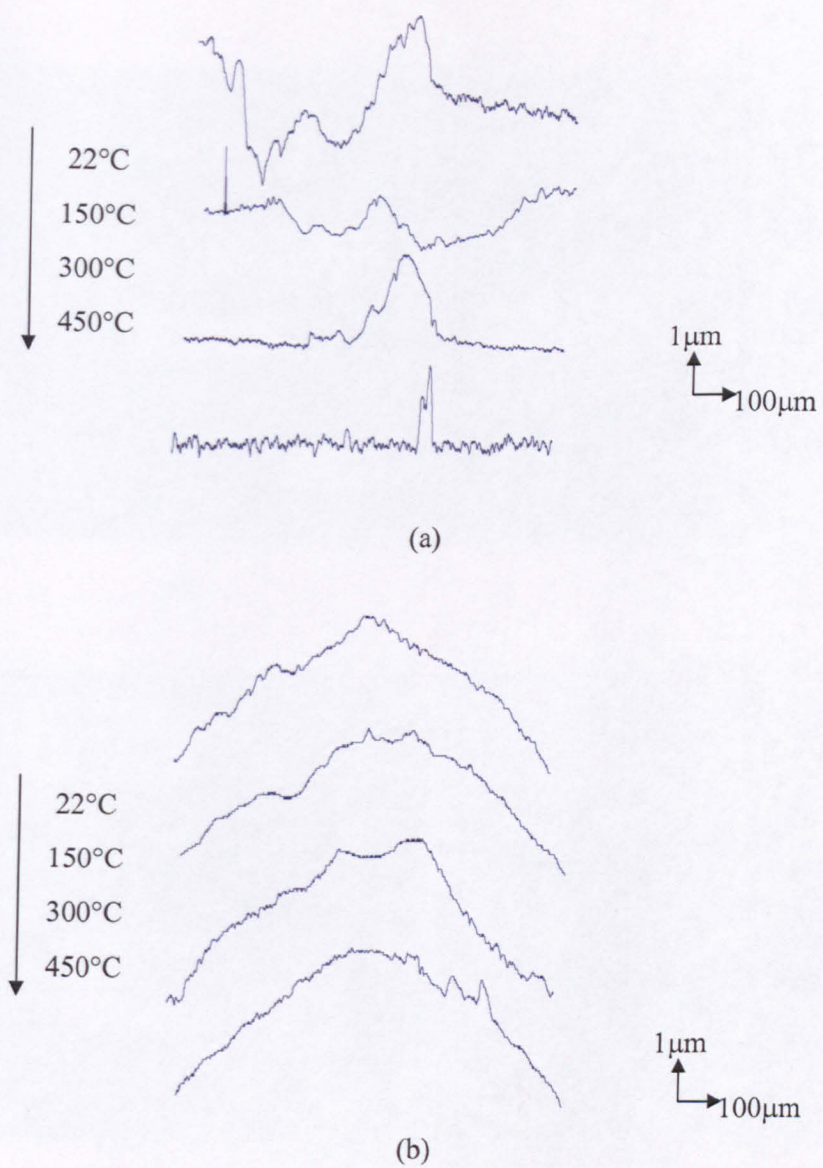


Figure 6-4: Wear scar profiles taken after 200,000 cycles corresponds to the four test temperature tests: (a) flat and (b) round specimen.

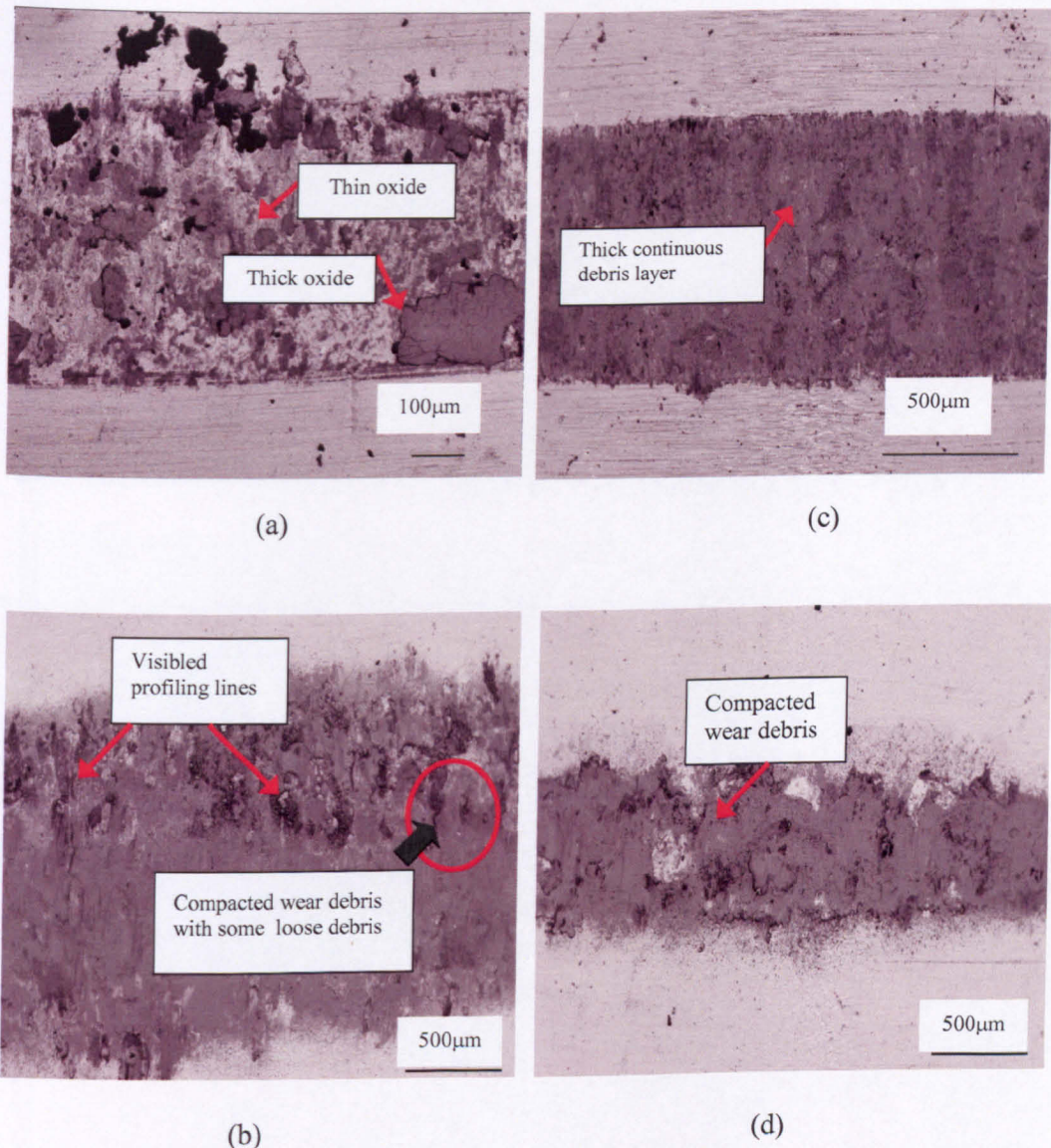


Figure 6-5: BEIs of wear scars corresponding to the worn flat specimens after 200,000 cycles, test temperature: (a) 22°C ,(b) 150°C ,(c) 300°C, and (d) 450°C (refer to Table 6-1 for test conditions).

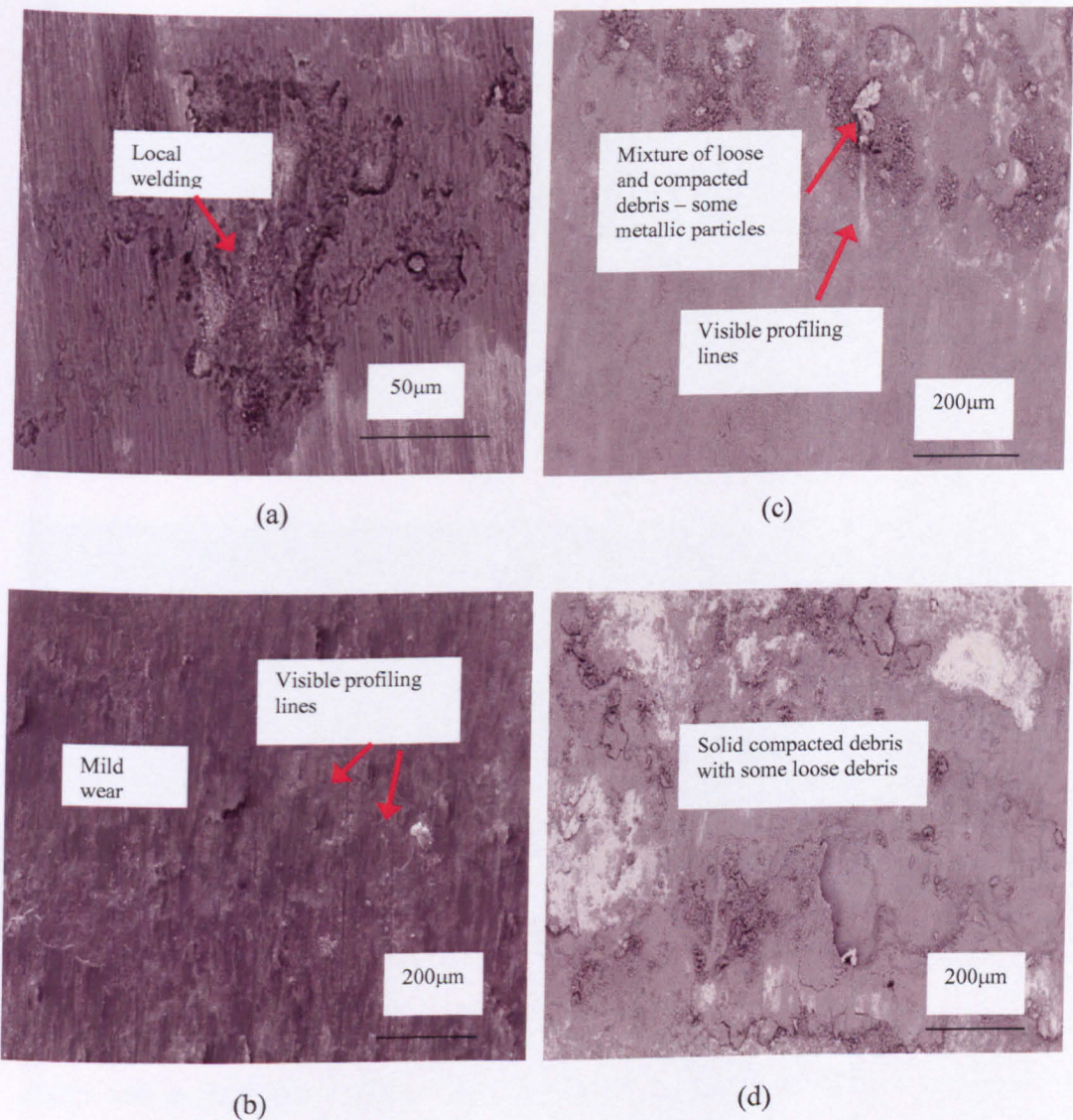


Figure 6-6: High magnification SEI and BEI corresponding to the worn flat specimen after 200,000 cycles, test temperature: (a) BEI at 22°C ,(b) SEI at 150°C ,(c) BEI at 300°C, and (d) SEI at 450°C (refer to Table 6-1 for test conditions).

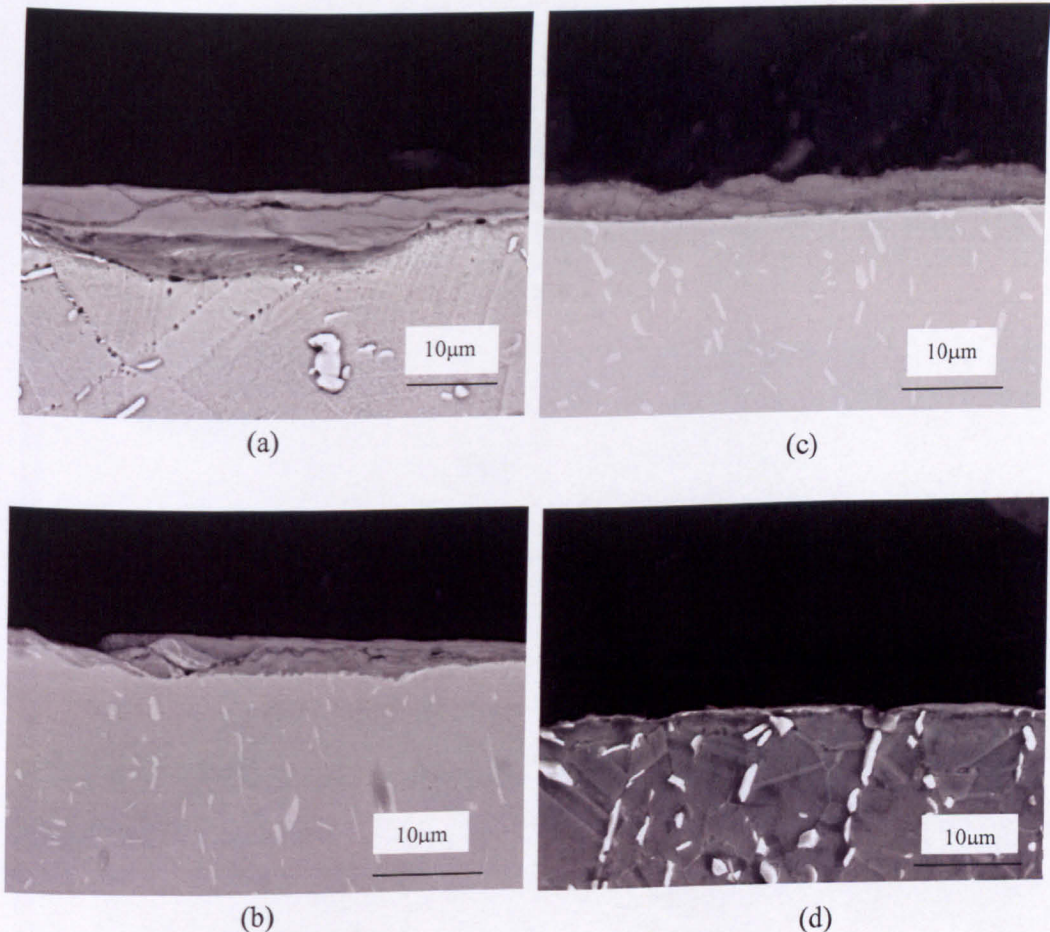


Figure 6-7: BEI cross sections of wear scars on worn flat specimens after 200, 000 cycles, test temperature: (a) BEI at 22°C ,(b) BEI at 150°C ,(c) SEI at 300°C, and (d) SEI at 450°C (refer to Table 6-1 for test conditions).

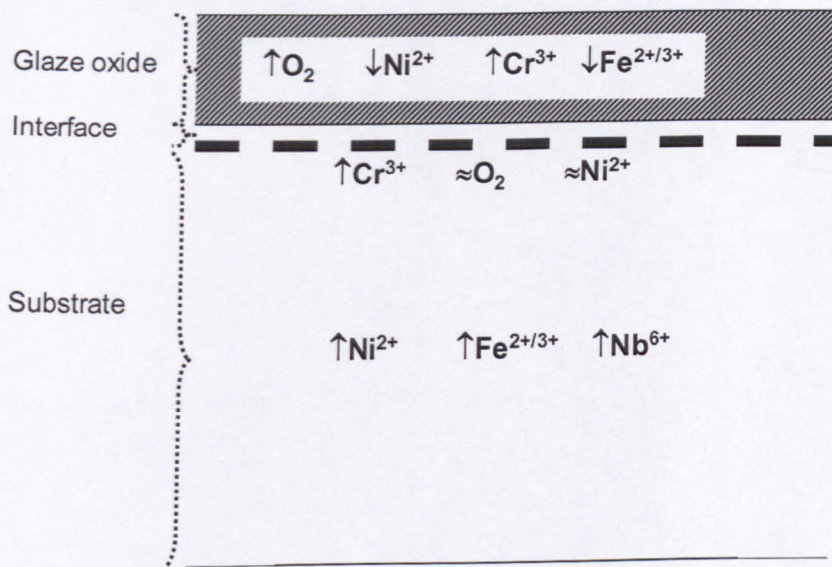


Figure 6-8: Schematic diagram representing the interchanging alloying elements within the glaze oxide.

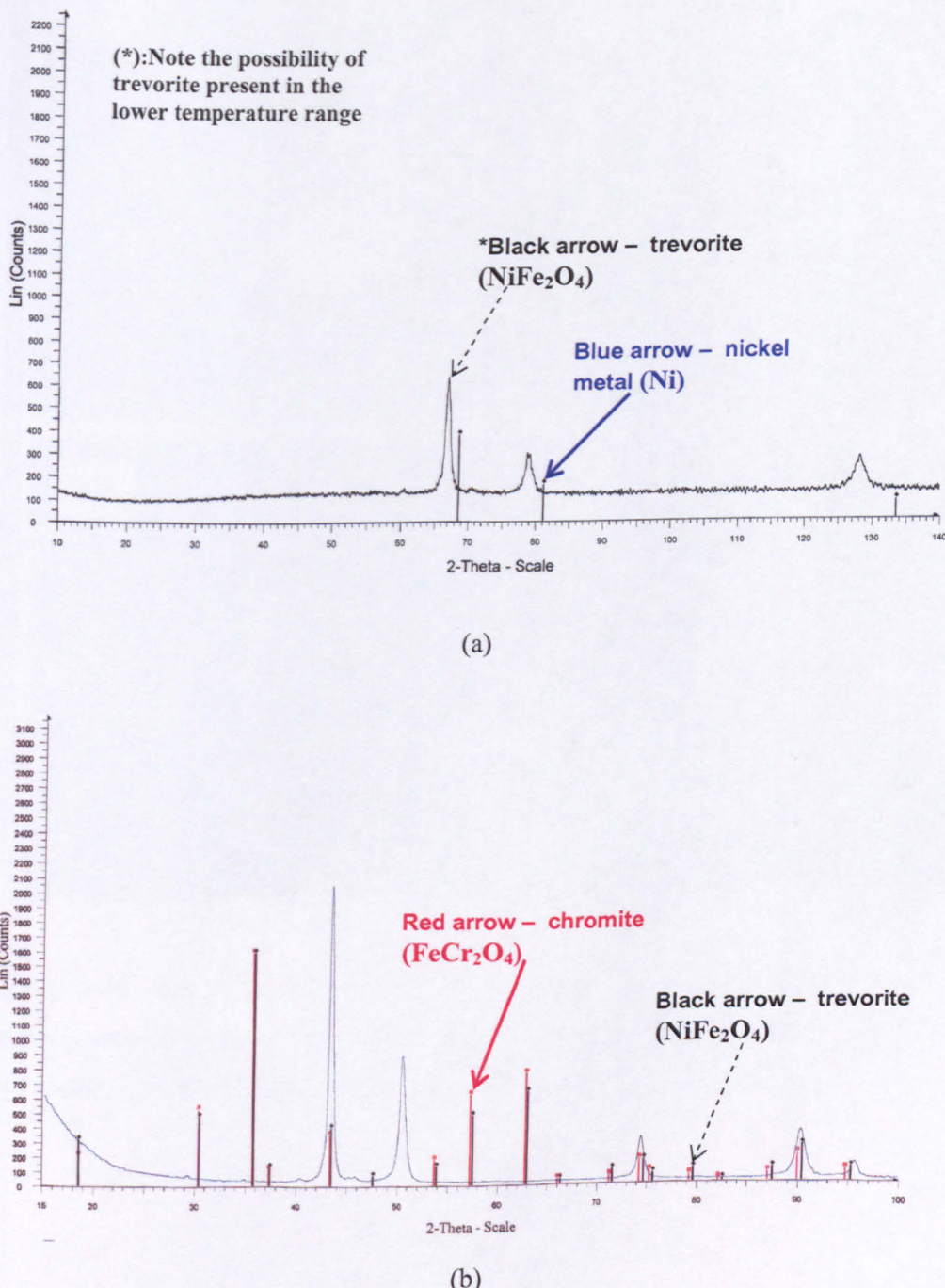


Figure 6-9: XRD detection of oxide phases corresponds to the 718 alloy wear debris: (a) at 22°C and (b) 450°C. Note that Figure 6-9(a) represents the XRD data for the 22°C, 150°C and 300°C cases (qualitatively similar).

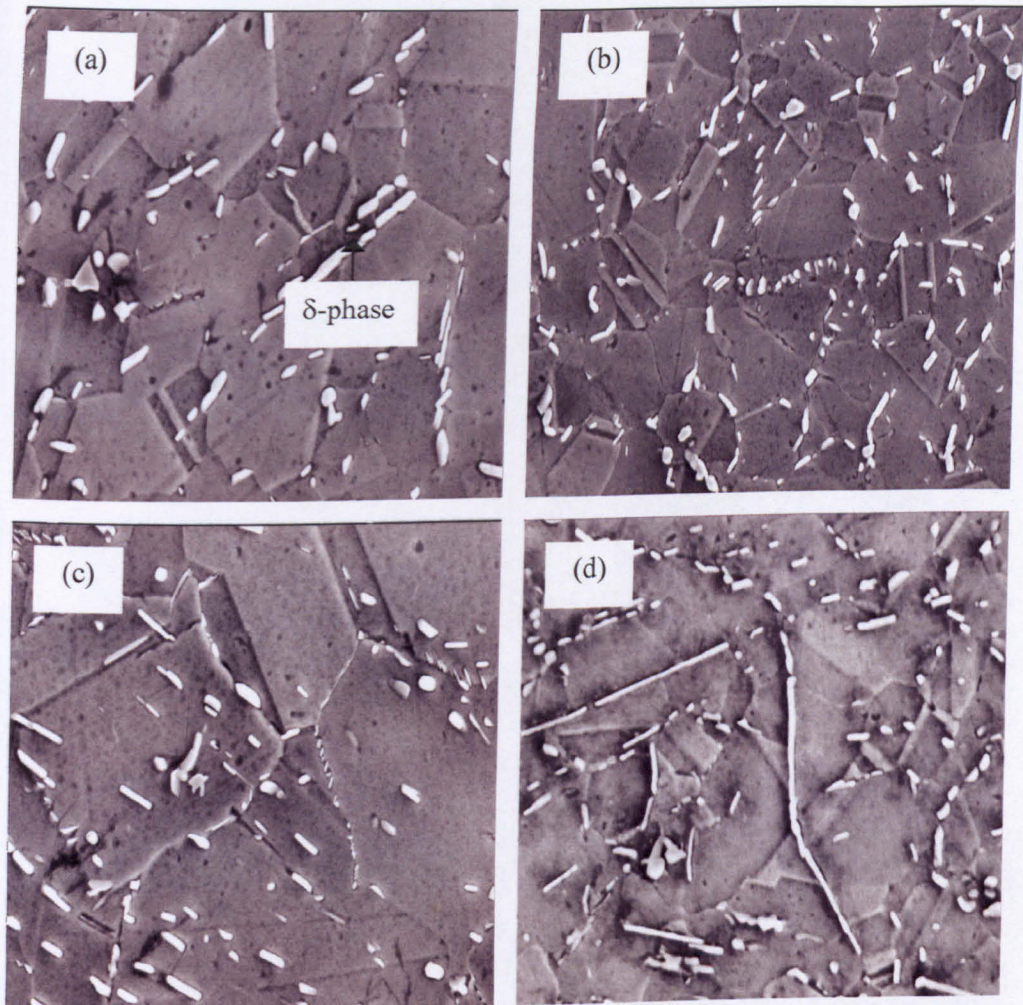


Figure 6-10: BEI of the  $\delta$  phase (white precipitate) versus temperature where the samples were taken from worn flat specimen and fretted for 2hours 47min : (a) 22°C, (b) 150°C, (c) 300°C, and (d) 450°C (refer to Table 6-1 for test conditions).

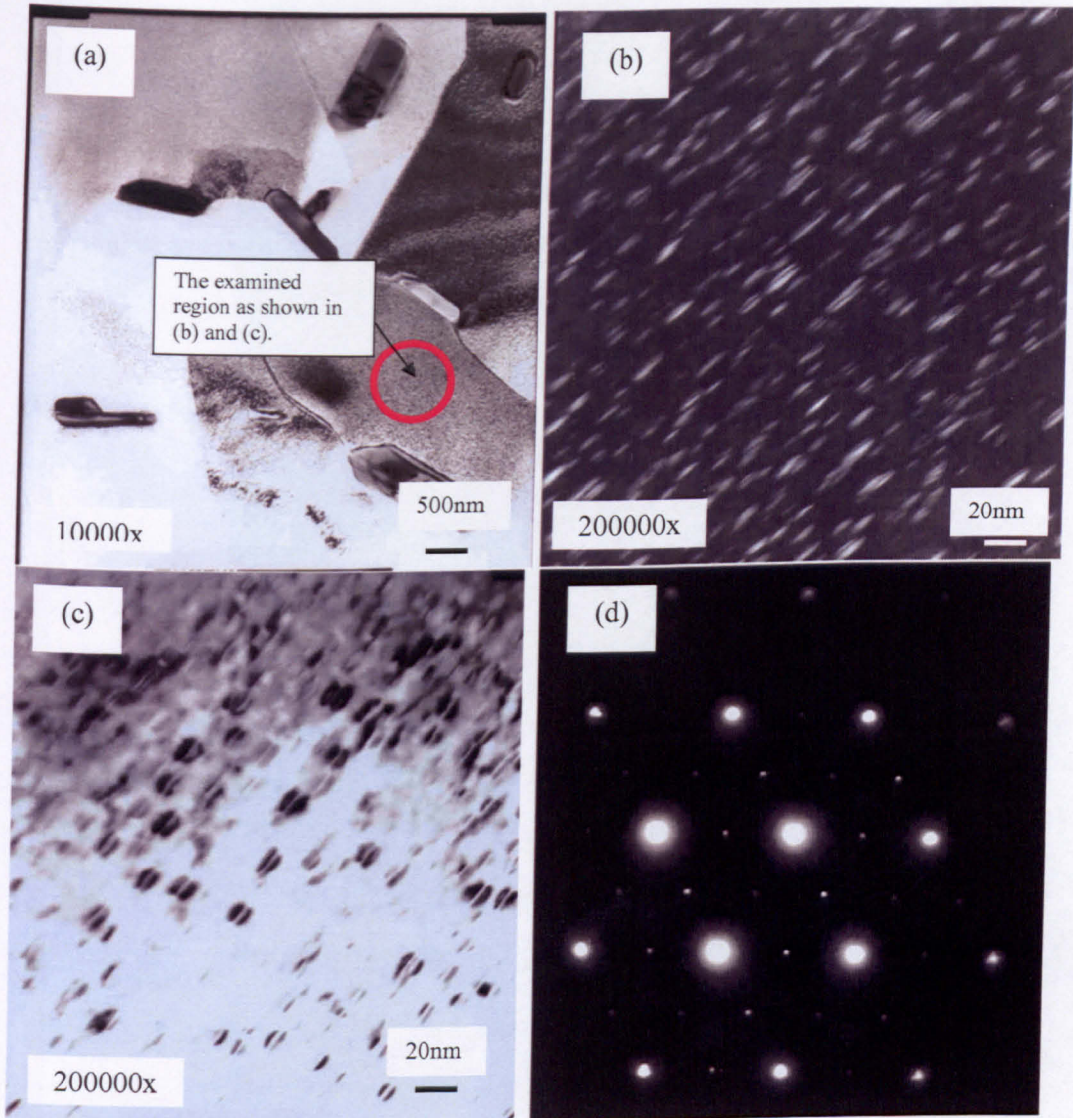


Figure 6-11: TEM micrographs of 718 alloy at 450°C: (a) General structure of 718 material, (b) Dark field image of  $\gamma''$ , (c) Bright field image of  $\gamma''$  and (d)  $\gamma''$  SAD patterns on the (111) plane.

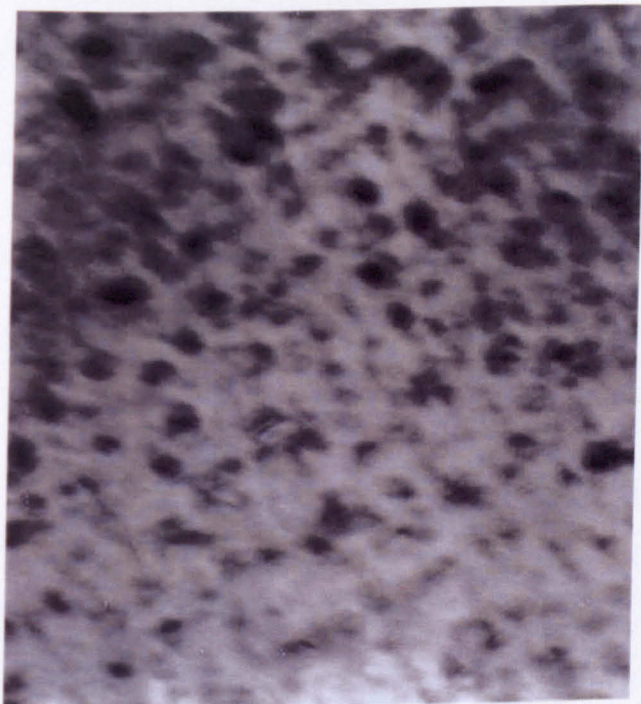


Figure 6-12: Bright field imaging of the  $\gamma'$  and  $\gamma''$  phases at 450°C (sample taken from a worn flat specimen).

---

## **Chapter 7: The effect of different material combinations on fretting wear**

---

### **7.1 INTRODUCTION**

Material capabilities have developed with engine technology, but the performance of current high performance materials are now reaching their limits. Better understanding of tribological behaviour of these materials will allow further improvement of existing properties. Therefore, the information will affect decision-making on safer employment of standard, cheaper, materials for higher stress levels. Furthermore, it may also be possible to control life cycle cost through the development of better lifing prediction methodologies.

This chapter investigates the fretting wear behaviour of three aeroengine transmission materials; Super S/CMV (SCMV), AerMet®100 (A100) and Inconel 718 (718) for the different material permutations, i.e. the counteracting bodies will be of self-against-self and self-against-nonself (dissimilar material) pairing types. These high performance materials were experimentally tested using a range of strokes (20 µm – 100 µm) and a constant applied load of 500 N. Microscopic examination on the wear scars was essential for identifying the level of wear damage corresponding to the different stroke regimes. The capability of the existing wear simulation to predict the fretting wear behaviour of dissimilar elastic bodies was tested. The chosen material permutation for this simulation was Super S/CMV against Inconel 718.

## **7.2 METHODS**

### **7.2.1 Materials and specimens**

The fretting specimen specifications and heat treatments were the same as listed in section 4.1 of Chapter 4.

### **7.2.2 Fretting tests**

The fretting tests were carried out using the specimen arrangement (Refer to section 4.2) and the test conditions summarized in Table 7-1. Tests were carried out using (i) self-against-self and (ii) self-against-nonsel. The materials tested were SCMV, A100 and 718. The experiments were undertaken to establish some understanding of the complex relationships between fretting wear and slip (stick/partial-sliding/sliding) regimes and the evolution/release of debris in the fretting interface. The initial Hertzian contact pressures for the different tests are listed in Table 7-2.

### **7.2.3 Characterisation**

The method used to investigate the microscopic changes were the same as described in section 4.3.2. Elemental analysis used the same method as in section 4.3.5.

## **7.3 RESULTS**

### **7.3.1 Coefficient of friction evolution**

The coefficient of friction (COF) data for the self-against-self (solid symbols) and self-against-nonsel (hollow symbols) tests showed two stages of behaviour, an initial 'run-in' period (Figures 7-1a, b, and c) followed by a more steady-state period (Table 7-3), regardless of material combinations. The plots showed the COF plateau after  $\approx$  5,000 wear cycles for both self-against-self and self-against-nonsel tests. Comparisons between the self-against-self and self-against-nonsel tests friction plots are categorised as a function of stroke as follows:

**a) Self-against-self versus self-against-nonsel at 20  $\mu\text{m}$  (Figure 7-1a)**

For the self-against-self test variations, the  $718_{(\text{f})}/718_{(\text{r})}$  pair has the highest COF, followed by the  $A100_{(\text{f})}/A100_{(\text{r})}$  pair and the  $SCMV_{(\text{f})}/SCMV_{(\text{r})}$  pair. There is a general increase in COF, from the initial ‘run-in’ period to the steady-state period. Friction values changed from 0.96 to 0.98 for the  $718_{(\text{f})}/718_{(\text{r})}$  pair, 0.72 to 0.84 for the  $A100_{(\text{f})}/A100_{(\text{r})}$  pair, and 0.64 to 0.69 for the  $SCMV_{(\text{f})}/SCMV_{(\text{r})}$  pair.

As for the self-against-nonsel test variations, the  $718_{(\text{f})}/A100_{(\text{r})}$  pair had the highest COF, followed by the  $SCMV_{(\text{f})}/718_{(\text{r})}$  pair and the  $SCMV_{(\text{f})}/A100_{(\text{r})}$  pair. Again, there is a general increase in COF. Friction values changed from 0.85 to 0.86 for the  $718_{(\text{f})}/A100_{(\text{r})}$  pair, 0.65 to 0.72 for the  $718_{(\text{f})}/A100_{(\text{r})}$  pair and 0.52 to 0.60 for the  $SCMV_{(\text{f})}/A100_{(\text{r})}$  pair.

Overall, the friction curves have shown the self-against-self test variations to have the highest COF at 20  $\mu\text{m}$  stroke.

**b) Self-against-self versus self-against-nonsel at 50  $\mu\text{m}$  (Figure 7-1b)**

As the stroke increased to 50  $\mu\text{m}$ , the  $718_{(\text{f})}/718_{(\text{r})}$  pair had the highest COF, followed by the  $SCMV_{(\text{f})}/SCMV_{(\text{r})}$  pair and the  $A100_{(\text{f})}/A100_{(\text{r})}$  pair. There was a general increase in COF, from the initial ‘run-in’ period to the steady-state period for the  $718_{(\text{f})}/718_{(\text{r})}$  pair and the  $A100_{(\text{f})}/A100_{(\text{r})}$  pair. Friction values changed from 1.02 to 1.05 and 0.62 to 0.71, respectively. For the  $SCMV_{(\text{f})}/SCMV_{(\text{r})}$  pair, the COF remained the same for the two friction periods, with a value of 0.69.

For the self-against-nonsel test variations, the  $SCMV_{(\text{f})}/718_{(\text{r})}$  pair has the highest COF, with friction values changing from 0.76 to 0.84. The  $SCMV_{(\text{f})}/A100_{(\text{r})}$  pair and

the  $718_{(f)}$ / $A100_{(r)}$  pair appeared to share similar COF values. Friction values changed from 0.75 to 0.76 and 0.67 to 0.76 respectively.

At 50  $\mu\text{m}$ , there is a significant narrowing of COF value boundaries (evolution positions) between the self-against-self and self-against-nonsel test variations. Note that the  $718_{(f)}$ / $718_{(r)}$  pair still exhibited the highest COF value.

**c) *Self-against-self versus self-against-nonsel at 100  $\mu\text{m}$***  (Figure 7-1c)

The friction curves are subdivided into two frictional boundaries of low and high COF. Again, there is a general increase in friction values, from the initial ‘run-in’ period to the steady-state period. For the low COF boundary, the  $A100_{(f)}$ / $A100_{(r)}$  pair, the  $SCMV_{(f)}$ / $A100_{(r)}$  pair, and the  $718_{(f)}$ / $A100_{(r)}$  pair appeared to share similar friction values from 0.54 to 0.61. For the high COF boundary, the  $718_{(f)}$ / $718_{(r)}$  pair, the  $SCMV_{(f)}$ / $SCMV_{(r)}$  pair, and the  $SCMV_{(f)}$ / $718_{(r)}$  pair reside in this region. The friction value for the  $718_{(f)}$ / $718_{(r)}$  pair increase from 0.83 to 0.91, with the  $SCMV_{(f)}$ / $SCMV_{(r)}$  pair and the  $SCMV_{(f)}$ / $718_{(r)}$  pair sharing similar values from 0.67 to 0.87.

### 7.3.2 Wear coefficient evolution

Tables 7-4a and b shows the calculated wear coefficient ( $k$ ) values of the various material pair permutations corresponding to the worn flat and round specimens.

**a) *Self-against-self test*** (Table 7-4a)

The  $k$  values for both flat and round specimens corresponding to three material pair variations were observed to increase, at least from one to three fold, with increasing stroke: from 1.56 to 2.55 for the  $SCMV_{(f)}$ / $SCMV_{(r)}$  pair, from 0.34 to 2.70 for the  $A100_{(f)}$ / $A100_{(r)}$  pair, and from 0.83 to 3.03 for the  $718_{(f)}$ / $718_{(r)}$  pair. Note that the

round specimen  $k$  values give similar trends to the flat specimen. However, it is difficult to know which material pair has the highest wear rate based on the given information.

**b) *Self-against-nonself test* (Table 7-4b)**

The increase of flat  $k$  values with stroke is from one to three fold: from 0.45 to 1.60 for the  $\text{SCMV}_{(f)}//\text{718}_{(r)}$  pair, from 0.16 to 0.75 for the  $\text{SCMV}_{(f)}//\text{A100}_{(r)}$  pair, and from 1.04 to 3.07 for the  $\text{718}_{(f)}//\text{A100}_{(r)}$  pair. Again, the round specimen  $k$  values give a similar trend to the flat specimens.

Overall, the data shows that the applied stroke has an effect on  $k$  but there is no dramatic difference between the  $k$  values of self-against-self pairs and self-against-nonself pairs.

### 7.3.3 Microscopic examination of wear scars

The secondary electron and backscattered-electron imaging modes were used to examine topographical changes of the wear scars, particularly the oxidised wear debris behaviour, i.e. level of retention or ejection during fretting wear. Note that the BEI of the worn round specimen for the self-against-self pairs are excluded from the analyses.

#### Self-against-self

**a) *Self-against-self – at 20  $\mu\text{m}$  stroke***

Figures 7-2a, b, and c showed the wear scars of the  $\text{SCMV}_{(f)}//\text{SCMV}_{(r)}$  pair, the  $\text{A100}_{(f)}//\text{A100}_{(r)}$  pair, and the  $\text{718}_{(f)}//\text{718}_{(r)}$  pair. It was noticed that the wear debris accumulated in two different regions. The wear debris is located in the centre and at the edges of the wear scars. In the centre region, the adhered debris appears compacted, while a mixture of compacted and loose debris was found at the edges

(Figures 7-2a and b). Figure 7-2c shows that the 718<sub>(f)</sub>//718<sub>(r)</sub> pair did not follow this pattern. Instead, the wear debris, which consists of a mixture of compacted and loose, was randomly scattered about the wear scar.

The adhered debris on the SCMV<sub>(f)</sub>//SCMV<sub>(r)</sub> pair wear scar had a relatively smooth morphology (Figure 7-2d); in contrast to the A100<sub>(f)</sub>//A100<sub>(r)</sub> pair and the 718<sub>(f)</sub>//718<sub>(r)</sub> pair (Figures 7-2e and f), the debris appeared particulate-like.

**b) *Self-against-self – at 50 μm stroke***

As the stroke magnitude increased to 50 μm, more and thicker debris layers were formed on the wear scar and these morphological characteristics were shared by the SCMV<sub>(f)</sub>//SCMV<sub>(r)</sub> pair, the A100<sub>(f)</sub>//A100<sub>(r)</sub> pair, and the 718<sub>(f)</sub>//718<sub>(r)</sub> pair (Figures 7-3a, b, and c). There was a possibility of material transfer occurring on the A100<sub>(f)</sub>//A100<sub>(r)</sub> pair and debris layer fracturing on the 718<sub>(f)</sub>//718<sub>(r)</sub> pair. However, in this stroke regime the wear debris appears less compacted. No evidence of severe wearing on the metal substrate is observed for any of the three alloys.

**c) *Self-against-self – at 100 μm stroke***

Figures 7-4a, b, and c shows the wear debris features of the SCMV<sub>(f)</sub>//SCMV<sub>(r)</sub> pair, the A100<sub>(f)</sub>//A100<sub>(r)</sub> pair, and the 718<sub>(f)</sub>//718<sub>(r)</sub> pair. The wear debris (Figure 7-4b) appeared to be discontinuous and semi-compacted. The whole of the wear scar was almost covered with uniformly distributed wear debris (Figure 7-4d). The worn metal substrate was protected by wear debris; the SEI shows mild wear markings on the metal substrate (Figure 7-4e).

### Self-against-nonself

#### a) *Self-against-nonself – at 20 µm stroke*

The BEIs (Figures 7-5 and 7-6) show the wear scars that correspond to the three self-against-nonself permutations that were fretted at 20 µm (both flat and round). Again, the debris appears to be fairly uniformly distributed. For the flat specimen of the SCMV<sub>(f)</sub>//718<sub>(r)</sub> pair, the local welded structure in Figure 7-5a suggests material transfer between the counteracting surfaces. The wear debris morphology of the SCMV<sub>(f)</sub>//718<sub>(r)</sub> pair consisted of a mixture of compacted and loose wear debris. Figure 7-5b shows uniform debris adhering (along the scar width) on the flat specimen of the SCMV<sub>(f)</sub>//A100<sub>(r)</sub> pair. This smooth appearance suggests a reasonable load-bearing region. More compacted wear debris is seen piling up at the contact edges on the worn flat specimen of the 718<sub>(f)</sub>//A100<sub>(r)</sub> pair (Figure 7-5c). Not also that the worn surface was more heavily scuffed than the other two test pairs. No evidence of severe metal substrate wearing was observed on the worn metallic substrate.

The BEIs (Figures 7-6a, b, and c) show patches of debris adhering along the scar length on the round specimens, with some form of discontinuity in the debris morphology. Also, the debris in Figure 7-6c showed signs of being fragmented from the existing compacted debris layer. The metal substrate appeared mildly worn.

#### b) *Self-against-nonself – at 50 µm stroke*

Fretting at the 50 µm gross-slip regime produces more wear debris on both the worn flat specimens and round specimens as shown by the sets of BEI in Figures 7-7 and 7-8. Figures 7-7a, b, and c showed the wear debris distribution corresponding to the worn flat specimens for the SCMV<sub>(f)</sub>//718<sub>(r)</sub> pair, the SCMV<sub>(f)</sub>//A100<sub>(r)</sub> pair, and the 718<sub>(f)</sub>//A100<sub>(r)</sub> pair. The wear debris was seen to be distributed into two regions,

compacted wear debris at the centre, loose debris at the edges. A possible material transfer site is present on the SCMV<sub>(f)</sub>//A100<sub>(r)</sub> pair (Figure 7-7b). No transferred material was found adhered on the 718<sub>(f)</sub>//A100<sub>(r)</sub> pair worn surface (Figure 7-7c).

The wear debris appears compacted on the wear track of the round specimens (Figures 7-8a, b, and c). The compacted wear debris is seen piling on the edges of the wear scar for the SCMV<sub>(f)</sub>//A100<sub>(r)</sub> pair (Figure 7-8b). The BEI of the 718<sub>(f)</sub>//A100<sub>(r)</sub> pair (Figure 7-8c) shows loose debris, possibly residing on the periphery of the scar width. No fractures were observed on the worn metal substrate of the self-against-nonsel f permutations.

### c) Self-against-nonsel f – at 100 µm stroke

At the longest stroke (100 µm), heavy debris adhered on the scar width/length of both round and flat specimens. Figures 7-9a, b, and c show the wear debris corresponding to the worn flat specimens of the SCMV<sub>(f)</sub>//718<sub>(r)</sub> pair, the SCMV<sub>(f)</sub>//A100<sub>(r)</sub> pair, and the 718<sub>(f)</sub>//A100<sub>(r)</sub> pair. The wear debris, which is uniformly distributed, appears semi-compacted and discontinuous (with minimal metal surface being exposed). The smooth debris bed adhered on the worn SCMV<sub>(f)</sub>//A100<sub>(r)</sub> pair suggests that material is being transferred from the counteracting body (Figure 7-9b). Figure 7-9c shows the attrition of wear debris from the existing compacted wear debris to form a new debris layer (the 718<sub>(f)</sub>//A100<sub>(r)</sub> pair). The wear debris on the worn round specimen appeared semi compacted (Figures 7-10a, b, and c). The metal substrate was mildly worn with no evidence of severe scuffing.

#### 7.3.4 Oxidised wear debris

The SEM micrographs (Figures 7-11a, b, and c) have identified three types of wear debris morphology. The observations are as follow:

*(i) Dense compacted wear debris (smooth feature) – Figure 7-11a*

*At 20  $\mu\text{m}$  stroke* - This morphological structure was observed on the wear scars corresponding to the  $\text{SCMV}_{(\text{f})}/\text{SCMV}_{(\text{r})}$  pair, the  $\text{SCMV}_{(\text{f})}/\text{718}_{(\text{r})}$  pair (worn round specimen), and the  $\text{SCMV}_{(\text{f})}/\text{A100}_{(\text{r})}$  pair (worn round specimen).

*(ii) Mixture of compacted and loose debris – Figure 7-11b*

*At 20 and 50  $\mu\text{m}$  strokes* - This morphological structure was observed on the wear scars for the three self-against-self material, i.e. the  $\text{SCMV}/\text{SCMV}$  pair, the  $\text{A100}_{(\text{f})}/\text{A100}_{(\text{r})}$  pair, and the  $\text{718}_{(\text{f})}/\text{718}_{(\text{r})}$  pair. As for the three self-against-nonselv pairs ( $\text{SCMV}_{(\text{f})}/\text{SCMV}_{(\text{r})}$ ,  $\text{A100}_{(\text{f})}/\text{A100}_{(\text{r})}$ ,  $\text{718}_{(\text{f})}/\text{718}_{(\text{r})}$ ), the worn specimens fretted at 50  $\mu\text{m}$  exhibited this feature.

*(iii) Semi-compacted wear debris (particulate-like) – Figure 7-11c*

*At 100  $\mu\text{m}$  stroke* – This characteristic was observed on the self-against-self and self-against-nonselv worn surfaces.

The microscopic cross-section examinations on the oxidised wear debris are shown in Figures 7-12a, b, and c; the photographs correspond to the different stroke regimes (20  $\mu\text{m}$ , 50  $\mu\text{m}$ , and 100  $\mu\text{m}$ ). Table 7-5 shows the averaged adhered debris thickness.

The observations are as follows:

- *20  $\mu\text{m}$*  – The wear debris was observed to be relatively thin at approximately 3  $\mu\text{m}$  thick (Figure 7-12a). However, cracks were seen propagating in two directions, namely, parallel to (near to) and normal (away from) to the contact surface. These characteristics were observed on the worn  $\text{SCMV}$  (Figure 7-13a) and  $\text{A100}$  alloys (Figure 7-13b).

- $50 \mu\text{m}$  – More compacted wear debris is retained within the scar (Figure 7-12b).  
The compacted wear debris layer was measured at about  $10\mu\text{m}$  thick. There was no sign of any surface cracks. These characteristics were observed on all three worn alloys.
- $100 \mu\text{m}$  – The wear debris was observed to be uniformly distributed along the wear scar (Figure 7-12c). The wear debris layer measured about  $5\mu\text{m}$  thick. There was no sign of any surface cracks present. These characteristics were observed on all three worn alloys.

### 7.3.5 EDX analysis

The worn surfaces of the flat and round specimens were analysed by the EDX method and the element compositions are shown in Tables 7-6a and b. The unworn surface was used as a reference point for the comparison work. Table 7-7 refers to the wear debris colour scheme. The analysis identified the presence of oxygen on all of the material permutations. All the pairs had iron and nickel elements within the oxides. Traces of niobium were found on both worn surfaces of the  $718_{(f)}/\text{A}100_{(r)}$  pair while cobalt was present in the  $\text{SCMV}_{(f)}/\text{A}100_{(r)}$  pair and the  $718_{(f)}/\text{A}100_{(r)}$  pair.

## 7.4 DISCUSSION

### a) *The effect of stroke and material on wear*

In the first 5000 wear cycles, it was difficult to determine any frictional trends from the fretting tests. This was because time is needed for the contact surface to stabilise and for the settlement of wear debris on the wear track. This explains the absence of clear trends in the COF plots. The wear results, which include the COF and  $k$  values, show that the effect of stroke on wear is greater than the effect of material, i.e. just like Vingsbo and Soderberg [1, 2] reported. Once wear reaches a steady-state

condition, two trends were identified (refer to Table 7-3) : (i) Trend I: COF increases with stroke (typical) and (ii) Trend II: COF decreases with stroke. These tribological characteristics may be attributed to structural changes of the debris as seen on the BEIs:-

- *Trend I*

This characteristic is exhibited by both the SCMV<sub>(f)</sub>//SCMV<sub>(r)</sub> pair and the SCMV<sub>(f)</sub>//718<sub>(r)</sub> pair. It is believed that the behaviour of the adhered debris affects its establishment on the worn surface and, hence the different frictional trends. For smaller strokes, the wear debris are not easily removed from this regime and the sliding distance is limited (Figure 7-1a). However, this limitation increases the probability of more wear debris being well compacted (deformed) and hence the formation of a smooth layer – the patches of compacted wear debris adhered at the centre point of the wear scar. As the stroke increases, this reduces the probability of wear debris entrapment and increases the local contact distance between loose wear debris. Therefore, the wear debris layer appeared semi compacted during microscopic examination. Moreover, the loose debris may act as an abrasive to cause further wear damage during fretting (Figures 7-3 and 7-4). However, if the contacting surfaces were of different materials, this would depend on the tribological properties of each material and its effect on wear. Mutual solubility of the materials forming the wear pair also has an effect; the greater the solubility, the greater the level of adhesion [3]. The EDX data showed high traces of iron associated with the SCMV alloy, more than the 718 alloy. Therefore, the SCMV alloy may be wearing more than the 718 alloy. However, the COF data for the SCMV<sub>(f)</sub>//718<sub>(r)</sub> pair is higher than that of the SCMV<sub>(f)</sub>//SCMV<sub>(r)</sub> pair. The topographical features, as seen in Figure 7-7b,

suggest that there is a possibility of wear debris layer detachment from the wear scar; the detached layer may act as an abrasive causing more detrimental wear damage.

- Trend II

This characteristic is exhibited by both the A100<sub>(f)</sub>//A100<sub>(r)</sub> pair and the 718<sub>(f)</sub>//A100<sub>(r)</sub> pair. The adhered wear debris did not show any dramatic changes, with respect to the A100<sub>(f)</sub>//A100<sub>(r)</sub> pair. The microscopic examination, however, did reveal a semi compacted wear debris layer, which is seen for the three strokes (Figures 7-3 and 7-4). Another topographical feature was the severely delaminated surface, which could possibly indicate material transfer from one contact surface to the other. The wear profiles confirmed the occurrence of this (Figure 7-14e), showing a collection of high-rise or rough profiles at the periphery; perhaps wear took place on the localised-welded region (small contact area) and the inflicted damage is therefore minimal. This would explain the low friction measurement recorded.

The 718<sub>(f)</sub>//A100<sub>(r)</sub> pair shared similar topographical features as the above case. The EDX data did clearly confirm that there was material transfer from the A100 surface (10.1 mass% of cobalt) to the 718 surfaces (7.4 mass% of cobalt) – cobalt is an important alloying element of A100. This clearly indicates that A100 is a primary source for wear debris production and controlling wear. There are two possible explanations for the tribological behaviour with respect to the Trend II:

- The presence of load-bearing wear debris. The EDX identified the presence of iron, chromium, and nickel in the composition [4] (section 7.3.5).
- Surface damage might have taken place locally on the compacted wear debris layer as the area of exposed metallic surface is limited, thereby preventing direct metal-to-metal contact. With some of the load shared by the oxides, the surface damage level in the metallic substrate and presumably the COF is lowered.

The 718 alloy appears to wear relatively rapidly compared to the SCMV alloy and A100 alloy i.e. greater surface damage and possible early stage of cracking. From the SEM micrograph, it is apparent that the adhered debris layers are prone to fracture and readily detach from the wear scar (Figure 7-2c). This characteristic was observed for all three strokes . Fragmentation of the compacted debris layer produces loose wear debris that may cause further wear of the protective layers. This has a damaging consequence, as direct metal-to-metal contact increases. 718 alloy is known to have poor tribological properties at room temperature due to the type of oxide phases formed [5]; the oxide phases were not of glaze oxides compositions. With the  $\text{SCMV}_{(f)}//\text{A100}_{(r)}$  pair (lowest COF), the A100 is likely to be the contributing material during wear and traces of cobalt were found transferred onto the SCMV surface. The low COF may be attributed to the load-carrying behaviour of the oxide as explained earlier.

Nonetheless, the stick-slip regime has been identified to be at the 20  $\mu\text{m}$  stroke (Figures 7-1a and b), with the cracks seen propagating away from the fretted surface.

**b) The effect of stroke on wear coefficient**

In Table 7-4,  $k$  is seen to increase with the stroke. According to the Archard wear equation,  $k$  is independent of the stroke, i.e. the larger the stroke, the more material removal. More debris is likely to escape easily with larger strokes; this increases the metal-to-metal contact area causing more debris formation, and hence, more surface wear. The BEIs (e.g. Figures 7-4, 7-8, and 7-10) show more debris adhering on the wear scar with increasing stroke. The effect of materials on the wear is less marked at higher stresses and this observation is seen on both the self-against-self and self-against-nonself pairs (sharing similar  $k$  values). The flat and round specimens involved in the self-against-nonself pair show negligible material influence on  $k$  value as well. This shows that using different materials for the flat and round specimens did not alter the wear rate.

**c) The effect of stroke on debris role**

The profiles show possible material build-up on the worn flat specimen of the A100//A100 pair and the 718//718 pair (Figures 7-14c and e), accumulating at the centre and the periphery of the scar width, respectively. The flat surface of the SCMV<sub>(f)</sub>//A100<sub>(r)</sub> pair (Figure 7-15c) had debris adhering on the centre region, while debris accumulated on the periphery area of the 718<sub>(f)</sub>//A100<sub>(r)</sub> pair flat specimen (Figure 7-15e). These characteristics are shared by some of the self-against-nonself material pairs, such as the SCMV<sub>(f)</sub>//718<sub>(r)</sub> pair (Figure 7-15a and b), which has a smooth wear depth profile like the SCMV<sub>(f)</sub>//SCMV<sub>(r)</sub> pair.

The type of wear mechanisms determines the role of debris retention in fretting. Two possible wear mechanisms, namely adhesive wear and abrasive oxidative wear, contribute to the damage. The microscopic examinations (Figures 7-3 and 7-7b) and

surface profiles (debris accumulation) indicated the presence of local-welding areas and potentially a damage initiation site. If this debris layer is strongly adhered to the underlying substrate, relative movement is restricted as well as surface damage; i.e. low COF. The A100 alloy seemed to be the material that displays the aforementioned characteristics. If, however, this welding point is severed, wear debris detachments are expected and the fragmented debris may embed itself in a softer layer. This configuration may act like an abrasive tool slowly gouging the surface, causing further damage to the contact surface. 718 alloy debris layers are susceptible to fracture and this was confirmed by the SEM images in Figures 7-4, which explain the high wear values. Varenberg et al. [6] have studied the role of debris in fretting wear. They have reported that with adhesive wear, the oxide debris acts like a solid lubricant, to reduce the damage caused by fretting. If abrasive wear predominates, the oxide debris will facilitate further wear damage. Also, this could affect the transition period from severe wear to mild wear as well. If the wear debris is well compacted and acquires a solid morphology, it will only take about 20% of this physical protection to minimise surface damage [7]. The type of oxide phase is crucial in determining the lifespan of this layer. The counteracting material composition plays an important role in production of the oxide phase of load-bearing capability.

#### ***d) Finite element prediction versus experimental***

The experimental data of the SCMV<sub>(f)</sub>/718<sub>(r)</sub> pair was validated by running the fretting wear simulation for 100,000 number of cycles. The contact pressure distribution versus number cycles and the FE-predicted wear depth/width were plotted (Figures 7-16a and b). The contact pressure quickly subsided into a uniform distribution as fretting wear proceeds. However, this change does not contribute much

to the surface wearing because of its low pressure. Therefore, it is likely that surface damage is governed by another source of surface stresses. The FE-prediction overestimated the wear width by 45%  $\mu\text{m}$  while it underestimated the wear depth by 30  $\mu\text{m}$  compared to the measurements from both the surface profile and BEI micrograph. The measured wear width and wear depth was 550  $\mu\text{m}$  and 7.5  $\mu\text{m}$ , respectively. The differences between predicted and measured scar dimensions can be attributed to the fact that the FE simulation tool does not incorporate the presence of debris during fretting wear and utilises a steady-state COF.

## **7.5 Summary**

Based on the investigation and the information given, the effect of stroke is greater than that of material on the COF and  $k$  values. The 718 alloy has relatively poor wear-resistance at room temperature while the A100 alloy exhibits desirable tribological characteristics. The local-welding points provide potential sites for adhesive wear and/or abrasive wear initiation. Ultimately, it will be the role of the debris to accommodate and protect the contact surface in the longer term. The FE simulation tool is an effective method to validate experimental results but further modification is required.

## **References**

1. O. Vingsbo and S. Soderberg, "Wear of Materials", 1987, *ASME*, pp. 885-894
2. O. Vingsbo and S. Soderberg, "On Fretting Maps", *Wear*, 1988, Vol. 126, pp. 131-147

3. I. A. Inman, P. K. Datta, H. L. Du, J. S. Burnell-Gray, S. Pierzgalski and Q. Luo, "Studies of high temperature sliding wear of metallic dissimilar interfaces", *Tribo. Int.*, Vol. 38 (9), September 2005, pp. 812-823
4. Ch. Colombie, Y. Berthier, A. Flouter, L. Vincent, and M. Godet, " Fretting: Load Carrying Capacity of Wear Debris", *Journal of Tribology*, 1984, Vol. 106, pp. 194-201
5. G. Beranger and M. Lanthesir, "Oxidation of Iron-Nickel alloy", pp. 223-237
6. Varenberg, M., et al., "The different aspects of the role of wear debris in fretting wear", *Wear*, 252, 2002, 902-910
7. J. Jiang, F. H. Stott, and M. M. Stack, "The Role of Triboparticles in Dry Sliding Wear", *Tribo. Int.*, Vol. 31 (5), 1998, pp. 245-256

Table 7-1: Fretting test conditions.

<b>Contact load</b>	500 N
<b>Stroke</b>	20 µm; 50 µm; 100 µm
<b>Frequency</b>	20 Hz
<b>Number of cycles</b>	100,000
<b>Room temperature</b>	14-20°C
<b>Relative humidity</b>	40-55%
<b>Material</b>	SCMV; A100; 718

Table 7-2: Initial maximum Hertzian stress.

Hertzian stress (MPa)			
Self-against-self		Dissimilar	
Case	Stress	Case	Stress
SCMV <sub>(f)</sub> //SCMV <sub>(r)</sub>	539	SCMV <sub>(f)</sub> //718 <sub>(r)</sub>	547
A100 <sub>(f)</sub> //A100 <sub>(r)</sub>	532	SCMV <sub>(f)</sub> //A100 <sub>(r)</sub>	536
718 <sub>(f)</sub> //718 <sub>(r)</sub>	554	718 <sub>(f)</sub> //A100 <sub>(r)</sub>	543

\* (f) and (r) are the flat and round specimens, respectively.

Table 7-3: The steady-state COF (after 5,000 cycles) for the various material pairs at 500 N tested for a duration of 100,000 cycles.

Stroke (µm)	SCMV <sub>(f)</sub> // SCMV <sub>(r)</sub>	A100 <sub>(f)</sub> // A100 <sub>(r)</sub>	718 <sub>(f)</sub> // 718 <sub>(r)</sub>	SCMV <sub>(f)</sub> // 718 <sub>(r)</sub>	SCMV <sub>(f)</sub> // A100 <sub>(r)</sub>	718 <sub>(f)</sub> // A100 <sub>(r)</sub>
20	0.69	0.84	0.98	0.72	0.60	0.86
50	0.79	0.71	1.05	0.84	0.76	0.73
100	0.83	0.61	0.91	0.87	0.61	0.56

Table 7-4: (a) The averaged wear coefficient data of the self-against-self pairs and (b) self-against-nonsel pairs fretted at 500 N and 100,000 cycles as a function of stroke.

Stroke (μm)	Wear coefficient - $k \times 10^8$ (MPa $^{-1}$ )					
	SCMV//SCMV		A100//A100		718//718	
	Flat	Round	Flat	Round	Flat	Round
20	1.56	0.98	0.34	0.31	0.83	0.79
50	1.78	2.12	1.01	3.12	1.03	0.73
100	2.55	2.18	2.79	3.84	3.02	1.77

(a)

Stroke (μm)	Wear coefficient - $k \times 10^8$ (MPa $^{-1}$ )					
	SCMV <sub>(f)</sub> //718 <sub>(r)</sub>		SCMV <sub>(f)</sub> //A100 <sub>(r)</sub>		718 <sub>(f)</sub> //A100 <sub>(r)</sub>	
	Flat	Round	Flat	Round	Flat	Round
20	0.45	0.56	0.16	0.33	1.04	1.66
50	1.03	0.68	1.17	1.51	1.23	2.14
100	1.60	2.68	0.75	4.02	3.07	4.00

(b)

Table 7-5: Loose wear debris colours collected from the fretting test.

Observation	SCMV <sub>(f)</sub> //SCMV <sub>(r)</sub>	A100 <sub>(f)</sub> //A100 <sub>(r)</sub>	718 <sub>(f)</sub> //718 <sub>(r)</sub>
	Reddish brown	Dark grey	Dark brown
	SCMV <sub>(f)</sub> //718 <sub>(r)</sub>	SCMV <sub>(f)</sub> //A100 <sub>(r)</sub>	718 <sub>(f)</sub> //A100 <sub>(r)</sub>
	Reddish brown	Dark brown	Dark brown

Table 7-6: EDX analyses of the worn surfaces (mass%): (a) Self-against-self pairs and (b) self-against-nonsel pairs.

Elements	SCMV <sub>(f)</sub> //SCMV <sub>(r)</sub>	A100 <sub>(f)</sub> //A100 <sub>(r)</sub>	718 <sub>(f)</sub> //718 <sub>(r)</sub>
<b>Fe</b>	71.3	17.3	17.3
<b>Ni</b>	0.3	55.5	55.5
<b>V</b>	0.3	-	-
<b>Nb</b>	-	5.1	5.1
<b>Co</b>	-	11.5	5.0
<b>O</b>	23.9	21.9	22.6

(a)

Elements	SCMV <sub>(f)</sub> //718 <sub>(r)</sub>		SCMV <sub>(f)</sub> //A100 <sub>(r)</sub>		718 <sub>(f)</sub> //A100 <sub>(r)</sub>	
	Flat	Round	Flat	Round	Flat	Round
<b>Fe</b>	69.7	53.2	75.9	76.1	21.9	57.7
<b>Ni</b>	1.08	10.8	9.1	7.8	42.7	7.7
<b>V</b>	0.4	0.2	0.4	-	-	-
<b>Nb</b>	-	7.4	-	-	3.5	4.8
<b>Co</b>	-	-	1.0	2.0	7.4	10.1
<b>O</b>	26.6	27.1	13.0	13.1	17.9	16.7

(b)

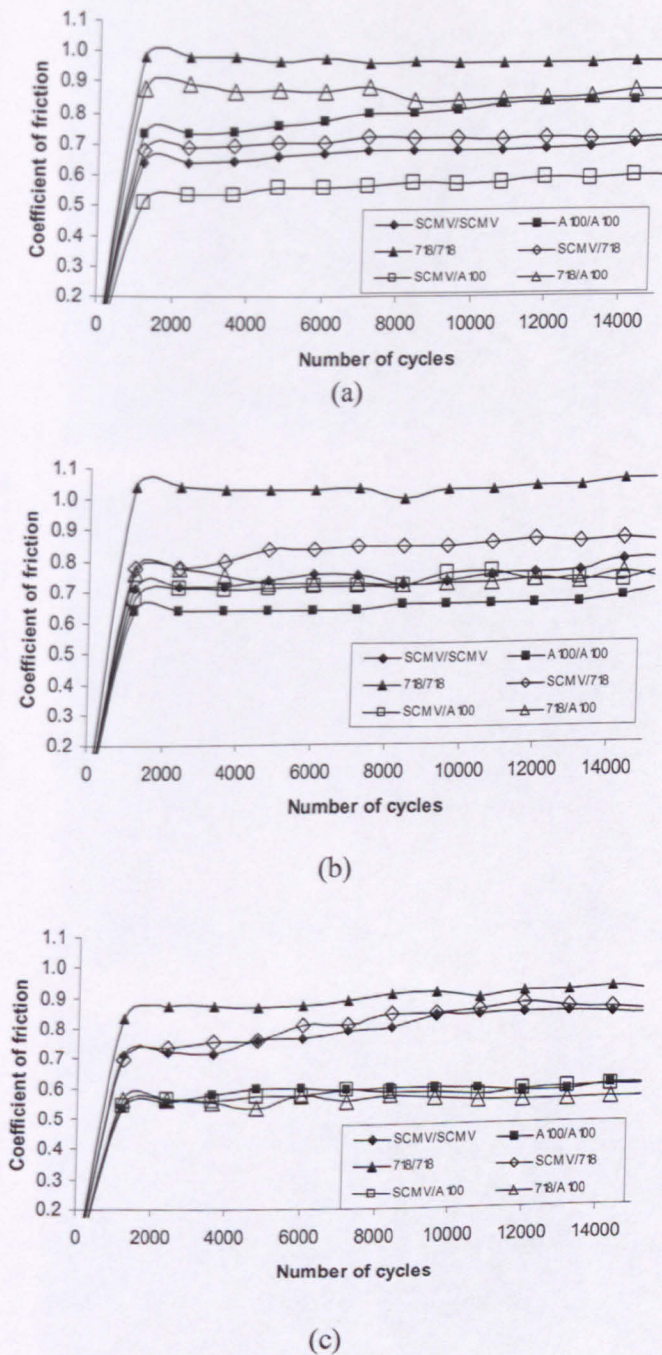
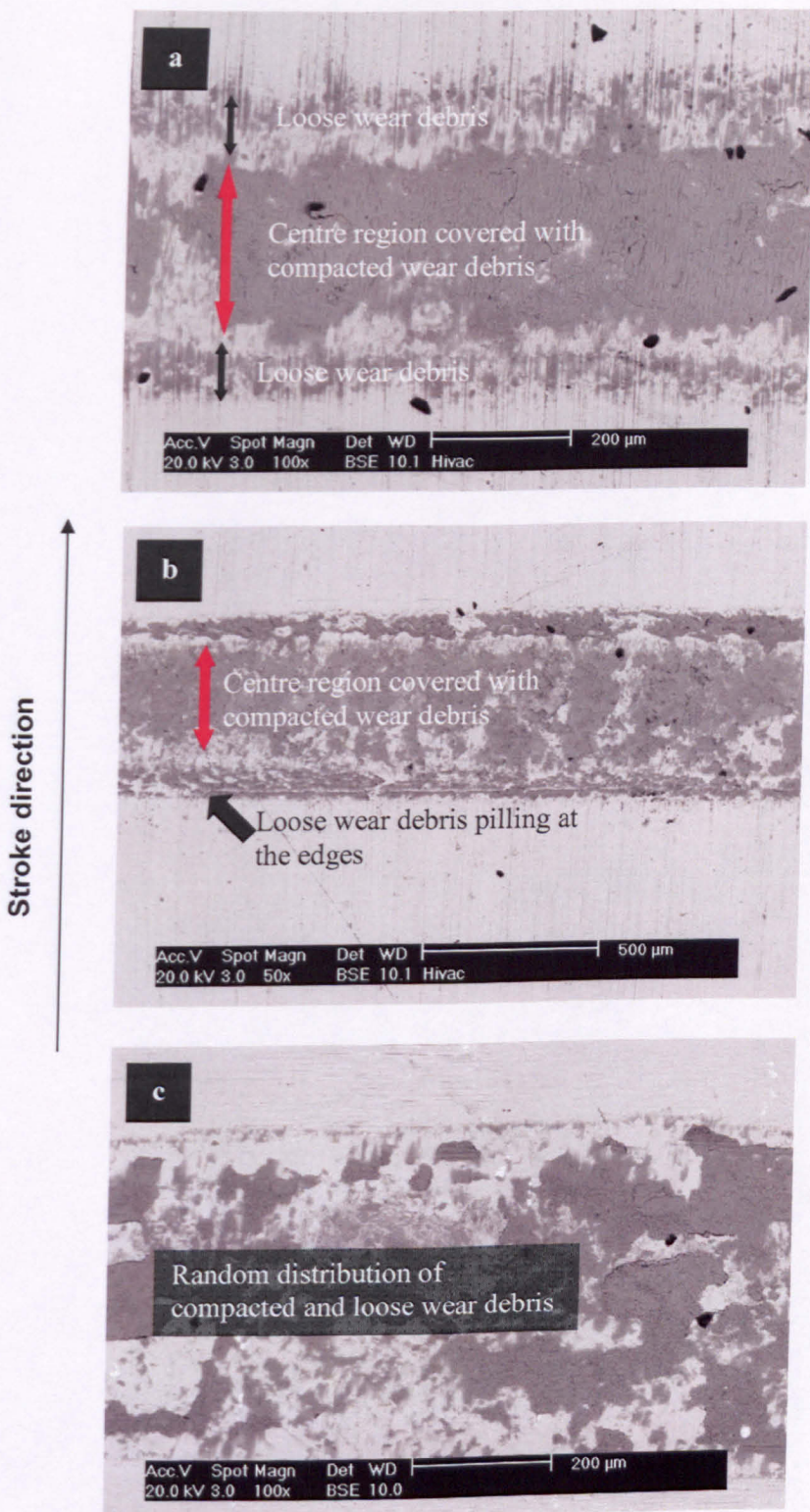
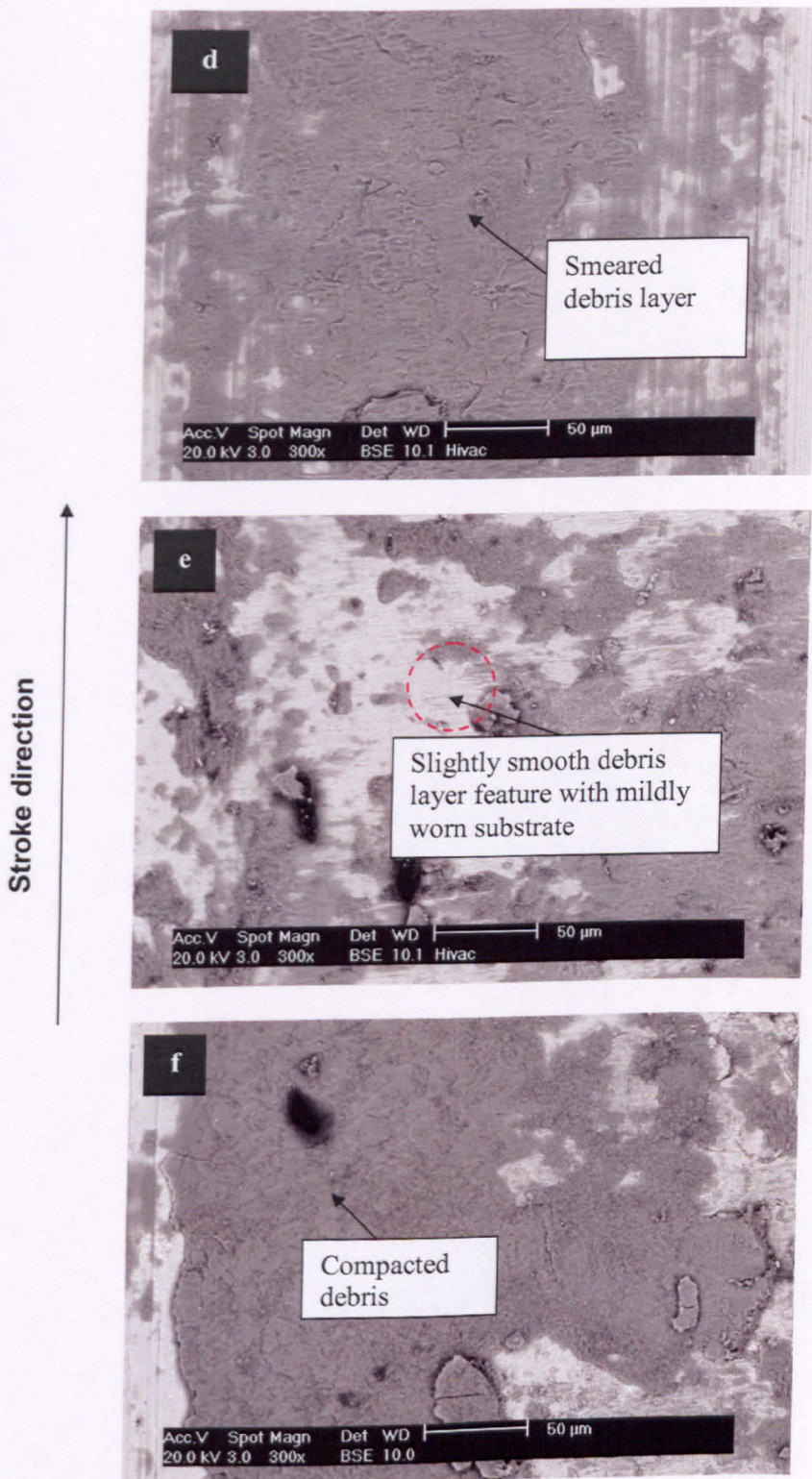


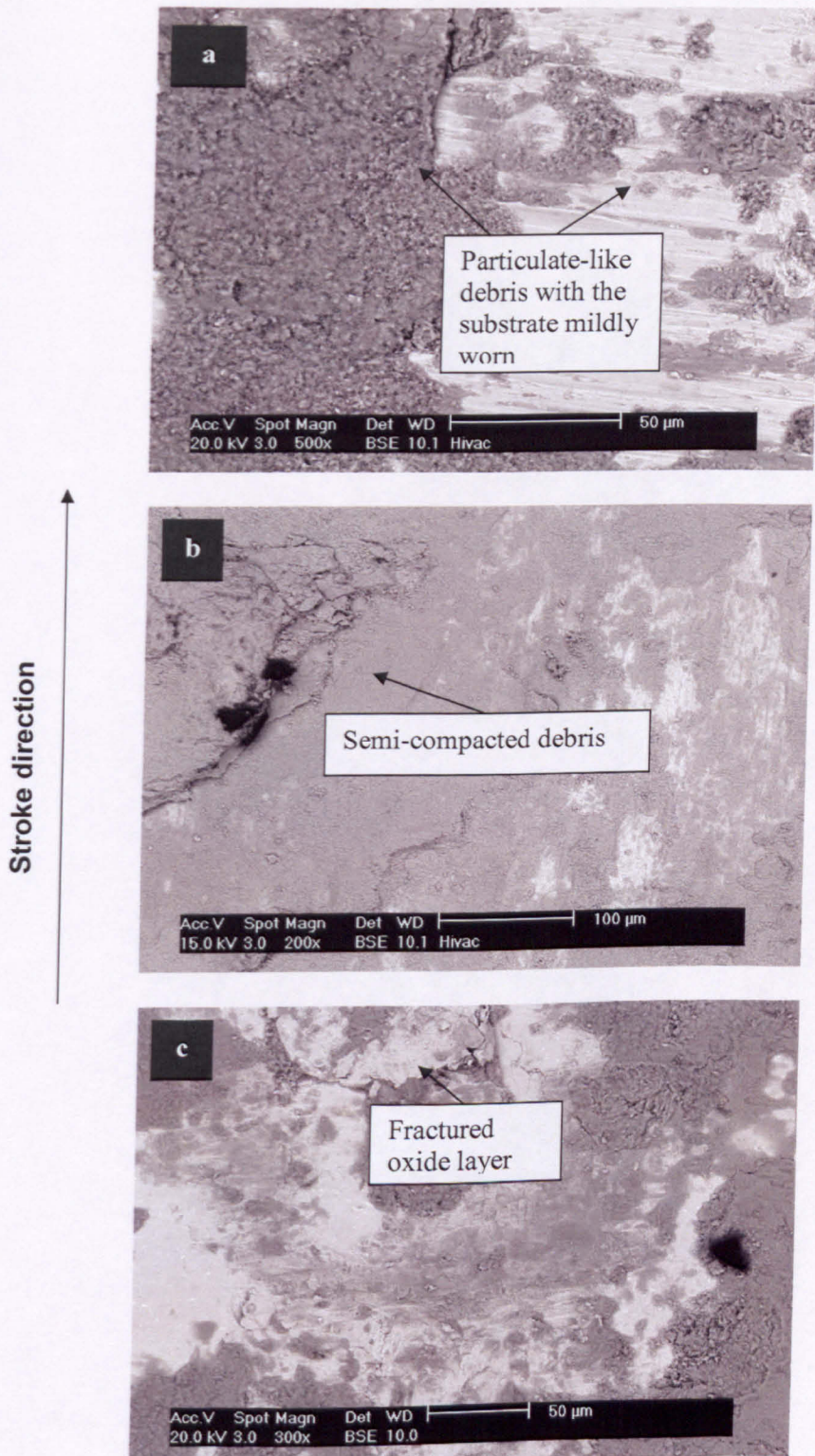
Figure 7-1: The initial ‘run-in’ period of COF evolutions from the 100,000 cycles for the self-against-self and self-against-nonslef pairs at strokes of: (a) 20  $\mu\text{m}$ , (b) 50  $\mu\text{m}$ , and (c) 100  $\mu\text{m}$  (Refer to Table 7-1 for the test conditions).



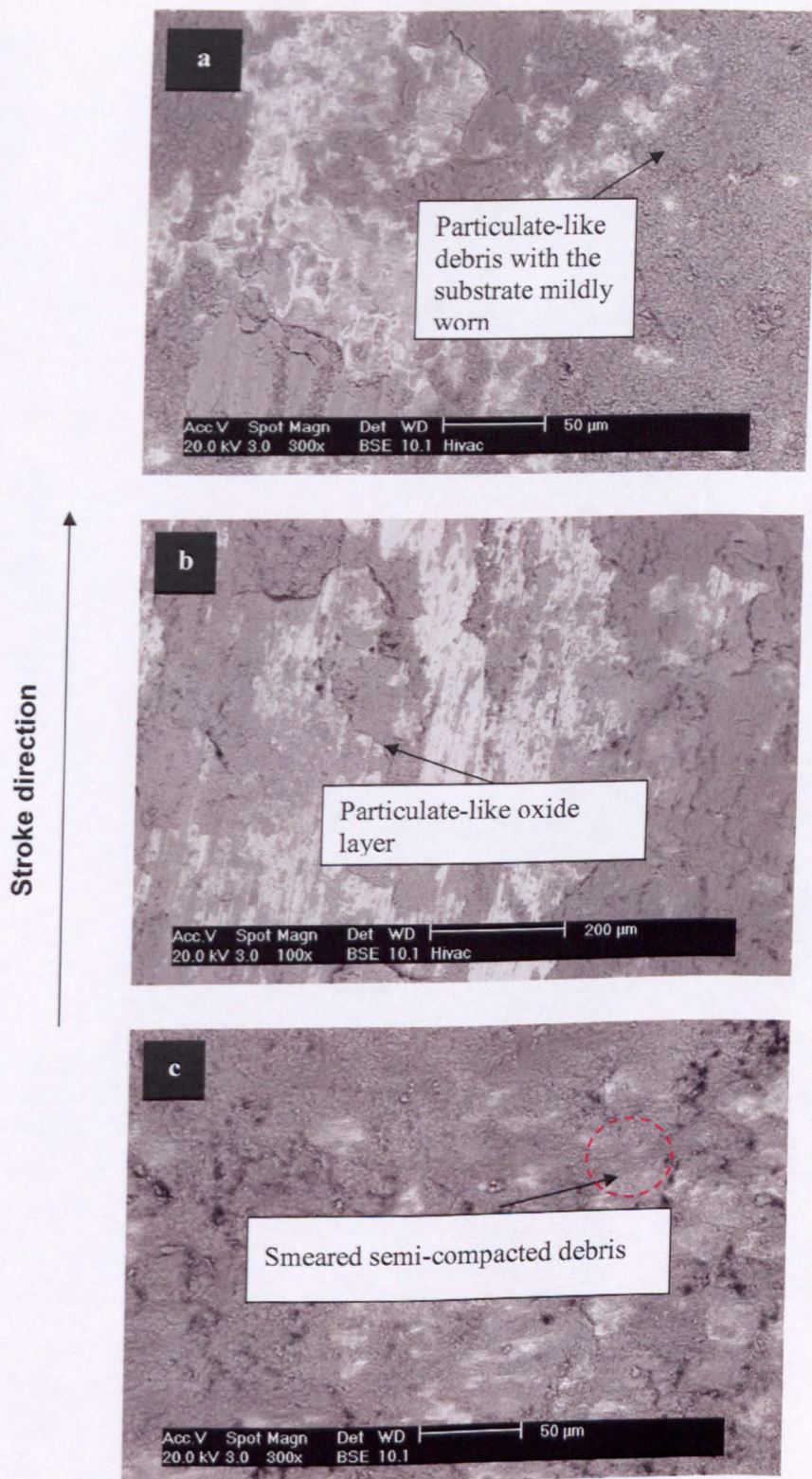
Figures 7-2 (cont'd): The backscattered images (BEI) of the worn surface tested and wear debris morphology at 20  $\mu\text{m}$ , 500 N and 100,000 cycles: (a) SCMV<sub>(f)</sub>//SCMV<sub>(r)</sub>, (b) A100<sub>(f)</sub>//A100<sub>(r)</sub>, and (c) 718<sub>(f)</sub>//718<sub>(r)</sub> (refer to Table 7-1 for the test conditions).



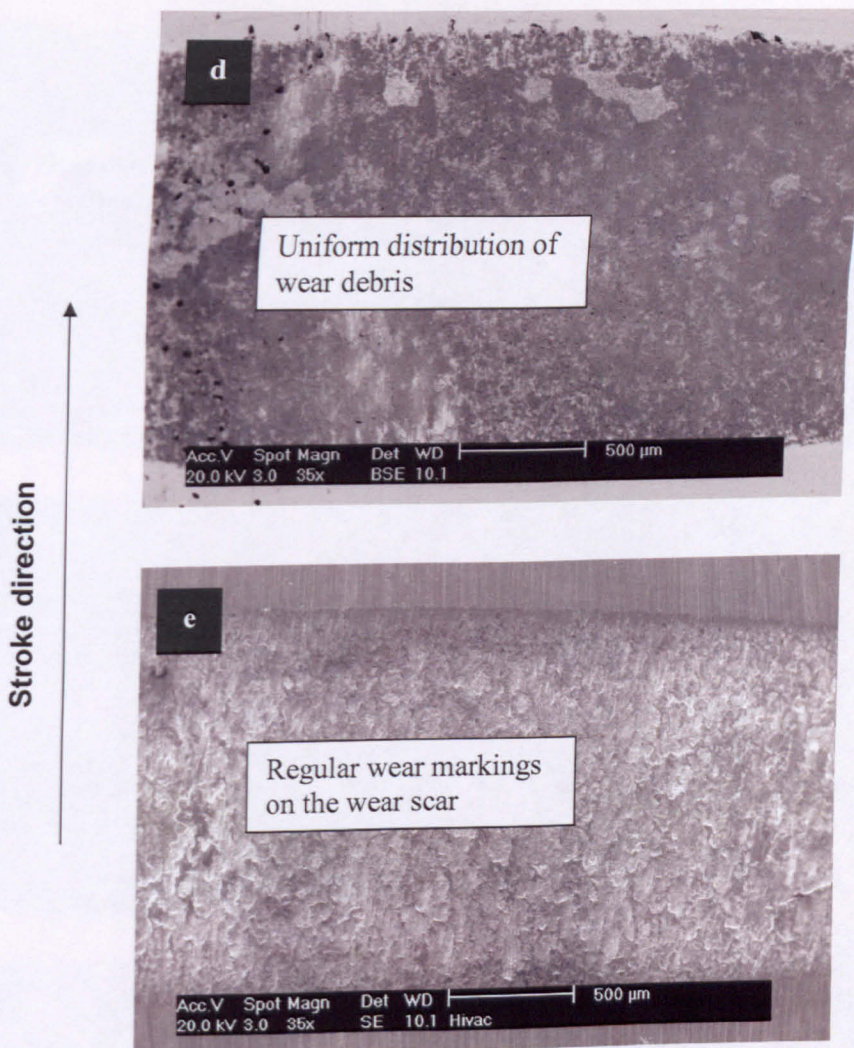
Figures 7-2: The backscattered images (BEI) of the worn surface tested and wear debris morphology at 20 µm, 500 N and 100,000 wear cycles: (d) SCMV<sub>(f)</sub>/SCMV<sub>(r)</sub>, (e) A100<sub>(f)</sub>//A100<sub>(r)</sub>, and (f) 718<sub>(f)</sub>//718<sub>(r)</sub>.



Figures 7-3: Backscattered images (BEI) of the worn surface tested at 50  $\mu\text{m}$ , 500 N and 100,000 cycles: (a)  $\text{SCMV}_{(\text{f})}/\text{SCMV}_{(\text{r})}$ , (b)  $\text{A}100_{(\text{f})}/\text{A}100_{(\text{r})}$ , and (c)  $718_{(\text{f})}/718_{(\text{r})}$ .



Figures 7-4 (cont'd): The backscattered images (BEI) of the worn surface tested at 100 µm, 500 N and 100,000 cycles: (a)  $\text{SCMV}_{(\text{f})}/\text{SCMV}_{(\text{r})}$ , (b)  $\text{A}100_{(\text{f})}/\text{A}100_{(\text{r})}$ , and (c)  $718_{(\text{f})}/718_{(\text{r})}$ .



Figures 7-4: (d) The backscattered image (BEI) showing uniform distribution of the wear debris on the wear scar at 100  $\mu\text{m}$ , and (e) the secondary image (SEI) showed the worn surface to have worn surface to have regular wear topography feature.

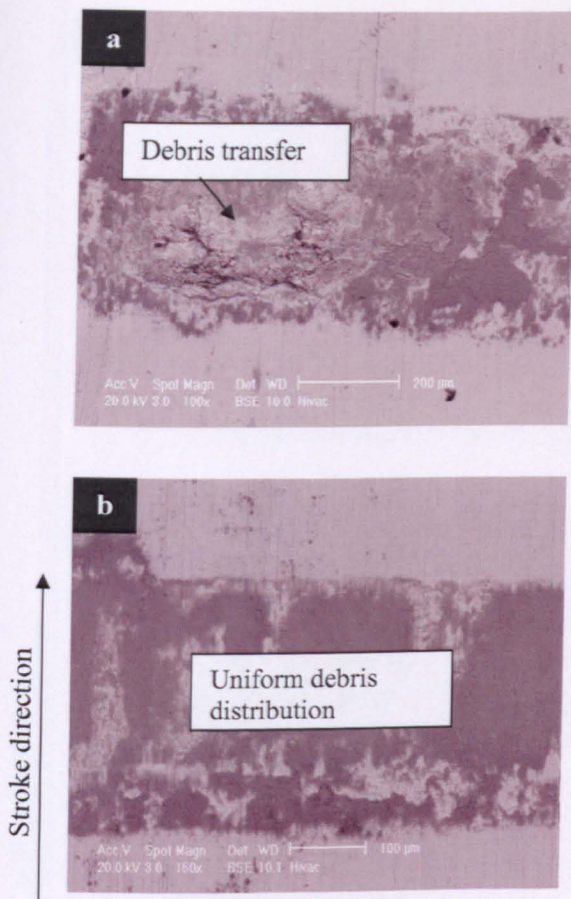


Figure 7-5: BEI of the worn areas on the flat specimens at a stroke of 20  $\mu\text{m}$ :

- End of contact edge ( $\text{SCMV}_{(f)}//718_{(r)}$ ).
- Along all scar length ( $\text{SCMV}_{(f)}//A100_{(r)}$ ).
- Contact edges along scar width ( $718_{(f)}//A100_{(r)}$ ).

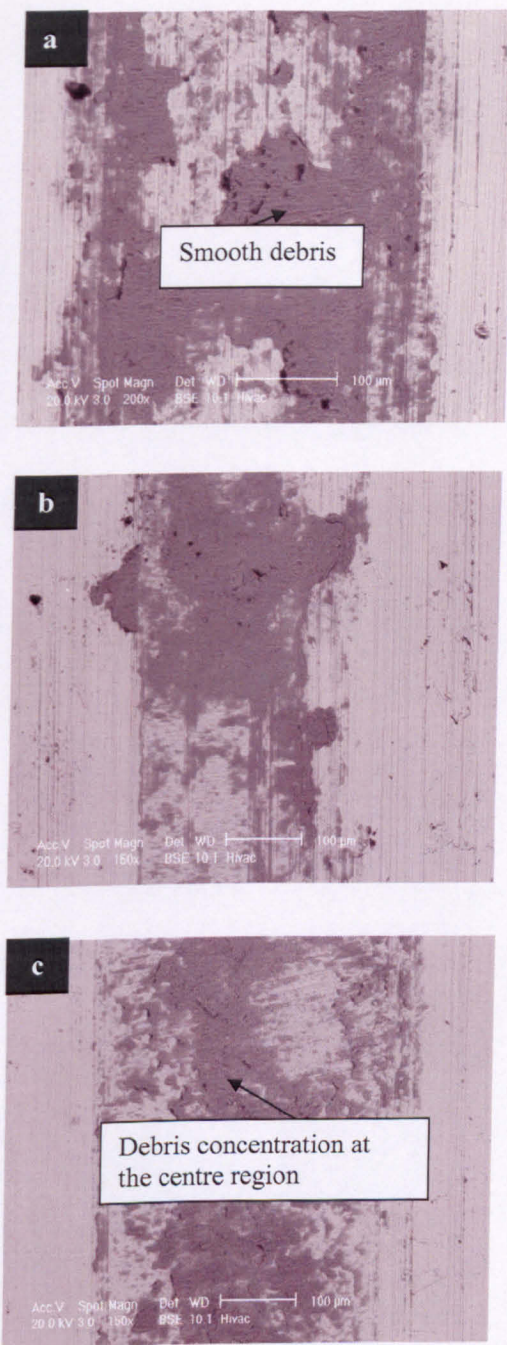


Figure 7-6: BEI of the worn areas on the round specimens at a stroke of 20  $\mu\text{m}$ :

- Along all scar width ( $\text{SCMV}_{(f)}//718_{(r)}$ ).
- Centre region ( $\text{SCMV}_{(f)}//A100_{(r)}$ ).
- Along all scar width ( $718_{(f)}//A100_{(r)}$ ).

Stroke direction ↑

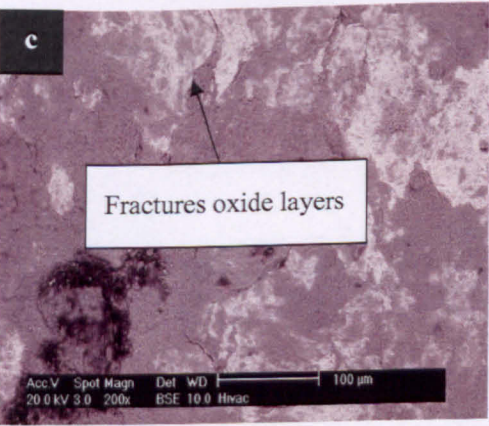
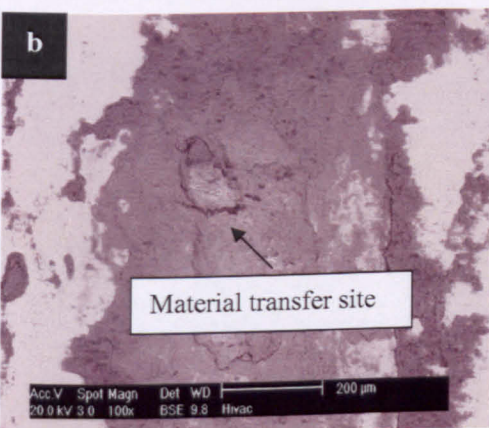
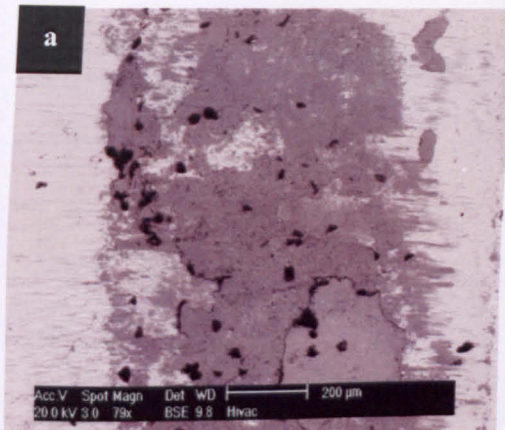


Figure 7-7: BEI of the worn areas on the flat specimens at a stroke of 50  $\mu\text{m}$ :

- Along all scar width ( $\text{SCMV}_{(f)}//718_{(r)}$ ).
- Centre region ( $\text{SCMV}_{(f)}//\text{A}100_{(r)}$ ).
- Random along scar width ( $718_{(f)}//\text{A}100_{(r)}$ ).

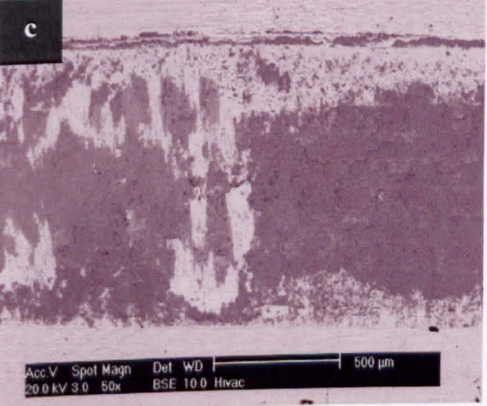
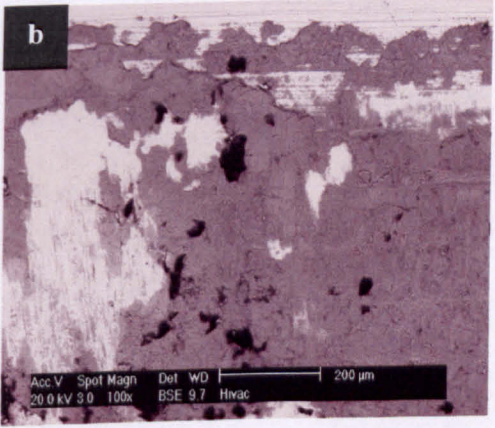
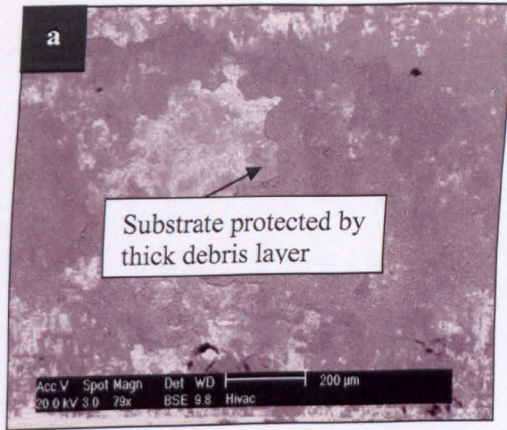


Figure 7-8: BEI of the worn areas on the round specimens at a stroke of 50  $\mu\text{m}$ :

- Along all scar width ( $\text{SCMV}_{(f)}//718_{(r)}$ ).
- Along all scar width ( $\text{SCMV}_{(f)}//\text{A}100_{(r)}$ ).
- Along all scar width ( $718_{(f)}//\text{A}100_{(r)}$ ).

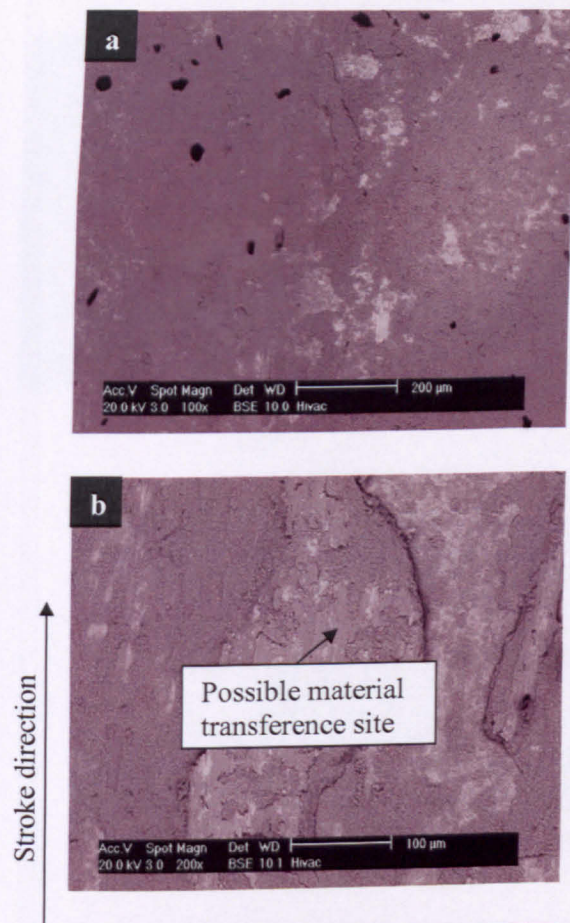


Figure 7-9: BEI of the worn areas on the flat specimens at a stroke of 100  $\mu\text{m}$ :

- Along all scar width ( $\text{SCMV}_{(f)}//718_{(r)}$ ).
- Along all scar width ( $\text{SCMV}_{(f)}//\text{A}100_{(r)}$ ).
- Along all scar width ( $718_{(f)}//\text{A}100_{(r)}$ ).

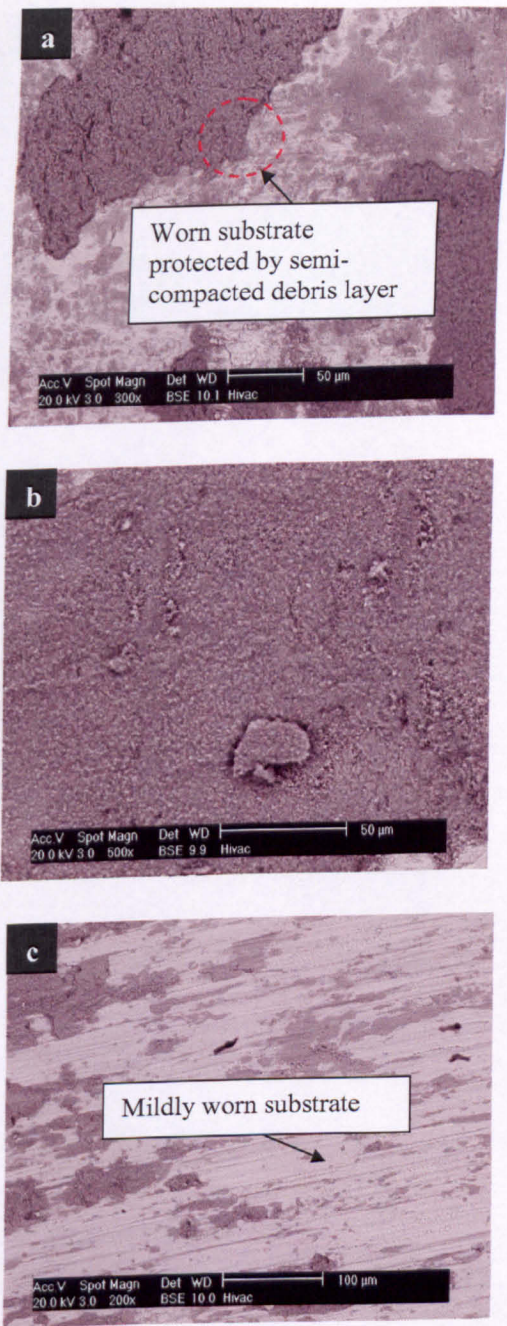
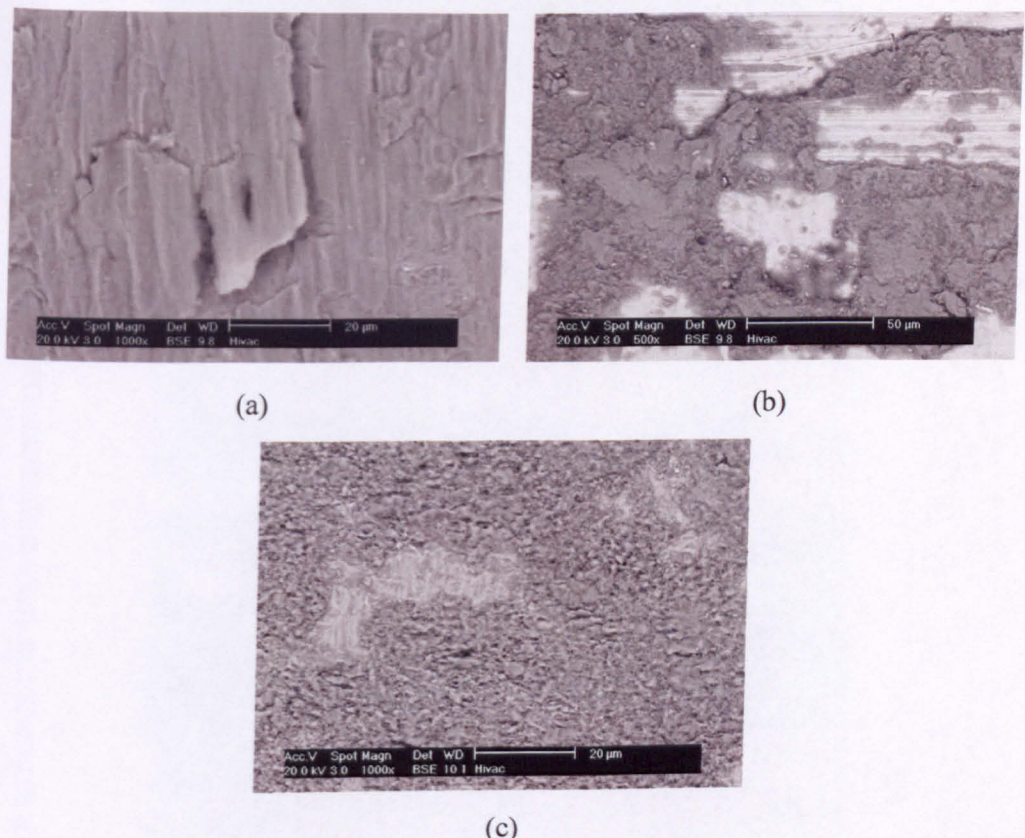


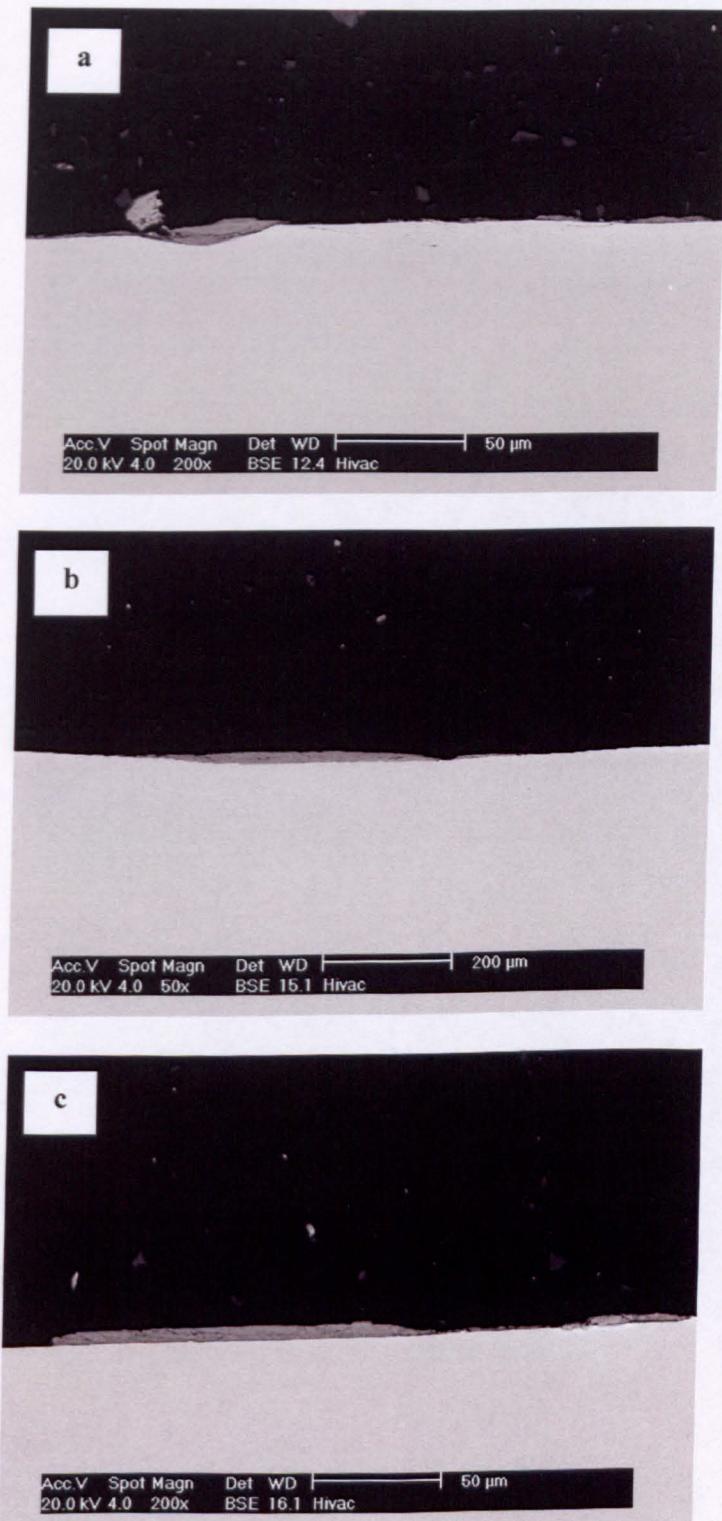
Figure 7-10: BEI of the worn areas on the round specimens at a stroke of 100  $\mu\text{m}$ :

- Along all scar width ( $\text{SCMV}_{(f)}//718_{(r)}$ ).
- Along all scar width ( $\text{SCMV}_{(f)}//\text{A}100_{(r)}$ ).
- Along all scar width ( $718_{(f)}//\text{A}100_{(r)}$ ).

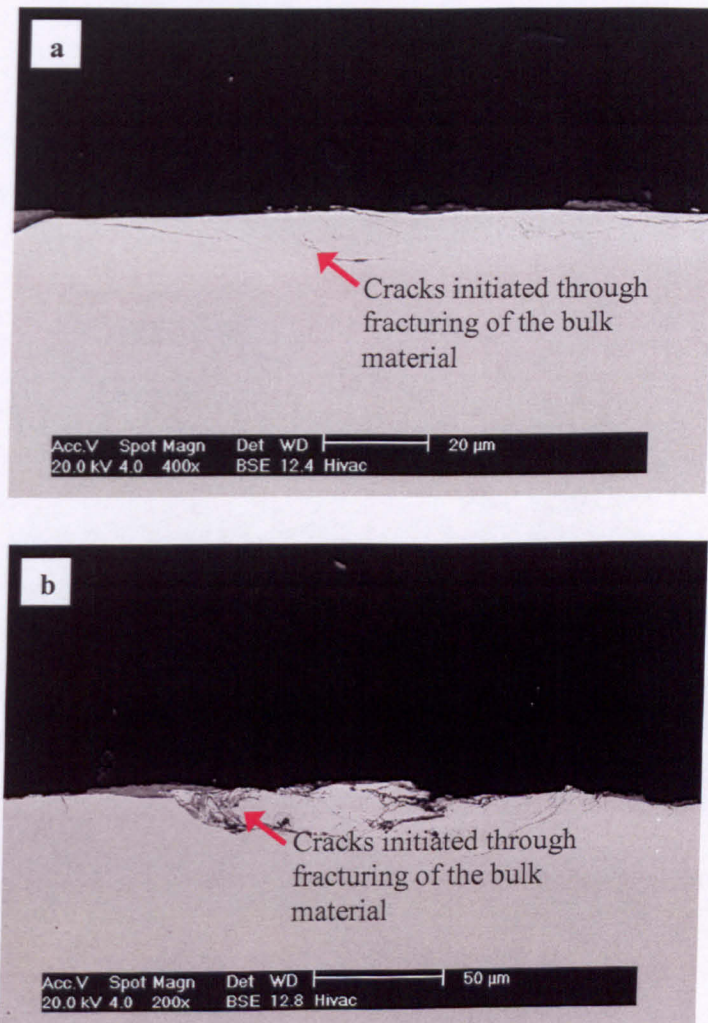


Figures 7-11: BEI of the different debris morphological features for the various material pairs (from flat specimen):-

- (a) Smeared debris at 20  $\mu\text{m}$  stroke (SCMV<sub>(f)</sub>//SCMV<sub>(r)</sub>).
- (b) Semi-particulate and smooth debris layers at 50  $\mu\text{m}$  stroke (SCMV<sub>(f)</sub>//A100<sub>(r)</sub>).
- (c) Particulate-like debris feature of the three self-against-nonself pairs at 100  $\mu\text{m}$  stroke (SCMV<sub>(f)</sub>//718<sub>(r)</sub>).



Figures 7-12: The cross-sectional view of the different debris layer thickness: (a) 20  $\mu\text{m}$ , (b) 50  $\mu\text{m}$ , and (c) 100  $\mu\text{m}$ .



Figures 7-13: The cross-sectioned view confirming the crack initiation site at 20  $\mu\text{m}$ :  
(a) SCMV alloy and (b) A100 alloy.

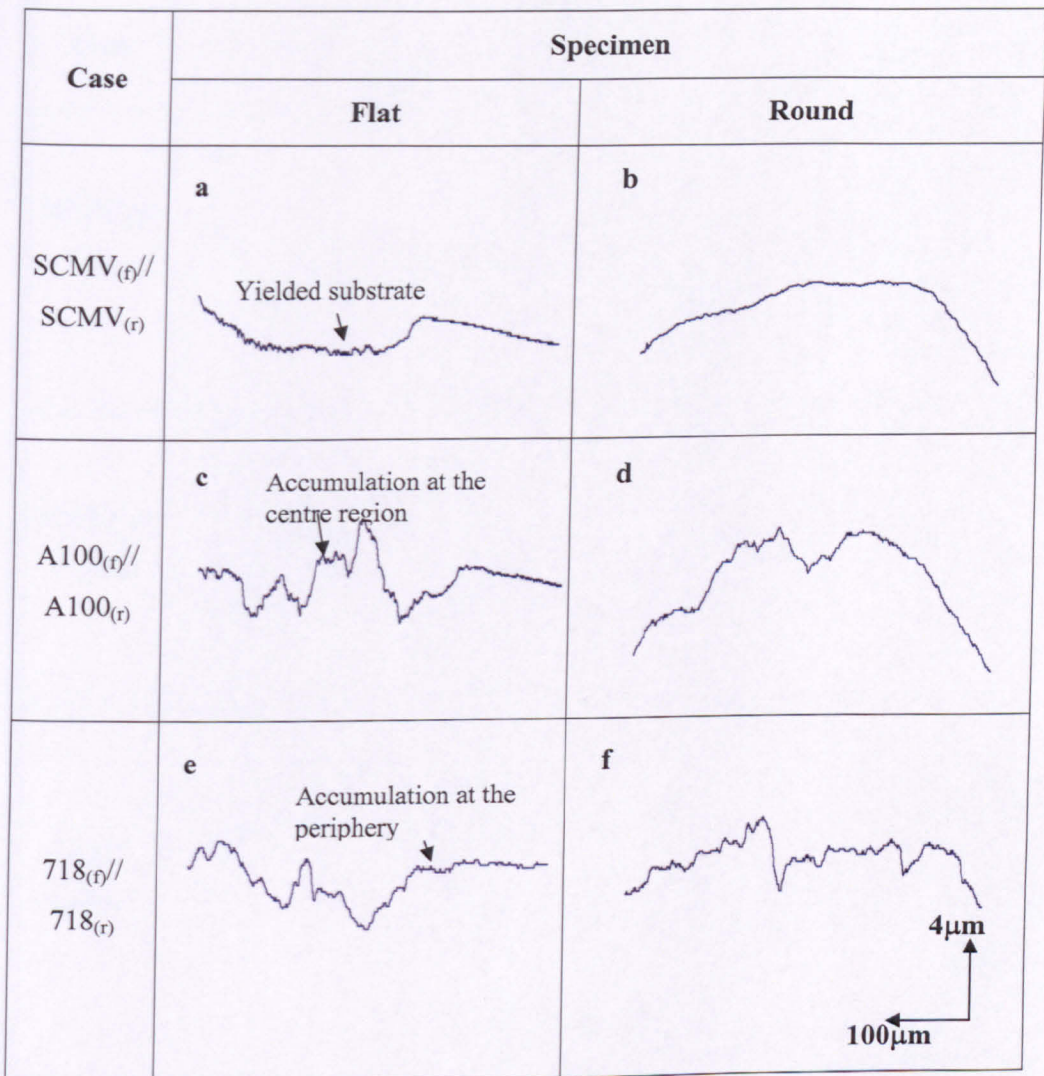


Figure 7-14: The surface profiles of both worn flat and round specimens involving self-against-self material pair fretted 500 N for 100,000 cycles.

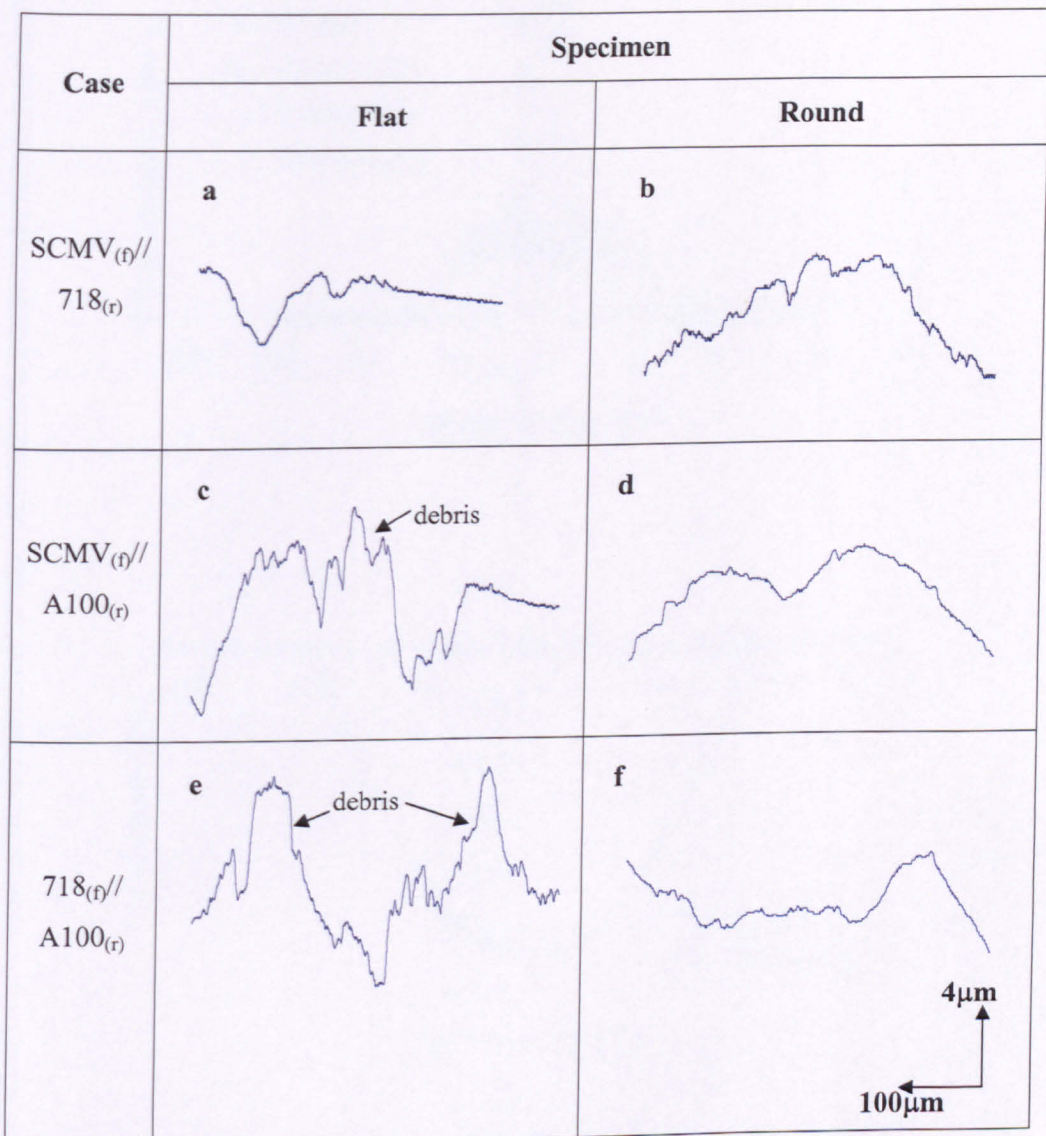


Figure 7-15: The surface profiles of both worn flat and round specimens involving the self-against-nonself pair fretted at 500 N for 100,000 cycles.

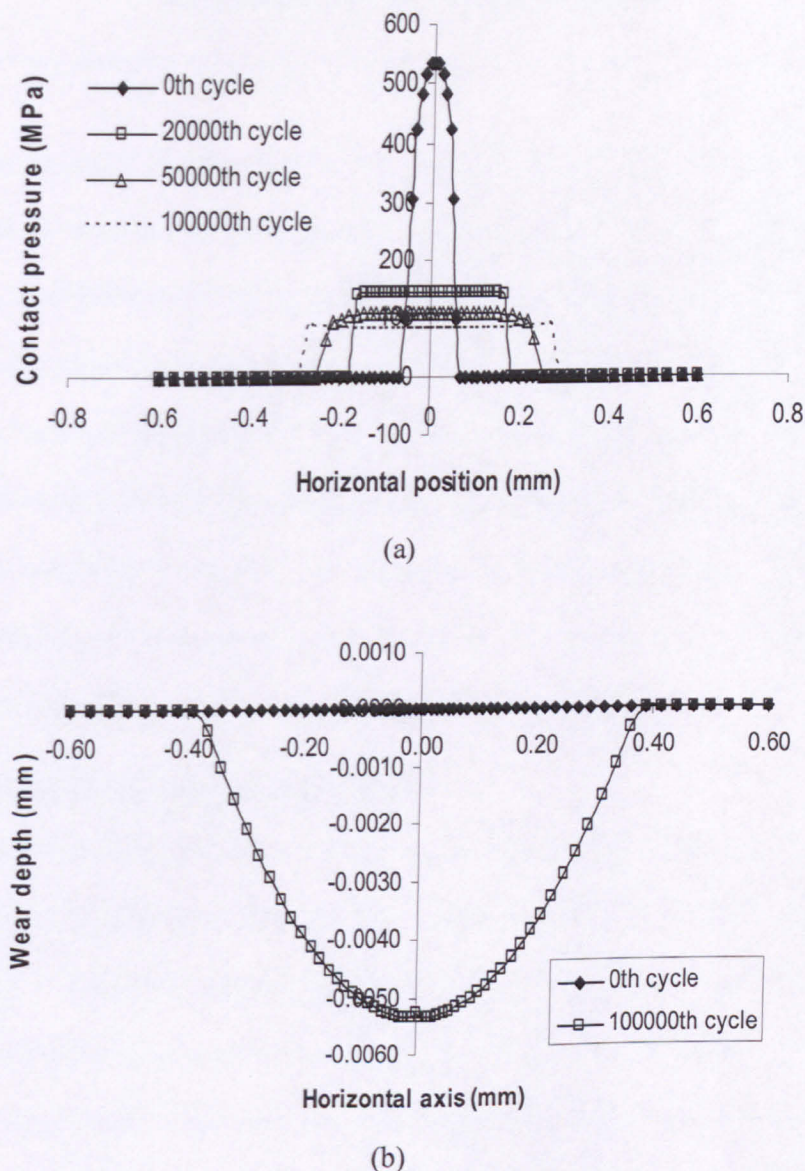


Figure 7-16: (a) Contact pressure versus number of cycles distribution and (b) FE predicted wear depth for  $\text{SCMV}_{(\text{f})}/\text{A}100_{(\text{r})}$  at 500 N and 50  $\mu\text{m}$  stroke.

---

## Chapter 8: Final discussion

---

The main objective of this research was to study and characterise the fretting wear behaviour of candidate high strength aeroengine materials, namely Super S/CMV (SCMV), AerMet®100 (A100) and Inconel 718 (718) alloys, particularly for use in main shaft spline couplings. The work was done by investigating the effect of variables such as temperature, lubrication, material combinations and surface modification, all of which encompass current and projected conditions experienced by spline couplings in service. The findings show interdependency between the fretting parameters and microstructure of the wear debris that determines the tribological behaviour of these transmission aeroengine materials.

### **Coefficient of friction and wear coefficient**

The fretting tests were carried out under stroke-controlled conditions making data measurement, such as tangential force and displacement easier to obtain and analyse. In this type of controlled regime, coefficient of friction (COF) and wear coefficient ( $k$ ) are affected by the applied fretting parameters and the effect is clearly reflected in the morphology of the wear scars. At room temperature, the three materials, Super S/CMV, AerMet®100, and Inconel 718 show average COF values ranging from 0.6 to 0.9. As the steady-state condition was reached, little difference in COF and  $k$  were noticed between the three materials, whether tested against themselves or each other. This indicates that the effect of the different material combinations on COF and  $k$  is relatively insignificant. Back-scattered images (Figures 7-5 to 7-10) show no visible morphological difference involving the worn specimens (round and flat) of the three

materials. However, these back-scattered images suggest that during the early cycles, a high COF can be related to the breaking of surface asperities, loose wear debris formation, and transition from two-body contact to third-body contact. Once the wear debris forms a compacted layer and third-body contact is established, the tribosystem stabilises and so does the wear. The experiments show that stroke has an effect on COF and  $k$ , i.e. as stroke increases, COF and  $k$  increase as well (Tables 7-3 and 7-4). The Archard wear equation shows a proportional relation between stroke and wear. Altering the magnitude of the stroke and wear will affect the slip and contact stress distributions. The bigger the stroke, the more wear debris produced and hence, wear damage is enhanced. However, it must be borne in mind that the wear coefficient is found to reduce with wear per unit sliding distance. As for the test duration,  $k$  is affected but not COF. This is only true when a constant stroke and normal load are applied. The finite element predictions show that slip (Figure 5-9b) is very little affected by wear but suggest that contact pressure contributes most to the wear damage (Figures 5-10a and b). Over longer duration, it is unlikely that the stresses will change dramatically and wear damage is reduced, i.e. reduction of  $k$  was observed (Table 5-2).

It is important to understand how the round-on-flat fretting test results of the present work can be related to the typical application of aeroengine spline couplings, including the issue of stroke-controlled versus load-controlled conditions [1]. As discussed in Chapter 5, in addition to the use of candidate materials and representative lubrication conditions, all tests in this thesis employed a contact load of 500 N, equivalent to an initial maximum Hertzian contact pressure of 550 MPa (for the specimen geometry), and three different strokes of 20  $\mu\text{m}$ , 50  $\mu\text{m}$ , and 100  $\mu\text{m}$  were investigated. FE modelling of scaled spline coupling tests [2] carried out at the

University of Nottingham under laboratory test conditions, have shown that both contact pressure and slip vary significantly over the length of engagement, from tooth-to-tooth and during the loading cycles. From these analyses, the round-on-flat load-stroke conditions have been identified as typical for a near end-of-engagement location under design loading. The rationale behind the present work is the development of techniques to model fretting wear in finite element models of test specimens or real assemblies. The key fretting data required in such finite element simulation techniques from round-on-flat tests are evolution of COF and wear coefficient. The rationale adopted here is that each round-on-flat test and the associated data corresponds to a local region of the finite element contact surface, e.g. one element, so that identification of the local, instantaneous FE contact pressure and slip (stroke) values then permits identification of an appropriate COF value and wear coefficient value, viz. from the appropriate round-on-flat test. Of course, in the absence of the required large database of experimental results covering the complete range of likely contact pressure and slip values, it is necessary to make some simplifying assumptions, e.g. that the local COF and wear coefficient values can be assumed to equal the global round-on-flat values. Further work is therefore required to expand the fretting database. An example methodology of how the present round-on-flat data can be employed with FE models to furnish wear predictions for complex couplings is described by Ratsimba et al. [3]. This work showed that simplified FE predictions, based on data obtained in this thesis, could provide predictions of wear depth which approximately envelop the measured data. Work is ongoing on the development of a more rigorous approach based on the extension of the incremental wear modelling technique of Ding [4] to more complex couplings.

### **Nitriding and lubrication**

The lifespan of contacting surfaces are affected by the fretting conditions as well as by the prevention methods used. The effectiveness of nitriding relies on fretting taking place on the different layers (hardness). The mixed nitrided (nitrided/non-nitrided) Super S/CMV specimen tests have the highest COF and  $k$ , followed by non-nitrided (non-nitrided/non-nitrided) specimens and lastly nitrided (nitrided/nitrided) specimens. The effect of hardness can be seen from the non-nitrided/nitrided combination. It is believed that the high COF was due to wearing of the porous layer, which is brittle and relatively hard. Once this porous layer fractures, the hard debris formed can act as an abrasive to cause further surface damage i.e. on uncoated surfaces. As for the non-nitrided/non-nitrided combination, direct metal-to-metal contact is involved and the core material is removed almost immediately as fretting wear proceeds. With the nitrided combination, fretting wear is taking place on the porous layer while the underlying material is initially spared. Once the nitrided layer is penetrated, fretting takes place on the underlying material, causing further damage. The porous region could serve as the crack initiation site, therefore suggesting that removal of the porous layer is crucial, but in the presence of lubricant, the porous structure is beneficial, acting as a reservoir to retain lubricant [5]. However, the availability and retention of lubricant is determined by the slip; the larger the slip, the more surface area is exposed to the lubricant, but more pores are also removed by fretting [6]. For the non-lubricated condition, slip and  $k$  are easier to predict because the variability of COF due to lubricant is removed. When lubricant is present, the slip and  $k$  are harder to predict due to the level of penetration and retention within the contact surface. This would also involve further complicated modelling. Nonetheless, COF and wear reduce when lubricant is present.

## Temperature

The Inconel 718 alloy wear-resistant property improves with temperature. The temperature has a profound effect on COF and  $k$ , both parameters were seen to reduce with temperature. The reduction is associated with the formation of an oxidised debris layer (a “glaze”), which is time dependent. It is believed that the glaze will continue to grow above 450°C, even when the tribosystem reaches stability [7]. At elevated temperatures, ion diffusion (metal and oxygen) is facilitated and enhances further growth of the glaze, which is believed to consist of a combination of oxide and spinel oxides [8]. The results suggested that the glaze layer formed in the temperature range from 150°C to 450°C is rich in iron and nickel.

## Debris role

In the longer term, the debris will eventually become the protective barrier by sharing part of the load, thereby minimising further damage (for Super S/CMV, AerMet®100, and Inconel 718). It is hoped that when the local surface breaks down and material is lost, the fretting action repairs the damage by creating more debris (depending on stroke magnitude), which is oxidised and compacted. This would depend on the type of oxides present i.e. first body material composition) and its stability at different temperatures. A strong bonding between the debris-substrate is vital to ensure structural integrity, if the debris layer is to remain intact (not fracture) and protect the surface. Figure 6-6a shows disrupted and fractured debris layers, indicating a possible poor bonding between the debris and substrate (Super S/CMV, AerMet®100, and Inconel 718). If this layer is removed, metal-to-metal contact (from third-body to two-body contact) is expected, hence causing more wear damage (COF and  $k$  increased). There will always be wear damage present and the contact

stresses determine this phenomenon; wear is affected by stroke, which in turn affects the shear traction. Unless an alternative method is available, lubrication is the main method for reducing COF and  $k$ , followed by surface modification.

### **Finite element (FE)**

The FE wear simulation tool gave insight into the contact stress evolution that contributed to fretting damage. This cannot be determined experimentally. This approach is based on a modified Archard equation and utilises local wear simulation to calculate the contact pressure. However, this method is currently computationally intensive. The new ‘UMESHMOTION’ subroutine in ABAQUS reduces the computational intensity during the simulation of material removal. Nonetheless, the fretting process is a complex process to model, and significant further developments are required to simulate effects such as the evolution of debris or transition from two-body to third-body contact. The absence of such complexities suggests reasons why the simulation is only accurate within about 30% to 50% compared to measured data.

### **References**

1. H. Mohrbacher, J.P. Celis, and J. R. Roos, “Laboratory testing of displacement and load induced fretting”, *Tribology International*, Vol. 28, No. 5, August 1995. pp. 269-278
2. S. B. Leen, I. J. Richardson, I. R. McColl, E.J. Williams, and T. R. Hyde, “Macroscopic fretting variables in a splined coupling under combined torque and axial load”, *Journal of Strain Analysis*, Vol. 36 (5), 2001, pp. 481-497
3. C. H. H. Ratsimba, I. R. McColl, E. J. Williams, S.B. Leen, and H. P. Soh, “Measurement, analysis, and prediction of fretting wear damage in a representative aeroengine spline coupling”, *Wear*, 257, 2004, pp. 1193-1206

4. J.Ding, Modelling of Fretting Wear, Ph.D Thesis, University of Nottingham, 2003
5. R. Leppanen and H. Jonsson, "Properties of Nitrided Components – A Result of the Material and the Nitriding Process", *Ovako Steel*, Report 1/1999, pp. 3-14
6. Q. Y. Liu and Z.R. Zhou, "Effect of displacement in oil-lubricated fretting", *Wear*, No. 239, 2000, pp. 237-243
7. F. H. Stott, D. S. Lin, and G. C. Wood, "The Structure And Mechanism of Formation of the 'Glaze' Oxide Layers Produced on Nickel-Based Alloys During Wear at High Temperatures", *Corrosion Science*, Vol. 13, 1973, pp. 449-469
8. F. H. Stott, D. S. Lin, G. C. Wood, and C. W. Stevenson, "The tribological behaviour of nickel and nickel-chromium alloys at temperature from 20°C to 800°C", *Wear*, Vol. 36, 1976, pp. 147-174

---

## Chapter 9: Conclusions

---

A study of the fretting wear behaviour of three high strength aeroengine materials (Super S/CMV, AerMet®100, and Inconel 718) has shown:

1. **Coefficient of friction and wear coefficient**

- a. There was little difference in coefficient of friction and wear coefficient between the three materials (Super S/CMV, AerMet®100, and Inconel 718) tested at room temperature whether, tested against themselves or each other.
- b. The coefficient of friction and wear coefficient were observed to increase with stroke for the three materials (Super S/CMV, AerMet®100, and Inconel 718) tested at room temperature when tested against themselves or each other. AerMet®100 alloy (self-against-self and mixed material combinations) has shown a reduction of coefficient of friction and wear coefficient with stroke when compared to Super S/CMV and Inconel 718.
- c. There was a negligible effect of test duration on coefficient of friction for the three materials (Super S/CMV, AerMet®100, and Inconel 718) tested at room temperatures. However, the wear coefficient was seen to decrease with increasing test duration. Little difference was observed between the three test materials (Super S/CMV, AerMet®100, and Inconel 718).

## 2. Effect of nitriding and lubrication

- a. Mixed nitrided and non-nitrided Super S/CMV specimens result in higher values of wear coefficients over shorter duration tests. There was negligible difference between the nitrided, mixed nitrided and non-nitrided Super S/CMV specimen tests in coefficient of friction and wear coefficient over the long term.
- b. Nitriding has no discernible lasting effect on coefficient of friction and wear coefficient.
- c. The lubricant has an effect on coefficient of friction and wear coefficient for the Super S/CMV specimens. Three coefficient of friction variation trends were observed; (i) typical – gradual increment, (ii) lower bound – low coefficient of friction, and (iii) upper bound – high coefficient of friction. These three regimes determine the magnitude of fretting damage and the wear coefficient. Limited lubrication makes wear prediction very difficult as well.
- d. The wear coefficient of the non-lubricated condition is approximately ten times that of the boundary-lubricated condition.
- e. The brittle porous layer is a potential reservoir for retaining lubricant.

## 3. Effect of temperature

- a. There was an appreciable reduction of coefficient of friction and wear coefficient for tests involving Inconel 718 alloy at moderate temperature, approximately 50% lower than the room temperature test.
- b. The reduction of wear damage was attributed to the formation of compacted debris beds, which consisted of a mixture of oxide and spinel oxide phases (the oxide phase acting as the precursor). It is

believed that this layer formation is temperature and time dependent; the layer becomes fully developed above 450°C.

- c. The Inconel 718 alloy is suitable for elevated temperature application due to better stability of the glaze layer in this temperature range.

#### 4. **Finite element correlation**

- a. The finite element wear simulation programme, based on modified Archard wear equation for material removal, is a valid tool capable of predicting fretting damage and contact stresses. The accuracy of the finite element predictions requires further improvement. The fretting phenomenon is complex; it is difficult to emulate other fretting phenomena such as debris contact, intermittent coefficient of friction evolution, and wear mechanism transitions.
- b. The built-in FORTRAN programme needs further improvements such as automated mesh updating of the contact area for better prediction accuracy.
- c. The fretting wear competes with fatigue cracking by both the removal of cracked material and the attenuation and displacement of the fatigue pertinent stresses. The predicted wear scar dimensions are generally in agreement with the measured values.

---

## **Chapter 10: Future work**

---

The purposes of this research to study the fretting behaviour of the various aeroengine materials that are likely to be used for manufacturing spline couplings, have been fulfilled. Also, various wear databases that are available to validate predicted data from finite element analyses have been initiated. However, numerous attempts in the area of fretting still require exploring by means of experimental and/or numerical techniques. The proposed ideas following are suggestions of directions this research could take:-

**1. Investigation into the fretting wear of different aeroengine materials at high temperatures.**

It is clearly that the existence of the oxide debris helps in minimising further fretting damage of the contact surface, at room temperature. Despite the beneficial effect from the oxide layer, it must be borne in mind that the engine operates at temperatures of 150°C and higher. Also, it is believed that the attained friction data resulted from fretting on the actual oxide layer itself. Therefore, the rheology of the oxide layer and its role at elevated temperatures should be investigated experimentally and potentially, by finite element simulation.

**2. Finite element simulation of dissimilar material combination**

The existing wear model simulates and validates the wear data using a simple two dimensional round-on-flat FE model for self-against-self combination.

Studying the effect of stress on the fretting wear behaviour of dissimilar elastic bodies may give an insight into the relation between fretting fatigue and fretting wear phenomenon. The stress components are the salient parameters controlling fatigue crack initiation and early crack growth. These investigations involve using 2D and 3D FE models.

### **3. Studying the evolution of oxide layer in association with fretting**

Loose oxide debris was produced during wear and compacted to form thicker agglomerates. Depending on the magnitude of the applied force, the debris remains loose but some is transformed into a new material (a new layer) with favourable properties. The morphological changes of the oxide features maybe associated with cracking phenomenon or even wear. The formed oxide layer provided protection for the underlying substrate (metal) and experienced minimal wear or possibly suppressed crack propagation (compressed). With loose debris, the features act as stress concentrators and possible areas for crack initiation, hence accentuating further surface damage. However, further investigation needs to be carried out to establish an understanding on the interaction between the oxide-substrate interface and the stresses.